

7-2-2011

Analysis, design and implementation of front-end reconfigurable antenna systems (FERAS)

Youssef Tawk

Follow this and additional works at: https://digitalrepository.unm.edu/ece_etds

Recommended Citation

Tawk, Youssef. "Analysis, design and implementation of front-end reconfigurable antenna systems (FERAS)." (2011).
https://digitalrepository.unm.edu/ece_etds/246

This Dissertation is brought to you for free and open access by the Engineering ETDs at UNM Digital Repository. It has been accepted for inclusion in Electrical and Computer Engineering ETDs by an authorized administrator of UNM Digital Repository. For more information, please contact disc@unm.edu.

Youssef Antoine Tawk

Candidate

Electrical and Computer Engineering Department

Department

This dissertation is approved, and it is acceptable in quality and form for publication:


Approved by the Dissertation Committee:


Dr. Christos Christodoulou

, Chairperson


Dr. Ganesh Balakrishnan


Dr. Sameer Hemmady


Dr. Thomas Atwood


Dr. Joseph Costantine

**ANALYSIS, DESIGN AND IMPLEMENTATION OF FRONT-END
RECONFIGURABLE ANTENNA SYSTEMS (FERAS)**

BY

YOUSSEF ANTOINE TAWK

Bachelor of Engineering-Computer and Communication Engineering, Notre
Dame University, 2006

Master of Engineering-Computer and Communication Engineering, The
American University of Beirut, 2007

DISSERTATION

Submitted in Partial Fulfillment of the
Requirements for the Degree of

Doctor of Philosophy

Engineering

The University of New Mexico
Albuquerque, New Mexico

May, 2011

©2011, Youssef Antoine Tawk

DEDICATION

To my parents, Antoine and Vicky

My brother, Charbel

My sister, Patricia

ACKNOWLEDGMENTS

I deeply acknowledge Dr. Christos Christodoulou for all his advising and mentoring throughout my studies. I thank him for everything he has done for me since the first day I joined his research group. He taught me how to be a good researcher. Dr. Christodoulou is a great mind and an amazing advisor.

My great acknowledgments and gratitude are to my committee members, Dr. Sameer Hemmady and Dr. Ganesh Balakrishnan, for their support, feedback and advice throughout this work.

I would like to thank Dr. Tom Atwood for being a member on my committee. I thank him for his great knowledge, kindness and modesty.

I am heartily grateful to Dr. Joseph Costantine for all his help; he taught me how to believe in my work, and how to inquire knowledge wherever that knowledge existed.

Finally, my greatest acknowledgments go to my parents who always supported and believed in me. Also special thanks to my friends, everywhere in this world, for their constant support throughout my studies.

**ANALYSIS, DESIGN AND IMPLEMENTATION OF FRONT-END
RECONFIGURABLE ANTENNA SYSTEMS (FERAS)**

BY

YOUSSEF ANTOINE TAWK

ABSTRACT OF DISSERTATION

Submitted in Partial Fulfillment of the
Requirements for the Degree of

Doctor of Philosophy

Engineering

The University of New Mexico
Albuquerque, New Mexico

May, 2011

**ANALYSIS, DESIGN AND IMPLEMENTATION OF FRONT-END
RECONFIGURABLE ANTENNA SYSTEMS (FERAS)**

By

Youssef Antoine Tawk

B. E. Computer and Communication Engineering, Notre Dame University, 2006

M.E. Computer and Communication Engineering, The American University of
Beirut, 2007

Ph.D., Engineering, University of New Mexico, 2011

ABSTRACT

The increase in demand on reconfigurable systems and especially for wireless communications applications has stressed the need for smart and agile RF devices that sense and respond to the RF changes in the environment. Many different applications require frequency agility with software control ability such as in a cognitive radio environment where antenna systems have to be designed to fulfill the extendable and reconfigurable multi-service and multi-band requirements. Such applications increase spectrum efficiency as well as the power utilization in modern wireless systems.

The emphasis of this dissertation revolves around the following question:

“Is it possible to come up with new techniques to achieve reconfigurable antenna systems with better performance?”

Two main branches constitute the outline of this work. The first one is based on the design of reconfigurable antennas by incorporating photoconductive switching elements in

order to change the antenna electrical properties. The second branch relies on the change in the physical structure of the antenna via a rotational motion.

In this work a new photoconductive switch is designed with a new light delivery technique. This switch is incorporated into new optically pumped reconfigurable antenna systems (OPRAS). The implementation of these antenna systems in applications such as cognitive radio is demonstrated and discussed. A new radio frequency (RF) technique for measuring the semiconductor carrier lifetime using optically reconfigurable transmission lines is proposed. A switching time investigation for the OPRAS is also accomplished to better cater for the cognitive radio requirements.

Moreover, different reconfiguration mechanisms are addressed such as physical alteration of antenna parts via a rotational motion. This technique is supported by software to achieve a complete controlled rotatable reconfigurable cognitive radio antenna system. The inter-correlation between neural networks and cellular automata is also addressed for the design of reconfigurable and multi-band antenna systems for various applications.

Table of Contents

LIST OF FIGURES	XV
LIST OF TABLES	XXV
CHAPTER 0 MOTIVATION	1
CHAPTER 1 WHY RECONFIGURABLE ANTENNAS?	4
1.1 Introduction	4
1.2 Advantages of reconfigurable antennas	6
1.3 The different types of reconfigurable antennas	7
1.4 How to achieve reconfigurable antennas?	9
CHAPTER 2 LITERATURE REVIEW ON RECONFIGURABLE ANTENNAS...	12
2.1 Introduction	12
2.2 Antenna Designs Based on the Integration of RF-MEMS	13
2.2.1 Reconfigurable Radiation Pattern Antenna:	14
2.2.2 Reconfigurable Polarization Antenna:	15
2.2.3. Reconfigurable Antenna with Resonant Frequency Tuning:	16
2.2.4. Reconfigurable Antenna with Notch Frequency Tuning:	18
2.2.5. Biasing of RF-MEMS Switches:	18
2.3 Antenna Designs Based on the Integration of PIN diodes	21
2.3.1 Reconfigurable Polarization Antenna:	22
2.3.2 Reconfigurable Pattern and Polarization Antenna:	22
2.3.3 Reconfigurable Radiation Pattern Antenna:	24
2.3.4 Band Reject Reconfigurable Antenna:	25

2.3.5. Biasing of PIN Diode Switches:	26
2.4 Antenna Designs Based on the Integration of Varactors:	27
2.4.1 Reconfigurable Antenna with Resonance Tuning:.....	28
2.4.2 Reconfigurable Polarization Antenna with Resonance Tuning:	29
2.4.3 Biasing of the Varactor Switches:	30
2.5 Antenna Designs Based on the Integration of Photoconductive Switches	30
2.6 Conclusion	39
CHAPTER 3 PHYSICS AND RF PROPERTIES OF SEMICONDUCTOR SWITCHES	41
3.1 Introduction	41
3.2 Energy Band Models of Semiconductor Materials	42
3.2.1 Direct and Indirect Bandgap Semiconductors:.....	44
3.2.2 Electrons and Holes:.....	45
3.3 Doped Semiconductors	46
3.4 Electron and Hole Statistics.....	48
3.4.1 Density of States:	48
3.4.2 Probability of occupancy:.....	49
3.4.3 Formulas for n and p:.....	50
3.5 Modeling the RF Properties of the Silicon under Light Illumination	51
3.6 Switch Fabrication.....	56
3.7 Conclusion	59

CHAPTER 4 OPTICALLY PUMPED RECONFIGURABLE ANTENNA SYSTEM

(OPRAS)	61
4.1 Introduction	61
4.2 Optically Switched Transmission Line	62
4.3 Frequency Reconfigurable Antenna Design.....	65
4.3.1 Stripline Fed Optically Reconfigurable Antenna Structure:	65
4.3.2 CPW Fed Optically Reconfigurable Antenna Structure:.....	70
4.4 Determining the Gain of the Stripline fed Antenna	75
4.4.1 The Reflection Measurement Technique:	75
4.4.2 The Experiment Setup for Calculating the Gain:.....	77
4.5 Conclusion	78

CHAPTER 5 DEMONSTRATION OF A COGNITIVE RADIO FRONT-END USING OPTICALLY PUMPED RECONFIGURABLE ANTENNA SYSTEMS

(OPRAS)	80
5.1 Introduction	80
5.2 What is Cognitive Radio?	80
5.2.1 Open Sharing:.....	82
5.2.2 Hierarchical sharing:	83
5.2.3 Dynamic Spectrum Allocation:	84
5.3 Comparison between “OPRAS” and RF-MEMS/PIN Diodes Based Reconfigurable Antenna Systems.....	86
5.4 Reconfigurable Antenna Design.....	90

5.5 Cognitive Radio Antenna Structure	92
5.6 Laser Diode Integration.....	94
5.7 Fabrication and Results.....	96
5.7.1 UWB Antenna:.....	97
5.7.3 Narrowband Reconfigurable Antenna:	99
5.7.3 Coupling:.....	100
5.7.4 Radiation Pattern:.....	103
5.8 Additional Cognitive Radio Antenna Design.....	103
5.8.1 Reconfigurable Antenna Design:	104
5.8.2 The cognitive radio antenna structure:	110
5.9 Conclusion	115
CHAPTER 6 IMPLEMENTATION OF A COGNITIVE RADIO RECEIVE	
ALGORITHM.....	116
6.1 Introduction	116
6.2 The experimental Setup.....	117
6.3 Conclusion	121
CHAPTER 7 MEASURING THE SWITCHING SPEED OF AN OPTICALLY	
RECONFIGURABLE ANTENNA SYSTEM.....	123
7.1 Introduction	123
7.2 Carrier Lifetime.....	123
7.2.1 Recombination Lifetime:.....	124
7.2.2 Generation Lifetime:.....	127

7.3 Microwave Photoconductive Decay (μ -PCD).....	128
7.4 Switching Speed Experiment for an Optically Driven Transmission Line.....	133
7.5 The turning ON and OFF for an Optically Pumped Reconfigurable Antenna System (OPRAS)	142
7.5.1 Antenna Structure:	143
7.5.2 Experimental Setup:	148
7.6 Delay Measurement.....	157
7.7 Conclusion	158
CHAPTER 8 SOFTWARE CONTROLLED ROTATABLE RECONFIGURABLE ANTENNA SYSTEM	123
8.1 Introduction	159
8.2 Frequency Reconfigurable Rotatable Microstrip Antenna Design	159
8.3 A Cellular Automata Reconfigurable Microstrip Antenna Design.....	166
8.4 A New Reconfigurable Antenna for Cognitive Radio	177
8.4.1 Sensing Antenna Design:	178
8.4.2 Reconfigurable Communicating Antenna Design:.....	181
8.4.3 Cognitive Radio Antenna Design:	184
8.5 Cognitive Radio Front-End Using Rotatable Controlled Reconfigurable Antennas.....	188
8.5.1 Antenna Structure:	189
8.5.2 Stepper Motor Controller:	191
8.5.3 Fabrication and Results:.....	194
8.6 Conclusion	203

CHAPTER 9 CONCLUSIONS AND FUTURE WORK	204
REFERENCES	206

List of Figures

Figure 2.1 Reconfigurable single-arm rectangular spiral antenna integrated with four RF-MEMS switches. (a) Top and side view of spiral configuration and its feeding. (b) Spiral antenna with its dc biasing network (left) and microscopic picture of the fabricated RF-MEMS capacitive switch (center and right) [15].....	15
Figure 2.2 (a) The basic dimension of the antenna structure (b) zoom-in of the feeding system and the series MEMS-switch structure [24].....	17
Figure 2.3 Architecture of the microstrip fed reconfigurable annular slot (a) Top view (b) bottom view [25].....	19
Figure 2.4 Antenna schematic (a) U-shaped slot (b) L-shaped slot [23]	20
Figure 2.5 (a) Schematic and cross-section of the switch model (b) Top view of the switch model illustrating the bias lines (c) Photograph of the fabricated switch [16].....	21
Figure 2.6 Example of the antenna layout in [16] plus the bias network	21
Figure 2.7 (a) Geometry of the antenna structure (b) The operation mechanism of the antenna [37].....	23
Figure 2.8 Antenna layers: (a) radiating elements (b) coupling elements (c) active and passive circuit components [34].....	24
Figure 2.9 The fabricated antenna prototype [40]	25
Figure 2.10 The fabricated antenna in [48]	26
Figure 2.11 An example of the biasing of PIN diodes [30].....	27
Figure 2.12 Topology of the reconfigurable dual-band slot antenna using varactors [51].	29
Figure 2.13 Layout of the slot-ring antenna [55].....	30

Figure 2.14 The antenna structure discussed in [58]	32
Figure 2.15 Schematic drawing for the RECAP antenna (monopole form) showing which switches are open and closed when wires are used for closed switches. (a) Broadband, bidirectional, broadside design. (b) Narrow-band, unidirectional, end-fire design [62]	34
Figure 2.16 Schematic drawing showing the arrangement of the major components that makes up the prototype RECAP antenna. Details are given for the control of a single switch	34
Figure 2.17 Switched dipole antenna [63].....	35
Figure 2.18 Reconfigurable patch antenna with silicon switches [69]	36
Figure 2.19 Schematic diagram of a spatially light modulator reconfigurable photoconductive antenna [71]	38
Figure 2.20 Projected images of a phased array and bow-tie antenna of the GaAs substrate [71].....	38
Figure 3.1 Energy band model in Si.....	43
Figure 3.2 The energy band models for insulators, semiconductors, and conductors	44
Figure 3.3 Electrons in the conduction band and holes in the valence band	46
Figure 3.4 “DC+RF” conductivity of the silicon switch.....	55
Figure 3.5 Change in the real part of the silicon dielectric constant at $f=5\text{GHz}$	56
Figure 3.6 Change in the imaginary part of the silicon dielectric constant at $f=5\text{GHz}$	57
Figure 3.7 The mask used to produce the corresponding image	58
Figure 3.8 The printed pattern on the silicon wafer.....	58

Figure 3.9 Silicon wafer	59
Figure 4.1 An optically switched transmission line	62
Figure 4.2 The fabricated prototype for the optically switched transmission line	63
Figure 4.3 The back side view of the fabricated prototype	63
Figure 4.4 The simulated return loss for the optically switched transmission line.....	64
Figure 4.5 The measured return loss for the optically switched transmission line.....	65
Figure 4.6 The measured transmission for the optically switched transmission line.....	66
Figure 4.7 The stripline fed optically reconfigurable antenna structure	67
Figure 4.8 The top view of the fabricated antenna structure.....	68
Figure 4.9 The antenna bottom layer	68
Figure 4.10 The simulated antenna return loss	69
Figure 4.11 The measured antenna return loss	69
Figure 4.12 The computed radiation pattern at 18.4 GHz (solid line) and 12.2 GHz (dotted line) in the xz plane	70
Figure 4.13 The CPW fed antenna structure.....	71
Figure 4.14 The top layer of the CPW reconfigurable antenna structure.....	72
Figure 4.15 The bottom layer of the antenna	72
Figure 4.16 The simulated antenna return loss for the CPW fed antenna	73
Figure 4.17 The measured return loss for the CPW fed antenna.....	73
Figure 4.18 The computed antenna radiation pattern at $f= 1$ GHz when both switches are OFF (solid line) and at $f= 3$ GHz when both switches are ON (dotted line) in the XZ plane	74

Figure 4.19 The computed antenna radiation pattern at $f= 2.5$ GHz when both switches are OFF (solid line) and ON (dotted line) in the (a) XZ plane and the (b)YZ plane..	75
Figure 4.20 The reflection method for gain determination.....	76
Figure 4.21 The experiment setup to determine the gain of the CPW fed optically reconfigurable antenna structure.....	78
Figure 5.1 The proposed FCC solutions to the spectrum underutilization.....	82
Figure 5.2 The generic cognitive radio work-flow diagram.....	86
Figure 5.3 The relation between the optical power and the voltage/current for the laser diode used in this work.....	89
Figure 5.4 The optically reconfigurable antenna structure	90
Figure 5.5 The antenna return loss for different cases of the photoconductive switches...	91
Figure 5.6 The normalized radiation pattern in the X-Z plane (thick line: 3.6 GHz, dotted line: 4.6 GHz, thin line: 5.2 GHz)	91
Figure 5.7 The top layer of the cognitive radio antenna structure.....	92
Figure 5.8 The bottom layer of the cognitive radio antenna structure.....	93
Figure 5.9 The physical structure of a laser diode	94
Figure 5.10 The integration of the laser diode into the antenna structure.....	95
Figure 5.11 The drilled copper piece which supports the laser diodes	95
Figure 5.12 The antenna radiation pattern in the YZ plane ($\Phi=90^0$)	96
Figure 5.13 The top view of the fabricated antenna prototype	97
Figure 5.14 The bottom view of the fabricated antenna prototype.....	97

Figure 5.15 The measured and simulated return loss for the sensing antenna when both switches are OFF.....	98
Figure 5.16 Contour map of the normalized radiation pattern for the UWB antenna in the XZ plane ($\Phi=0^0$)	99
Figure 5.17 The simulated antenna return loss for the reconfigurable antenna	100
Figure 5.18 The measured antenna return loss for the reconfigurable antenna	101
Figure 5.19 The simulated and the measured coupling for the case when both switches are OFF and when S1:OFF / S2:ON.....	102
Figure 5.20 The simulated and the measured radiation pattern for the three different cases of the switches in the XZ plane ($\Phi=0^0$).....	103
Figure 5.21 The antenna structure (a) top layer (b) bottom layer	105
Figure 5.22 The fabricated antenna (a) bottom layer (b) top layer.....	106
Figure 5.23 The comparison between the simulated and the measured return loss.....	108
Figure 5.24. The measured return loss for the three different cases.....	108
Figure 5.25 The normalized antenna radiation pattern in the XZ plane (solid line) and the YZ plane (dotted line)	109
Figure 5.26 The cognitive radio antenna structure	110
Figure 5.27 The fabricated antenna prototype.....	111
Figure 5.28. The antenna return loss for the sensing antenna when both switches are OFF	112
Figure 5.29. Comparison between the simulation and the measurement for the case when S2 is ON	113

Figure 5.30. The measured coupling for Case 1 (both OFF) and Case 2 (S1 ON).....	113
Figure 5.31 The normalized antenna radiation pattern in the XZ plane ($\Phi=0^\circ$) for the three different cases	115
Figure 6.1 A cognitive radio chain.....	116
Figure 6.2 The cognitive radio receive channel experiment work-flow	117
Figure 6.3 The experiment setup	118
Figure 6.4 The sensing antenna spectrum	119
Figure 6.5 Controlling the frequency sweeper and the spectrum analyzer.....	120
Figure 6.6 The switching decision tree which determines which switch to be activated .	121
Figure 7.1 Recombination mechanisms: (a) SRH, (b) radiative, (c) direct Auger, and (d) trap assisted auger	125
Figure 7.2 The change in the reflected power due to the change in the sample conductivity	130
Figure 7.3 The μ -PCD system used at Sandia National Laboratory.....	130
Figure 7.4 The three different regions of the μ -PCD technique	131
Figure 7.5 The optically switched transmission line and its return loss for 0 mW and 50 mW	133
Figure 7.6 The flowchart for the experiment setup using the optically switched transmission line	134
Figure 7.7 The experiment setup for measuring the switching time for the optically reconfigurable transmission line	136
Figure 7.8 A zoomed view for the experiment setup.....	137

Figure 7.9 The reflected voltage for the CW driven laser diode.....	138
Figure 7.10 The driving and the triggering pulse for the experiment setup	139
Figure 7.11 The change in the reflected voltage for the pulsed driven laser diode.....	140
Figure 7.12 The change in the reflected voltage when the laser diode in ON/OFF for a duration of 80 μ sec	140
Figure 7.13 The turning ON of the switch integrated with the optically switched transmission line.....	141
Figure 7.14 The turning OFF of the switch integrated with the optically switched transmission line.....	142
Figure 7.15 The antenna structure for the switching speed experiment.....	144
Figure 7.16 The fabricated antenna structure (a) top layer (b) bottom layer	145
Figure 7.17 The measured tuning in the antenna return loss.....	146
Figure 7.18 The comparison between the simulated and the measured antenna return loss (a) switch OFF (b) switch ON	147
Figure 7.19 The normalized antenna radiation pattern in the XZ plane when the switch is OFF (solid line, $f=2.21$ GHz) and ON (dotted line, $f=2.17$ GHz).	147
Figure 7.20 The change in the received voltage by the reconfigurable antenna at $f=2.21$ GHz.....	148
Figure 7.21 The change in the antenna received voltage when the horn antenna is transmitting at $f=2.17$ GHz.....	149
Figure 7.22 The flowchart to compute the turning ON and OFF of the OPRAS.....	151
Figure 7.23 The experiment setup for the switching speed of the OPRAS.....	151

Figure 7.24 The spectrum of the output of the mixer	152
Figure 7.25 The spectrum of the output of the low pass filter	152
Figure 7.26 The change in the antenna received voltage at $f=2.21$ GHz	153
Figure 7.27 The change in the received voltage by the reconfigurable antenna when tuning from 2.21 GHz to 2.17 GHz.....	154
Figure 7.28 The change in the received voltage by the reconfigurable antenna when tuning from 2.17 GHz to 2.21 GHz.....	155
Figure 7.29 The flowchart to compute the delay in the cables used in the experiment....	157
Figure 7.30 The flowchart to compute the delay in the cables and the equipments used in the experiment.....	158
Figure 8.1 Rotatable Reconfigurable Antenna Structure	160
Figure 8.2 The dimensions for the different shapes of the reconfigurable antenna structure	160
Figure 8.3 The fabricated antenna prototype.....	161
Figure 8.4 The comparison between the simulated and the measured return loss for the reconfigurable antenna structure	164
Figure 8.5 The antenna radiation pattern in the xz plane	165
Figure 8.6 The antenna gain for the rotatable reconfigurable antenna design	165
Figure 8.7 Common neighborhood in 2-D cellular automata (a) 5-cell von Neuman neighborhood (b) 9-cell Moore neighborhood.....	167
Figure 8.8 A cellular automata “Game of Life” example	170
Figure 8.9 The two antennas set (a) For stages 1 and 3 (b) For stages 2 and 4.....	171

Figure 8.10 Fabricated Antenna Structure for Stages: (a) 1 and 3 (b) 2 and 4	171
Figure 8.11 The simulated and the measured antenna return loss for (a) stage 1 (b) stage 3	173
Figure 8.12 The simulated and the measured antenna return loss for (a) stage 2 (b) stage 4	174
Figure 8.13 An example of “Game of Life” cellular automata applied to a microstrip antenna	175
Figure 8.14 The fabricated antenna structure for the fuzzy ARTMAP neural network testing	177
Figure 8.15 The simulated, measured and ARTMAP tested return loss.....	178
Figure 8.16 The antenna structure and its return loss.....	179
Figure 8.17 The sensing antenna structure.....	180
Figure 8.18 The return loss for the sensing antenna	180
Figure 8.19 The normalized antenna radiation pattern for $f=4.5$ GHz (thin line), $f=7.5$ GHz (thick line) and $f=10.5$ GHz (dotted line) in the XZ plane	181
Figure 8.20 The “reconfigurable communicating” antenna structure	182
Figure 8.21 The process of rotation.....	183
Figure 8.22 Frequency tuning for the “reconfigurable communicating” antenna	183
Figure 8.23 The normalized reconfigurable antenna radiation pattern at $f=6.65$ GHz (thick line) and $f=4$ GHz (thin line).....	184
Figure 8.24 The cognitive antenna structure.....	185
Figure 8.25 The fabricated antenna prototype.....	185

Figure 8.26 The sensing antenna return loss for position 1	186
Figure 8.27 The “reconfigurable communicating” return loss for (a) position 2 (b) position 1	187
Figure 8.28 The antenna coupling for both positions	188
Figure 8.29 The antenna structure (dimensions in mm)	190
Figure 8.30 UWB Antenna Radiation Pattern at $f=3$ GHz (thin line), 6 GHz (thick line), and 9 GHz (dotted line).....	190
Figure 8.31 Antenna reconfigurability process	191
Figure 8.32 The number of steps needed for each rotation.....	192
Figure 8.33 The stepper motor used in this work.....	193
Figure 8.34 The experiment setup	193
Figure 8.35 The flowchart of the LABVIEW algorithm.....	194
Figure 8.36 The fabricated antenna prototype.....	195
Figure 8.37 The sensing antenna return loss	196
Figure 8.38 A zoomed view of the connection between the feed line and the rotating part	197
Figure 8.39 A comparison between the measured and simulated return loss for the reconfigurable antenna section.....	198
Figure 8.40 The coupling between the two sections.....	199
Figure 8.41 The simulated (solid line) and the measured (dotted line) radiation pattern for the reconfigurable antenna.....	203

List of Tables

Table 1.1 The different wireless standards	6
Table 1.2 The process of achieving the required reconfigurability	8
Table 1.3 Reconfigurable antennas applications	9
Table 1.4 The different types of switches used in the design of reconfigurable antennas ..	10
Table 2.1 Correspondence between the antenna radiation states and the required RF- MEMS switches	16
Table 3.1 Semiconductor Materials	41
Table 3.2 Properties of some semiconductor materials.....	47
Table 3.3 Intrinsic carrier concentration at $T=300^0$ K.....	48
Table 3.4 The mobility parameters for silicon	52
Table 3.5 Relation between power levels and carrier concentration.....	53
Table 4.1 The simulated and the measured gain.....	78
Table 5.1 Comparison between different switching techniques.....	89
Table 5.2 The measured coupling (dB) for the three different states of the switches....	102
Table 5.3 The covered bands by the reconfigurable antenna for the different cases of the switches	112
Table 5.4 The measured coupling (dB) for the three different states of the switches....	114
Table 7.1 The switching time for the optically driven transmission line and the OPRAS	156
Table 8.1 The antenna peak gain values.....	166

Table 8.2 Coil activation sequence	194
Table 8.3 Frequency reconfigurability.....	197
Table 8.4 The measured coupling	199
Table 8.5 The antenna peak gain.....	200

Chapter 0

Motivation

Reconfigurable antennas have the capacity to change their operating characteristics through different methods that may be electrical, mechanical or optical. Redistribution of surface currents or of the effective aperture's electromagnetic fields is the basis for such antenna reconfiguration. The reconfiguration of an antenna is simplified to a reversible change in the antenna impedance and radiation properties. Such antennas have major benefits especially in servicing highly complicated systems by their ability to change their topology and behavior to adapt to environmental conditions and to remain synchronized with system requirements.

The use of reconfigurable antennas in the past ten years has been based on traditional switching elements. Such switching elements (RF MEMS, PIN diodes, Varactors) require a complicated biasing networks that interfere with the antenna radiation mechanism as well as they add undesired resonances to the antenna performance. The rise of optically pumped switching elements and the incorporation of such elements into the antenna structure have alleviated the problem and added a new tool for antenna designers to utilize. This type of switching mechanism lacks the need for biasing networks which suppresses undesired radiation interference.

Two main branches constitute the outline of this work. The first one is based on the design of reconfigurable antennas by incorporating photoconductive switching elements in order to change the antenna electrical properties. The second branch relies on

the change of the physical structure of the antenna via a rotational motion. The major contributions in these two branches can be summarized as follows:

- Proposing a new technique for light delivery to the photoconductive switching elements
- Designing and integrating new optically pumped reconfigurable antenna systems (OPRAS)
- Implementing fully software controlled optically reconfigurable cognitive radio antenna system
- Proposing a new RF technique for measuring the carrier lifetime in a semiconductor material using optically reconfigurable transmission line
- Measuring the switching time of an optically reconfigurable antenna
- Investigating a new design technique for the implementation of reconfigurable antennas based on the physical alteration of the antenna radiating parts via a rotational motion
- Implementing a software controlled rotatable reconfigurable cognitive radio antenna system
- Designing reconfigurable and multi-band antennas using the inter-correlation between Neural Networks and Cellular Automata

This dissertation is composed of the following nine chapters:

Chapter 1 entitled “*Why Reconfigurable Antennas?*” discusses the importance of using such antennas. The different types of these antennas and their design process are discussed as well.

Chapter 2 entitled “*Literature Review on Reconfigurable Antennas*” presents a summary of some interesting previously published reconfigurable antennas.

Chapter 3 entitled “*Physics and RF properties of semiconductor switches*” details the basic physical properties and the change in the RF characteristics of a photoconductive switch under different light illumination.

Chapter 4 entitled “*Optically Pumped Reconfigurable Antenna System (OPRAS)*” presents novel frequency reconfigurable antenna designs using photoconductive silicon elements as optical switches.

Chapter 5 entitled “*Demonstration of a Cognitive Radio Front-End using Optically Pumped Reconfigurable Antenna Systems (OPRAS)*” presents different cognitive radio front-end using optically reconfigurable antennas.

Chapter 6 entitled “*Implementation of a Cognitive Radio Receive Algorithm*” shows a cognitive radio experiment using one of the optically pumped reconfigurable antenna systems presented in the previous chapter.

Chapter 7 entitled “*Measuring the Switching Speed of an Optically Reconfigurable Antenna System*” deals with measuring the carrier lifetime of a semiconductor switch and the switching speed of an optically reconfigurable antenna system (OPRAS).

Chapter 8 entitled “*Software Controlled Rotatable Reconfigurable Antenna System*” proposes a new technique to produce a frequency reconfigurable antenna design without resorting to switches.

Chapter 9 entitled “*Conclusion and Future Work*” summarizes the work done in this dissertation and proposes future steps.

Chapter 1

Why Reconfigurable Antennas?

1.1 Introduction

Antennas are a necessary and critical component of all personal electronic devices, microwave and satellite communication systems, radar systems and military surveillance and reconnaissance platforms. In many of these systems, there is a requirement to perform a multitude of functions across several frequency bands and operating bandwidths. In most cases, these requirements cannot be served by a single antenna but rather require the use of multiple antennas of varying form-factors and geometries. This results in an increase in fabrication costs, system weight, system volume, and resources required for maintenance/repair.

Reconfigurable antennas show significant promise in addressing these system-requirements, given their ability to modify their geometry and behavior to adapt to changes in environmental conditions or system requirements (such as enhanced bandwidth, change in operating frequency, polarization, radiation pattern etc.). Reconfigurable antennas can deliver the same throughput as a multi-antenna system using dynamically variable and adaptable single-antenna geometry without increasing the real estate required to accommodate these antennas. Reconfigurable antennas can thus provide great versatility in applications such as cognitive radio, MIMO systems, RFIDs, smart antennas, etc. The ultimate aim of antenna engineering is to morph antennas to maintain system-level performance under widely varying and challenging environmental conditions, the occurrence of faults or failures, and shifting operational demands. In this manner,

reconfigurable antennas can be devised and produced rapidly to provide “custom” solutions compiled from “commodity” hardware and software components.

The concept of reconfigurable antennas first appeared in the 1983 patent of D. Schaubert [1]. In 1999, the Defense Advanced Research Projects Agency (DARPA) launched a multi-university program between 12 well-known universities, research institutes and companies in the United States under the name “Reconfigurable Aperture Program (RECAP),” in order to investigate reconfigurable antennas and their potential applications [2]. Since then, reconfigurable antennas have drawn considerable attention especially for broadband wireless communication, space-time adaptive processing, cognitive radio, and MIMO systems. Today, reconfigurable antennas exist in a multitude of different configurations and are well-suited to address the ever-present need for continual miniaturization of commercial and military wireless electronic devices (laptops, cell-phones, satellite phones, etc).

Reconfigurable patch antennas are of particular interest given their ease of fabrication, ruggedness and low form-factor which allows for easy integration into small electronic devices such as cell-phones and laptops. The typical reconfigurable patch antenna consists of a main-patch element which is fed through either a balanced or unbalanced feed line, and separate metalized regions which lie on the plane of the main-patch, and which are connected to the main-patch through switches or tuning-elements. These elements can be fabricated from several technologies. By dynamically controlling the state of the switches, different metalized sections can be brought in contact with the main-patch, thereby altering the radiation performance of the antenna as a whole.

1.2 Advantages of reconfigurable antennas

With the advancement in wireless communication, more radios are being integrated into a single wireless platform to allow maximum connectivity. An increasing effort is currently underway in order to develop multiradio mobile platforms, such as laptops, mobile internet devices and smart phones. The purpose is to be able to cover the different wireless services that are scattered over a wide frequency range. Table 1.1 shows the frequency bands of the different wireless services and the number of antennas needed to be integrated in a single mobile platform [3]. In order to support these different wireless standards simultaneously, a reconfigurable antenna is needed to minimize the space requirements and to provide the required isolation between the different wireless standards [4-5].

Table 1.1 The different wireless standards

<i>Wireless Services</i>	<i>Frequency Bands</i>	<i>Number of Antennas</i>
Wi-Fi	IEEE 802.11 b/g/n: 2.4-2.48 GHz IEEE 802.11 a/n: 5.15-5.85 GHz	3 X 3 MIMO
WiMAX	IEEE 802.16: 2.3-2.4 GHz, 2.5-2.7 GHz, 3.3-3.8 GHz, 5.15-5.85 GHz	Diversity: main and aux (1 X Tx, 2 X Rx)
3G	GSM 850: 824-894 MHz GSM 900: 880-960 MHz DCS 1800: 1.71-1.88 GHz PCS 1900: 1.85-1.99 GHz	Diversity: main and aux (1 X Tx, 2 x Rx)

	<i>UMTS: 1.92-2.17 GHz</i>	
Bluetooth	<i>IEEE 802.15.1: 2.4-2.48 GHz</i>	<i>Single</i>
GPS	<i>1.575 GHz</i>	<i>Single</i>
UWB	<i>3-10 GHz</i>	<i>Single</i>

The advantages of using reconfigurable antenna compared to multi-band/wideband antennas or multiple antennas can be summarized as follows:

- 1- Ability to support more than one wireless standard →
 - a- Minimizes cost
 - b- Minimizes space requirement
 - c- Allows easier integration
 - d- Good isolation between different wireless standards
- 2- Lower front-end complexity →
 - a- No need for front-end filtering
 - b- Good out-of-band rejection
- 3- Best candidate for software defined radio →
 - a- Capability to adapt and learn
 - b- Automated via a microcontroller or a field programmable gate array (FPGA)

1.3 The different types of reconfigurable antennas

A reconfigurable antenna can be classified into four different categories [6]:

- Category 1: A radiating structure that is able to change its operating frequency by hopping between different frequency bands is called: *frequency reconfigurable antenna*. This is achieved by producing tuning or notches in the antenna return loss.
- Category 2: A radiating structure that is able to tune its radiation pattern is called: *radiation pattern reconfigurable antenna*. For this category, the antenna radiation pattern changes in term of shape, direction or gain.
- Category 3: A radiating structure that can change the polarization (horizontal/vertical, \pm slant 45° , Left-hand/Right-hand CP etc) is called: *polarization reconfigurable antenna*. For this case the antenna can tune for example from vertical to left-hand circular polarization.
- Category 4: It is a combination of the above three categories to exhibit many properties combined together. For example, one can achieve a frequency reconfigurable antenna with polarization diversity at the same time.

Table 1.2 summarizes the key steps for an antenna designer to be able to produce the corresponding reconfigurability.

Table 1.2 The process of achieving the required reconfigurability

Category #	Process
1	<i>Change the surface current distribution</i>

2	<i>Change the radiating edges, slots or the feeding network</i>
3	<i>Change the antenna surface structure or the feeding network</i>
4	<i>Combination of the above processes depending on the antenna functionality</i>

Table 1.3 summarizes the applications of the different categories of reconfigurable antennas.

Table 1.3 Reconfigurable antennas applications

<i>Category #</i>	<i>Applications</i>
1	<i>WLAN, GSM, UMTS, PCS, Bluetooth, Cognitive Radio</i>
2	<i>MIMO, Software Defined Radio,</i>
3	<i>Satellite Communication, MIMO, Cognitive Radio</i>
4	<i>Combination of the above applications</i>

1.4 How to achieve reconfigurable antennas?

The key challenging point in a reconfigurable antenna design lies in the methodology adopted to connect the radiating elements together, such that the resulting

structure will yield the desired RF response over the frequency bands of interest [7]. The most common methodology adopted in the design of this type of antenna is based on the inclusion of some form of switches.

Switches are used to connect and disconnect parts of an antenna or to simply redirect antenna surface currents across a slot. Antenna designers resort to different types of switches to accommodate their design requirements.

The idea behind using a switch is to be able to control the flow of current across a certain structure. The ON state of a switch allows the current to pass through as in a short circuit; the OFF state prevents current from passing through. To control the activation and de-activation of a switch biasing networks are needed. The different types of switches that have been used in the design of reconfigurable antennas are summarized in Table 1.4:

Table 1.4 The different types of switches used in the design of reconfigurable antennas

<i>Switch Type</i>	<i>Operation</i>
RF MEMS	<i>They use mechanical movement to achieve a short circuit or an open circuit in the path between two radiating elements of an antenna structure. The forces required for the mechanical movement can be obtained using electrostatic, magnetostatic, piezoelectric, or thermal designs [8].</i>
PIN Diodes	<i>They operate in two modes. The “ON” state, where the diode is forward biased and the “OFF” state, where the</i>

	<i>diode is reverse biased [9].</i>
Varactors	<i>They consist of a p-n junction diode. As the bias applied to the diode is varied, the varactor capacitance is going to be changed. Typical values are from tens to hundreds of picofarads [10].</i>
Photoconductive Elements	<i>The movement of electrons from the valence band to the conduction band allows the switch to go from “OFF” state to “ON” state. This is achieved by illuminating the switch by light of appropriate wavelength [11].</i>

Chapter 2

Literature Review on Reconfigurable Antennas

2.1 Introduction

Reconfigurable antennas have gained a lot of attention in recent years, especially their implementation in wireless communications. In particular, cognitive radio, MIMO systems, RFID and space antennas have benefited from this design outburst. Many challenging questions face antenna designers though, these challenges are summarized as follows:

- 1- How to connect/disconnect the different radiating elements of the antenna structure in order to obtain the required reconfiguration?
- 2- Which connection type has the least destructive effect on the antenna structure radiation characteristics?
- 3- Which reconfigurability property (frequency/radiation pattern/polarization) needs to be achieved?

In this chapter, answers to these questions are presented by reviewing previously designed reconfigurable antennas. These antennas and the biasing networks of their reconfiguring elements are also discussed and detailed. Four major types of reconfiguration techniques are considered. These techniques are divided based on the reconfiguring elements used as shown below:

1- RF-MEMS [12-28]

2- PIN diodes [29-50]

3- Varactors [51-56]

4- Photoconductive Elements [57-71]

The design of appropriate bias lines for RF MEMS, PIN diodes, and varactors requires extreme attention since these lines can have a destructive effect on the antenna performance by:

- 1- Interfering with the antenna radiation pattern
- 2- Resonating at undesired frequencies
- 3- Including additional RF components

On the other hand, the use of photoconductive elements requires optical fiber cables and structure complication to allow light delivery to the semiconductor switches.

The disadvantages of using such approach are summarized in the following points:

- 1- Increasing the cost and the complexity of the RF front-end in a complete communication system
- 2- Limiting the practicality of integrating such reconfigurable antenna systems in commercial applications such as wireless handheld devices.

2.2 Antenna Designs Based on the Integration of RF-MEMS

Antenna researchers have used RF MEMS to reconfigure different antenna structures. Such switches are designed to operate at RF-to millimeter-wave frequencies (0.1 to 100 GHz). RF MEMS reconfigurable antennas achieve many reconfigurable properties. In the following sub-section, some examples of different antenna reconfigurability properties are presented. These properties are summarized as follows:

- 1- Reconfigurable Radiation Pattern Antennas
- 2- Reconfigurable Polarization Antennas
- 3- Reconfigurable Antennas with Resonance Tuning
- 4- Reconfigurable Antennas with Notch Frequency Tuning

2.2.1 Reconfigurable Radiation Pattern Antenna:

The antenna shown in Fig. 2.1 is a reconfigurable rectangular spiral antenna with a set of RF-MEMs switches, which are monolithically integrated and packaged onto the same substrate [15]. The antenna is printed on a PCB substrate with a dielectric constant of 3.27 and fed through a coaxial cable at its center point. Using the coaxial feed, the antenna is excited through a vertical probe, which is formed by extending the inner conductor of the coaxial line while the external side of the coax is connected to the ground plane in the back of the substrate. The spiral antenna consists of five sections that are connected with four RF-MEMS switches. The spiral arm is increased by discrete steps in the following manner $U, 2U, 2U, 3U, 3U \dots NU$, where U is length of the first segment of the rectangular spiral and N is integer. The spiral arm is increased following the right hand direction to provide right hand circular polarization for the radiated field. The location of switches is determined such that the axial ratio and gain of the antenna are optimum at the frequency of interest.

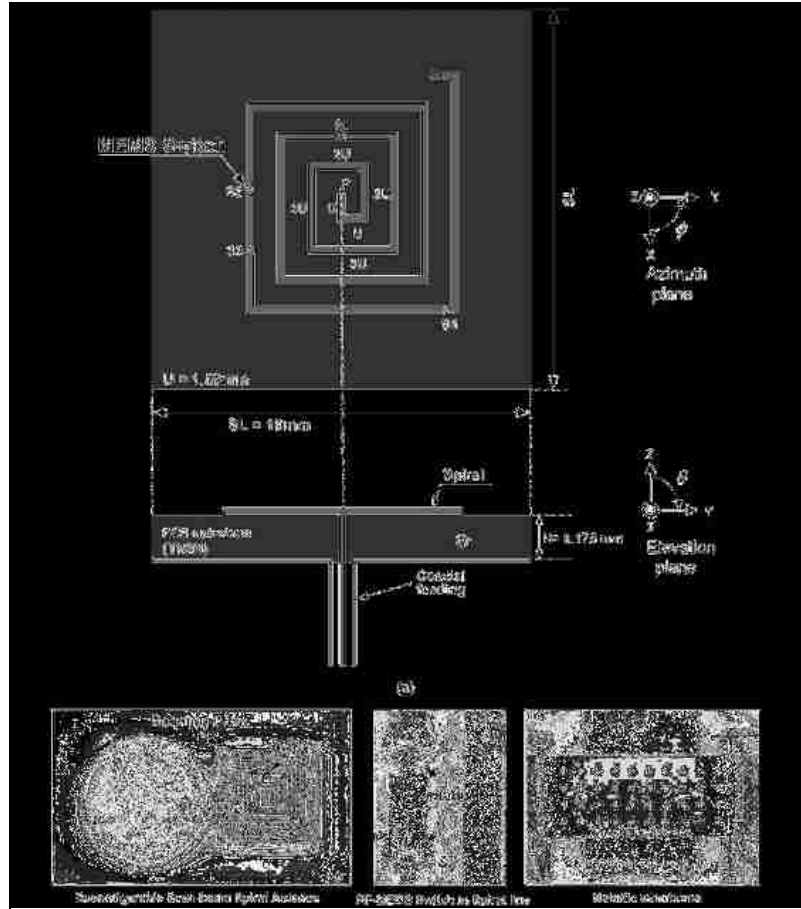


Figure 2.1 Reconfigurable single-arm rectangular spiral antenna integrated with four RF-MEMS switches.

(a) Top and side view of spiral configuration and its feeding. (b) Spiral antenna with its dc biasing network (left) and microscopic picture of the fabricated RF-MEMS capacitive switch (center and right)

[15]

2.2.2 Reconfigurable Polarization Antenna:

A dual-linearly-polarized reconfigurable 2-port antenna is presented in [24]. The antenna can operate in two selectable linear polarization bases, thus being capable of reconfiguring/rotating its polarization base from vertical/horizontal ($0^0/90^0$), to slant $\pm 45^0$. The antenna has been implemented on a Quartz substrate, and uses monolithically integrated RF-MEMS switches to select between the aforementioned polarization bases. The antenna structure consists of a single octagonal microstrip patch, as shown in Fig. 2.2,

in which two ports always excite two orthogonal polarizations of the radiated electric field. This is achieved by exciting the patch from two points located in perpendicular sides of the octagonal patch. Moreover, the antenna has the capability to reconfigure/rotate its polarization base in two different radiation states.

Most of the design complexity of this antenna resides in the feeding structure. Each 50Ω port connects to a quarter wavelength transformer through a high impedance line which, after a few millimeters, splits into two high-impedance lines that connect to the octagonal patch two adjacent sides. At each location where the high-impedance quarter wave transformer splits into two lines, four switches were located. For a proper operation of the antenna, the activation of these switches has to guarantee that the current do not pass through the two split high-impedance lines simultaneously, but only through one of them. Table 2.1 shows the relation between the antenna radiation states and the required states of the RF-MEMS switches to excite a particular polarization.

Table 2.1 Correspondence between the antenna radiation states and the required RF- MEMS switches



2.2.3. Reconfigurable Antenna with Resonant Frequency Tuning:

The antenna in [25] presents a new kind of double- and single-arm cantilever type DC-contact RF MEMS actuators that are integrated within the antenna structure to develop a frequency reconfigurable antenna. The antenna is built on two separate layers

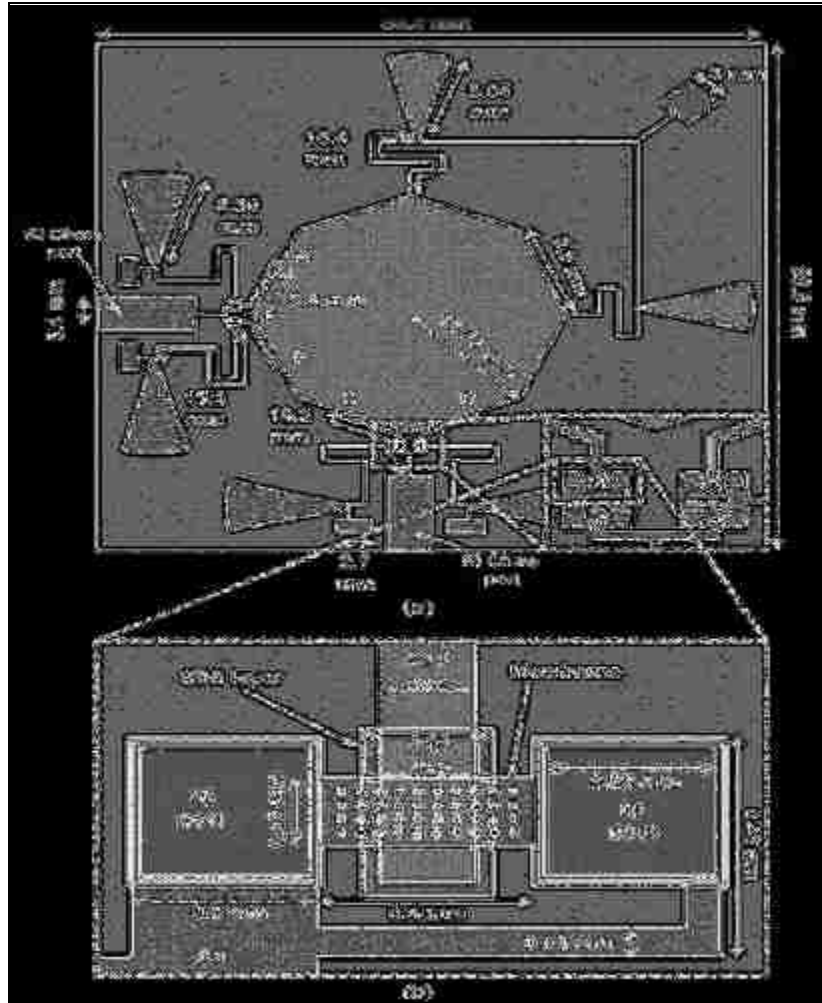


Figure 2.2 (a) The basic dimension of the antenna structure (b) zoom-in of the feeding system and the series MEMS-switch structure [24]

of TMM10i microwave laminate each with 0.635 mm thickness. The antenna structure is shown in Fig. 2.3. The microstrip feed line is placed on one layer and the annular slot is placed on the other layer, which are bonded together having a total thickness of 1.27 mm. The antenna has two concentric circular slots, each of which can be excited individually in order to achieve frequency reconfigurability. The microstrip feed line is broken into two segments, which are spanned by a single-arm cantilever type MEMS actuator. The actuator enables either the outer or the inner slot to be excited by changing the length of

the microstrip. Moreover two RF MEMs actuators are located on the opposite sides of the outer slot. These switches enable the metallic annular ring, which stays between the outer and inner slots, to be shorted to RF ground so that when the inner slot is excited. The reconfigurable antenna annular slot has two reconfigurable frequencies of operation, compatible with IEEE 802.11 WLAN standards.

2.2.4. Reconfigurable Antenna with Notch Frequency Tuning:

Two CPW-fed elliptical monopoles are fabricated on liquid crystal polymer (LCP) with reconfigurable rejection band (band-notch) characteristics in the frequency range between 5 GHz and 6 GHz [23]. The first antenna uses a $\lambda/2$ long, U-shaped slot and the second antenna uses two symmetrically placed $\lambda/4$ long, inverted L-shaped stubs as resonating elements. RF-MEMs switches are used to activate and deactivate the resonating elements. The two antenna structures are shown in Fig. 2.4. In the middle of the third edge of the U-slot and along the symmetry plane of the antenna, one RF-MEMs switch is integrated to selectively short the 0.2 mm wide slot. For the inverted L-slots, two MEMs switches are used to electrically connect and disconnect the two stubs to the elliptical radiator.

2.2.5. Biasing of RF-MEMS Switches:

Bias lines should be incorporated within the antenna structure in order to ensure the correct operation of the RF-MEMS switches. These switches are based on an electrostatically actuated suspension membrane or cantilever, and the biasing voltage is a

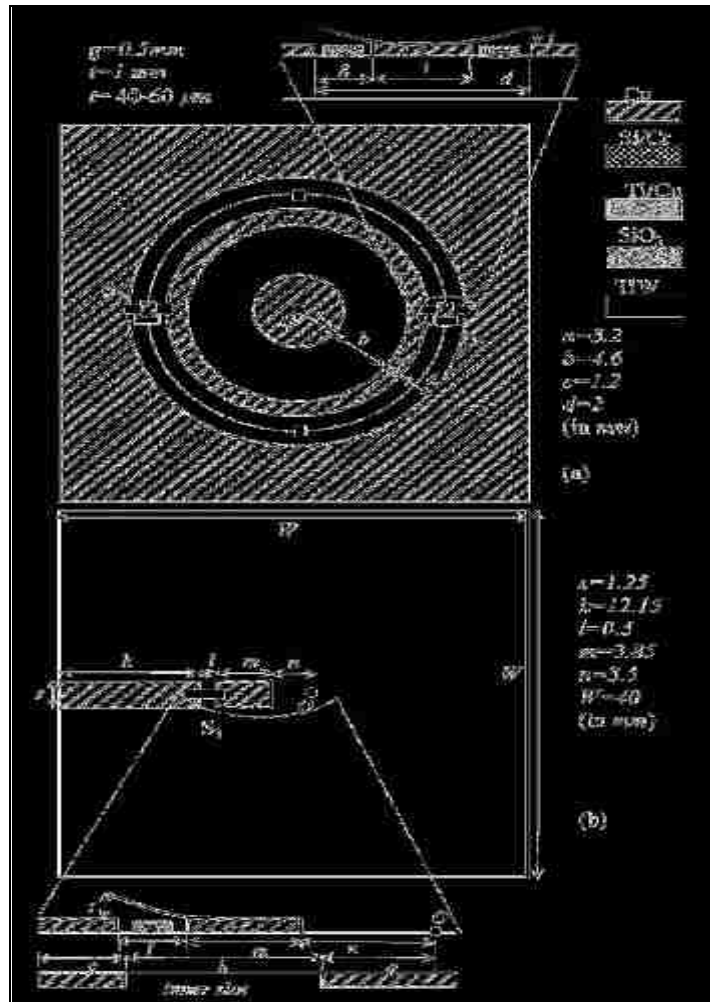


Figure 2.3 Architecture of the microstrip fed reconfigurable annular slot (a) Top view (b) bottom view [25]

function of the area of the cantilever that is directly above the biasing electrode, the distance of the beam from the electrode when the cantilever is up, the relative permittivity of the dielectric material between the beam and the electrode, the flexibility and the thickness of the membrane material. The biasing voltage determines also the minimum distance between the biasing lines according to the breakdown voltage of the substrate material. Side/top view illustrations of the RF-MEMS switch used in [16] is shown in Fig. 2.5. A photo of the fabricated model is also included.

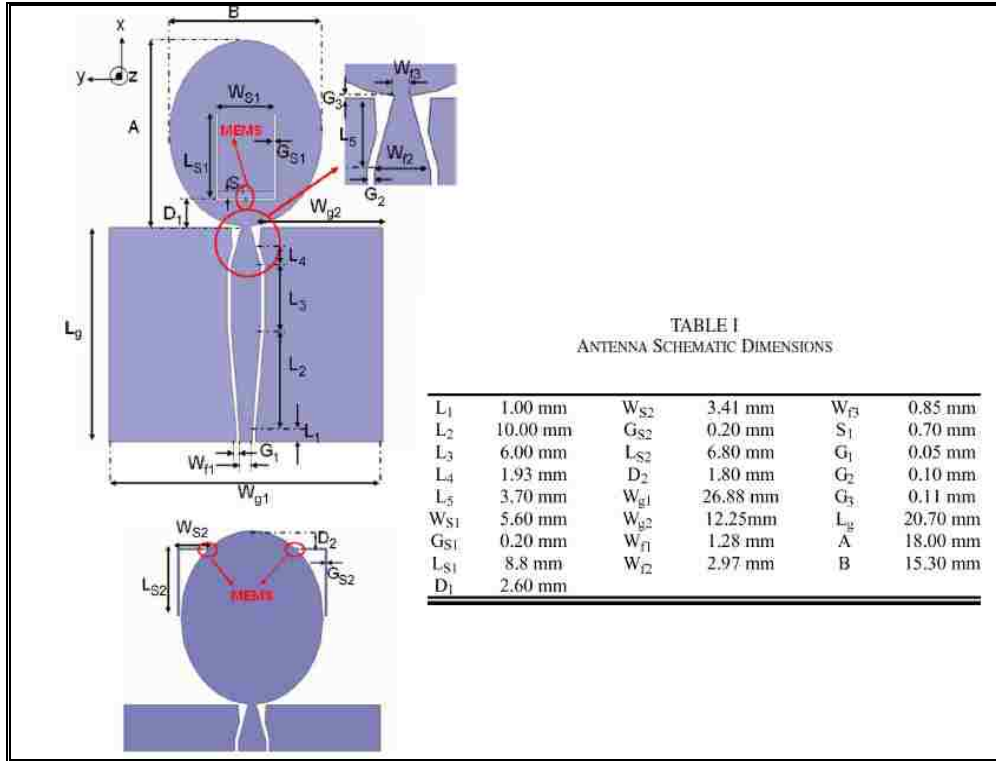


Figure 2.4 Antenna schematic (a) U-shaped slot (b) L-shaped slot [23]

Electrostatic biasing occurs by applying a dc voltage of approximately 40 Volts between the probe pad that is connected to the pull-down electrode and the membrane. The dc biasing pads are placed a distance away from the furthest conductive part of the antenna, to minimize the deformation of the radiation pattern caused by the metallic surface of the probe heads. The connections of the bias lines on a switch is shown in Fig. 2.5(b), where Bias 1 and Bias 2 refer to ground, and Bias 0 is where the dc voltage is applied. Metallic bias lines completely alter the antenna's behavior. To avoid this, one must use high resistive materials for the construction of bias lines. The layout of the fragmented mesh bowtie plus the structure and the direction of the incorporated bias lines discussed in [16] are shown in Fig. 2.6.

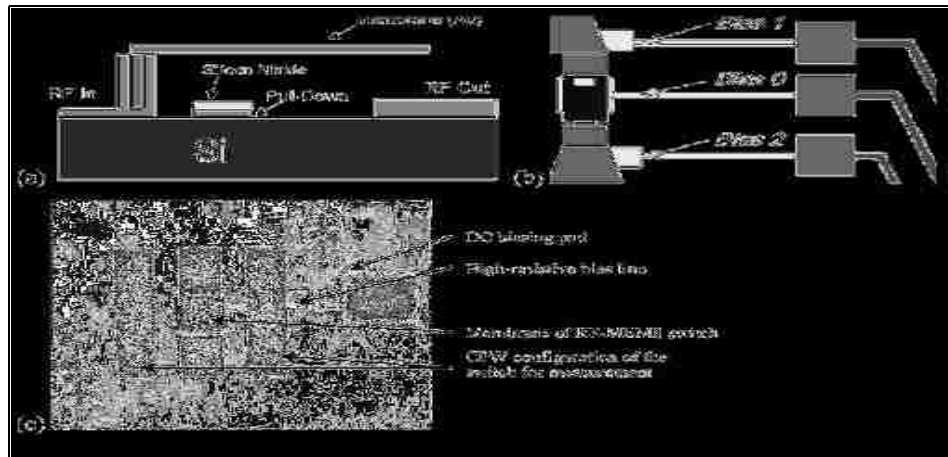


Figure 2.5 (a) Schematic and cross-section of the switch model (b) Top view of the switch model illustrating the bias lines (c) Photograph of the fabricated switch [16]

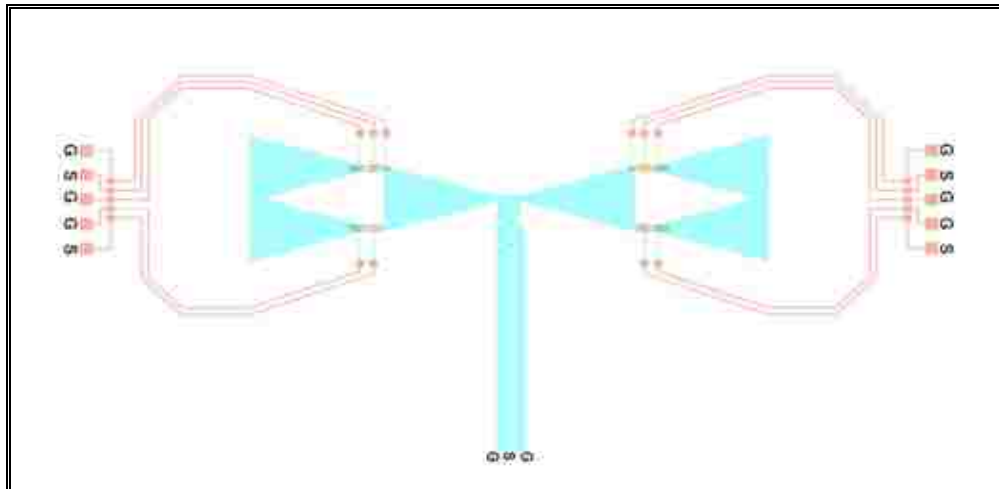


Figure 2.6 Example of the antenna layout in [16] plus the bias network

2.3 Antenna Designs Based on the Integration of PIN diodes

The p-i-n diode structure consists of an Intrinsic “I” region sandwiched between heavily doped P+ and N+ regions. The Intrinsic region is a very lightly doped, high resistivity material which controls the fundamental properties of the PIN diode. Many researchers have investigated the use of PIN diode to achieve reconfigurable antenna

systems with different properties. The reconfigurability properties of PIN diodes antennas studied in this section are summarized as follows:

- 1- Reconfigurable Polarization Antennas
- 2- Reconfigurable Polarization and Radiation Pattern Antennas
- 3- Reconfigurable Radiation Pattern Antennas
- 4- Band Reject Reconfigurable Antennas

2.3.1 Reconfigurable Polarization Antenna:

A single-feed circular microstrip antenna with reconfigurable polarization capability is proposed in [37]. The antenna has a simple structure, which consists of a radiating circular patch, five switches (PIN diode), three matching stubs, and a 50Ω microstrip feed line. It can be switches between 4 different states: two states for linear polarization (high and low frequency), one state for left hand circular polarization (LHCP) and one for right hand circular polarization (RHCP) by controlling the bias voltage of two PIN diodes. At the same time, three switchable matching stubs are used for matching every polarization state. The antenna structure is shown in Fig. 2.7.

To radiate linearly polarized waves, both PIN diodes on the circular patch should be biased in either the “on-state” or the “off-state” simultaneously in order to guarantee the physically and electrically symmetric shape of the circular microstrip patch required to excite the TM_{11} mode. To radiate circularly polarized waves, one of the diodes on the circular patch should be in the “on-state” while the other should be in the “off-state”.

2.3.2 Reconfigurable Pattern and Polarization Antenna:

A reconfigurable parasitic patch array is designed to provide polarization and pattern diversities [34]. The prototype antenna operating at 5.8 GHz is shown in Fig. 2.8. It is a three-element parasitic antenna array where aperture-coupled square patches are used as radiating elements. The central patch is printed on top of a 5880 Duroid substrate and can be excited by one of the two orthogonal crossed slots and feedlines etched on the top and bottom sides of an AR 1000 substrate.

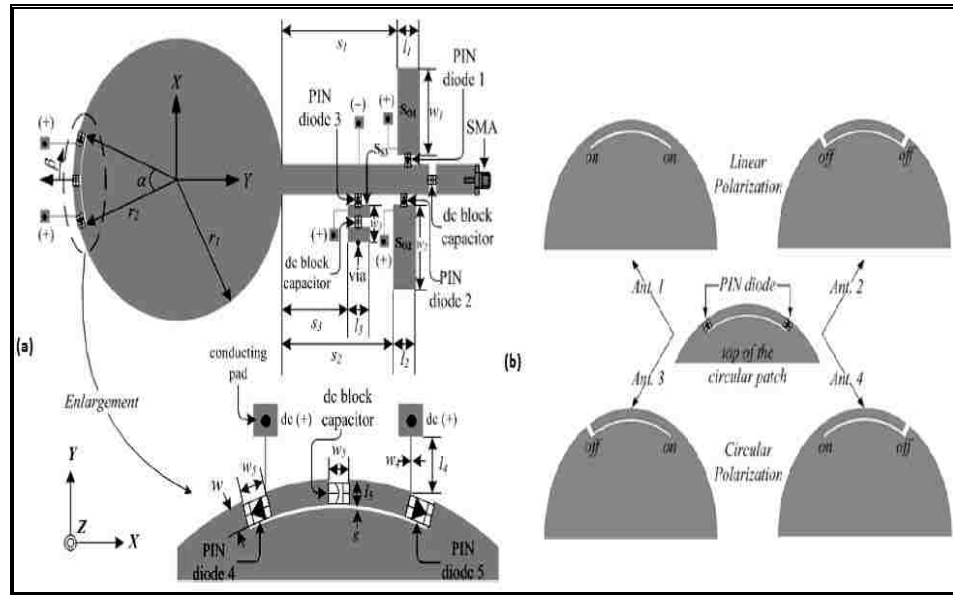


Figure 2.7 (a) Geometry of the antenna structure (b) The operation mechanism of the antenna [37]

The slot selection enforces one of the two linear orthogonal polarizations and it is done by two beam-lead PIN diodes that are directly connected to the feeding microstrip line below the ground plane. By switching ON a diode while the other is OFF, the antenna can switch between horizontal or vertical polarization states with a single feeding port. To realize the pattern diversity, each of the slot pairs in the parasitic patches is loaded by a switchable stub. The stub lengths are adjusted by pin diodes which allow four different patterns for one of the polarization state.

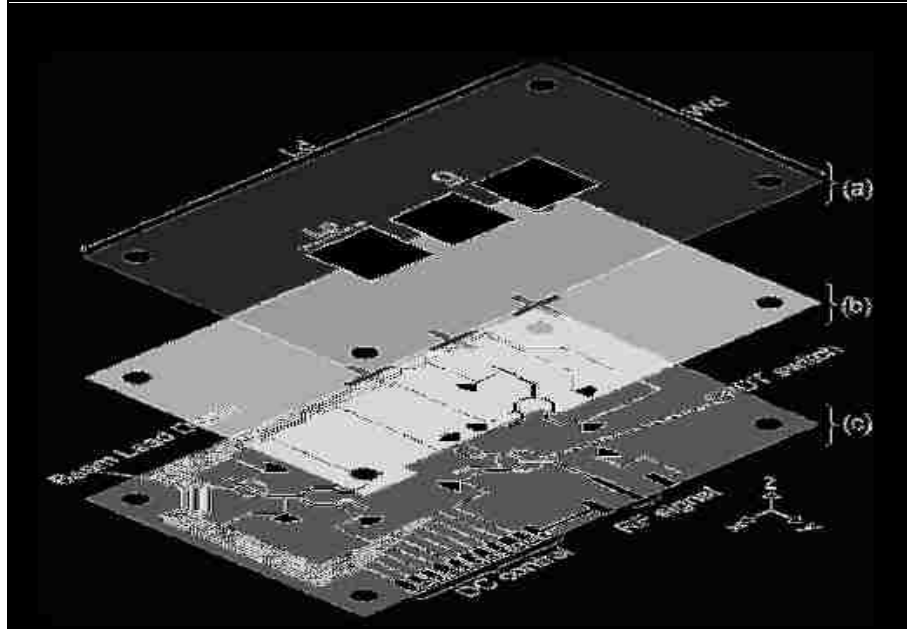


Figure 2.8 Antenna layers: (a) radiating elements (b) coupling elements (c) active and passive circuit components [34]

2.3.3 Reconfigurable Radiation Pattern Antenna:

The proposed structure in [40] is based on a metallic cubic cavity which radiates through rectangular slots. The pattern reconfiguration is achieved with PIN diodes switches by short-circuiting slots in their center to cancel their radiation contribution. The designed antenna structure is fed by a probe penetrating through one cube corner. The radiation is achieved through the 6 slots etched on the 6 cube sides which enable the radiation in a 4π steradian range. The switch in the OFF state (open-circuit) allows the radiation through the corresponding slot whereas the switch in the ON state (short-circuit) cancels the radiation and the slot can be considered a metallic wall. Fig 2.9 shows the fabricated antenna structure.

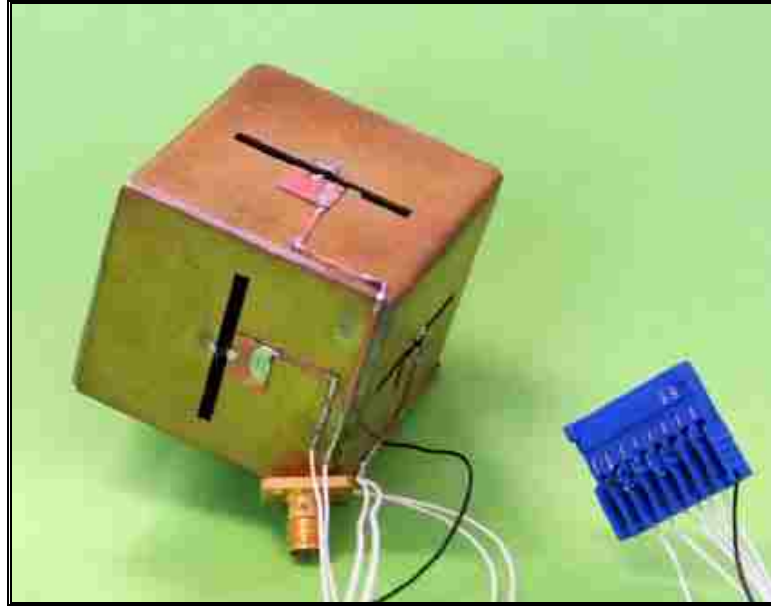


Figure 2.9 The fabricated antenna prototype [40]

2.3.4 Band Reject Reconfigurable Antenna:

An antenna exhibiting a very wide bandwidth with reconfigurable rejection band within the band is presented in [48]. The antenna structure consists of CPW-fed wideband slot bowtie, and a slot etched along the bowtie upper edge provides the rejection of a certain band. This topology allows a very simple mechanism for the reconfigurable band rejection capability, by electrically shorting the slot at variable distances from the antenna symmetry axis using PIN diodes. A picture of the fabricated antenna prototype is shown in Fig. 2.10. The diodes are represented in the simulations by equivalent impedances extracted from TRL-calibrated diodes measurements. The diode impedance in OFF state corresponds to a RLC series network with $R=10.5 \Omega$, $L= 614 \text{ pF}$, and $C=206 \text{ fF}$, while the ON state is modeled by a resistance $R=4 \Omega$ in series with $L=1240 \text{ pF}$.

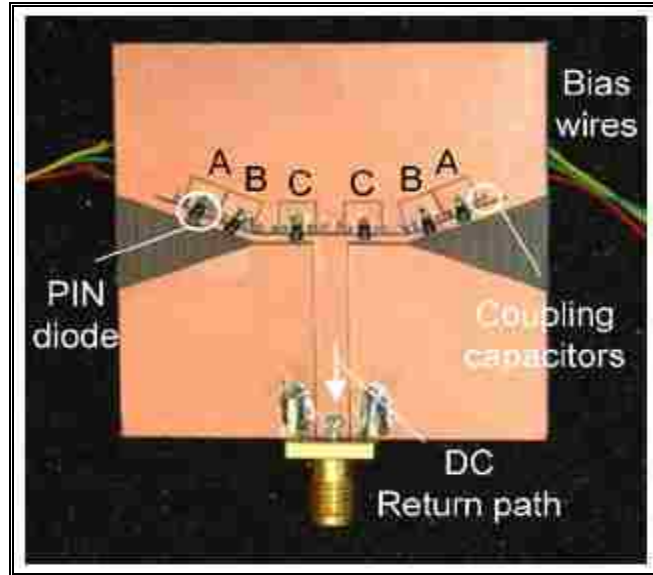


Figure 2.10 The fabricated antenna in [48]

2.3.5. Biasing of PIN Diode Switches:

Similar to RF-MEMS, the design of a reconfigurable antenna system based on PIN diodes integration requires the inclusion of the appropriate bias circuit for activation/deactivation purpose. The biasing of PIN diodes has to be achieved by connecting one endpoint of each diode to ground when the other endpoint is connected to a DC voltage. The voltage value depends on the diode used. The connection to ground or VCC has to be done using quarter wave transformers and radial stubs at the end for better matching. RF components such as capacitors to block the dc bias current and inductors to block the RF signal from going through the diodes can be included as well.

Fig. 2.11 shows the biasing of the diodes that are integrated within the microstrip feed line of an annular slot antenna [30]. The radial stubs are 70° wide and all the microstrip lines are 0.92 mm which results in a Z_0 of 50Ω . The thin feeding lines are $120 \mu\text{m}$ wide and are used as the dc bias lines. Their respective lengths are optimized for the

frequency used, so they are equivalent to an open for the RF signal while they are perfect conductors for any applied dc current. The dc lines however are thin enough (very high RF impedance) to prevent leakage for the frequencies for which they are not optimized. Tapered segments are used to match the wider linear stubs to the small diodes in order to minimize reflections.

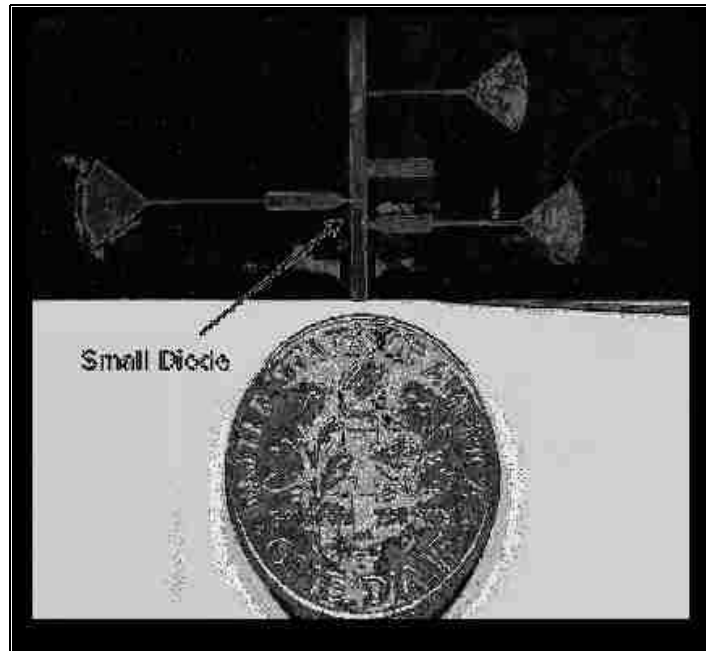


Figure 2.11 An example of the biasing of PIN diodes [30]

2.4 Antenna Designs Based on the Integration of Varactors:

Variable capacitors are also used in the design of reconfigurable antennas. In this reconfiguration technique, the current that passes through the capacitor, or the varactor, is small in comparison with the current that goes through a PIN diode or an RF-MEM switch. Hence the finite quality factor (Q) of the element doesn't deteriorate the antenna efficiency which gives this reconfiguration technique a good advantage over previously discussed techniques [54].

Many researchers have investigated the use of variable capacitors to achieve reconfigurable antenna systems with different properties. The reconfigurability properties of varactors reconfigurable antennas are summarized as follows:

- 1- Reconfigurable Antennas with Resonance Tuning
- 2- Reconfigurable Polarization Antennas with Resonance Tuning

2.4.1 Reconfigurable Antenna with Resonance Tuning:

A varactor-tuned dual-band slot antenna is presented in [51]. The technique is based on loading a slot antenna with a lumped capacitor (or varactor) at a certain location along the slot. A picture of the proposed antenna structure is shown in Fig. 2.12.

By choosing a fixed capacitor location along the slot, decreasing the capacitance results in increasing the first and second resonant frequencies of the slot antenna. However, the changes in the resonant frequencies are significantly different for the first and second resonances and, hence, a dual-band antenna with considerable frequency ratio tuning range can be obtained. Based on this technique, an electronically tunable dual-band antenna with a frequency ratio in the range of 1.2-1.65 is designed and fabricated using a single varactor. The antenna has similar radiation patterns with low cross-polarization levels at both bands and across the entire tunable frequency range. The antenna is fed with an off-centered microstrip line, and the length of the open circuited line L_m and its position L_s are tuned to obtain good simultaneous match at both bands. The antenna is designed to operate on a 0.5 mm thick RO4350B substrate with $\epsilon_r = 3.4$, $\tan \delta = 0.004$, and ground plane size of 12 cm x 10 cm. A high quality varactor manufactured by Metelics (SODT 3001) with a tuning range of 0.5 to 2.2 pF for $0V \leq V_{dc} \leq 30 V$ is used.

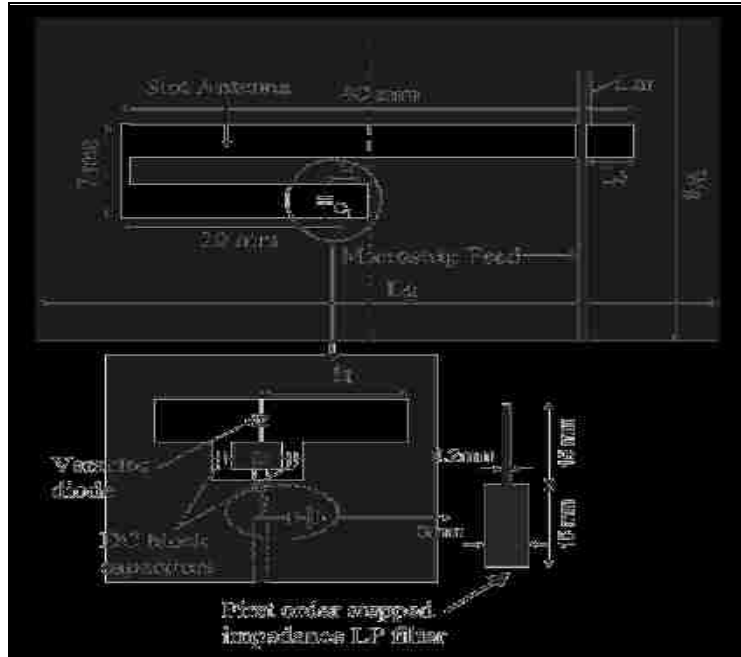


Figure 2.12 Topology of the reconfigurable dual-band slot antenna using varactors [51]

2.4.2 Reconfigurable Polarization Antenna with Resonance Tuning:

In [55], single and dual-polarized slot-ring antennas with wideband tuning using varactor diodes have been demonstrated. The single polarized antenna tunes from 0.95 to 1.8 GHz with better than -13 dB return loss. Both polarizations of the dual-polarized antenna tune from 0.93 to 1.6 GHz independently with better than -10 dB return loss and > 20 dB port-to-port isolation over most of the tuning range. The capacitance of the varactor diodes varies from 0.45 to 2.5 pF, and the antennas are printed on 70 x 70 x 0.787 mm² substrates with $\epsilon_r = 2.2$. The dual-polarized slot-ring antenna can either be made both frequency and polarization agile simultaneously, or can operate at two independent frequencies on two orthogonal polarizations. The corresponding antenna structure for the dual-polarized slot ring antenna is shown in Fig. 2.13.

2.4.3 Biasing of the Varactor Switches:

The bias network of the varactor used in tuning the antenna discussed in [51] is shown in Fig. 2.12. The dc bias voltage is isolated from the RF by cutting the ground plane around the varactor cathode. The RF connectivity around the slot antenna is achieved by using two large capacitors that connect the cathode path to the surrounding ground plane. In order to improve the dc/RF isolation, a first-order low-pass filter is placed in the path of the dc bias line. The filter is implemented using stepped impedance microstrip lines with a rejection band covering the frequency range of 1.5 to 4 GHz, which covers the entire band of operation of the antenna.

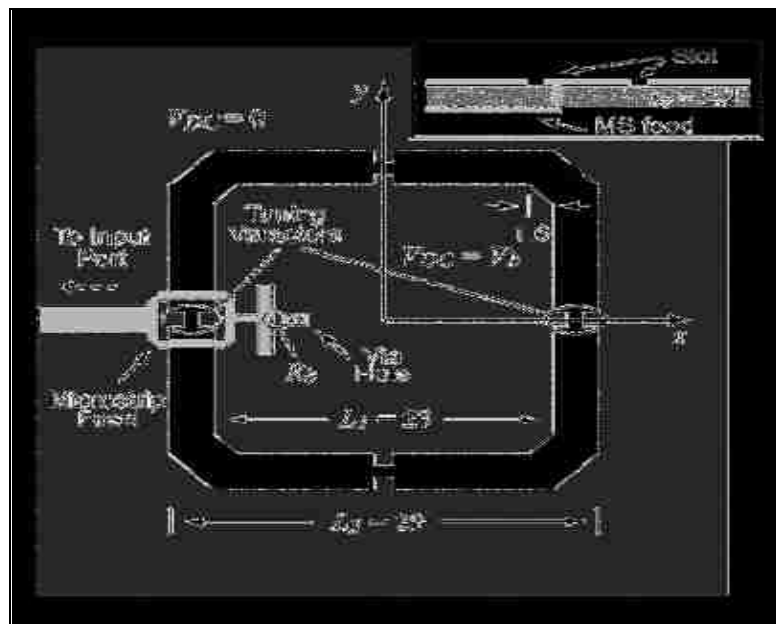


Figure 2.13 Layout of the slot-ring antenna [55]

2.5 Antenna Designs Based on the Integration of Photoconductive Switches

To overcome the limitations of regular electronic switches discussed previously and to avoid biasing lines and their effect on the antenna performance, the use of an

optically gated photoconductive switch has risen. For such a switch to perform adequately and efficiently at microwave frequencies, it must have sufficient voltage blocking capability which is necessary for adequate output power, and acceptable small on-state resistance and turn-on and turn-off times. Factors affecting these requirements include the properties of the semiconductor material itself, the electrical contacts, the dimensions of the switch, and the properties of the laser pulses used to gate the switch [70].

If the conductivity of a semiconductor material changes when laser radiation of a suitable wavelength falls on the surface then the material can be said to be a photoconductor. Many semiconductor materials show these properties such as chromium-doped gallium arsenide (Cr-GaAs), low-temperature grown gallium arsenide (LT-GaAs), indium phosphide (InP), amorphous silicon, and silicon on sapphire (SoS). The exact material properties that determine if a semiconductor is photosensitive are complex but are largely the result of added impurities and material processes that affect the structure of the material, causing trapping and recombination centers [58].

Some research has been done on the design of optically pumped reconfigurable antenna system. For example, a structurally embedded photoconductive silicon bowtie antenna is discussed in [60]. Silicon bowtie was fabricated from 4-in diameter wafers with a bulk resistivity at 7000 Ω -cm and a thickness of 25 mils. Ohmic contacts were made by ion implantation and sputtering technique. N^+ phosphorous ions were introduced as donors at 150 keV implantation energy and with a concentration of 10^{16} cm^{-3} . Light from a laser output fiber to the bowtie is transferred by means of “light tank”- a thin quartz slab waveguide. Schematic of the light tank delivery system is shown in Fig. 2.14. The

dimensions of the light tank for the 1.5 - 3.5 GHz silicon bowtie are 1 x 2 in² with the thickness of about 2 mm. A pair of equilateral triangular silicon elements with edge length of 0.754 in was bonded on the light tank waveguide as the “bowtie”. A compensated balun feed was fabricated using conventionally metallic conductors, and indium soldered to the contact tip of each triangle.

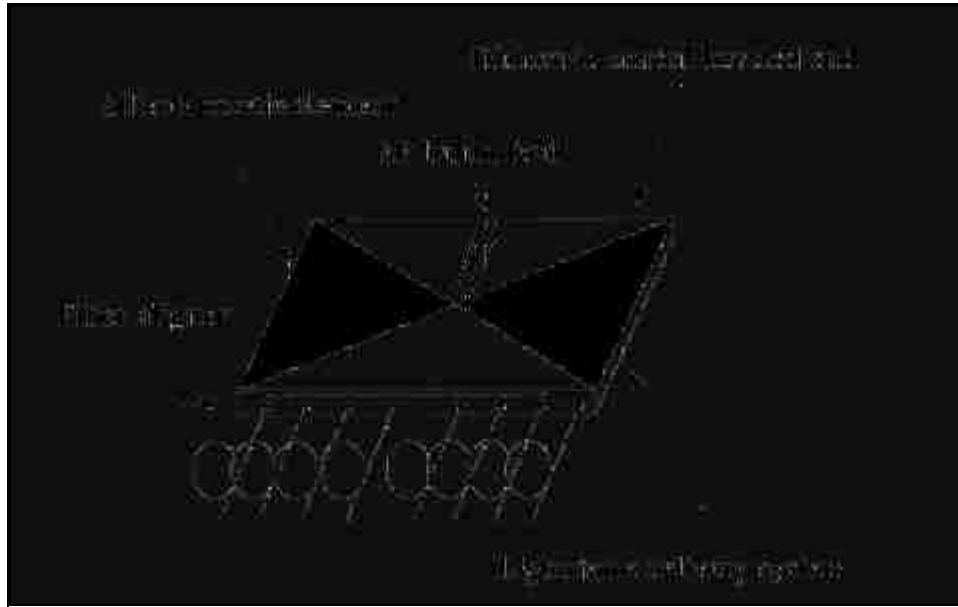


Figure 2.14 The antenna structure discussed in [58]

The antenna design shown in Fig. 2.15 is a reconfigurable aperture antenna (RECAP) [62]. FET based electronic switches with their optically coupled control system are used. The reconfigurable design consists of a thin dielectric substrate that supports an array of square, metallic patches. The patches are electrically small, that is, $l/\lambda_0 \ll 1$, where l is the side length of the patch and λ_0 is the free space wavelength at the operating frequency. It is important to recognize that these elements are not conventional microstrip patch antennas. Each patch is connected to the surrounding patches by switched links, indicated by the arrows in the figure. Each switch may be open or closed depending upon

the design requirements. There is a single feed point (pair of terminals) located at the center of the antenna. The switches and the accompanying control system are an integral part of the RECAP antenna. In the prototype antenna, the switches were electronic and the control was via infrared illumination.

Fig. 2.16 is a schematic drawing showing the overall arrangement of the major components of the prototype antenna [62]. It shows the control path for a single electronic switch. A light-emitting diode in the control circuitry sends infrared radiation (peak at 880 nm) through a hole in the reflector. The beam then passes through a channel (light tube) in the honeycomb spacer. The sides of the channel are painted to make them reflective and opaque; this increases the efficiency of light transfer and prevents crosstalk between channels. The light beam finally strikes a photo-detector located on the backside of the dielectric substrate containing the metallic patches. Here, the light beam activates an electronic switch connecting two patches—when the light is on the switch is closed, and when the light is off the switch is open.

A design for an optically reconfigurable printed dipole antenna is shown in Fig. 2.17 [63]. The antenna is printed on 1.17 mm thick TLY-5 substrate that has a dielectric constant $\epsilon_r = 2.2$. There is no ground plane on the underside of the printed dipole, allowing the antenna to radiate above and below the substrate. The antenna is fed at the CPW using a 50 Ω SMA connector. The CPW is an unbalanced transmission line but since the dipole is a balanced antenna, a transformation of the input signal is required. The circular balun is used to convert the unbalanced CPW to a balanced CPS. The balun is based on a CPW to slotline T-junction.

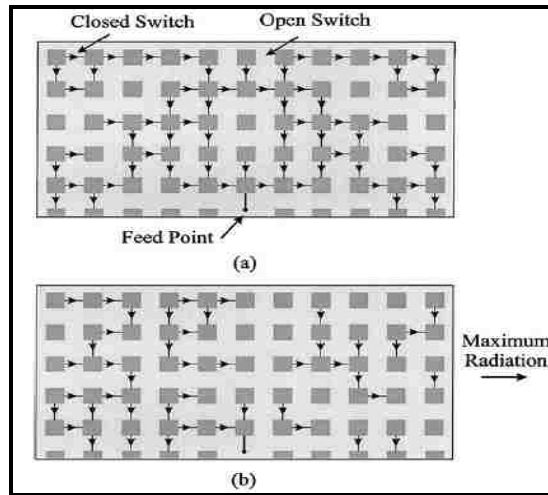


Figure 2.15 Schematic drawing for the RECAP antenna (monopole form) showing which switches are open and closed when wires are used for closed switches. (a) Broadband, bidirectional, broadside design.

(b) Narrow-band, unidirectional, end-fire design [62]

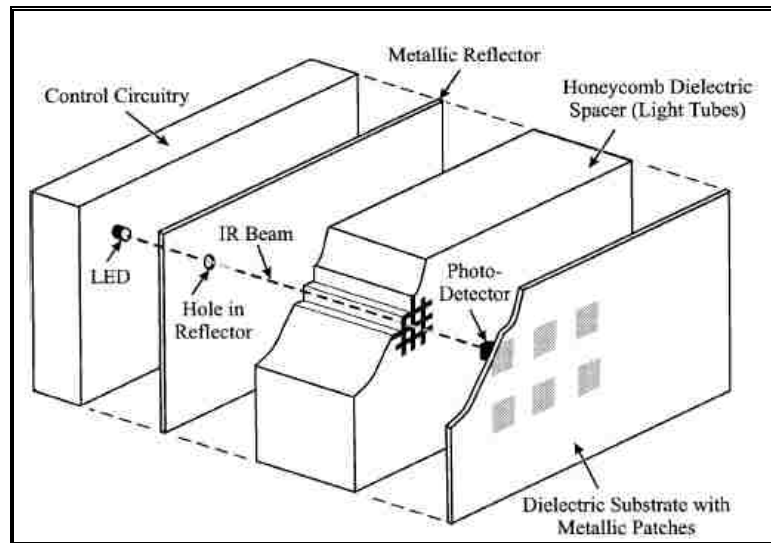


Figure 2.16 Schematic drawing showing the arrangement of the major components that makes up the prototype RECAP antenna. Details are given for the control of a single switch

The dipole antenna resonates when its length is equal to $\lambda_{\text{eff}}/2$ where λ_{eff} is the effective wavelength. The dipole is printed with two gaps, each one 14.4 mm from the end of each arm. Silicon dice of dimension 1 mm x 1 mm x 0.3 mm are then placed over the

gaps and are held in place using silver loaded epoxy which ensures good contact between the copper and silicon. Two 980 nm lasers operating at 200 mW are coupled to two glass fiber optic cables, which are then angled over the silicon wafers using plastic clamps. When both switches are turned off, the silicon acts as an insulator and so the dipole resonates at its shorter length of 35.5 mm. When both lasers are operating at 200 mW, the silicon conducts and the gaps are bridged, increasing the dipole arm lengths to 62.3 mm and hence reducing the resonance frequency.

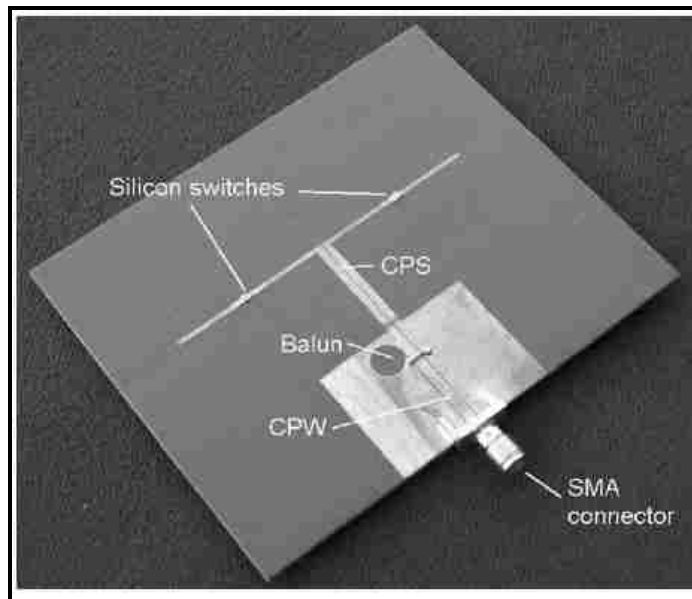


Figure 2.17 Switched dipole antenna [63]

Individual operation of the silicon switches creates an offset feed as one dipole arm becomes longer than the other. The E-plane pattern rotates to the left when only the left switch is activated and conversely it rotates to the right when only the right switch is operated. In both these operational states, the resonance frequency is fixed close to 2.7 GHz. When shifted right, the maximum gain is 12° off boresight and when shifted left, the maximum gain is 7° off boresight. This mismatch is due to the asymmetry in the balun and

CPW ground planes with respect to the dipole arms. A much larger shift of about 50° in the dipole pattern nulls is observed when the silicon switches are activated alternatively.

Another antenna consists of a square patch fabricated on a 62 mil thick Arlon PCB with a relative permittivity of 2.2 and it is edge fed using a quarter-wave transformer and a 50Ω microstrip line is shown in Fig. 2.18 [69].

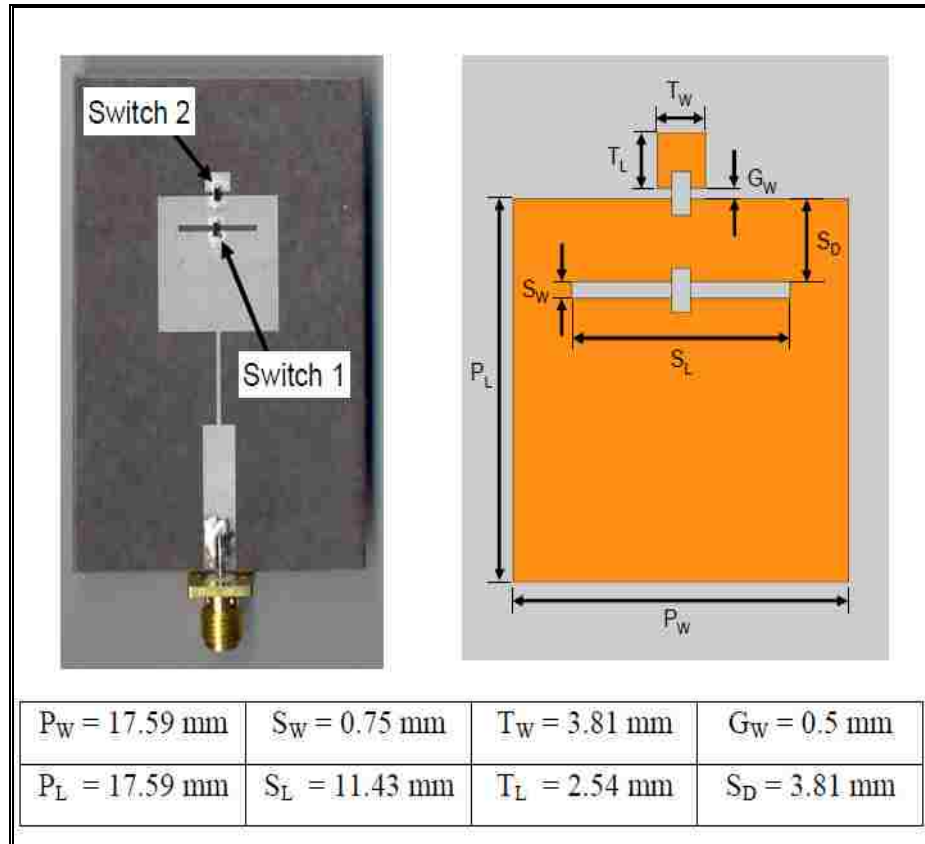


Figure 2.18 Reconfigurable patch antenna with silicon switches [69]

The switches are 1 mm wide, 2 mm long, and 0.38 mm thick, and they are cut from a phosphorus-doped silicon wafer with $3000 \Omega\text{-cm}$ resistivity. The switches are bonded to the antenna using conductive epoxy. When the switch across the slot is on while the switch to the capacitive tab is off, the capacitive tab is disconnected, and the slot is shorted. This causes the antenna to resonate at its highest frequency. When both switches

are off, the capacitive tab is still disconnected, but the slot, now seen by the antenna, causes the antenna to operate at its middle resonant frequency. Currents on the patch flow around the slot making the antenna look electrically longer and decreasing its resonant frequency. When the switch across the slot is off while the switch to the capacitive tab is on, the antenna now sees the effects of both the slot and the capacitive tab. The added capacitance combined with the effect of the slot causes the antenna to operate at its lowest resonant frequency.

A reconfigurable photoconductive antenna is created by projecting an image onto a semiconductor substrate [71]. The image is controlled via a digital micro-mirror device array which is illuminated by a laser source. Based on the photoconductive nature of semiconductors, the areas illuminated by the laser become metallic in nature and form either a single antenna or a phased array antenna comprised of multiple radiating elements. The antenna is reconfigured by electronically driving the digital micro-mirror device (DMD) array, which serves as a spatial light modulator. Changing the pattern of the DMD array changes the pattern of the reflected light, and thus results in a modification of the antenna pattern. This technique allows the radiating antenna to be modified such that many planar antenna patterns are possible. Example patterns include patch radiators, bow-tie antennas, and phased array antennas comprised of multiple radiating elements as shown in Fig. 2.20.

The use of the DMD allows the pattern to be dynamically adjusted simply by changing the position of the individual mirrors in the device. The DMD is an array, of 16 micrometer mirrors with 1 micrometer separation between each mirror. Each mirror

consists of three physical layers and two air gap layers. The air gap layers separate the three physical layers and allow the mirrors to tilt $\pm 10^\circ$. It is the tilting action of the mirrors that modulates the light source to form the image. Laser light is brought in via

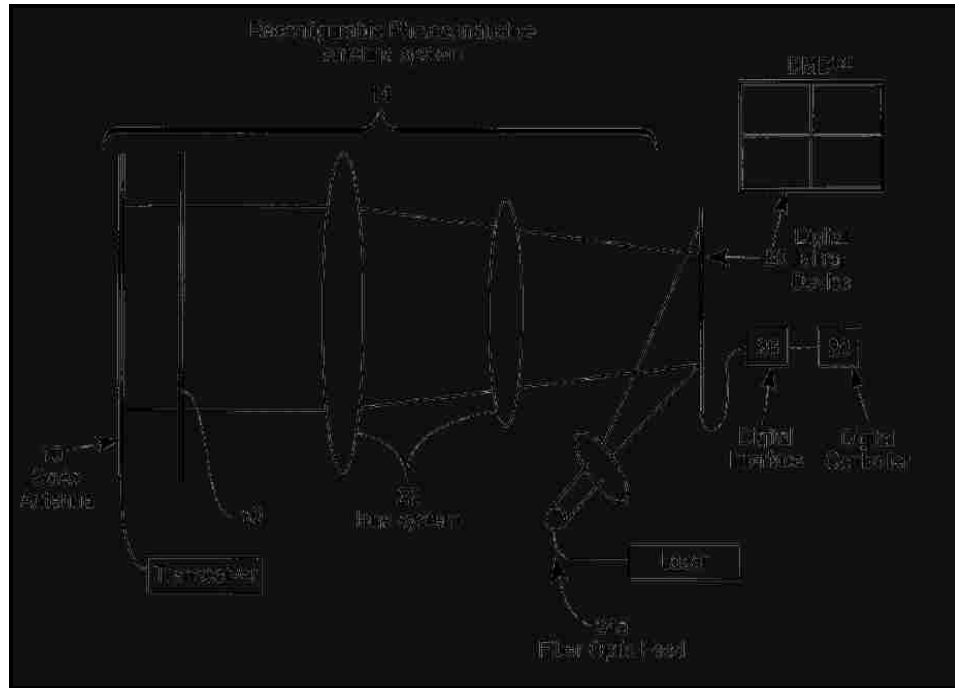


Figure 2.19 Schematic diagram of a spatially light modulator reconfigurable photoconductive antenna [71]

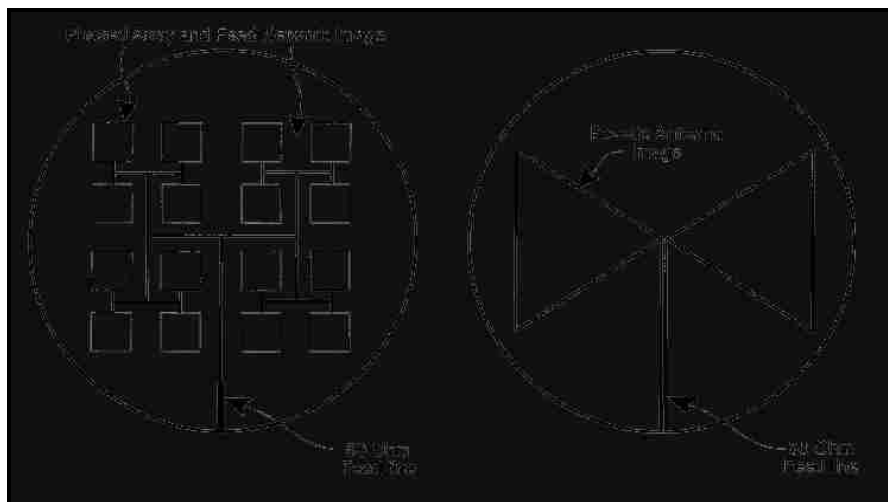


Figure 2.20 Projected images of a phased array and bow-tie antenna of the GaAs substrate [71]

fiber optical cable to a beam expander to illuminate the DMD. The device operates through a standardized digital interface and can be switched between patterns in a period of approximately 20 μ sec. The pattern of the DMD can therefore be readily and easily controlled through the use of a digital control system. The reflected image from the DMD is projected through a lens system and focused on the GaAs surface forming the antenna.

2.6 Conclusion

In this chapter, many challenging questions are answered by reviewing in details many reconfigurable antenna designs that have been previously published. The review is divided based on the type of switching elements. For RF-MEMS, PIN diodes and varactor integration, bias lines should be included for activation purpose. The inclusion of these bias lines has a negative effect on the antenna performance in terms of undesired resonant frequencies and destructive interference with the antenna radiation pattern. Extreme attention is required when dealing with such tuning elements to insure the minimization of their biasing lines effects on the antenna radiation characteristics. Also the inclusion of additional RF components (capacitors, inductor ...) increases the complexity of the antenna structure by adding additional components.

On the other hand, the implementation of optically reconfigurable antenna structures eliminates the use of bias lines which improves the performance of the antenna. However, for this technique optical fiber cables are needed which complicates the realization of such optically pumped antennas. Delivering light to the photoconductive switches adds to the antenna structural complexity which reduces the applicability of such reconfiguration technique in practical applications. In the following chapters, a new light

delivery procedure is discussed as well as new designs and reconfiguration techniques for the implementation of front-end reconfigurable antenna systems (FERAS).

Chapter 3

Physics and RF Properties of Semiconductor Switches

3.1 Introduction

Understanding the underlying physical principles of photoconductive switches is necessary to grasp their operation mechanisms. Particularly the motion of electrons and their interaction with light characterizes the functioning of such switches. Table 4.1 lists the atomic compositions of semiconductor materials which are likely to be encountered in the majority of photoconductive based devices [72]. The semiconductor materials used in the fabrication of photoconductive switches includes:

1. The elemental semiconductor Si and Ge
2. Compound semiconductors such as GaAs
3. Alloys

Due to the advancement in its fabrication technology, Si is the most important material totally dominating the present commercial market [73]. GaAs, exhibiting superior electrical properties and special optical properties, is finding increased usage in a number of applications, including high speed integrated circuits (IC's).

Table 3.1 Semiconductor Materials

General Classifications	Specific Examples
Elemental Semiconductors	<i>Si, Ge</i>
III-V Compounds	<i>AlP, AlAs, AlSb, GaN, GaP, GaAs, InP</i>
II-VI Compounds	<i>ZnO, ZnS, ZnSe, ZnTe, CdS, CdSe, CdTe</i>

Alloys	$Al_xGa_{1-x}As, GaAs_{1-x}P_x, Ga_xIn_{1-x}As_{1-y}P_y$
---------------	--

All of the semiconductors listed in Table 3.1 are composed of elements appearing in column IV of the periodic table, or are a combination of elements in the periodic table that have equal distance to either side from column IV. For example, the column III element “Ga” plus the column V element “As” yields the III-V compound semiconductor GaAs. On the other hand, the fractional combination of the column III elements “Al” and “Ga” plus the column V element “As” yields the alloy semiconductor $Al_xGa_{1-x}As$. This general property is related to the chemical bonding in semiconductors, where, on the average, there are four valence electrons per atom [73].

The basic physical properties of semiconductor materials are studied in this chapter. The energy band model and the interaction of a photoconductive switch with light are discussed. The calculation of the electrons/holes concentration is presented. Moreover, the change in the RF properties of a photoconductive switch under light illumination is derived. The fabrication process of a photoconductive switch is detailed in the last section of this chapter.

3.2 Energy Band Models of Semiconductor Materials

A semiconductor is a crystalline or amorphous solid whose electrical conductivity is typically intermediate between that of a metal and that of an insulator. Its conductivity can be significantly altered by modifying the temperature or doping concentration of the material, or by illuminating it with light [74-75]. The atoms comprising solid-state materials have sufficiently strong interatomic interactions that they cannot be treated as

individual entities. Their conduction electrons are not bound to individual atoms; rather, they belong to the collection of atoms as a whole. The solution of the Schrodinger equation for the electron energy results in a splitting of the atomic energy levels and the formation of energy bands. Each band contains a large number of densely packed discrete energy levels that is well approximated as continuum [74]. As illustrated in Fig. 3.1, the valence and conduction bands are separated by the bandgap energy E_g , which plays an important role in determining the electrical and optical properties of the material.

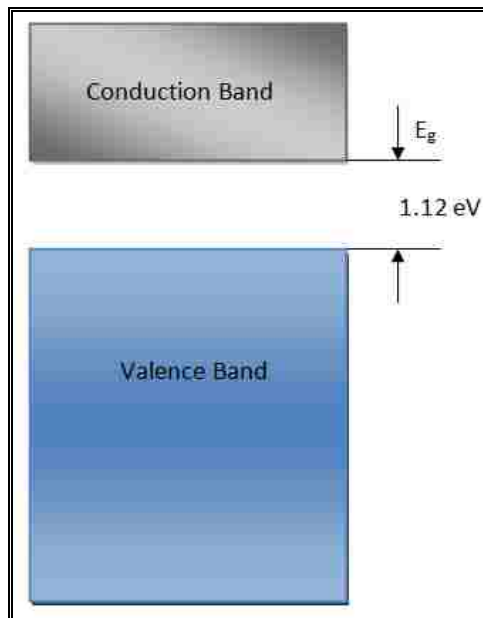


Figure 3.1 Energy band model in Si

The energy band model of Fig. 3.1 can be applied with only slight modification to all materials. The major difference between materials lies not in the nature of the energy bands but rather in the magnitude of the energy band gap. Insulators, as shown in Fig. 3.2, are characterized by very wide band gaps, with E_g for diamond and SiO_2 being ≈ 5 eV and 8 eV. In these wide band gap materials the thermal energy available at room temperature

excites very few electrons from the valence band into the conduction band; thus few carriers exist inside the material and it is therefore a poor conductor of current.

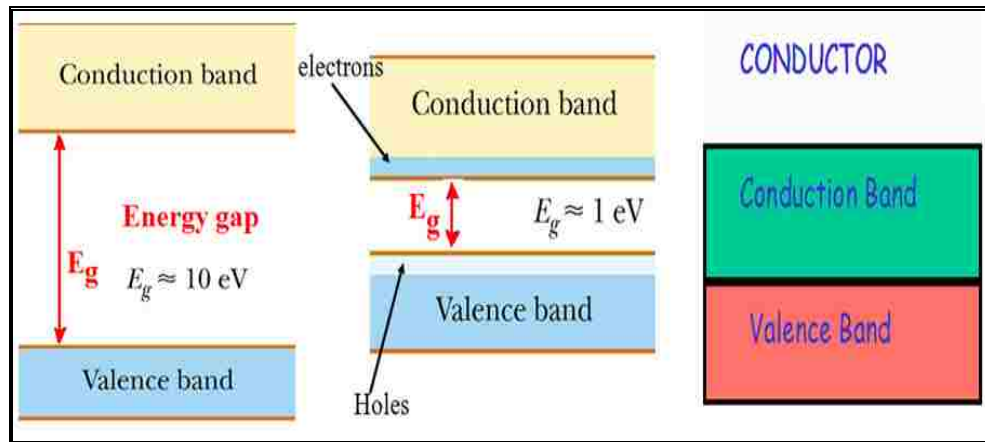


Figure 3.2 The energy band models for insulators, semiconductors, and conductors

The band gap in metals is either very small or no band gap exists at all due to an overlap between the valence and conduction bands. There is always an abundance of carriers in metals, and hence they are excellent conductors. In fact, semiconductors present an intermediate case between insulators and metals as shown in Fig. 3.2.

3.2.1 Direct and Indirect Bandgap Semiconductors:

Semiconductor materials can be classified into two different categories [75]:

Category 1: Direct Bandgap Semiconductor

Category 2: Indirect Bandgap Semiconductor

Semiconductors for which the conduction band minimum energy and the valence band maximum energy correspond to the same value of the wavenumber K (same momentum) are called direct bandgap materials. Semiconductors for which this is not the case are known as indirect bandgap materials. For example, GaAs is direct bandgap semiconductor whereas Si is an indirect bandgap semiconductor. The distinction between the two

categories is very essential because a transition between the bottom of the conduction band and the top of the valence band in an indirect bandgap semiconductor must accommodate a substantial change in the momentum of the electron. In fact, direct bandgap semiconductors are efficient photon emitters, whereas indirect bandgap semiconductors cannot serve as efficient light emitters.

3.2.2 Electrons and Holes:

The wavefunctions of the electrons in a semiconductor material overlap so that the Pauli Exclusion Principle applies. This principle dictates that no two electrons may occupy the same quantum state and that the lowest available energy levels fill first [74]. The silicon has four valence electrons per atom that form covalent bands. Under no light, the number of quantum states that can be accommodated in the valence band is such that it is completely filled while the conduction band is completely empty. The material cannot conduct electricity under these conditions [75].

Under light illumination of specific wavelength, some electrons can be excited from the valence band into the empty conduction band, where unoccupied states are abundant. The electron departing from the valence band leaves behind an unoccupied quantum state, which in turn allows the remaining electrons in the valence band to exchange places with each other. The collection of electrons remaining in the valence band thus undergoes motion. This can equivalently be regarded as motion, in the opposite direction, of the hole left behind by the departed electron. The hole therefore behaves as if it has a positive charge $+e$. An example of such scenario is shown in Fig. 3.3 [74].

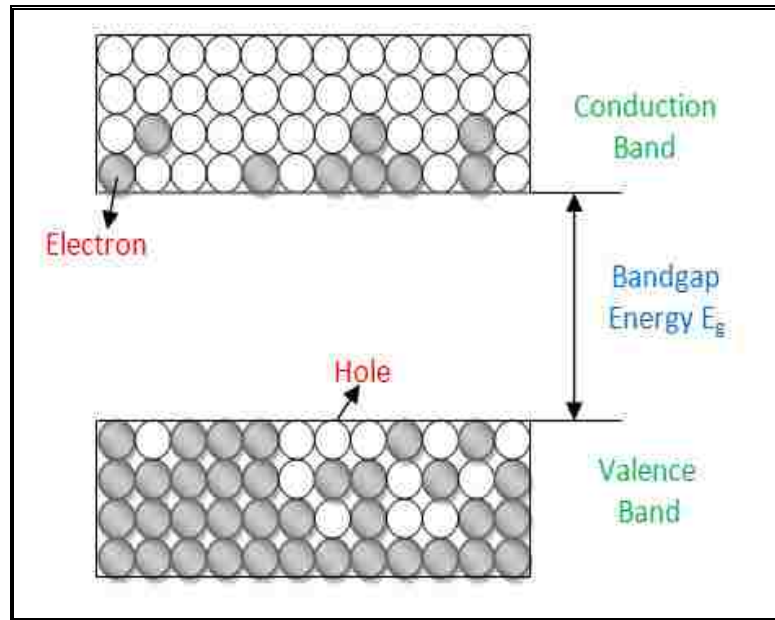


Figure 3.3 Electrons in the conduction band and holes in the valence band

The net result is that each electron excitation creates a free electron in the conduction band and a free hole in the valence band. The material behaves as a semiconductor whose conductivity increases sharply by increasing the power level of the light since more carriers are generated. The basic properties of some semiconductor materials are summarized in Table 3.2.

3.3 Doped Semiconductors

The electrical and optical properties of semiconductors can be modified substantially by the controlled introduction into the material of small amounts of specially chosen impurities called dopants [72-73]. The introduction of these impurities can alter the concentration of mobile charge carriers by many orders of magnitude. Dopants with excess valence electrons, called donors, replacing a small proportion of the normal atoms in the crystal lattice, create a predominance of mobile electrons. The material is then said

to be n-type semiconductor [74]. Thus, atoms from column V (e.g. “P” or “As”) replacing column IV atoms in an elemental semiconductor (e.g. “Si” or “Ge”), or atoms from column VI (e.g. “Se” or “Te”) replacing column V atoms in a III-V binary semiconductors (e.g. “As” or “Sb”), produce an n-type material. Similarly, a p-type semiconductor is made by using dopants with a deficiency of valence electrons, called acceptors. The result is then a predominance of mobile holes. Column IV atoms in an elemental semiconductor replaced with column III atoms (e.g. “B” or “In”), or column III atoms in a III-V binary semiconductor replaced with column II atoms (e.g. “Zn” or “Cd”), yield p-type material. Column IV atoms act as donors for column III and as acceptors for column V, and therefore can be used to produce an excess of both electrons and holes in III-V materials. The charge neutrality of the material is not altered by the introduction of dopants [74-75].

Table 3.2 Properties of some semiconductor materials

Material	Bandgap Type (Direct/ Indirect)	Bandgap Energy Eg (eV)
Si	I	1.12
Ge	I	0.66
GaAs	D	1.42
InSb	D	0.17

Undoped semiconductors which are devoid of intentional doping are referred to as intrinsic materials, whereas doped semiconductors are called extrinsic materials. The concentration of mobile electrons and holes are equal in an intrinsic semiconductor,

$n=p=n_i$, where the intrinsic concentration n_i grows with increasing temperature at an exponential rate. On the other hand, the concentration of mobile electrons in an n-type semiconductor (majority carriers) is far greater than the concentration of holes (minority carriers), i.e. $n \gg p$. The opposite is true in a p-type semiconductor, where holes are the majority carriers and $p \gg n$. A doped semiconductor at room temperature typically has a majority-carrier concentration that is approximately equal to the doping concentration [74].

The values of n_i for different materials vary because of differences in the bandgap energies and effective masses. The room temperature intrinsic carrier concentrations for Si, GaAs, and GaN are shown in Table 3.3 [74].

Table 3.3 Intrinsic carrier concentration at $T=300^0$ K

Material	n_i (cm^{-3})
Si	$1.5 * 10^{10}$
GaAs	$1.8 * 10^6$
GaN	$1.9 * 10^{10}$

3.4 Electron and Hole Statistics

Determining the concentration of carriers as a function of energy requires knowledge of two features [72]:

- 1- The density of allowed energy levels (density of states)
- 2- The probability that each of these levels is occupied

3.4.1 Density of States:

The density of states shows how many states were to be found at any given energy in the conduction and valence bands. We are interested in this energy distribution of states since it is an essential component in determining the carrier distributions and concentrations. For energies not too far removed from the band edges, the density of states can be written as [73]:

$$\begin{aligned}
 g_c(E) &= \frac{m_n^* \sqrt{2m_n^*(E - E_c)}}{\pi^2 h^3}, & E \geq E_c \\
 g_v(E) &= \frac{m_p^* \sqrt{2m_p^*(E_v - E)}}{\pi^2 h^3}, & E \leq E_v
 \end{aligned}
 \tag{Eq. 3.1}$$

Where:

$g_c(E)$ and $g_v(E)$ are the density of states at an energy E in the conduction and valence bands respectively.

m_n^* and m_p^* are the effective mass of the electrons and holes

h is the Plank constant ($6.63 * 10^{-35}$ Joule-sec)

By considering closely spaced energies E and $E + dE$ in the respective bands, one can state:

$g_c(E)dE$: represents the number of conduction band states/cm³ lying in the energy range between E and $E + dE$ (if $E \geq E_c$)

$g_v(E)dE$: represents the number of valence band states/cm³ lying in the energy range between E and $E + dE$ (if $E \leq E_v$)

3.4.2 Probability of occupancy:

The laws of statistical mechanics dictate that under conditions of thermal equilibrium at temperature T, the probability that a given state of energy E is occupied by an electron is determined by the Fermi function [74].

$$f(E) = \frac{1}{1 + e^{(E - E_F)/KT}} \quad \text{Eq. 3.2}$$

Where:

K is the Boltzmann's constant (at T=300⁰ K, KT=0.026 eV)

E_F Fermi energy or Fermi level

Each energy level E is either occupied with probability f(E) or empty with probability 1-f(E). The function f(E) is not itself a probability distribution and it does not integrate to unity; rather it is a sequence of occupation probabilities for successive energy level. The Fermi function is universal in the sense that it applies with equal validity to all materials (insulators, semiconductors, and metals). Although introduced here in relationship to semiconductors, the Fermi function is not dependent in any way on the special nature of semiconductors, but is simply a statistical function associated with electrons in general [73].

3.4.3 Formulas for n and p:

Since $g_c(E)dE$ represents the number of conduction band states / cm³ lying in the E to E + dE energy range, and f(E) specifies the probability that an available state at an energy E will be occupied by an electron, it then follows that $g_c(E)f(E)dE$ gives the number of conduction band electron / cm³ lying in the E to E +dE energy range, and

$g_c(E)f(E)dE$ integrated over all conduction band energies must yield the total number of electrons in the conduction band. In other words, integration over the equilibrium distribution of electrons in the conduction band yields the equilibrium electron concentration. A similar statement can be made relative to the holes concentration [73]. Therefore one can write:

$$\begin{aligned}
 n &= \int_{E_c}^{E_{top}} g_c(E) f(E) dE \\
 p &= \int_{E_{bottom}}^{E_v} g_v(E) [1 - f(E)] dE
 \end{aligned}
 \tag{Eq. 3.3}$$

Explicit expressions for n and p can be found in [72-76].

3.5 Modeling the RF Properties of the Silicon under Light Illumination

In this section, we present a solid-state physics model that predicts the change in the RF properties of semiconductor materials as a function of incident light intensity from a suitably energetic laser. We then apply this model to a piece of silicon (smaller than a wavelength at the microwave frequencies of interest) and predict the change in its dielectric constant, RF conductivity and dielectric losses as a function of the laser power

Under illumination by light of suitable wavelength, the mobility of charges in a semiconducting material decreases but their density increases. This increase in the charge carrier density results in a general increase in the conductivity of a semiconducting

material [77]. In general, the dependence of the mobility of electrons and holes in silicon can be described by the following equation [78]:

$$\mu = \mu_{\min} + \frac{\mu_{\max} - \mu_{\min}}{1 + \left(\frac{N}{N_{ref}}\right)^\alpha} \quad \text{Eq. 3.4}$$

Where:

μ is the electrons or holes mobility ($\text{cm}^2/\text{V.s}$)

μ_{\min} , μ_{\max} , α , and $N_{ref}(\text{cm}^{-3})$ are the fitted coefficients given in Table 3.4.

Table 3.4 The mobility parameters for silicon

<i>Parameter</i>	<i>Electrons</i>	<i>Holes</i>
μ_{\min}	52.2	44.9
μ_{\max}	1417	471
N_{ref}	$9.68 \cdot 10^{16}$	$2.23 \cdot 10^{17}$
α	0.68	0.719

The first step is to derive the total carrier concentration which is a function of the incident laser power level. The silicon piece under investigation in this work is a doped n-type material with an initial concentration of 10^{15} cm^{-3} and has the dimension of 1 mm X 1 mm and a thickness of 0.28 mm [79-80]. The total steady-state generation rate of carriers per unit volume is [75]:

$$G = \frac{n}{\tau} = \frac{\eta(P_{opt} / h\nu)}{WLD}$$

Eq. 3.5

Where:

n is the total carrier concentration

τ is the carrier lifetime

η is the quantum efficiency (i.e. number of carrier generated per photon)

P_{opt} is the incident optical power

$h\nu$ is the photon energy

$W, L,$ and D are the dimensions for the silicon switch

The results for the charge carrier concentration as a function of incident power level are summarized in Table 3.5.

Table 3.5 Relation between power levels and carrier concentration

Power Level (mW)	Total Electrons Concentration (cm⁻³)
0	$1*10^{15}$
50	$6.8*10^{15}$
120	$1.5*10^{16}$
212	$2.6*10^{16}$

The change in the dielectric constant of the silicon piece due to the increase in the total carrier concentration is given by **[81]**:

$$\begin{aligned}\epsilon_r &= \epsilon_r^{initial} - \sum_{i=e,h} \frac{Nq^2}{\epsilon_0 m_i [(2\pi f)^2 + \nu_i^2]} \left(1 + j \frac{\nu_i}{2\pi f} \right) \\ &= \epsilon' - j\epsilon''\end{aligned}$$

Eq. 3.6

Where:

$\epsilon_r^{initial}$ is the dielectric constant of the silicon (11.9)

q is the electron charge ($\approx 1.602 * 10^{-19}$ C)

ν is the collision angular frequency

m is the electron/hole effective mass

f is the operating frequency

From the above equation, the physical properties such as the conductivity (σ), the loss tangent ($\tan \delta$), and the dielectric constant (ϵ) of the silicon under different power levels can be derived as follows [77]:

$$\tan \delta = \frac{\sigma_{static}}{w\epsilon'} + \frac{\epsilon''}{\epsilon'}$$

$$\sigma = \sigma_{static} + \sigma_{RF}$$

where

$$\sigma_{static} = (\sigma_{static})_{electrons} + (\sigma_{static})_{holes}$$

$$= N_e q_e \mu_e + N_h q_h \mu_h$$

and

$$\sigma_{RF} = 2\pi f \epsilon''$$

Eq. 3.7

The trend of variation of the silicon RF+DC conductivity is shown in Fig. 3.4. It is noticed that as the carrier concentration increases, the silicon switch becomes more conductive.

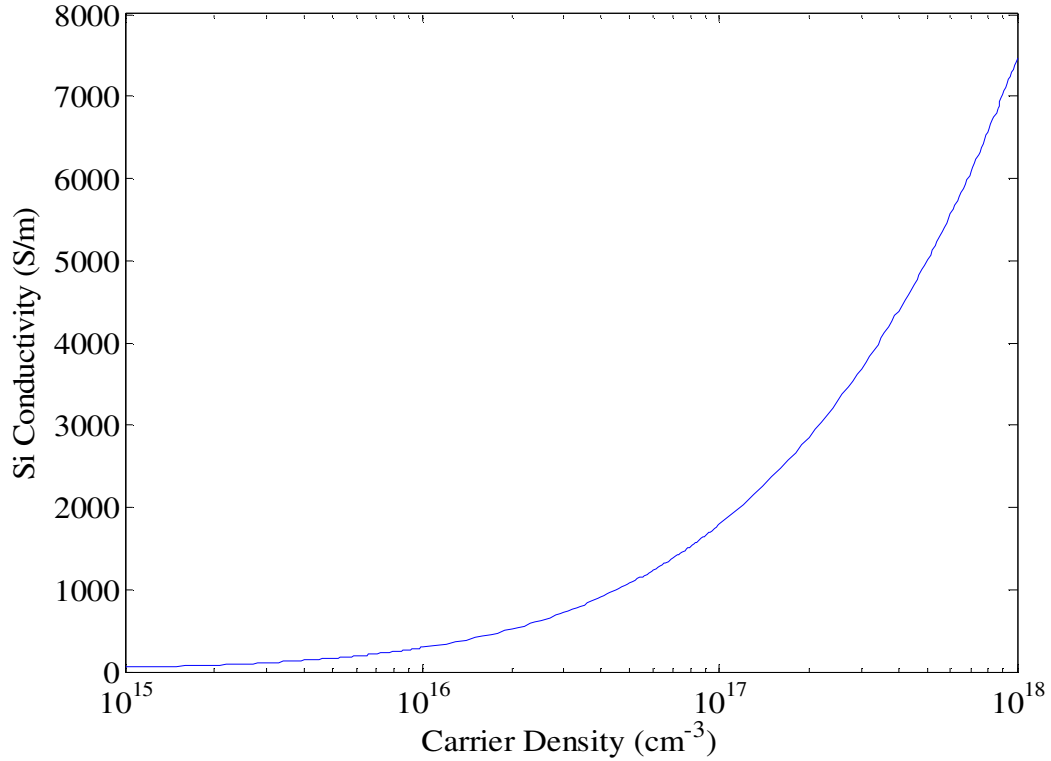


Figure 3.4 “DC+RF” conductivity of the silicon switch

The change in the real part of the dielectric constant of the silicon switch is shown in Fig. 3.5. As the power level of the light increases, the dielectric constant of the silicon switch is going to decrease. The imaginary part of the dielectric constant shown in Fig. 3.6 gives an idea about the loss that is produced by a silicon switch shined from a laser light.

In this section, a theoretical model for the change in the electromagnetic properties of silicon material as a function of the incident laser light power is discussed. It can be concluded that as the carrier concentration increases, the conductivity of the silicon also increases and its dielectric constant decreases. However, the silicon becomes lossier due to

the increase in its dielectric loss tangent. This model is used in the design of optically pumped reconfigurable antenna structures that will be discussed in the next chapters.

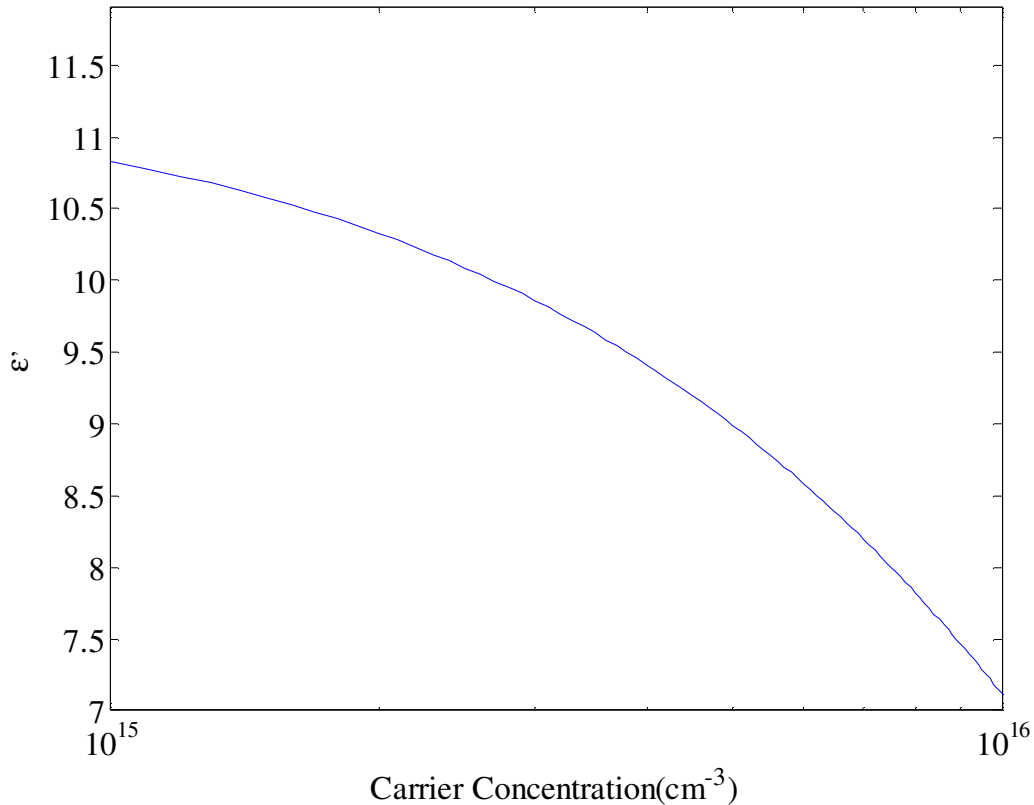


Figure 3.5 Change in the real part of the silicon dielectric constant at f=5GHz

3.6 Switch Fabrication

Switches have been incorporated in RF devices to achieve reconfiguration especially in antennas. Reconfigurable antennas have relied on these devices to tune between different functions. A new type of reconfigurable antennas that relies on optical switches is introduced in this dissertation. These optically pumped reconfigurable antenna systems (OPRAS) [82-83] rely on n-type silicon switches. In this section, the fabrication process of such switches is detailed.

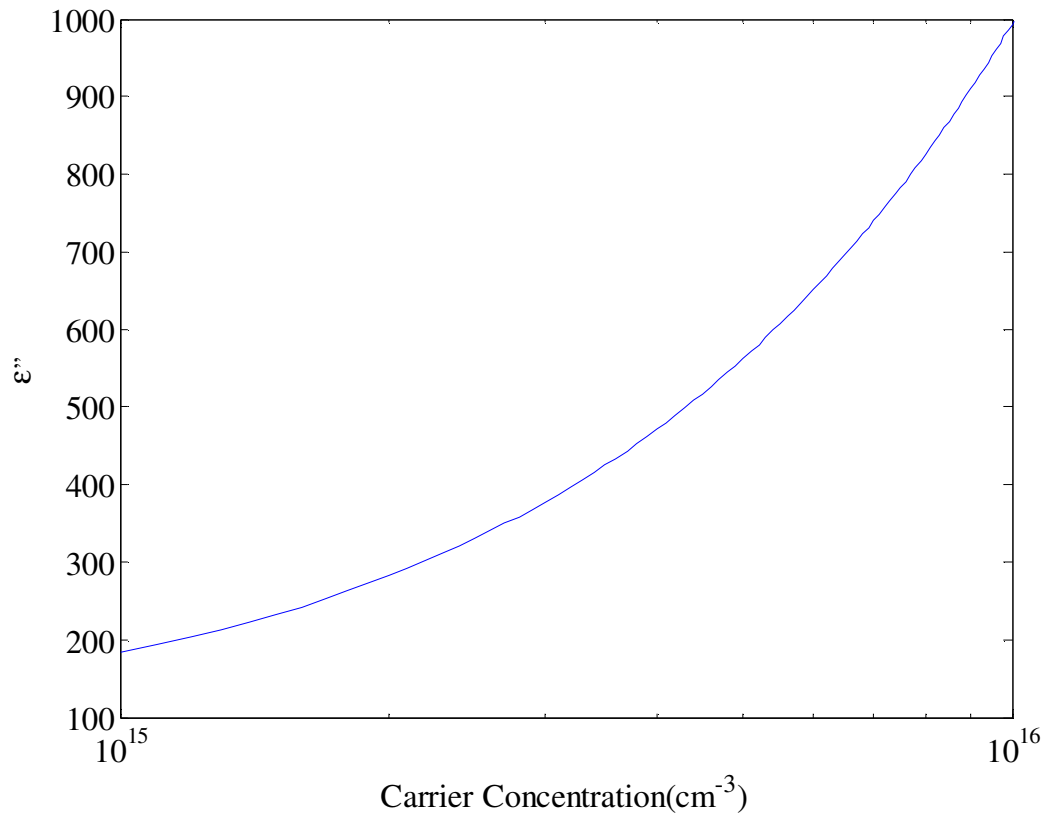


Figure 3.6 Change in the imaginary part of the silicon dielectric constant at $f=5\text{GHz}$

The objective in the fabrication process is to achieve an ohmic contact in order to allow carriers to flow in and out of the semiconductor switch. The different steps can be summarized as follows:

Step 1: The first step of the fabrication process is to execute a surface cleaning via chemical etching. This step is very essential since the fabrication of contacts relies on the extreme cleanliness of the semiconductor surface especially to avoid the formation of an oxide layer on the surface of the silicon.

Step 2: In this step the wafer is coated with photo-resist and patterned using light. The mask used to produce the image on the silicon wafer is shown in Fig. 3.7. At this point an image of the pattern is printed on the wafer as shown in Fig. 3.8.

Step3: The third step is to deposit the metal uniformly across the silicon wafer.

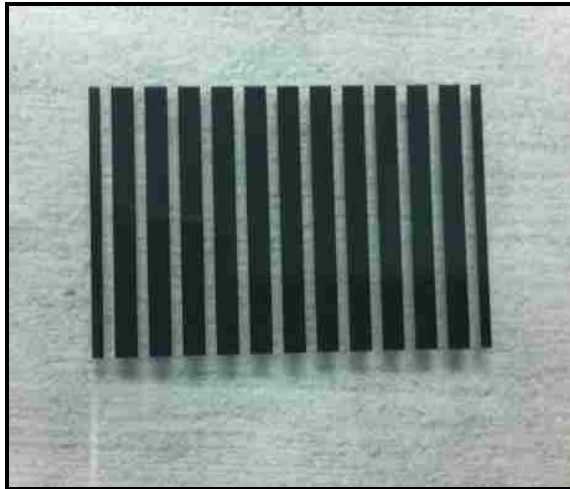


Figure 3.7 The mask used to produce the corresponding image

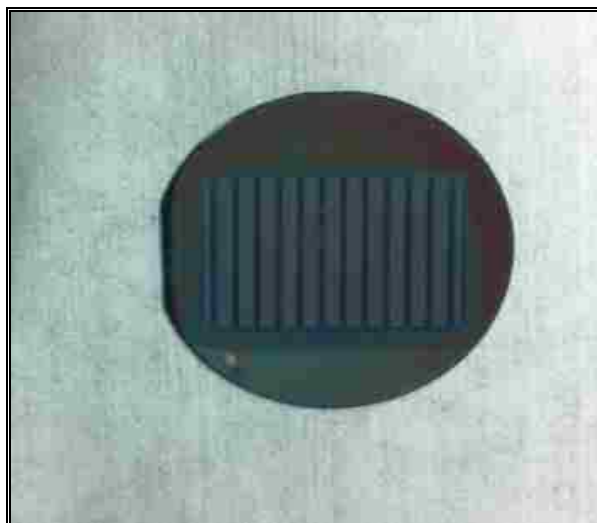


Figure 3.8 The printed pattern on the silicon wafer

Step 4: The fourth step is the etching step where chemicals (such as acids) are used to remove the undesired materials. Fig. 3.9 shows the final silicon wafer structure. The investigated switch in this work is rectangular with dimensions of 3 mm x 1mm. Each switch terminal has a 1 mm x 1mm of metal coating for ohmic contact. For example, the pattern shown on the silicon wafer in Fig. 3.9 consists successively of a column of metal followed by a column of silicon with 1 mm width of each column.

Step 5: The final step of the switch fabrication process consists of cutting the silicon wafer appropriately to match the desired dimensions of the silicon switch.

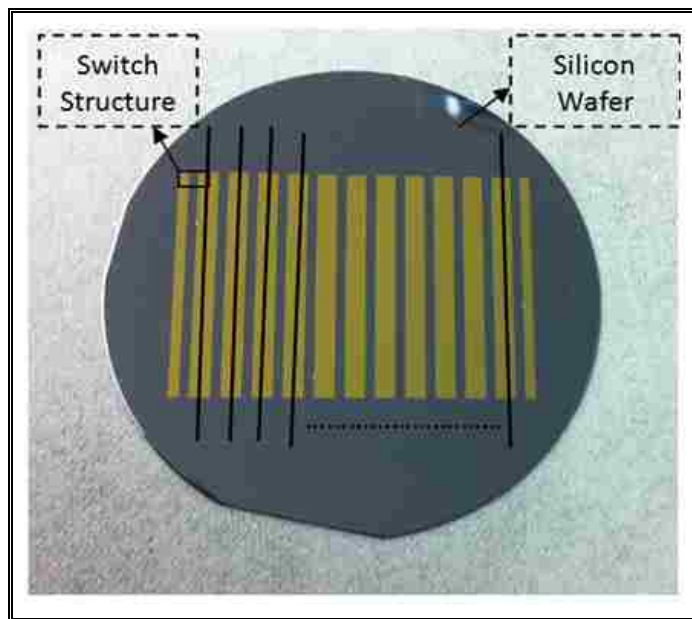


Figure 3.9 Silicon wafer

3.7 Conclusion

In this chapter a detailed discussion about the physical properties of semiconductor based photoconductive switches is presented. The energy band model for such switches

and the difference between direct and indirect semiconductor materials is discussed. The process of producing doped semiconductor switches is shown and the process of fabricating n-type silicon switches is detailed.

The calculation of the RF properties of a semiconductor switch is derived. This RF model is used to design optically pumped reconfigurable antenna system (OPRAS). The design and analysis of this type of antennas are discussed in the next chapter.

Chapter 4

Optically Pumped Reconfigurable Antenna System (OPRAS)

4.1 Introduction

The ability to alter the Radio Frequency (RF) conductivity of semiconductor materials by exposing them to light of suitable wavelength is creating several exciting possibilities in the field of reconfigurable microwave systems. For instance, such materials can be used as optically-activated switches to dynamically alter the RF behavior of microwave circuit components and antennas in a rapid and controlled fashion, thereby paving the way for reconfigurable systems such as Cognitive Radios.

This chapter presents novel frequency reconfigurable antenna designs using photoconductive silicon elements as optical switches. By illuminating these silicon elements with light of suitable wavelength their physical properties can be altered from that of a semiconductor to almost metal-like, which in turn alters the radiation properties of the antenna structure.

The work in this chapter demonstrates a new methodology for coupling the light energy onto the silicon switches. This technique facilitates the conformal integration of reconfigurable antennas into the next-generation wireless devices. First, the experimental results on a stripline circuit employing a single silicon switch under light illumination are presented and the theoretical model is compared next with the experimental data. A novel frequency reconfigurable antenna design utilizing this new coupling methodology is

designed and its experimentally-measured RF performance is compared with numerical simulations.

4.2 Optically Switched Transmission Line

In Chapter 3, a model for n-type silicon semiconductor is described under different illuminations. To test this model, a transmission line shown in Fig. 4.1 is designed. A silicon switch (S1) is placed in the middle of the structure. The chosen substrate is Rogers Duroid with a dielectric constant of 2.2 and a height of 1.6 mm.

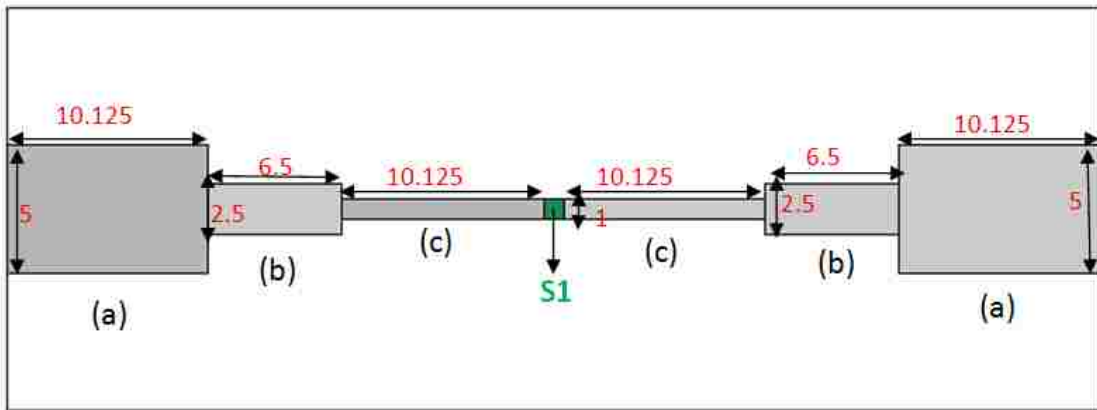


Figure 4.1 An optically switched transmission line

The stripline structures on either side of the silicon switch are identical. The sections labeled (a) in Fig. 4.1 have a characteristic impedance of 50Ω . The silicon switch used has a width of 1 mm. Assuming the silicon switch to be a perfect metal, then the 1 mm width corresponds to an impedance of 118Ω . Therefore the transmission line (parts (c)) has an impedance of 118Ω . A quarter wavelength transformer (parts (b)) is used to match the two transmission lines sections-parts (a) and (c). It has a length of 6.5 mm which translates to a resonant frequency of 8.4 GHz. The fabricated prototype is shown in Fig. 4.2.

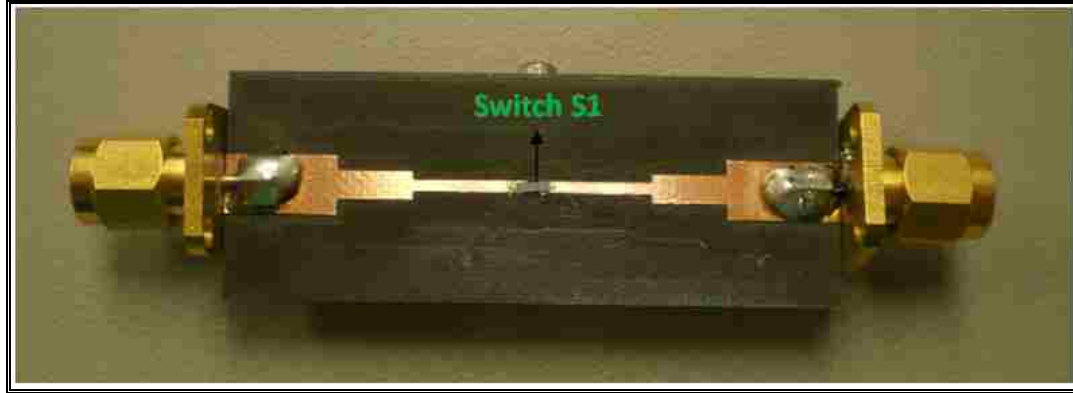


Figure 4.2 The fabricated prototype for the optically switched transmission line

The light from an 808 nm laser diode is delivered to the silicon switch via an optical fiber cable. It is placed underneath the substrate and held via a plastic fixture as shown in Fig. 4.3. A 1 mm hole is drilled through the substrate to allow the delivery of light to the photoconductive switch S1.

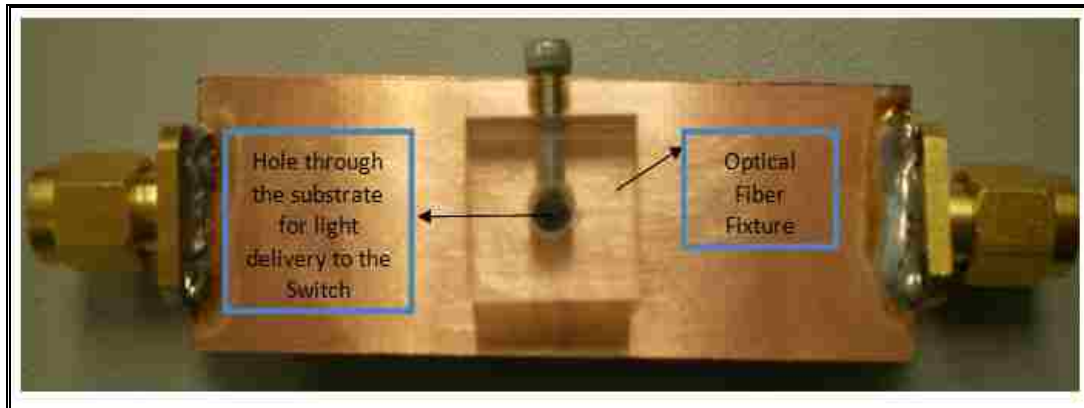


Figure 4.3 The back side view of the fabricated prototype

The return loss for this transmission line structure for different power levels shows that the silicon acts as a switch. As the power level increases, the conductivity of the silicon piece increases thereby reducing the reflection loss. At 212 mW, a minimal reflection is observed. The simulated and the measured transmission line return loss is shown in Fig. 4.4 and Fig 4.5.

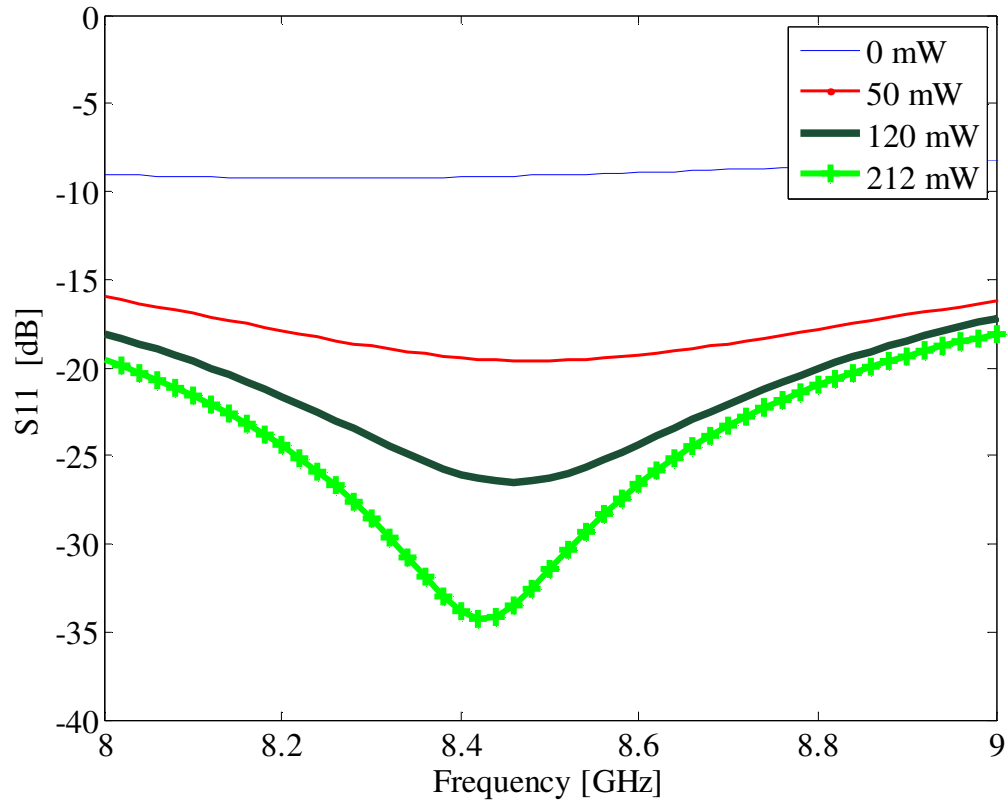


Figure 4.4 The simulated return loss for the optically switched transmission line

By comparing both plots one can notice that a good agreement is found between both data. In such structure, it is instructive to also look at the transmission between port 1 and port 2. The measured transmission is shown in Fig. 4.6 As expected, the higher the power level the more RF signal is being delivered to the load. In this experiment, the losses in the optical fiber cable are assumed to be negligible and that all the laser energy is assumed to be coupled to the silicon switch. This experiment enables us to conclude that the silicon piece acts as an RF switch and can be used in the design of reconfigurable antennas.

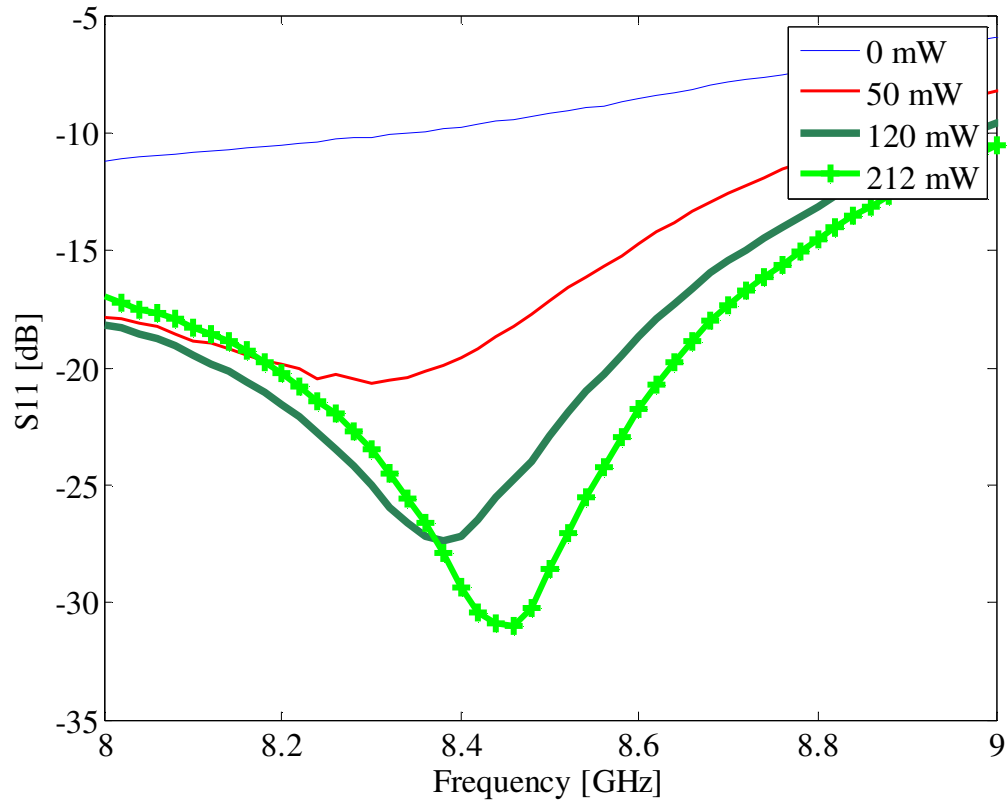


Figure 4.5 The measured return loss for the optically switched transmission line

4.3 Frequency Reconfigurable Antenna Design

Following the experiment in section II, two optically reconfigurable antennas are designed and tested. These antennas achieve reconfigurability with the same type of silicon switches. The first antenna is based on a stripline fed structure while the second one is a CPW fed reconfigurable antenna.

4.3.1 Stripline Fed Optically Reconfigurable Antenna Structure:

The antenna structure consists of an outer circular annular ring (Region 1) and an inner circular patch (Region 2). Both structures are separated via a 1 mm gap and

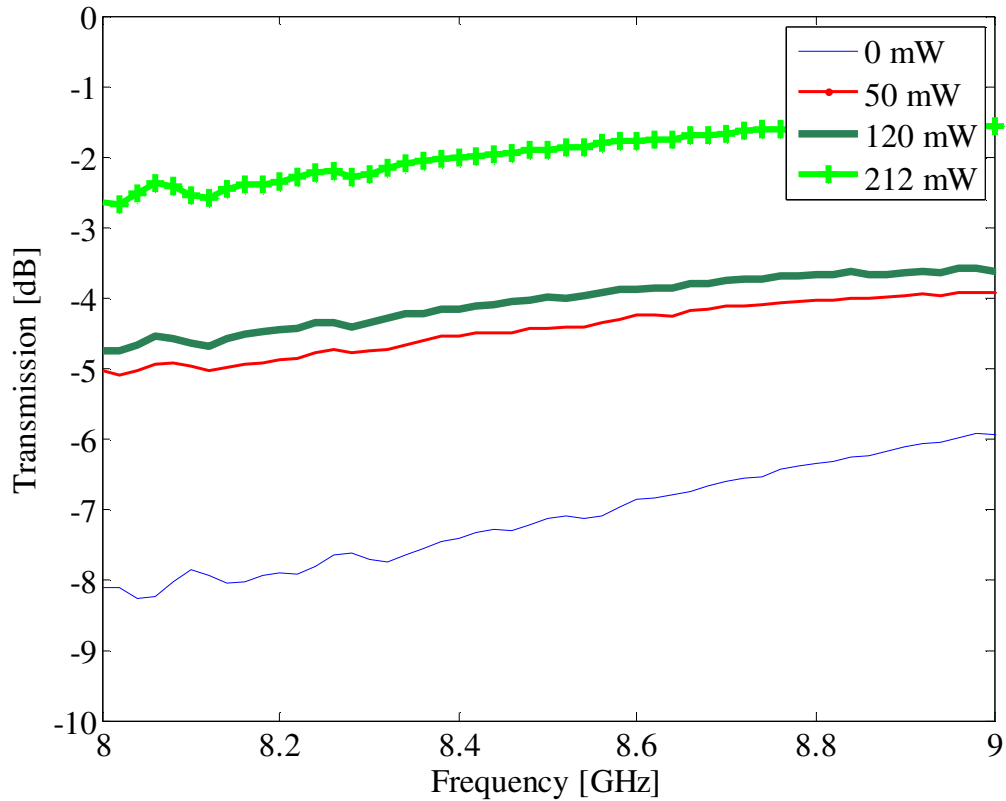


Figure 4.6 The measured transmission for the optically switched transmission line connected together via two silicon pieces that act as the RF switches. The dimensions of the different parts of the antenna structure are shown in Fig. 4.7.

The top view of the fabricated antenna topology is shown in Fig. 4.8. The bottom view of the antenna structure is shown in Fig. 4.9. The chosen substrate is Rogers Duroid 5880 with a dielectric constant of 2.2 and a height of 1.6 mm. The light from an 808 nm laser diode is delivered to the silicon switch via an optical fiber cable. It is placed underneath the substrate and held via a plastic fixture. To couple light into the silicon switch, two holes of radius 1mm each are drilled into the substrate, as shown in Fig. 4.9. We again make the same assumption that the losses in the fiber cable are negligible and that all the laser energy is coupled to the silicon switch.

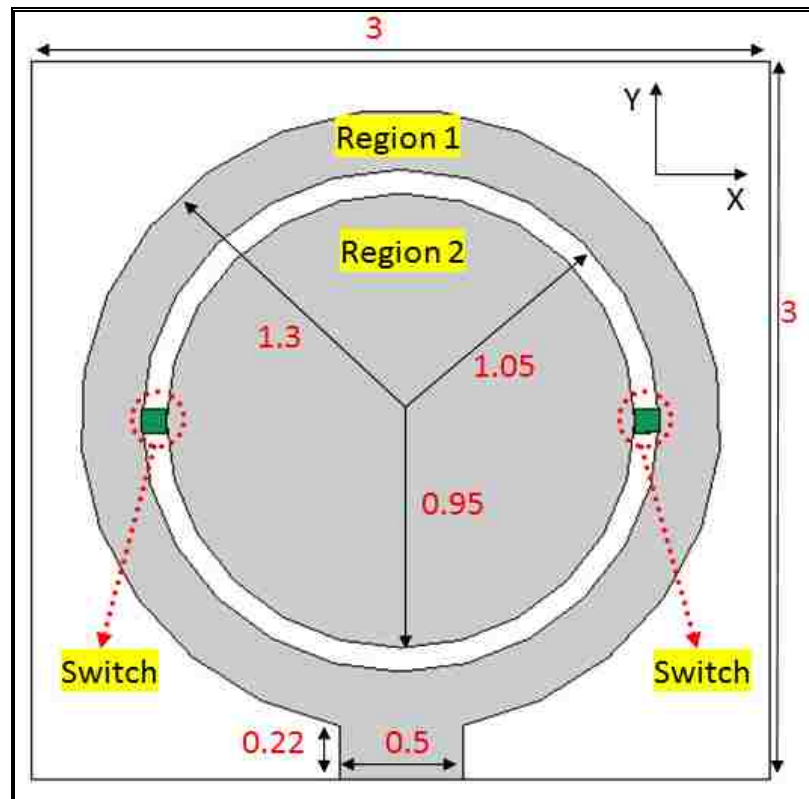


Figure 4.7 The stripline fed optically reconfigurable antenna structure

When the two silicon switches are not illuminated by a laser light (OFF state), only the circular ring (region 1) is fed. This results in an antenna resonance between 18 GHz and 19 GHz. Upon activation of the silicon switches, a new resonance begins to appear at 12 GHz. This is due to the mutual coupling between Region 1 and Region 2. Since the combined regions now represent an antenna with larger metalized surface area, the resonant frequency shifts lower. The simulated and the measured antenna returns loss for the different power levels are shown in Fig. 4.10 and Fig. 4.11. As the pumped power increases, the RF conductivity of the silicon switch increases thereby reducing the impedance mismatch between Region 1 and Region 2; and subsequently yields resonances with better matches and less reflection density. By comparing both plots, one can observe

a good qualitative agreement between the simulated and the measured data in terms of the observed resonances.



Figure 4.8 The top view of the fabricated antenna structure



Figure 4.9 The antenna bottom layer

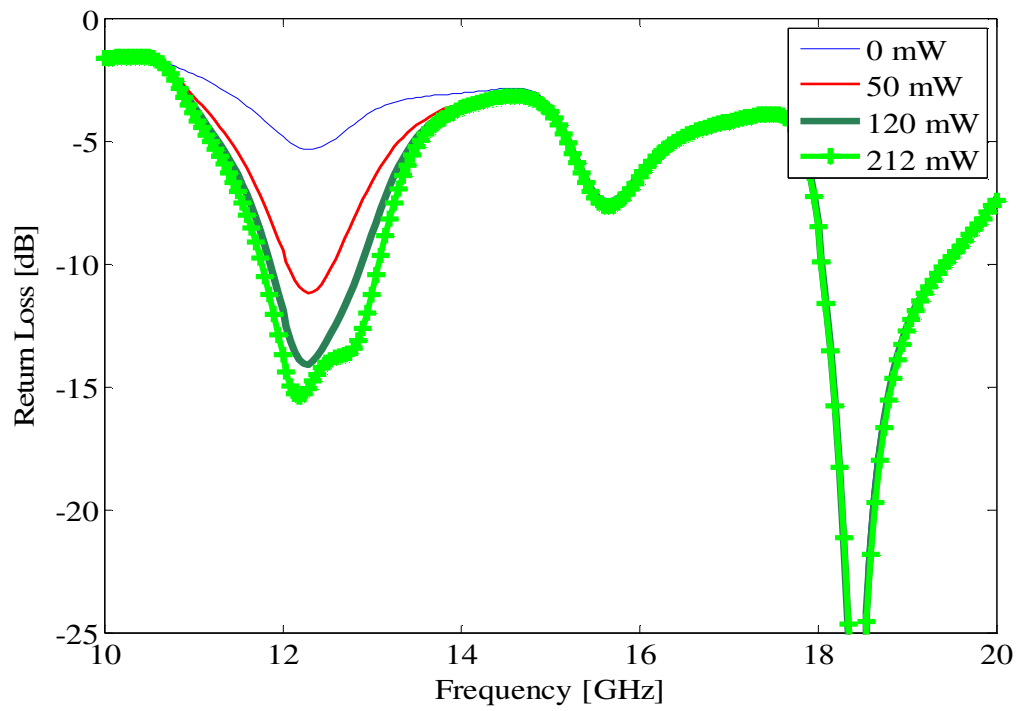


Figure 4.10 The simulated antenna return loss

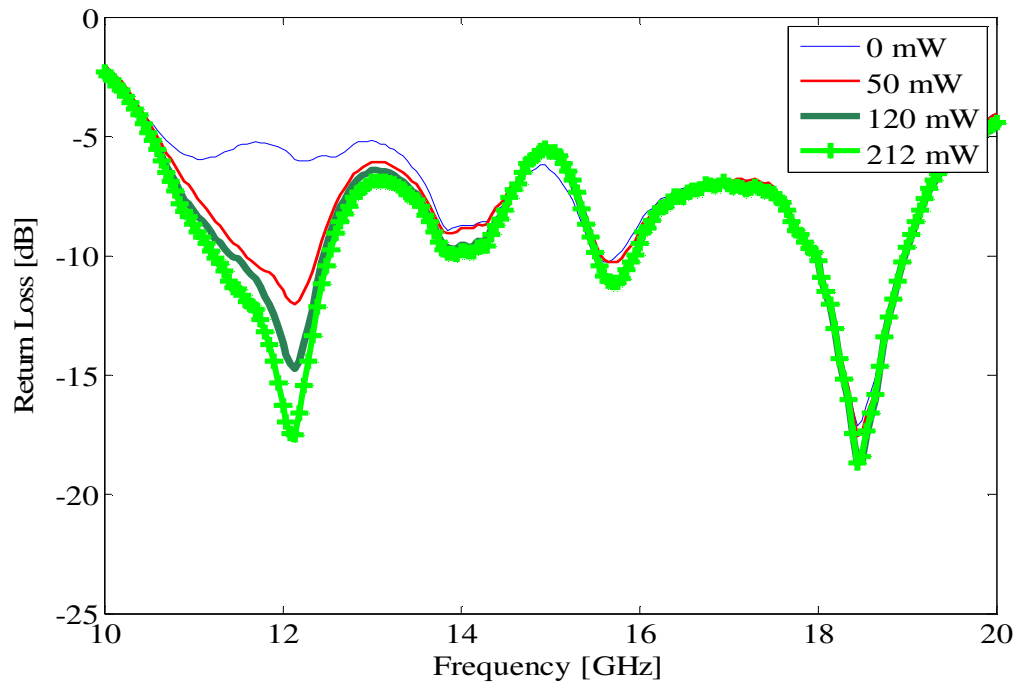


Figure 4.11 The measured antenna return loss

The simulated antenna radiation pattern at $\Phi=0^\circ$ (XZ plane) when both switches are OFF ($f=18.4$ GHz, solid line) and when both switches are ON ($f=12.2$ GHz, dotted line) for a 212 mW incident laser power are shown in Fig. 4.12. For both cases, the antenna preserves its omnidirectional radiation pattern property

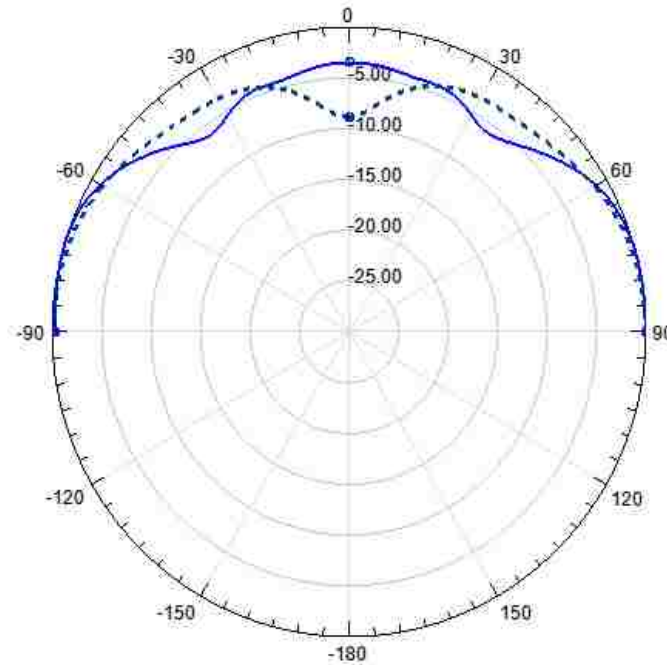


Figure 4.12 The computed radiation pattern at 18.4 GHz (solid line) and 12.2 GHz (dotted line) in the xz plane

4.3.2 CPW Fed Optically Reconfigurable Antenna Structure:

The antenna radiating structure is a polygon shaped patch fed by a CPW with dimensions shown in Fig. 4.13. The top view of the fabricated antenna is shown in Fig. 4.14 and the bottom view is illustrated in Fig. 4.15. The antenna substrate is Getek with a dielectric constant of 3.9 and thickness of 1.6 mm. Similar to the first design, the light generated by an 808 nm laser diode is delivered to the silicon switch via an optical fiber cable placed underneath the substrate and held via a plastic fixture. The light is also

coupled to the silicon switch through two 1 mm holes as shown in Fig. 4.15. Losses are also assumed negligible in the optical fiber cables.

When both switches are OFF, i.e. not illuminated by laser light, the antenna ground plane is constituted by two rectangular patches each one at a different side of the feed line. This allows the antenna to operate between 800 MHz-3.5 GHz. By activating both switches, the shape of the antenna ground changes. This allows the antenna to cover the frequency band from 1.6 GHz-3.5 GHz. The simulated and the measured antenna return loss for four different power levels are summarized in Fig. 4.16 and Fig. 4.17. Good agreement is observed between the simulation and the measurement data behavior

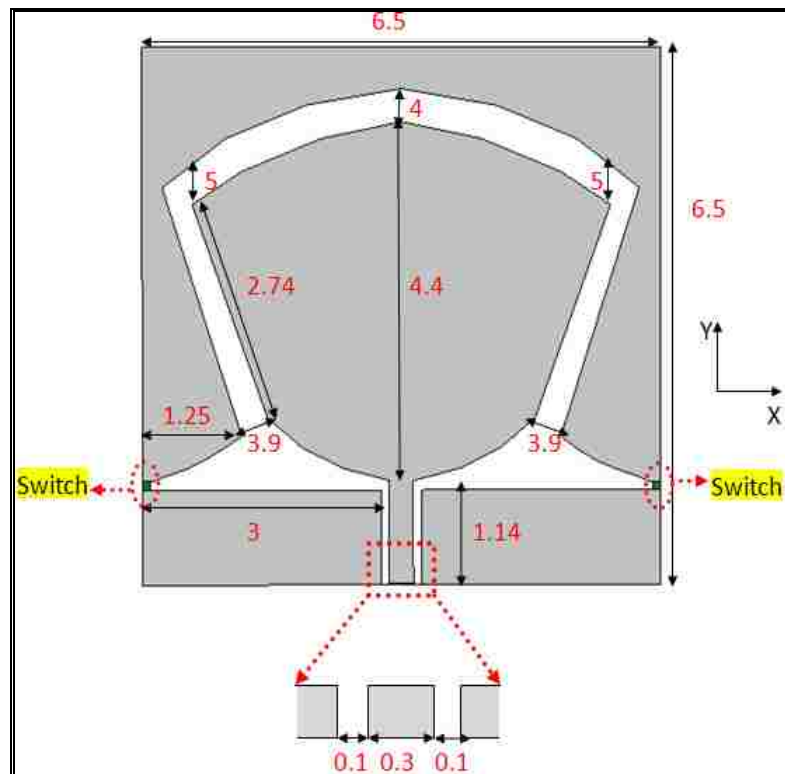


Figure 4.13 The CPW fed antenna structure

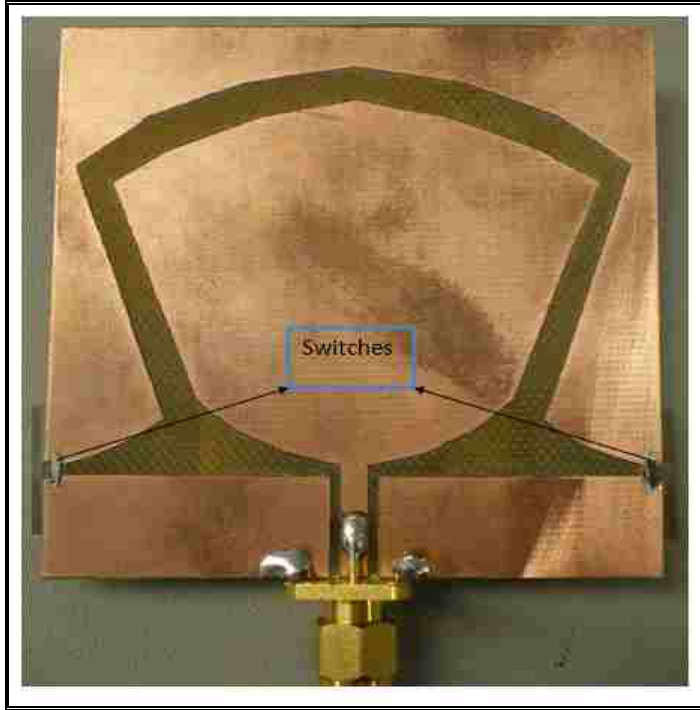


Figure 4.14 The top layer of the CPW reconfigurable antenna structure

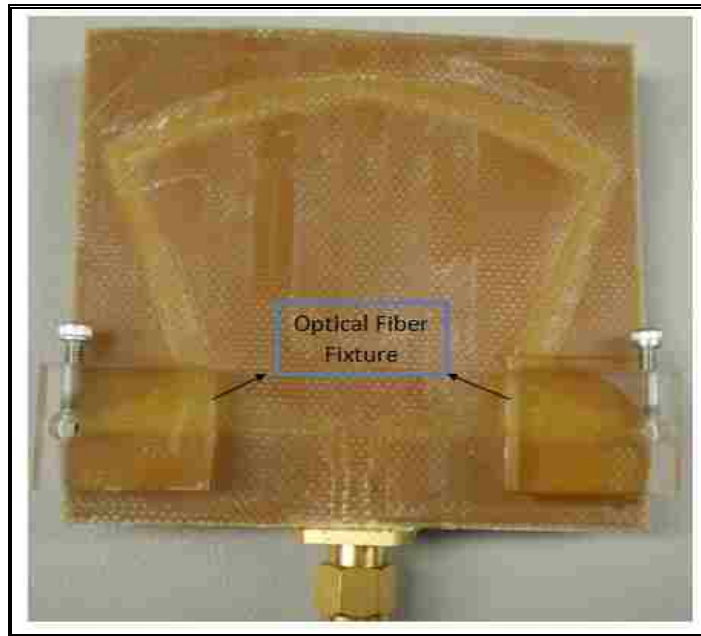


Figure 4.15 The bottom layer of the antenna

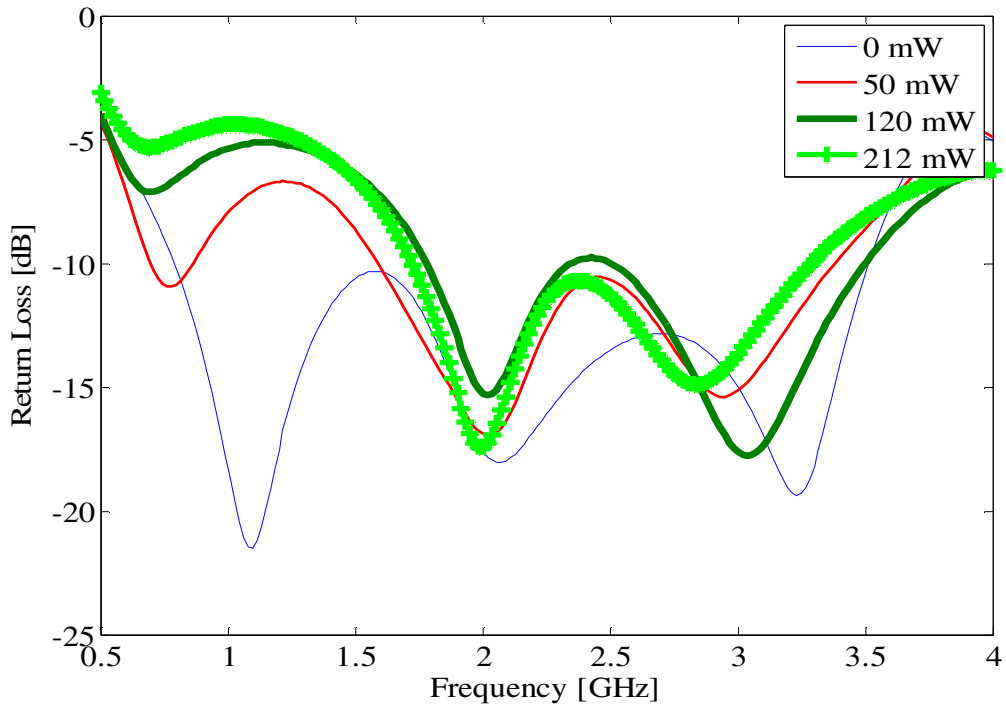


Figure 4.16 The simulated antenna return loss for the CPW fed antenna

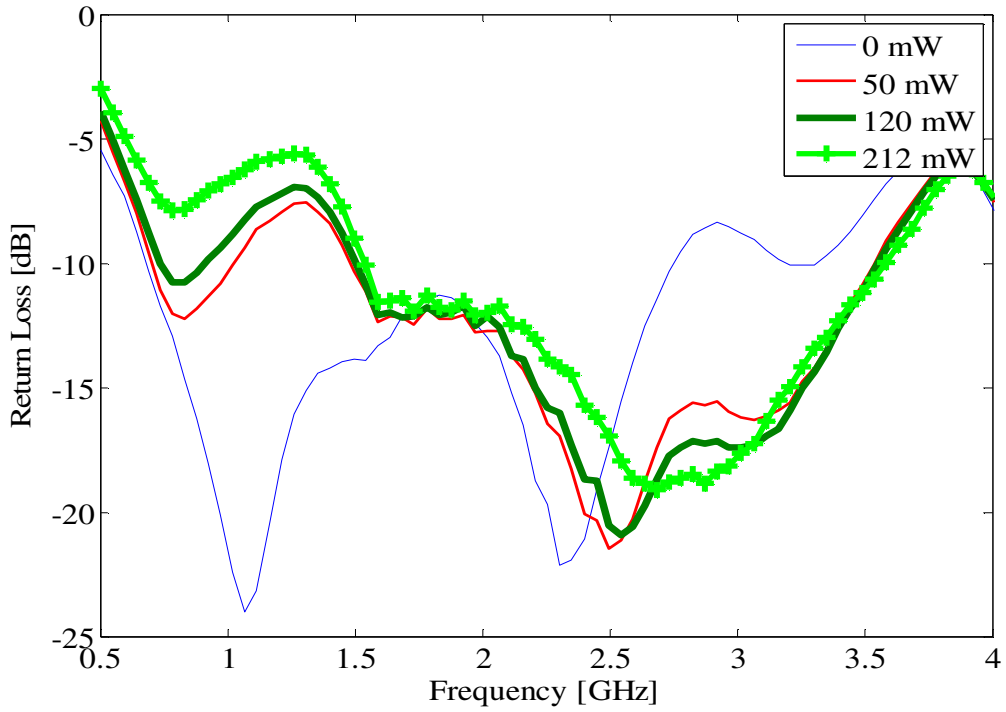


Figure 4.17 The measured return loss for the CPW fed antenna

The antenna radiation pattern at $f = 1$ GHz when both switches are OFF (solid line) and at $f = 3$ GHz when both switches are ON (dotted line) are depicted in Fig. 4.18. The antenna radiation pattern at $f=2.5$ GHz when both switches are OFF (solid line) and ON (dotted line) is shown in Fig. 4.19(a) for the XZ and Fig. 4.19(b) for the YZ plane. For all plots, the ON-state corresponds to a laser activation power of 212mW. The antenna preserves the same radiation pattern while performing frequency reconfigurability. The patterns are omnidirectional, with almost uniform radiation in the XZ plane and have the shape of an ‘8’ in the YZ plane corresponding to a 3D donut shape.

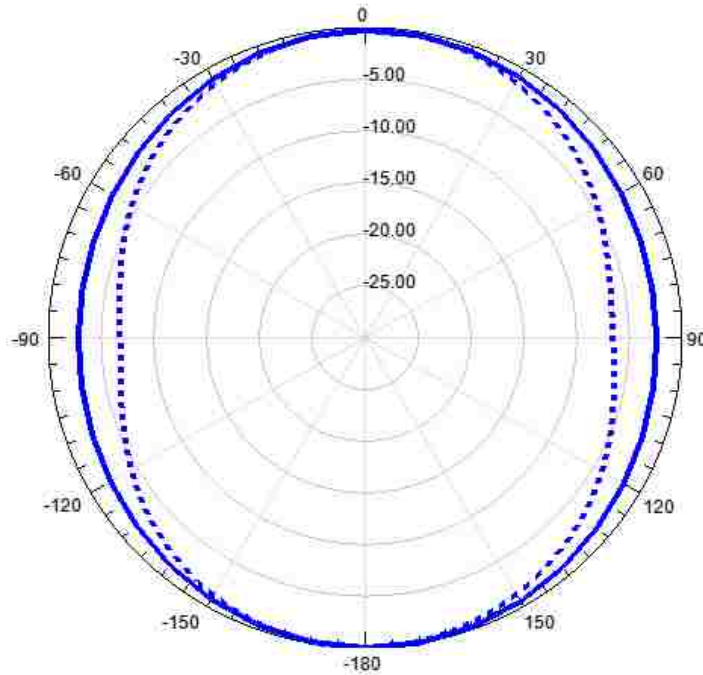


Figure 4.18 The computed antenna radiation pattern at $f= 1$ GHz when both switches are OFF (solid line) and at $f= 3$ GHz when both switches are ON (dotted line) in the XZ plane

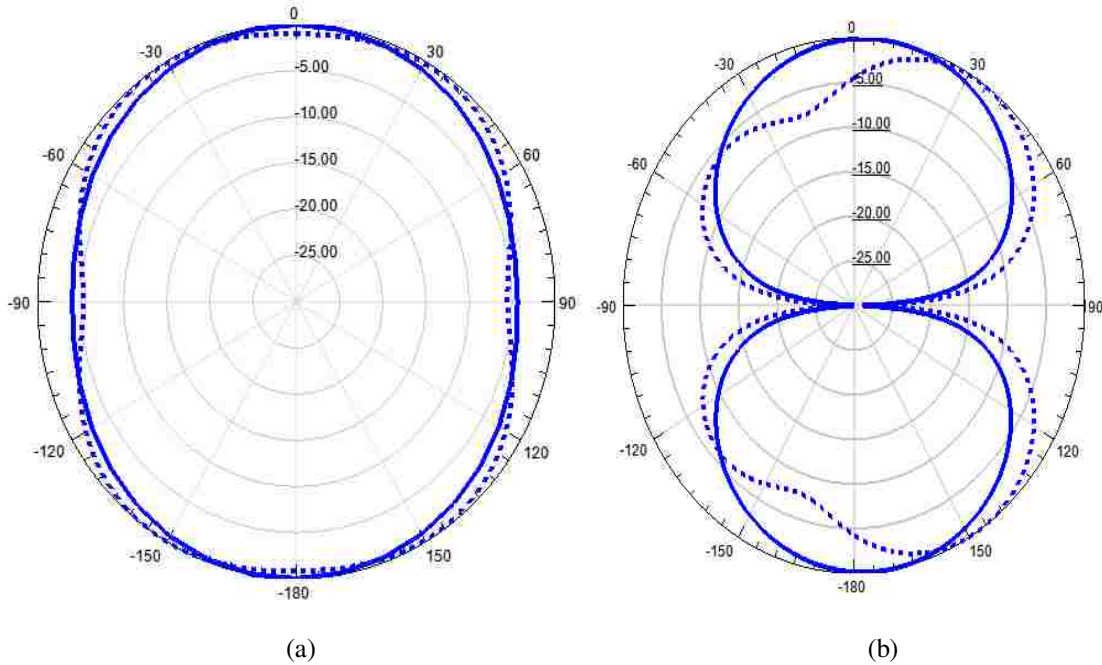


Figure 4.19 The computed antenna radiation pattern at $f= 2.5$ GHz when both switches are OFF (solid line) and ON (dotted line) in the (a) XZ plane and the (b)YZ plane

4.4 Determining the Gain of the Stripline fed Antenna

An antenna gain is defined as “The ratio of the intensity, in a given direction, to the radiation intensity that would be obtained by an isotropic source. The radiation intensity corresponding to the isotropically radiated power is equal to the power accepted (input) by the antenna divided by 4π ” [84-85].

In this section the gain of the stripline fed antenna shown previously is measured using the reflection measurement technique [86].

4.4.1 The Reflection Measurement Technique:

In order to measure the gain of the optically reconfigurable antenna, a new experimental technique is developed. This technique utilizes a single matched antenna and

a plane metallic reflecting surface as shown in Fig. 4.20. The presence of the antenna A facing a plane metallic surface allows the use of the antenna image (Antenna B = image of Antenna A) to measure the antenna gain. The energy incident on the metallic surface is reflected and absorbed by antenna “A” giving rise to a reflected wave in the transmission line. The ratio P_r/P_t is then found by measuring the standing wave ratio.

$$\frac{P_r}{P_t} = \left(\frac{r-1}{r+1} \right)^2 = \frac{G^2 \lambda^2}{(4\pi)^2 S^2} \quad \text{Eq. 4.1}$$

S is the distance from the antenna to its image in the reflector.

Solving for G , we obtain:

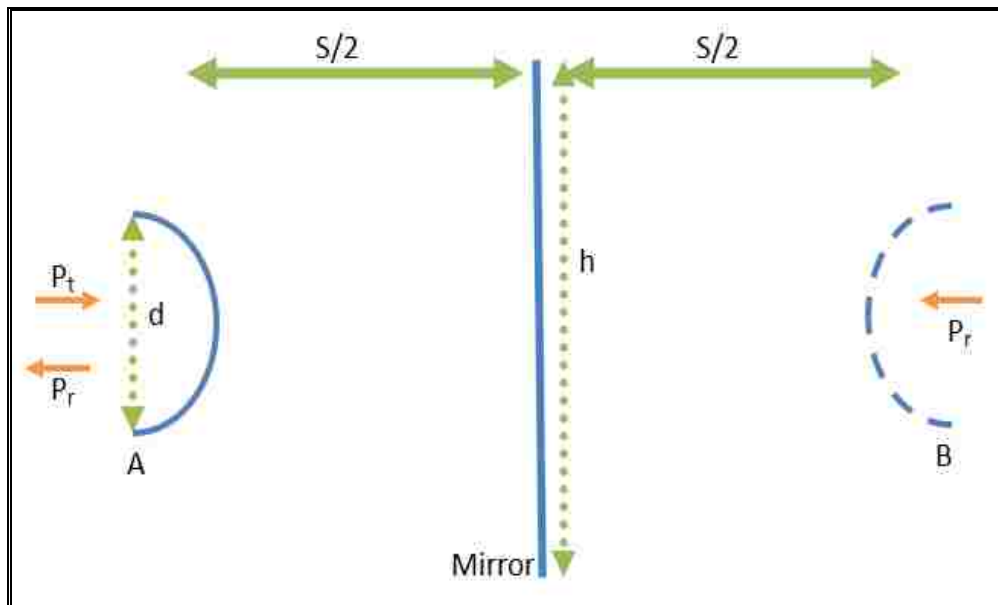


Figure 4.20 The reflection method for gain determination

$$G = \frac{4\pi S}{\lambda} \left(\frac{r-1}{r+1} \right) \quad \text{Eq. 4.2}$$

The practicality of the method depends on the distance $S/2$ that is required from the antenna to the mirror and the required dimensions of the metallic reflecting surface. The use of the image antenna is based on the ideal situation of an infinite reflector. The criterion for the distance S is $S \geq 2d^2/\lambda$, although distances less than $2d^2/\lambda$ have been tried without a significant error [86]. The mirror must be large enough to intercept most of the main beam whose width is of the order $2\lambda/d$ radians and to reduce any diffraction effect. For a square mirror of edge length h , we have then:

$$\boxed{\frac{2\lambda}{d} \leq \frac{2h}{S} \quad \text{or} \quad h \geq \frac{S\lambda}{d}} \quad \text{Eq. 4.3}$$

For $S = 2d^2/\lambda$, the dimension h required is equal to or greater than $2d$. The mirror must be flat to a small fraction of a wavelength, at least $\lambda/16$.

4.4.2 The Experiment Setup for Calculating the Gain:

The boresight directivity gain of the stripline fed optically reconfigurable antenna is determined using the reflection measurement technique [86]. The experiment setup is shown in Fig. 4.21.

By placing a ground plane of dimensions (25x25cm), 10 cm in front of the antenna, a VSWR value of 1.149 at 18.3GHz was obtained in the case when both switches are OFF, and VSWR=1.106 at 11.8GHz with both switches ON. This translates to a measured boresight gain of 10.26dB and 5.42dB. The comparison between the simulated and the measured gain for the antenna are summarized in Table 4.1.

Table 4.1 The simulated and the measured gain

<i>Frequency [GHz]</i>	<i>Simulated</i>	<i>Measured</i>
18.3	10.87	10.26
11.8	5.75 dB	5.42 dB

It is noticed that the increase in the material losses introduced by the silicon switches for increasing pumped laser power levels, results in reduced radiation efficiency of the antenna structure, and correspondingly reduces the boresight gain values.

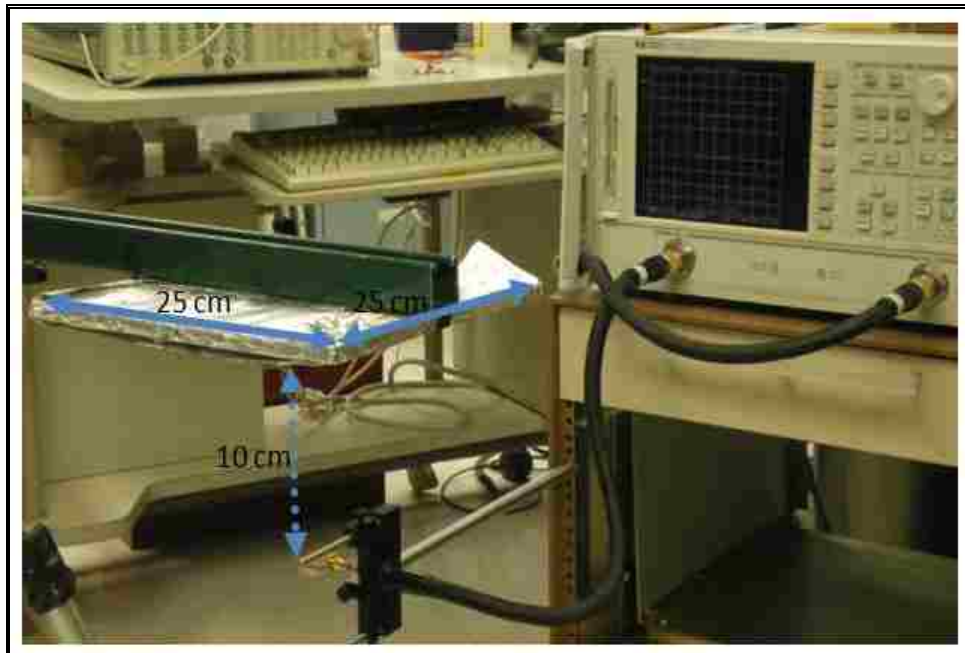


Figure 4.21 The experiment setup to determine the gain of the CPW fed optically reconfigurable antenna structure

4.5 Conclusion

In this chapter new reconfigurable antenna designs based on optical switching are presented. First a dual band antenna is designed and tested then a CPW wideband optically

reconfigurable antenna is discussed. The choice of the frequency range for both antennas is arbitrary and serves to only validate the proof-of-concept for the approach used. The physical integration methodology of the light energy coupling onto the silicon switch adopted in this work has several advantages. One major advantage is the ability of the antennas to be easily integrated into compact packages which can be included in next-generation wireless devices. Furthermore, our antenna designs can be easily tweaked to include frequency bands corresponding to established wireless standards such as GSM, CDMA, WiMAX, etc.

In the next chapter, another technique for light delivery to the photoconductive switches is discussed. Also, the use of optically pumped reconfigurable antenna system (OPRAS) for cognitive radio is presented.

Chapter 5

Demonstration of a Cognitive Radio Front-End Using Optically Pumped Reconfigurable Antenna Systems (OPRAS)

5.1 Introduction

This chapter presents a cognitive radio front-end using an optically pumped reconfigurable antenna system (OPRAS). The scheme consists of an UWB antenna and a reconfigurable narrow-band antenna in close proximity to one another. The narrow-band reconfigurability is achieved by integrating laser diodes within the antenna structure to control the switching state of photoconductive silicon switches. This scheme has the advantage of eliminating the use of optical fiber cables to guide light to the switches, and allows for easier integration of the reconfigurable antenna in a complete communication system. The performance of the proposed technique is presented and comparisons are made to other commonly used switching techniques for reconfigurable antennas, such as techniques based on PIN diodes and RF MEMs integration.

5.2 What is Cognitive Radio?

In recent years, the growth of communication systems and the high demand for frequency bands has caused a perceived shortage in the available RF spectrum. This shortage is, however, mainly due to the inefficient spectrum allocation management policies rather than the physical scarcity of usable frequencies [87-89]. In November 2002, the Federal Communications Commission (FCC) noted that the current overall spectrum is highly underutilized, where it is found that 70% of the allocated licensed spectrum remains

unused [90]. The Cognitive Radios (CR), built on a Software Defined Radio (SDR) platform, aimed to improve the spectral utilization by dynamically interacting with the RF environment. These cognitive radios are assumed to be intelligent communication systems that are able to *learn* from their environment and to *adapt* to the variations of their surroundings. The adaptation process consists of updating the operational parameters such as the transmit power, carrier frequency, modulation strategy and transmission data rate in response to the observed RF environment [91-92]. The two main objectives of cognitive radios can be stated as: to ensure highly reliable communication whenever and wherever needed, and to efficiently utilize the radio spectrum.

Following its findings on underutilization of the RF spectrum, the FCC suggested several broad solutions to improve the spectrum utilization by proposing three different categories: spectrum reallocation, spectrum leasing, and spectrum sharing, as shown in Fig. 5.1 [93].

Spectrum reallocation aims to provide a long-term solution, and has resulted in the opening of the 700 MHz TV band for cognitive radio operation. Spectrum leasing, as was identified by FCC, presents an off-line solution according to which spectrum licensees are allowed to sell or trade their channels to third parties. On the other hand, the spectrum sharing solution has stimulated a great amount of research activities aimed at dynamic sharing of spectrum [87], [93], [94]. Many of the proposed dynamic spectrum sharing (DSS) approaches can be broadly classified as follows:

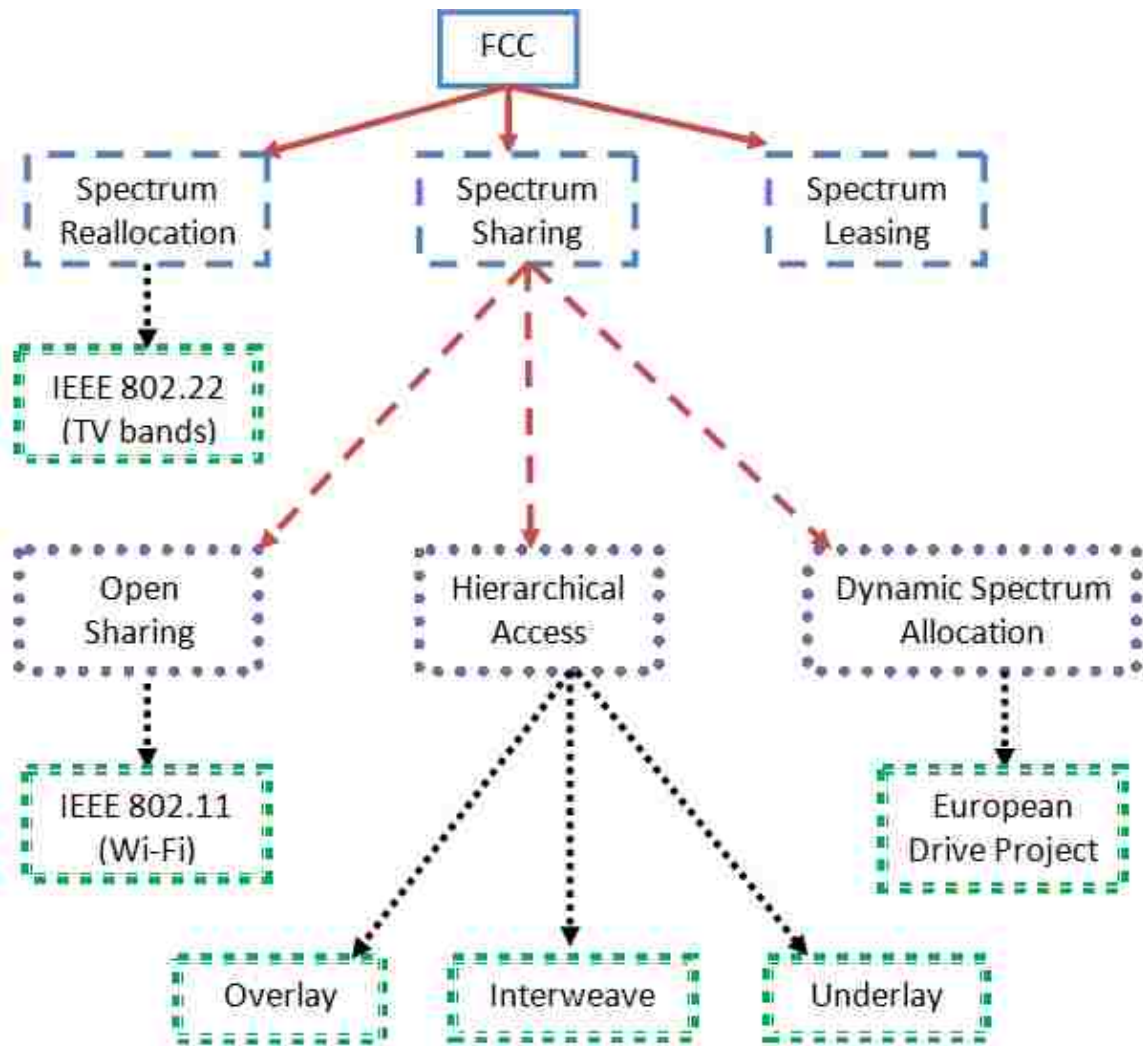


Figure 5.1 The proposed FCC solutions to the spectrum underutilization

5.2.1 Open Sharing:

Here all users can simultaneously access the spectrum with some constraints on the transmit signal. These constraints are regulated by standard protocols. This approach is currently being used in unlicensed Industrial, Scientific and Medical (ISM) radio bands, in which IEEE 802.11 Wi-Fi and Bluetooth, for example, coexists [95-96].

5.2.2 Hierarchical sharing:

In this model, the spectrum band is assumed to be owned by primary users that do not fully utilize their channels. These primary users may allow, or lease, their unused channels to unlicensed users, referred as secondary users, as long as their Quality of Service (QoS) is not compromised. In this category, three main paradigms have been considered so far, at least in current literature: Spectrum underlay, interweaving and overlay.

In spectrum underlay, secondary users are allowed to transmit simultaneously with primary users as long as the transmission power is below a specific interference margin or a noise floor tolerated by primary users. An example is that using UWB transmission, the secondary users can achieve a reasonable data rate with low power in short distance communication [97]. This approach is useful when primary users seem to transmit all the time. The underlay systems have been explored in many DSS proposals [93], [98-99]. Many of them have suggested the use of game theory to allocate primary and secondary resources.

Unlike spectrum underlay in which the restriction on the secondary users is imposed on their transmit powers, a cognitive user, operating in spectrum interweave system, should determine where and when it may transmit. The secondary users try to locate the spectral holes by using an appropriate sensing mechanism. A spectrum hole is a licensed spectrum band that is owned by a primary system and is not being utilized for a specific time and in a particular region. Namely, the interweave permits the secondary users to efficiently utilize the unused spectrum holes, while avoiding, or limiting, collisions

with primary transmissions. This technique was envisioned by the DARPA Next Generation (XP) program [100], and it was denoted as the Opportunistic Spectral Access (OSA) [101-102].

In spectrum overlay, the cognitive users are assumed to know the primary message and they can use this knowledge in order to reduce the interference at both the primary and the secondary receivers by using sophisticated implementation techniques. For example, the overlay architecture can be implemented by using Dirty Paper Coding (DPC) which allows eliminating the interference caused by the primary transmitter at the secondary receiver. On the other hand, spectrum overlay can be implemented in an asymmetric cooperative architecture in which the secondary transmitter spends a portion of its power to transmit its own signal, while the other portion is dedicated to relay the primary signal to its destination [97]. The advantage of the latter technique is that it allows the secondary users to improve their Signal-to-Noise Ratio (SNR) without degrading the quality of the primary link. For instance, the authors in [103] adopt a game theoretic approach to determine the modulation rate of secondary users in spectrum overlay cognitive radio network. The main feature of spectrum overlay is that it allows the cognitive users to improve their own transmission while assisting the primary communications through sophisticated techniques.

5.2.3 Dynamic Spectrum Allocation:

This was considered in the European DRiVE project, in which the frequency bands are dynamically assigned to wireless services depending on their spatial and temporal traffic statistics [87]. The dynamic assignment permits a wireless system to exclusively

utilize the spectrum in a given region and for specific time duration. However, this approach does not completely eliminate the temporal white spaces caused by the bursty traffic of wireless services.

In this work, new techniques are proposed to design antenna systems for hierarchical sharing cognitive radios based on Opportunistic Spectrum Access (OSA). The basic RF architecture of such a system comprises of a “sensing antenna” that continuously monitors the wireless channel and searches for unused frequency channels (spectrum holes), and a “reconfigurable transmit/receive antenna” to perform the required communication within those unused frequency channels [104-108]. A top-level logic work-flow for one possible implementation of a cognitive radio communication scheme is shown in Fig. 5.2. The sensing antenna is generally an UWB antenna and would communicate with the “Spectrum Sensing” module of the cognitive radio engine. The purpose of this module is to continuously search for unused frequency channels within the operating band of the sensing antenna. The information acquired by the “Spectrum Sensing” module is fed to the “Spectrum Decision” module which determines the appropriate frequency band for communication. The “Switch Controller” module then tunes the operating frequency of the reconfigurable antenna.

In the remaining of this chapter, we focus on demonstrating a cognitive radio application by utilizing a new technique to achieve frequency reconfigurability in photoconductive-switch based antennas. The design is based on integrating laser diodes within the antenna structure. This technique negates the need for optical fiber cables for delivering light to the photoconductive switches, thereby reducing the complexity of the

system and allowing for easier integration of such antennas in future wireless handheld devices. This technique requires no biasing lines for switch activation purpose in the antenna radiating plane, as is the case with RF MEMS, PIN diodes or varactors. In the following section a comparison between the proposed technique in this chapter and the previously work done on reconfigurable antenna is discussed.

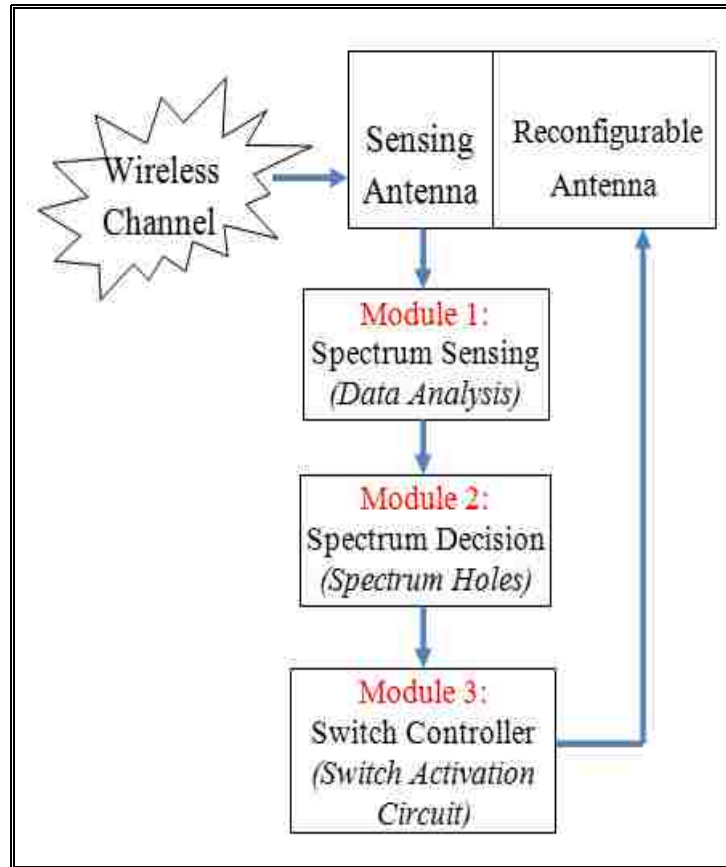


Figure 5.2 The generic cognitive radio work-flow diagram

5.3 Comparison between “OPRAS” and RF-MEMS/PIN Diodes Based Reconfigurable Antenna Systems

In this work, an n-type silicon (Si) piece with an initial carrier concentration of 10^{15} cm^{-3} is used as the switching element. It has physical dimensions of $1\text{mm} \times 1\text{mm}$. By

illuminating the silicon switches by light from the laser diode, the mobility of charges in the silicon decreases but their density increases. This increase in the charge carrier density results in a general increase in the conductivity of the switch.

In the design of reconfigurable antennas and reconfigurable arrays, it is always desired to minimize the power required to activate the switching elements. The laser diode used in this work requires a supply voltage in the range of 1.8V-2.07V and a driving current in the range of 0mA-129mA in order to generate an output laser power in the range of 0mW-90mW. The relation between the output power level (mW) and the current/voltage for this laser diode is shown in Fig.5.3, which shows that a voltage of 1.9V and a current of 87mA are required to drive the laser diode to produce an output laser power of 50mW. This power level is sufficient to make the silicon switch transition from the OFF state to the ON state and this transition is manifested by the increase in the Silicon total conductivity (DC+RF).

The silicon substrate used in this work has bandgap energy $E_g \approx 1.12$ eV, which corresponds to an activation bandgap wavelength: $\lambda_g \approx 1.24/E_g = 1.107 \mu\text{m} > \lambda_{\text{Laser Diode}} = 785$ nm. λ_g determines the cut off wavelength of the incident photons that are necessary to excite electrons from the silicon valence band to the conduction band.

RF MEMs/PIN diodes based reconfigurable antenna systems require the design of appropriate bias lines which lie in the plane of the antenna. Bias lines affect the antenna radiation pattern and increase the complexity of the structure by adding additional RF components. On the other hand, “OPRAS” is based on integrating laser diodes within the antenna substrate where no bias lines are needed to be printed on the plane of the radiating

structure of the antenna. A copper piece is attached to the back of the antenna ground. This piece has a minimal effect on the antenna radiation pattern since it has a small depth and the same (or smaller) width/height as the antenna ground plane. Also, this technique eliminates the use of optical fiber cables for light delivery which enables easier integration of the reconfigurable antenna.

RF MEMs also suffer from poor reliability [109]. The deployment of RF MEMs into commercial and defense applications is very limited. PIN diodes exhibit non-linear behavior at RF frequencies since the stored charge can be insufficient to control the RF current [110]. The non-linear behavior of PIN diodes manifests itself as undesired antenna resonances.

All the problems produced by RF MEMs and PIN diodes integration can be overcome by implementing the “OPRAS” technique. The copper piece that is used as a heat sink for the laser diode improves the reliability of the proposed technique as compared to RF MEMs by increasing the laser diode lifetime. Also the activation/deactivation of the photoconductive switch by shining light from the laser diode does not produce harmonics and inter-modulation distortion as with the case of PIN diodes.

Table 5.1 shows a comparison between the three different techniques in terms of voltage/current requirement, amount of power consumption and the switching speed [111-112]. The “OPRAS” performs faster than RF MEMs but needs more driving current. PIN diodes based reconfigurable antennas act faster than “OPRAS” but need higher level of driving voltage. The estimated power consumption of “OPRAS” lies between that of RF

MEMS and PIN diodes. The switching speed of the “OPRAS” is included here just for comparison. A detailed chapter about the transition speed experiment is presented in a different chapter.

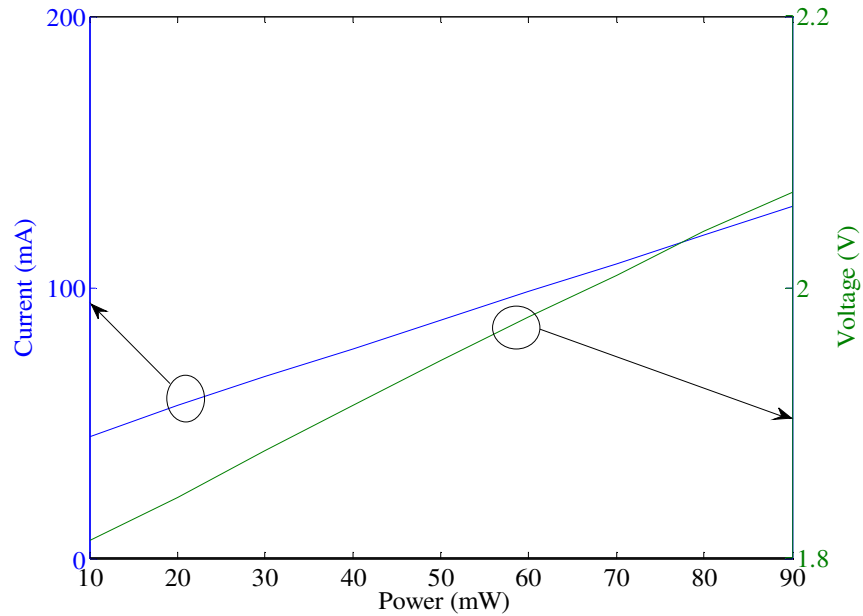


Figure 5.3 The relation between the optical power and the voltage/current for the laser diode used in this work

Table 5.1 Comparison between different switching techniques

	<i>OPRAS</i>	<i>RF MEMS</i>	<i>PIN diodes</i>
Voltage [V]	1.8-1.9	20-100	3-5
Current [mA]	0-87	0	3-20
Power Consumption [mW]	0-50	0.05-0.1	5-100
Switching Time	3-9 (μ sec)	1-200 (μ sec)	1-100 (nsec)

5.4 Reconfigurable Antenna Design

The reconfigurable antenna structure is printed on a Taconic TLY substrate with a dielectric constant of 2.2 and a height of 1.6 mm. It is fed via a stripline and has a partial ground of dimension 36mm x 9mm. Two silicon switches are included to connect the different radiating parts of the antenna structure. The detailed dimensions of the different parts of the reconfigurable antenna are shown in Fig. 5.4. The antenna substrate is taken to be 50mm x 45.5mm in order to have space for the sensing antenna. The simulated antenna return loss for the different cases of the optical switches is summarized in Fig. 5.5. Frequency tuning is achieved from 3 GHz till 6 GHz. The computed radiation pattern at $f=3.6$ GHz (thick line, S1: OFF-S2: ON), $f=4.6$ GHz (dotted, S1: OFF-S2: OFF) and at $f=5.2$ GHz (thin line, S1: ON - S2: OFF) are shown in Fig. 5.6. One can notice that a satisfactory omni-directional radiation pattern is obtained.

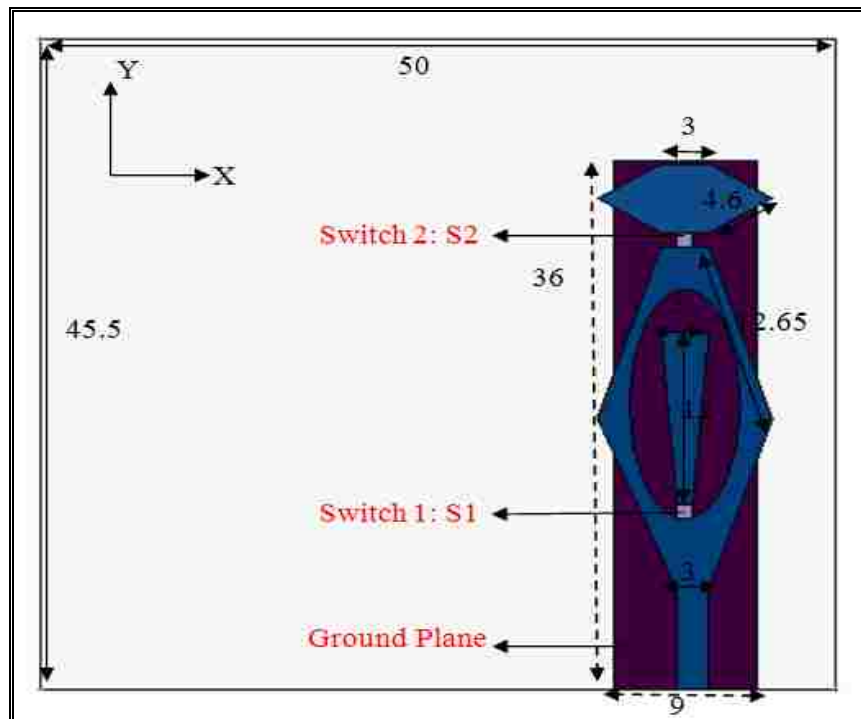


Figure 5.4 The optically reconfigurable antenna structure

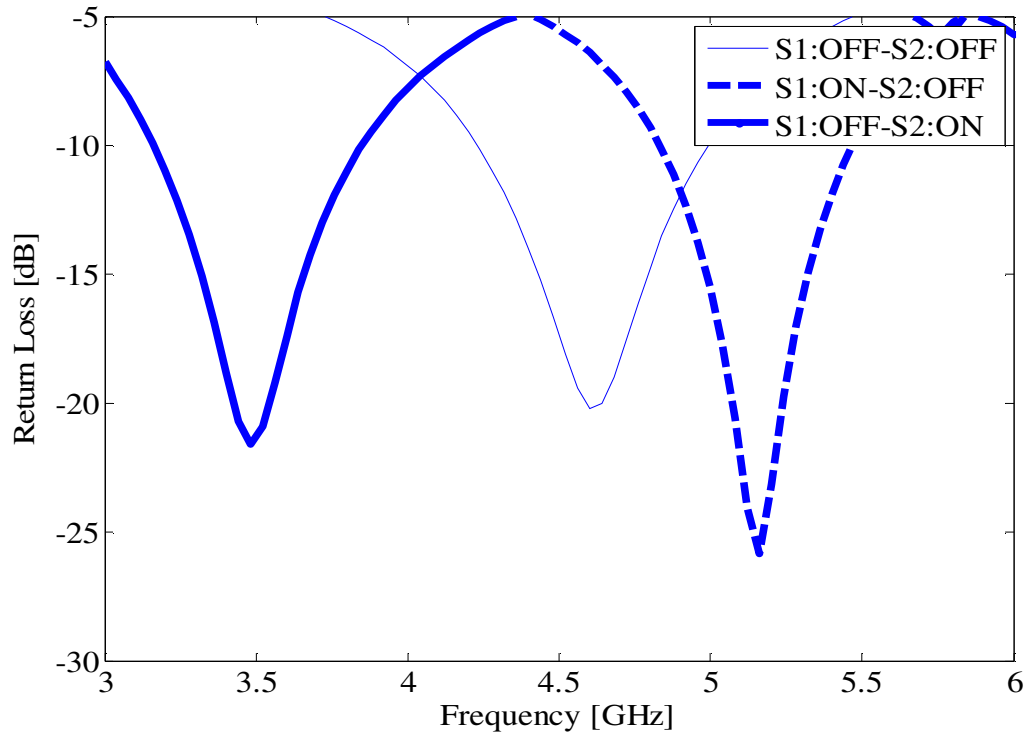


Figure 5.5 The antenna return loss for different cases of the photoconductive switches

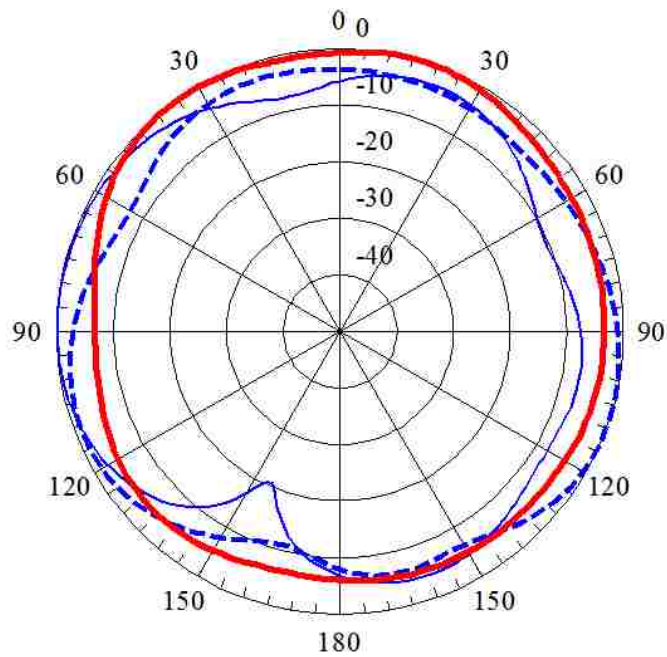


Figure 5.6 The normalized radiation pattern in the X-Z plane (thick line: 3.6 GHz, dotted line: 4.6 GHz, thin line: 5.2 GHz)

5.5 Cognitive Radio Antenna Structure

The cognitive radio front-end described in this chapter consists of an UWB and a reconfigurable narrow-band antenna placed next to each other. The antenna top view is shown in Fig. 5.7; its bottom view is shown in Fig. 5.8.

The cognitive antenna is printed on a Taconic TLY substrate with a dielectric constant of 2.2 and a height of 1.6 mm. The sensing and the reconfigurable structures are fed via a stripline. They both have a partial ground in order to allow radiation above and below the substrate. The reconfigurable antenna has a longer length than the ground of the sensing antenna in order to be able to accommodate the copper fixture. The separation between the two ground planes is chosen to be 8 mm. All the dimensions shown in Fig. 5.7 and Fig. 5.8 are in mm.

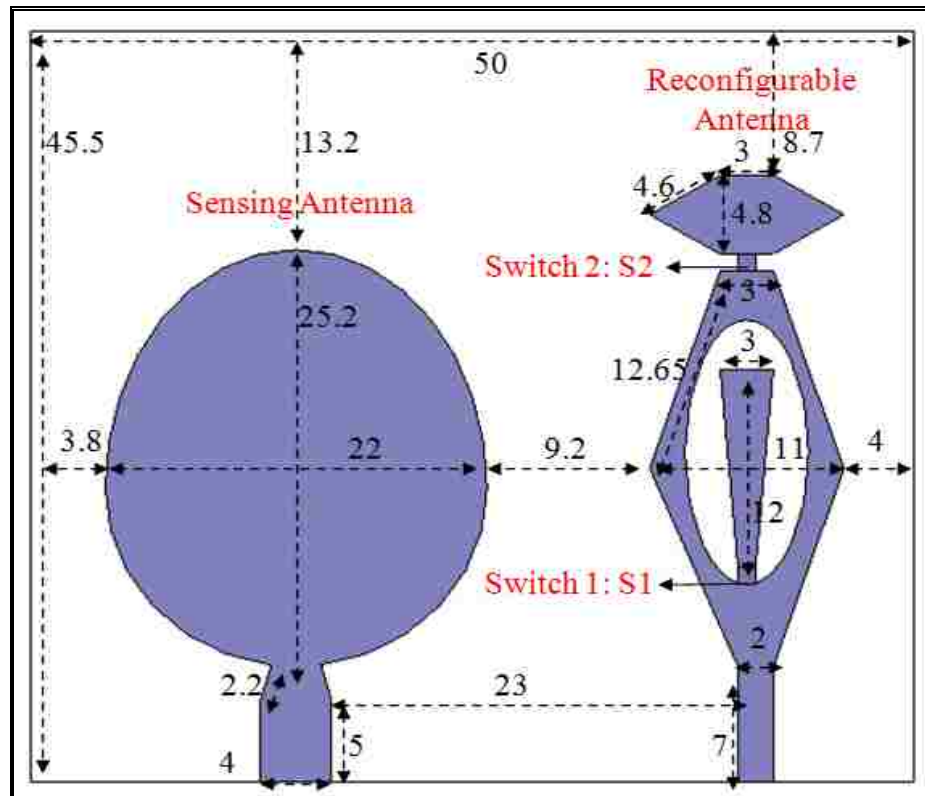


Figure 5.7 The top layer of the cognitive radio antenna structure

The UWB sensing antenna is a modified elliptical shaped monopole. It covers the band from 3GHz up till 11 GHz. It has a major axis of 25.2 mm ($\approx 0.38 * \lambda_{\text{eff}}$) and a minor axis of 22 mm ($\approx 0.35 * \lambda_{\text{eff}}$) where λ_{eff} corresponds to the lowest frequency (3 GHz). A small tapered microstrip section is used to match the UWB sensing antenna to the feed point.

The reconfigurable antenna is a modified printed monopole. It has an elliptical slot that contains a triangular arm. Both structures are connected together via a silicon switch (S1). At the end of the modified monopole, a hexagonal patch is attached via another silicon switch (S2). It has the same structure as the antenna discussed in the previous section.

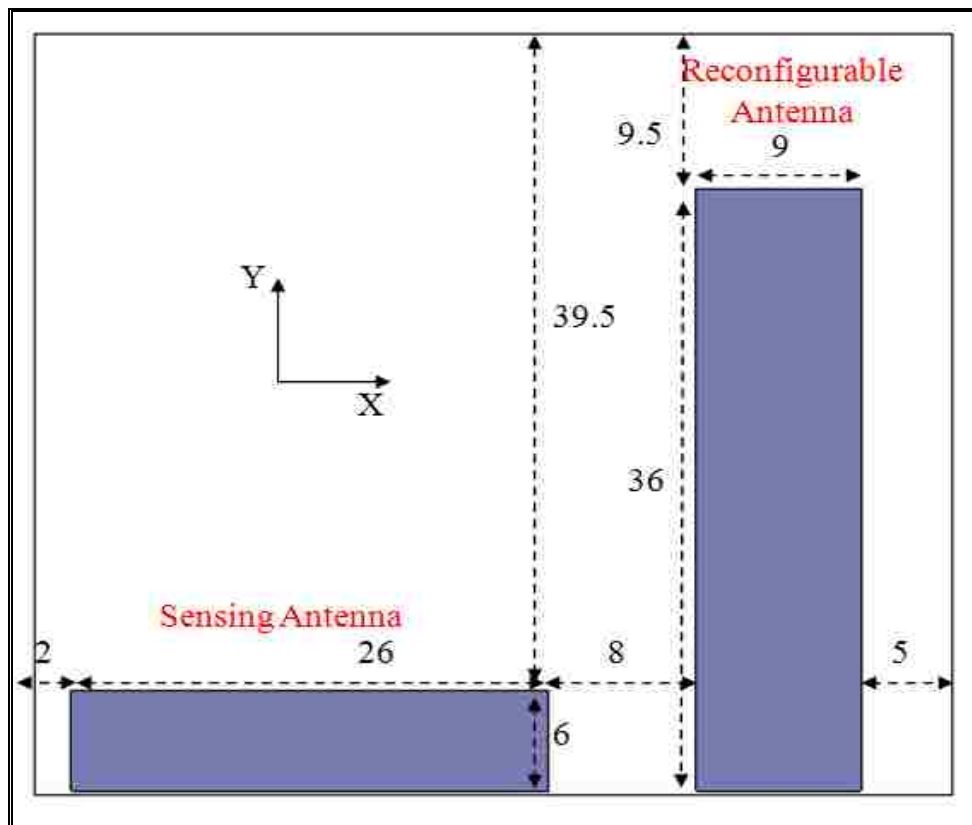


Figure 5.8 The bottom layer of the cognitive radio antenna structure

5.6 Laser Diode Integration

A semiconductor laser diode is a device that converts electrical energy into optical radiation. The laser radiation is highly monochromatic and it produces highly directional beams of light. The laser action is produced by simply passing a forward current through the diode itself. On account of its compact size and capability for high-frequency modulation, the semiconductor laser is one of the most important light sources for optical-fiber communication. Its basic element structure is shown in Fig.5.9 where the arrow indicates the direction of the generated laser light [74-75].

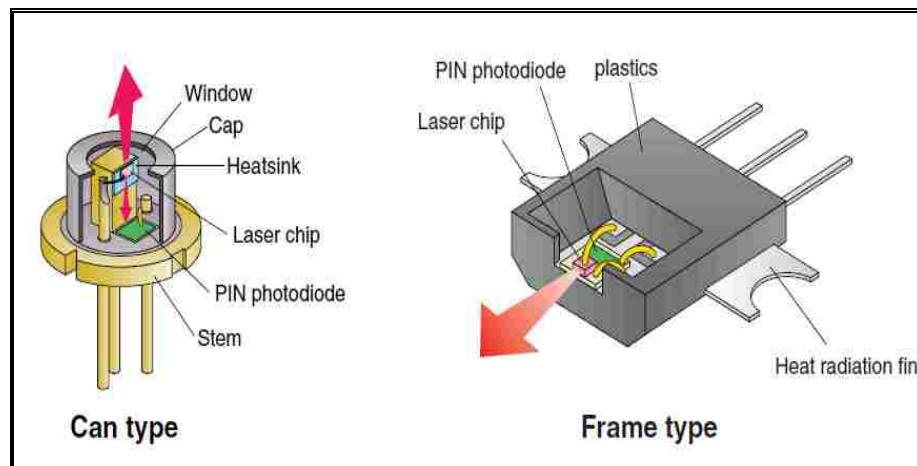


Figure 5.9 The physical structure of a laser diode

The laser diode used in this work operates at 785 nm and has a maximum output power of 90 mW. It has a Can type architecture and a part number L785P100 [22]. The integration of the laser diode is achieved by attaching it to the back of the ground of the reconfigurable antenna as shown in Fig. 5.10. In order to couple the light from the laser diodes efficiently, two holes of diameter 1mm are drilled through the substrate.

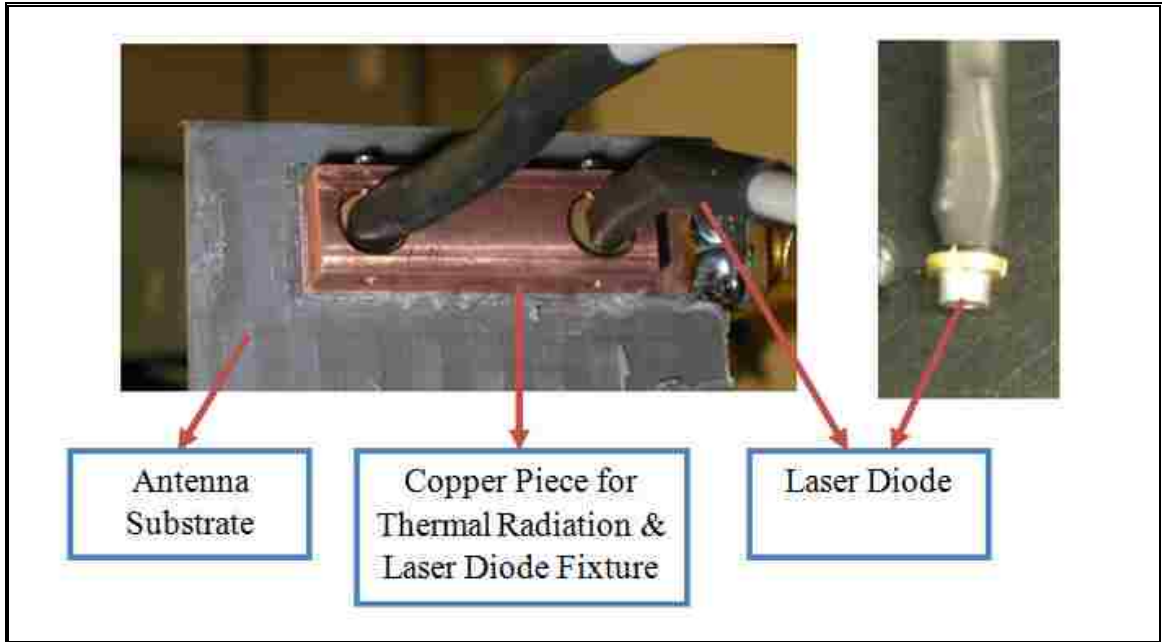


Figure 5.10 The integration of the laser diode into the antenna structure

The copper piece used to integrate the laser diodes with the antenna structure is shown in Fig. 5.11. It is included into the simulation environment with the antenna structure to take into consideration its effect on the antenna performance. Its width is same as the ground of the reconfigurable antenna ($W=9$ mm). It has a length of 21.5 mm and depth of 6.5 mm. This copper piece has two holes where inside each hole a laser diode is fixed.

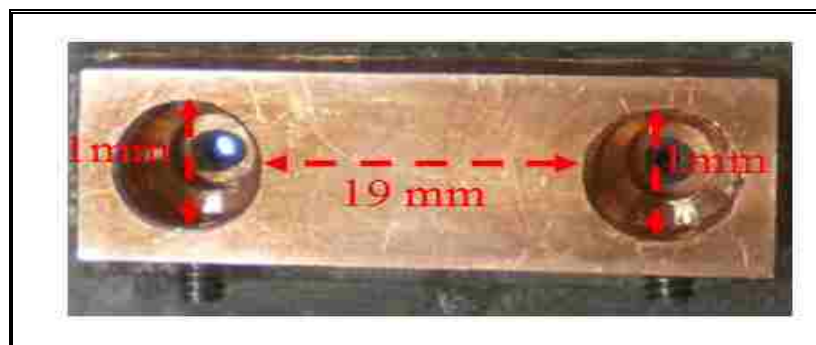


Figure 5.11 The drilled copper piece which supports the laser diodes

The reconfigurable antenna radiation pattern at $f=4.6$ GHz and $f=5.2$ GHz in the YZ plane for the case when the copper piece is removed and when it is present is shown in Fig. 5.12. One can notice that the inclusion of this piece has a minimal effect on the antenna radiation pattern. Also, the laser diode cables are shielded and therefore do not interfere with the antenna radiated field. These two frequencies are chosen only as a proof of concept.

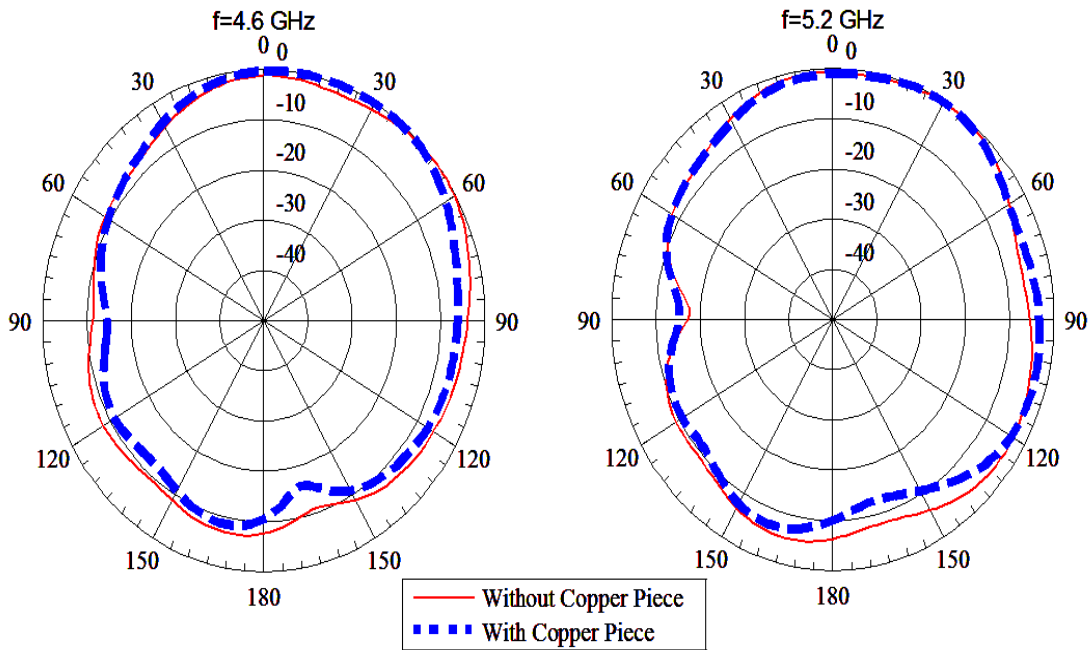


Figure 5.12 The antenna radiation pattern in the YZ plane ($\Phi=90^\circ$)

5.7 Fabrication and Results

The fabricated antenna structure is shown in Fig. 5.13 (top view) and Fig. 5.14 (bottom view). Two photoconductive switches are integrated within the reconfigurable antenna.

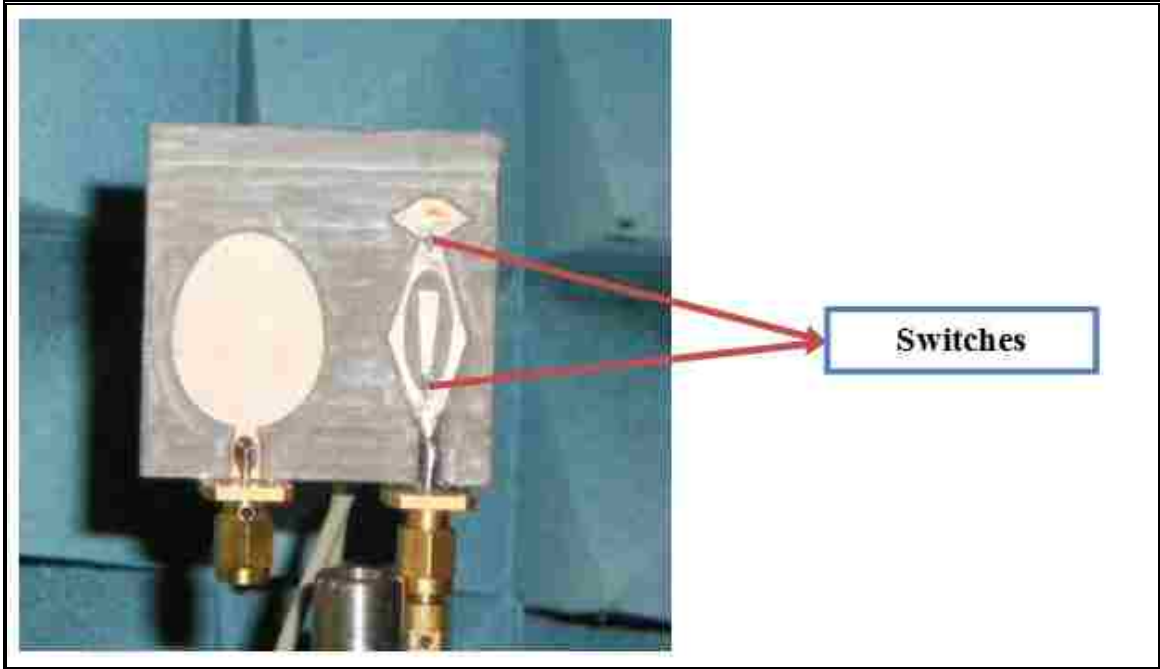


Figure 5.13 The top view of the fabricated antenna prototype

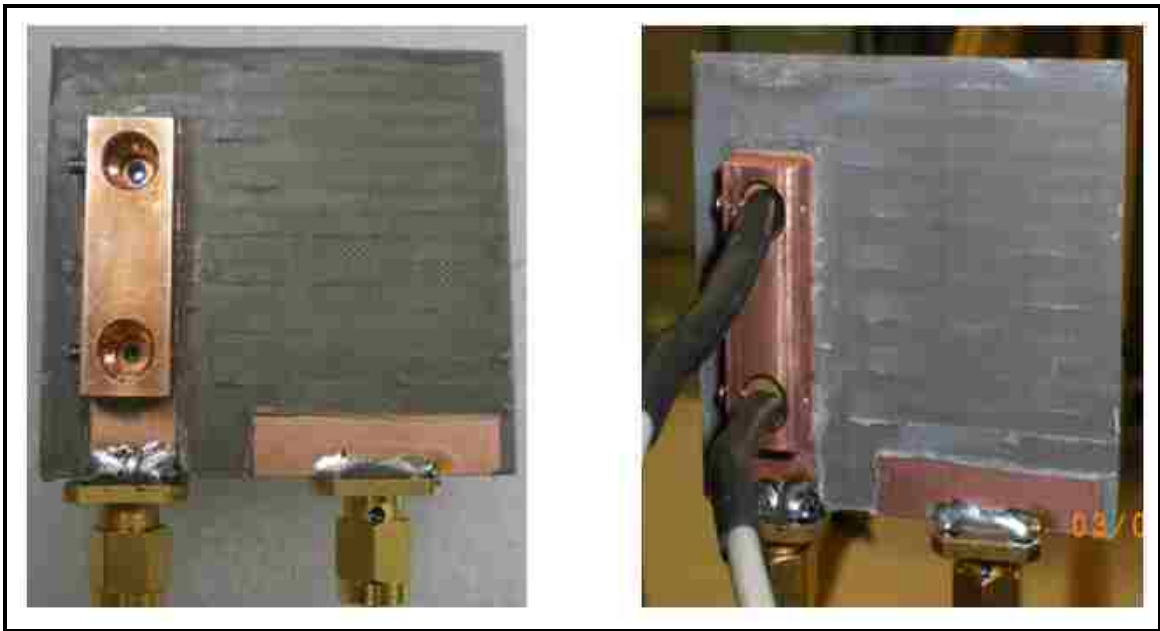


Figure 5.14 The bottom view of the fabricated antenna prototype

5.7.1 UWB Antenna:

The comparison between the measured and the simulated return loss for the UWB sensing antenna is shown in Fig. 5.15. The antenna is able to cover the spectrum from 3 GHz up to 11 GHz. Good agreement is noticed between the simulated and the measured return loss for the UWB sensing structure. This data corresponds to the case when both switches are OFF. We observed that the same UWB response is maintained for the different states of the two switches.

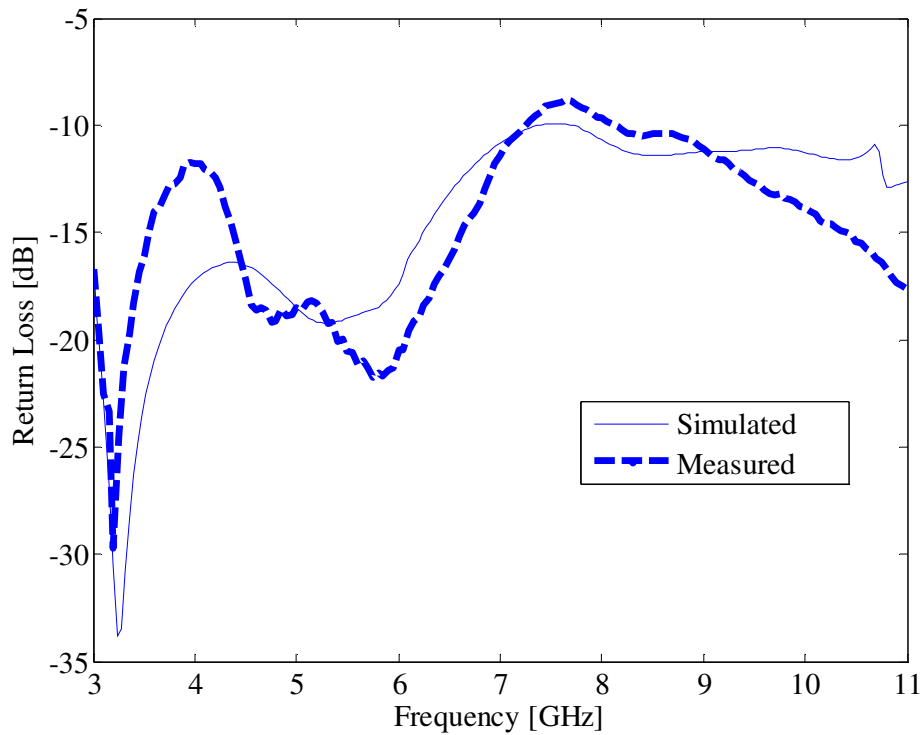


Figure 5.15 The measured and simulated return loss for the sensing antenna when both switches are OFF

The normalized UWB antenna radiation pattern in the XZ plane ($\Phi=0^0$) is shown in Fig. 5.16 as a colored contour plot for the case when both switches are OFF. The color code in the right side of the plot corresponds to the normalized values (dB) of the total radiated electric field for different frequency/angle values. It is observed that the UWB

antenna has minimal variation in the radiated E-field across the majority of the frequency bands / angle values.

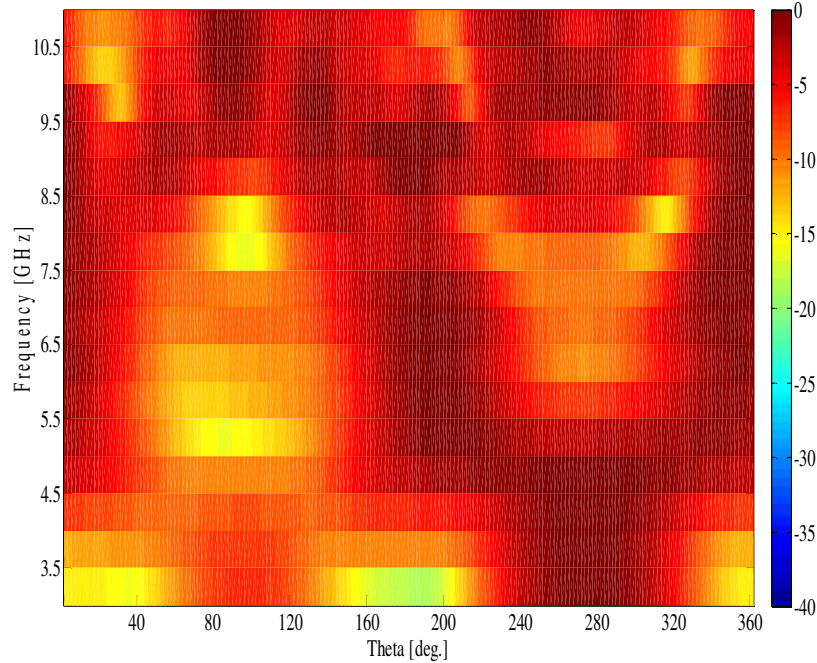


Figure 5.16 Contour map of the normalized radiation pattern for the UWB antenna in the XZ plane ($\Phi=0^{\circ}$)

5.7.3 Narrowband Reconfigurable Antenna:

For the narrow-band reconfigurable antenna (communicating antenna), when the two silicon switches (S1 and S2) are not illuminated by a laser light (OFF state), only the modified monopole is fed. This results in an antenna resonance between 4.15 GHz and 5.1 GHz. Upon activation of the first switch (S1) by driving the laser diode via a current of 87 mA and a voltage of 1.9 V (this correspond to 50 mW optical power), the antenna shifts its resonance to the 4.8-5.7 GHz band. By illuminating the second switch (S2) with the same amount of pumped power, the band 3.2-4.3 GHz is covered. The case when both

switches are ON produces a resonance outside the band of the UWB sensing antenna, and is not considered for our application. The simulated and the measured return loss for the reconfigurable narrow-band antenna are summarized in Fig. 5.17 and Fig. 5.18.

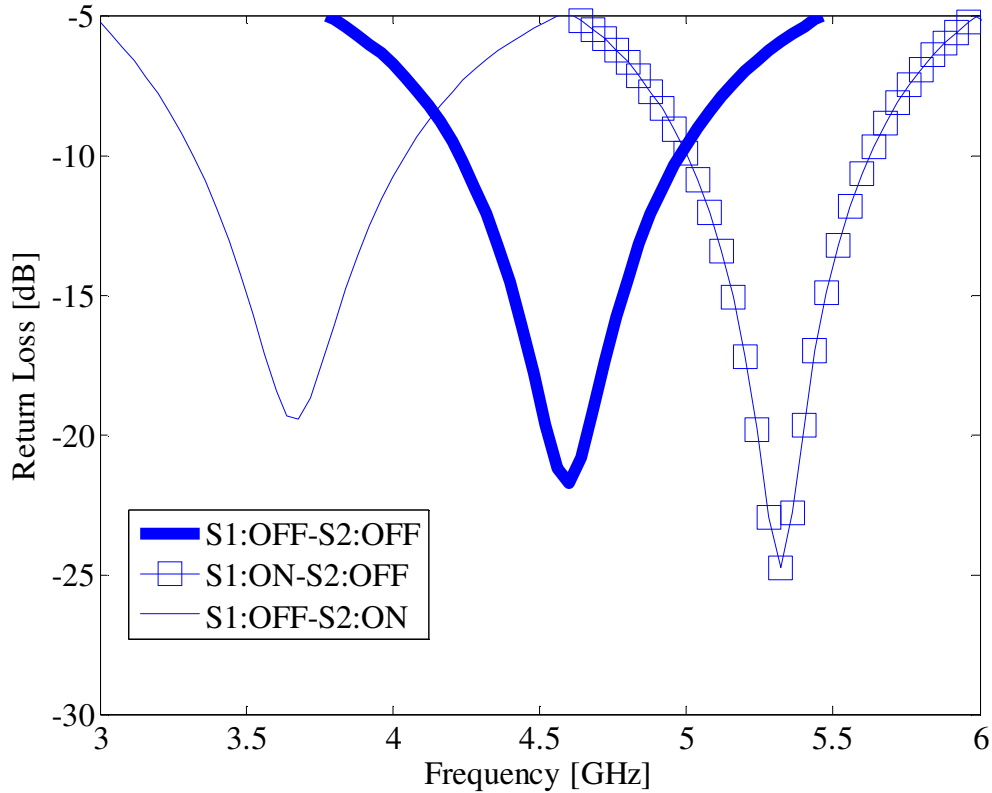


Figure 5.17 The simulated antenna return loss for the reconfigurable antenna

5.7.3 Coupling:

Since both structures are incorporated into the same cognitive antenna substrate, it is essential to look at the coupling between the UWB sensing and the reconfigurable narrow-band antenna. This coupling or “cross-talk” is quantified by the transmission (S_{21}) between the two antenna ports. The coupling between the two radiating structures is a function of their physical separation. In order to find the optimum distance between the

two radiating structures without making the overall cognitive antenna too large, an optimization study was performed in HFSS. It was observed that for separation distances less than 6 mm, there was considerable cross-talk between the two radiating structures. A separation of 8mm ensured that the measured S_{21} between the two radiating structures was less than -20 dB across the band from 3 GHz to 11 GHz.

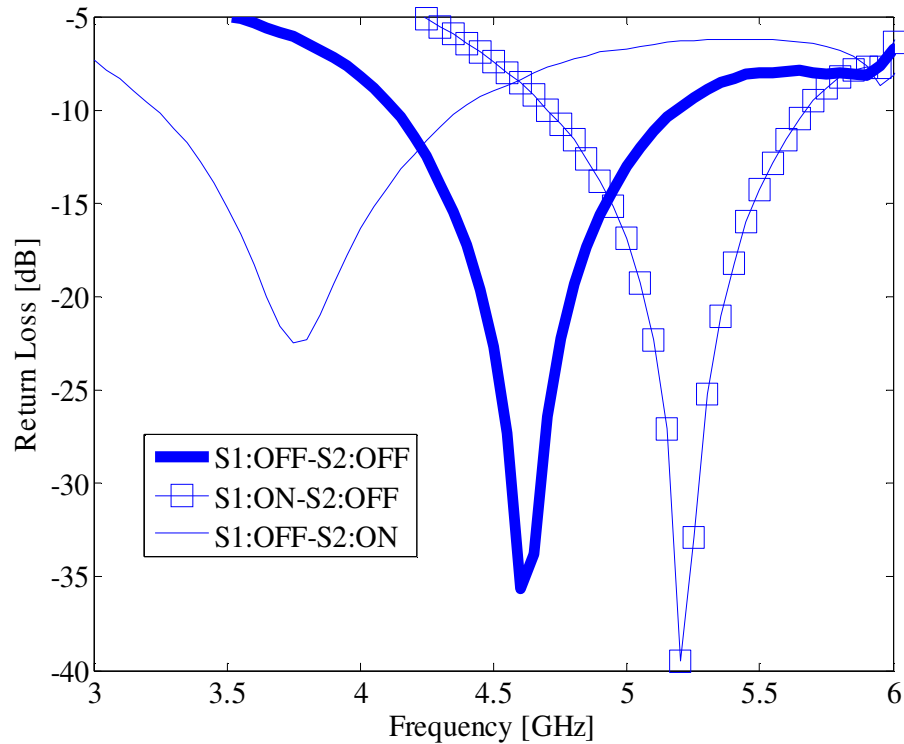


Figure 5.18 The measured antenna return loss for the reconfigurable antenna

The comparison between the simulated and the measured S_{21} for the case when S1: OFF-S2: OFF and S1: OFF-S2: ON for a separation of 8mm between the UWB and the reconfigurable narrow-band structures is shown in Fig. 5.19. A measured coupling of less than -20 dB was achieved throughout the whole band of the UWB sensing antenna. The

measured coupling for a set of frequencies for the three different states of the switches is shown in Table 5.2.

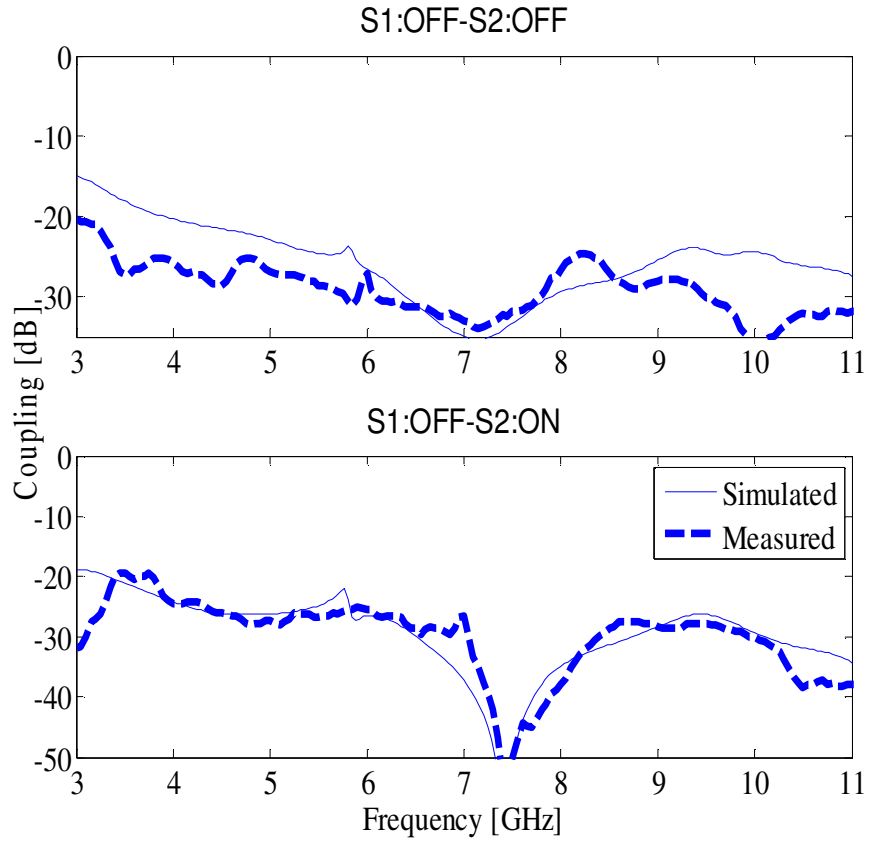


Figure 5.19 The simulated and the measured coupling for the case when both switches are OFF and when S1:OFF / S2:ON

Table 5.2 The measured coupling (dB) for the three different states of the switches

Frequency [GHz]	Both OFF	S1:ON	S2:ON
4	-25.7	-23.5	-24.61
6	-27.12	-23.2	-25.49
8	-26.65	-25.06	-37.85
10	-36.25	-26.8	-30.5

5.7.4 Radiation Pattern:

The comparison between the simulated and the measured radiation pattern in the XZ plane ($\Phi=0^\circ$) for the reconfigurable antenna is shown in Fig.10. The radiation pattern is taken at $f=3.6$ GHz (S1: OFF-S2: ON), $f=4.6$ GHz (S1: OFF-S2: Off) and at $f=5.2$ GHz (S1: ON-S2: OFF). A reasonably omni-directional radiation pattern was achieved.

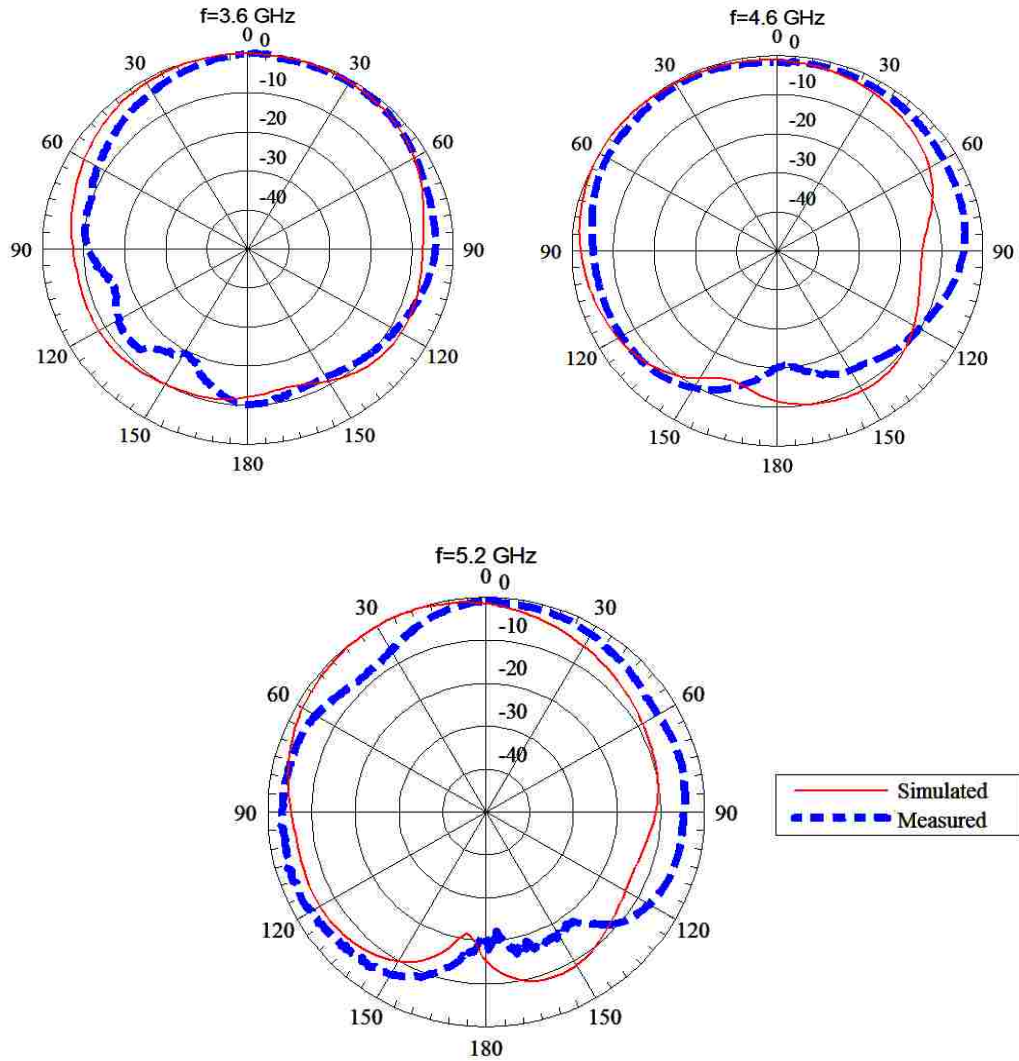


Figure 5.20 The simulated and the measured radiation pattern for the three different cases of the switches in the XZ plane ($\Phi=0^\circ$)

5.8 Additional Cognitive Radio Antenna Design

In the design discussed previously, the reconfigurable antenna is able to cover the band from 3 GHz up till 6 GHz with a minimum coupling of less than -20 dB between the sensing and the reconfigurable antenna structures. In this section, a new cognitive radio antenna design based on the integration of the laser diodes within the antenna substrate is proposed. The reconfigurable antenna is able to cover wider bands with a better coupling performance.

5.8.1 Reconfigurable Antenna Design:

The reconfigurable antenna studied in this example is a stripline fed structure. It consists of two layers: The top layer is the antenna radiating patch while the bottom layer is the antenna ground. The feeding line is 12 mm x 3 mm. The antenna substrate is Rogers 5880 with a dielectric constant of 2.2 and a height of 1.6 mm. The detailed structure of the antenna is shown in Fig. 5.21. It includes two switches to allow the antenna to tune its resonant frequencies.

The main antenna radiating patch consists of a modified monopole that has the shape of a diamond with a side length of 15.5 mm. It has an elliptical slot, with a major axis of 4.5 mm, for better impedance match at the resonant frequency. A silicon switch (S1) is included to make connection between the upper edge of the main patch and another patch that has a hexagonal shape. The second patch has two sides of length 4 mm and four sides of length 5 mm. An additional switch (S2) is also included to connect the feeding line of the antenna structure to a triangular shaped patch. This patch has two sides of equal length (12.5 mm) and the base side of length 3mm. The antenna ground is taken to be 45 mm x 20 mm to allow radiation above and below the substrate.

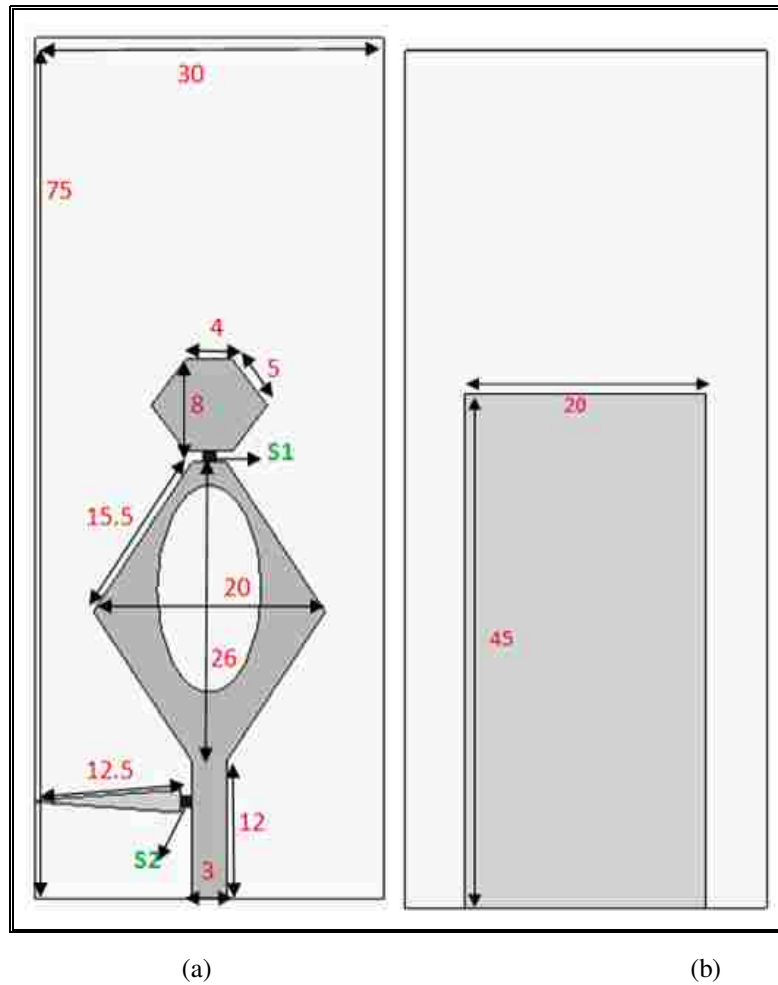


Figure 5.21 The antenna structure (a) top layer (b) bottom layer

The antenna structure is fabricated and tested. To activate the silicon switches, laser diodes are integrated within the antenna substrate. A 1 mm hole is drilled throughout the substrate in order to allow the light from the laser diode to be delivered to the silicon switches. The integration of each laser diode is done by attaching a small copper piece to the ground of the antenna as shown in Fig. 5.22 (a). The fabricated antenna top layer is shown in Fig. 5.22(b).

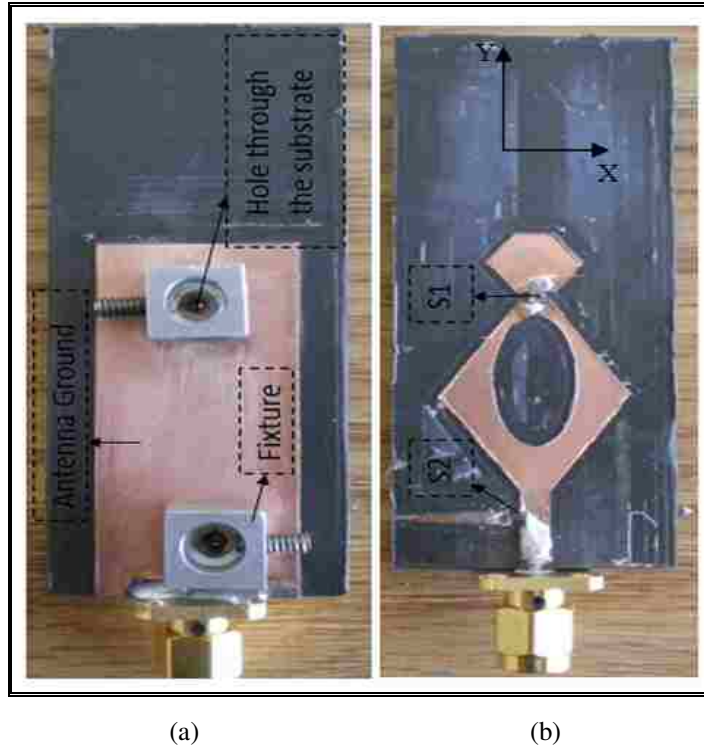
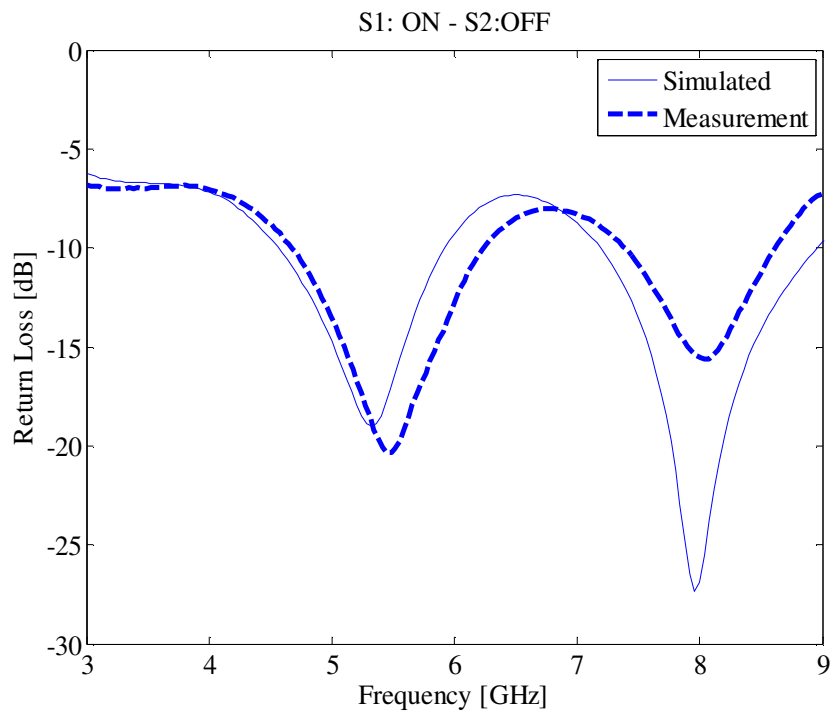
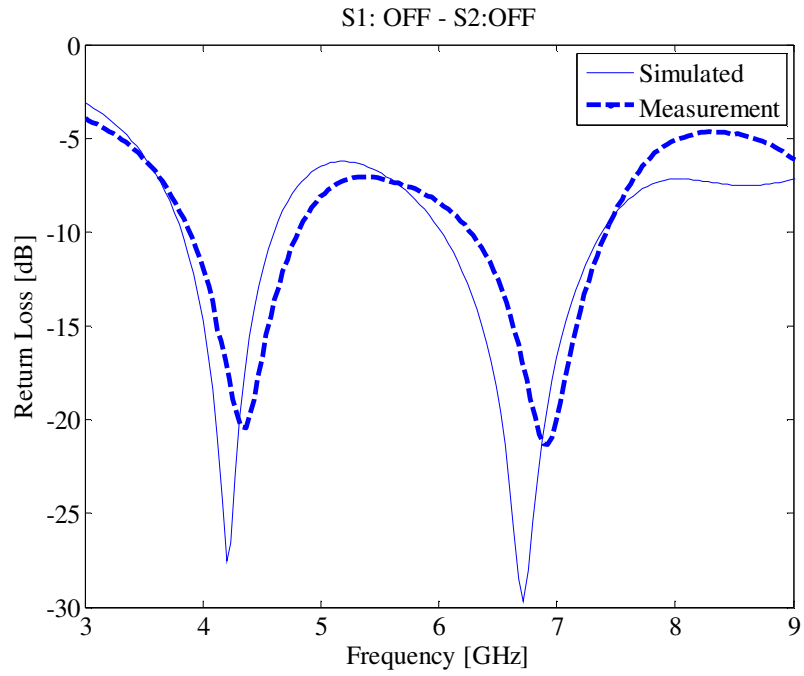


Figure 5.22 The fabricated antenna (a) bottom layer (b) top layer

When the two silicon switches are not illuminated by light from the integrated laser diodes, only the main antenna radiating patch is being fed. This makes the antenna covers the bands 3.84 GHz - 4.8 GHz and 6.2 GHz - 7.4 GHz. By activating the silicon switch S1 and keeping S2 OFF, the antenna now operates at 4.6 GHz - 5.92 GHz and 7.35 GHz – 8.6 GHz. The frequency bands 3.2 GHz - 4.1 GHz and 7 GHz-7.5 GHz are covered by turning S1 OFF and activating S2. The comparison between the simulation and the measurements for all the three cases is shown in Fig. 5.23. A good agreement between the simulation and measurement data is noticed. The measured return loss for the three cases is shown in Fig. 5.24. The case when the two switches are ON is not taken since most of the bands from 3 GHz till 9 GHz are covered by the three other combinations of the switches.



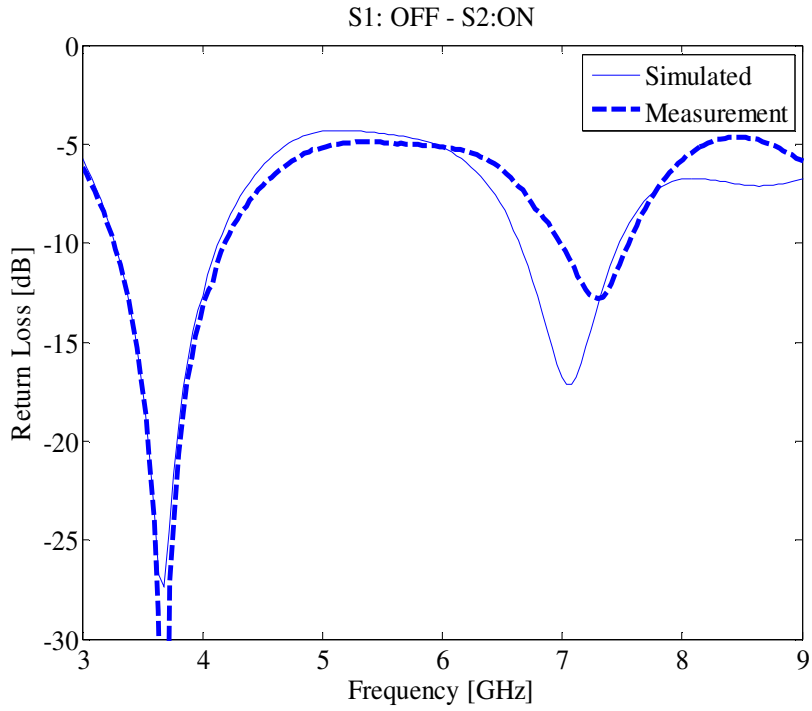


Figure 5.23 The comparison between the simulated and the measured return loss

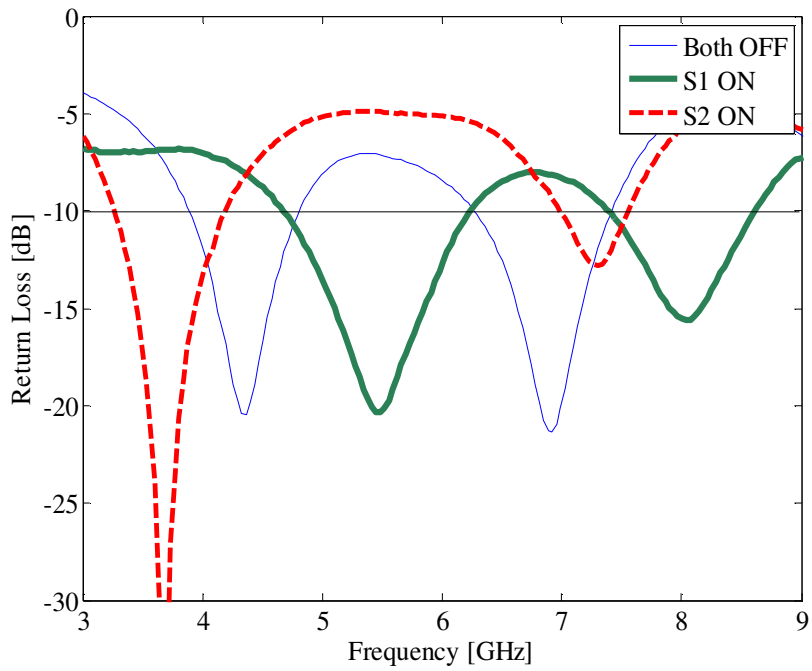


Figure 5.24. The measured return loss for the three different cases

The antenna radiation patterns at $f=4.2$ GHz, $f= 8$ GHz and $f=3.68$ GHz are shown in Fig. 4.25 in the XZ plane (solid line) and YZ plane (dotted line). A good omnidirectional radiation pattern is achieved.

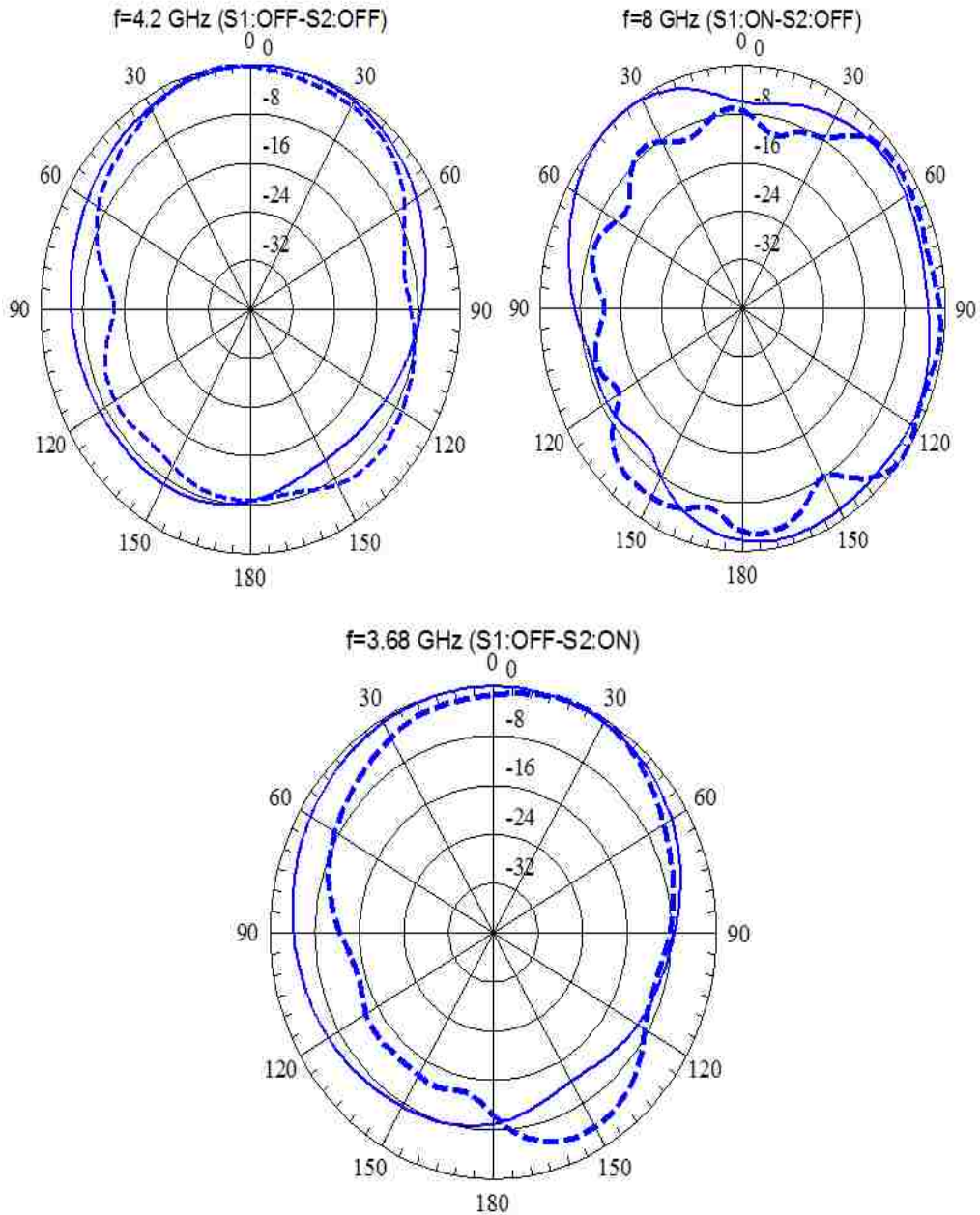


Figure 5.25 The normalized antenna radiation pattern in the XZ plane (solid line) and the YZ plane (dotted line)

5.8.2 The cognitive radio antenna structure:

The antenna structure consists of two ports. The first port is for the sensing antenna while the second one is for the reconfigurable antenna. The detailed antenna structure is shown in Fig. 5.26 [113].

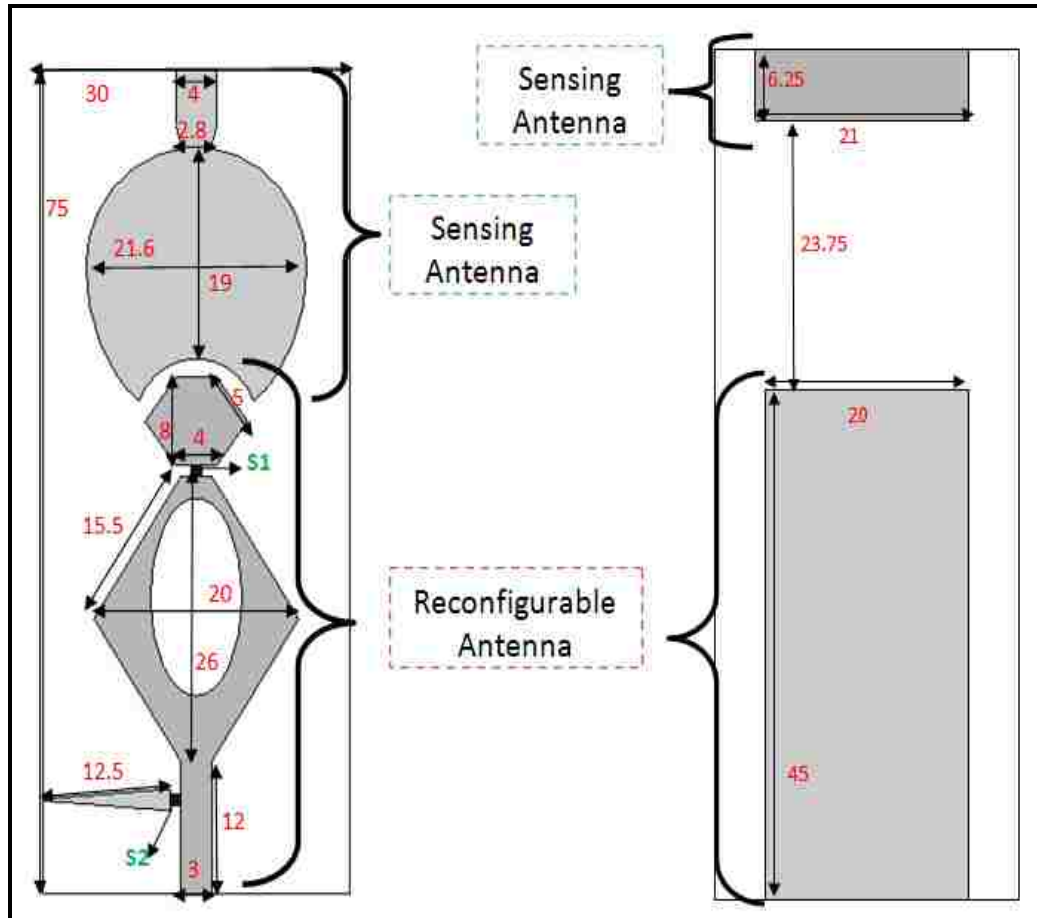


Figure 5.26 The cognitive radio antenna structure

The sensing antenna section is an egg shaped monopole. It has a partial ground of dimension 21 mm x 6.25 mm. This antenna structure covers the band from 3 GHz till 10 GHz. The upper edge of the sensing antenna has a circular shaped slot in order to have space for the reconfigurable antenna structure and to minimize the total length of the complete antenna substrate. The feeding line of the sensing antenna has an opening width

of 4 mm and an ending width of 2.8 mm for better impedance match. The sensing antenna occupies 40% of the total length of the complete antenna structure.

The reconfigurable antenna section includes two photoconductive switches in order to allow the antenna to tune its operating frequency. The antenna structure is detailed in the previous section. The fabricated antenna prototype is shown in Fig. 5.27.

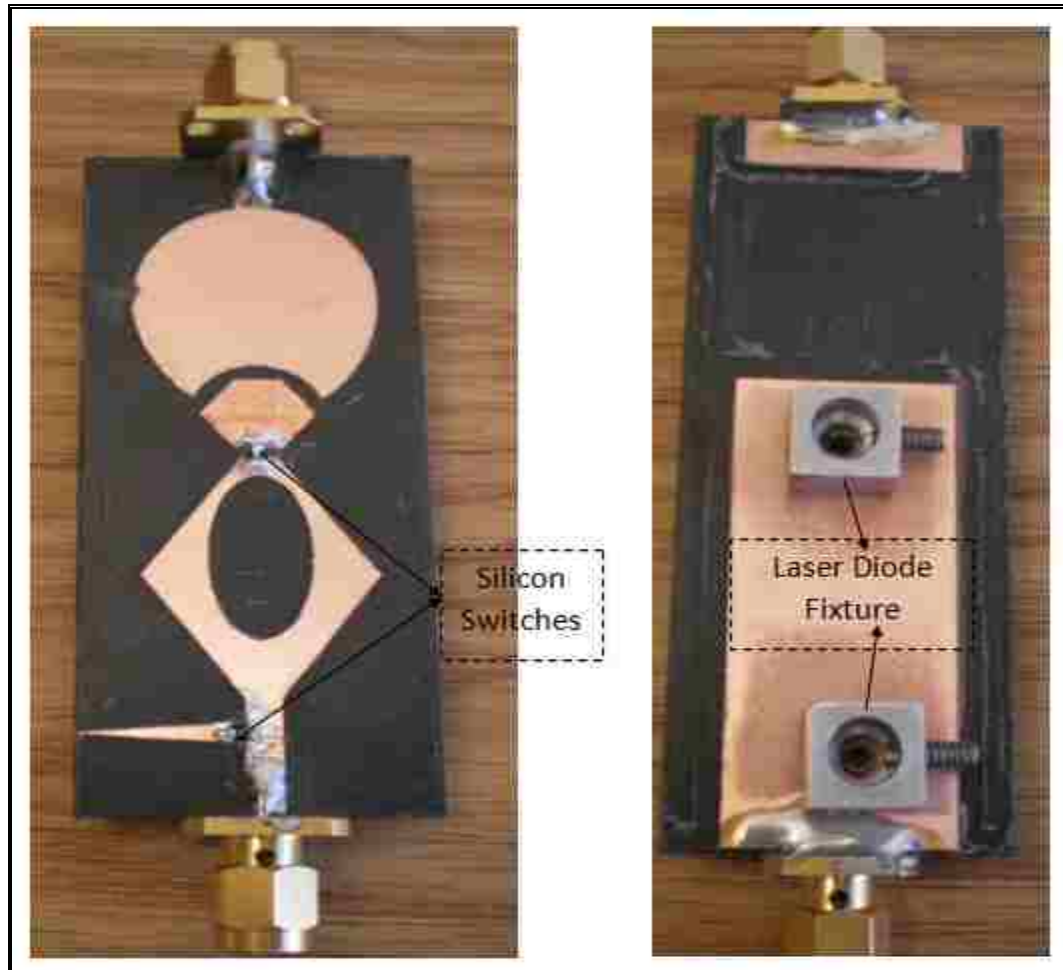


Figure 5.27 The fabricated antenna prototype

The comparison between the simulated and the measured return loss for the sensing antenna is shown in Fig. 5.28. It is able to cover the band from 3 GHz till 10 GHz.

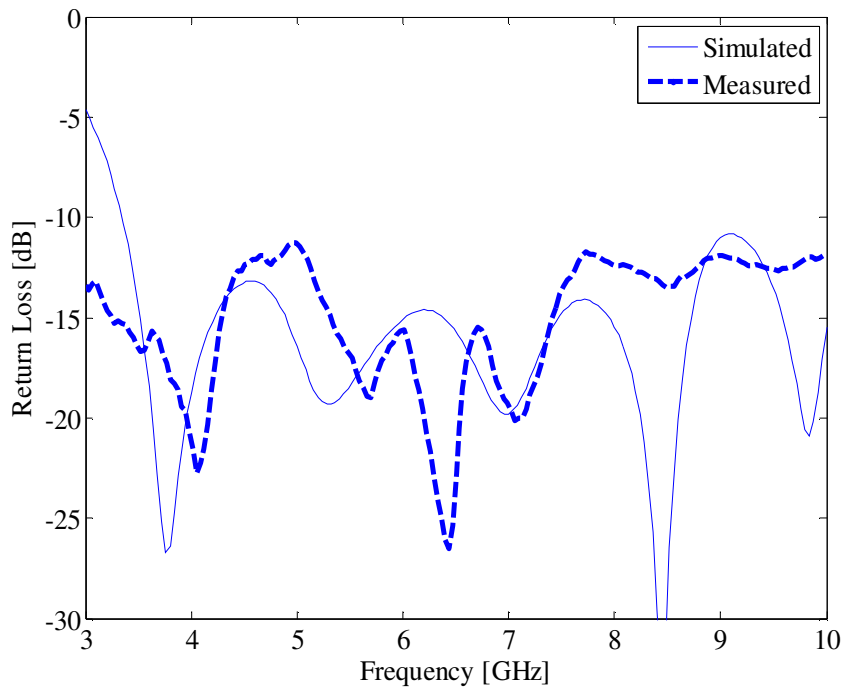


Figure 5.28. The antenna return loss for the sensing antenna when both switches are OFF

The tuning in the antenna return loss for the reconfigurable antenna is shown in the previous section. The covered bands for the different cases of the switches are summarized in Table 5.3. A little difference in the covered bands is obtained for when the sensing antenna is also integrated as compared to the previous section.

Table 5.3 The covered bands by the reconfigurable antenna for the different cases of the switches

<i>Switch Status</i>	<i>Covered Bands [GHz]</i>
Both OFF	3.875-4.82 / 6.3-7.4
S1 ON	4.68-6.255 / 7.34-8.6
S2 ON	3.28-4.22 / 7-7.855

The comparison between the simulated and the measured antenna coupling is shown in Fig. 5.29 for the case when S2 is ON. A good agreement is noticed between

both data. The measured coupling for the case when both switches are OFF (Case 1) and when S1 is ON (Case 2) are shown in Fig. 5.30.

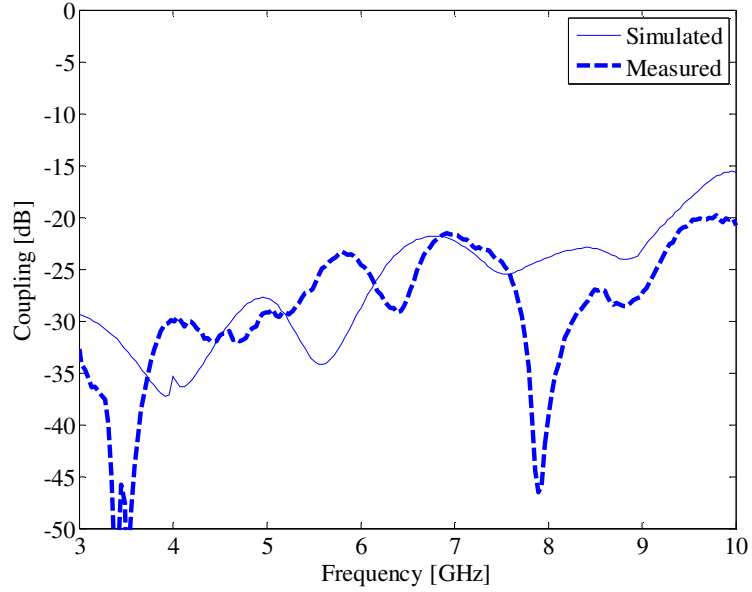


Figure 5.29 Comparison between the simulation and the measurement for the case when S2 is ON

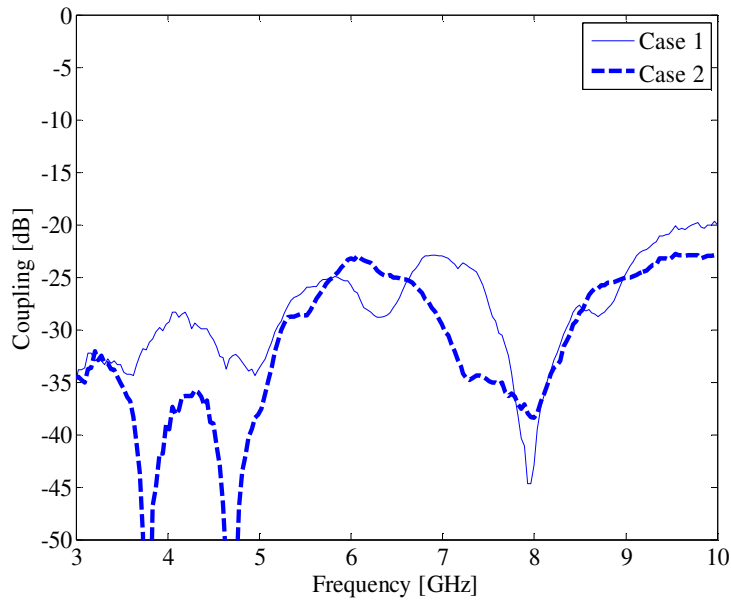


Figure 5.30 The measured coupling for Case 1 (both OFF) and Case 2 (S1 ON)

The measured coupling for a set of frequencies for the three different states of the switches is shown in Table 5.4.

Table 5.4 The measured coupling (dB) for the three different states of the switches

<i>Frequency [GHz]</i>	<i>Both OFF</i>	<i>S1:ON</i>	<i>S2:ON</i>
4	-30	-39.5	-30
6	-25.83	-24	-25
8	-44.7	-38.5	-46.56

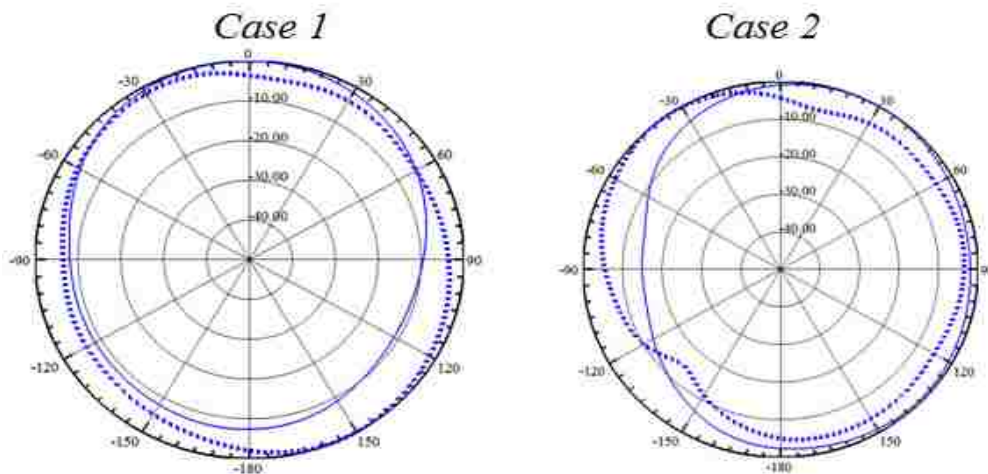
The antenna radiation pattern for the reconfigurable antenna for:

Case 1: at $f = 4.2$ GHz (solid line) and $f = 6.72$ GHz (dotted line);

Case 2: at $f = 5.32$ GHz (solid line) and $f = 7.92$ GHz (dotted line);

Case 3: at $f = 3.68$ GHz (solid line) and $f = 7.04$ GHz (dotted line)

in the XZ plane is shown in Fig. 5.31. A good omnidirectional radiation pattern is preserved. A property that is very essential for cognitive radio environment.



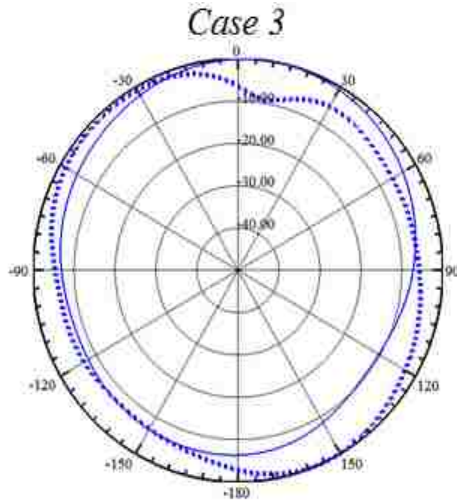


Figure 5.31 The normalized antenna radiation pattern in the XZ plane ($\Phi=0^\circ$) for the three different cases

5.9 Conclusion

In this chapter, a new antenna scheme for cognitive radio communications is presented. The cognitive radio antenna system consists of an UWB antenna and a frequency reconfigurable antenna incorporated both into the same substrate. The reconfigurable antenna is based on photoconductive switches. A novel approach for switch activation is proposed. This approach allows the laser diodes to be incorporated directly within the antenna structure. This approach allows for easier integration of such antennas into commercial wireless devices. Two prototype cognitive antennas are fabricated to test the proposed methodology. Good agreement is observed between the simulated and the measured RF performance of the antenna. In the next chapter, a cognitive radio receive channel experiment is conducted to demonstrate the applicability of the proposed scheme in a cognitive radio environment. The experiment is based on the cognitive radio antenna discussed in Section 5.7.

Chapter 6

Implementation of a Cognitive Radio Receive Algorithm

6.1 Introduction

In this chapter, a cognitive radio experiment using the optically pumped reconfigurable antenna system presented in the previous chapter is discussed. A work-flow diagram indicating the operation of a cognitive radio system is showing in Fig. 6.1.

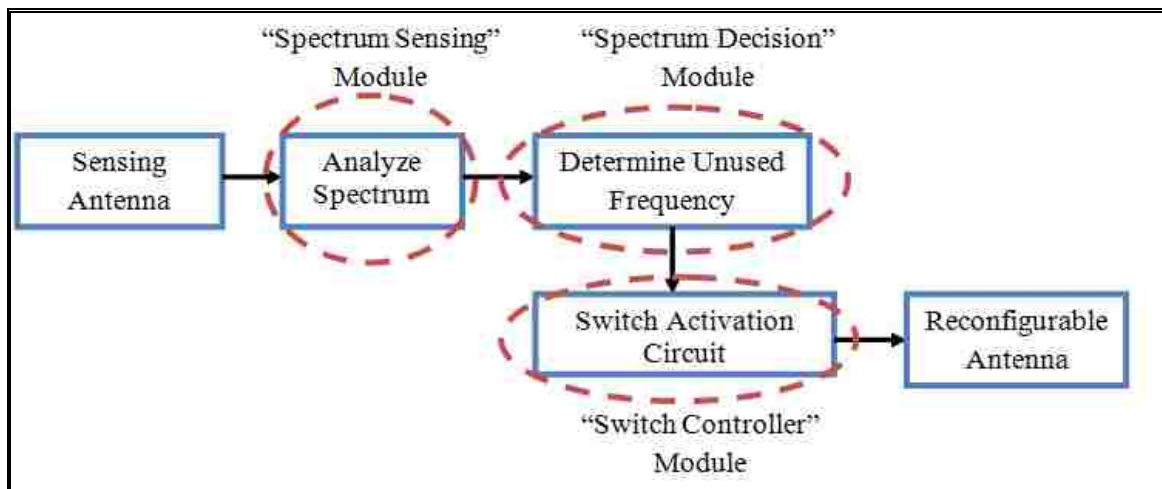


Figure 6.1 A cognitive radio chain

The sensing antenna is generally an UWB antenna with an operating band that spans the entire frequency spectrum over which the wireless communication is expected to occur. The “Spectrum Sensing” module of the cognitive radio engine continuously searches for unused frequency channels within this operating band. This information is fed to the “Spectrum Decision” module which determines the corresponding band for communication. The “Switch Controller” module then performs the required electronic operation (switching, multiplexing, etc.) to tune the operating frequency of the reconfigurable antenna which performs the data communication over the unused wireless

frequency channels determined by the “Spectrum Decision” module.

6.2 The experimental Setup

In this section, the applicability of the cognitive antenna is demonstrated, by incorporating it into a mock-up of a cognitive radio receive channel. The experiment flowchart is shown in Fig.6.2. The setup of this experiment is shown in Fig. 6.3.

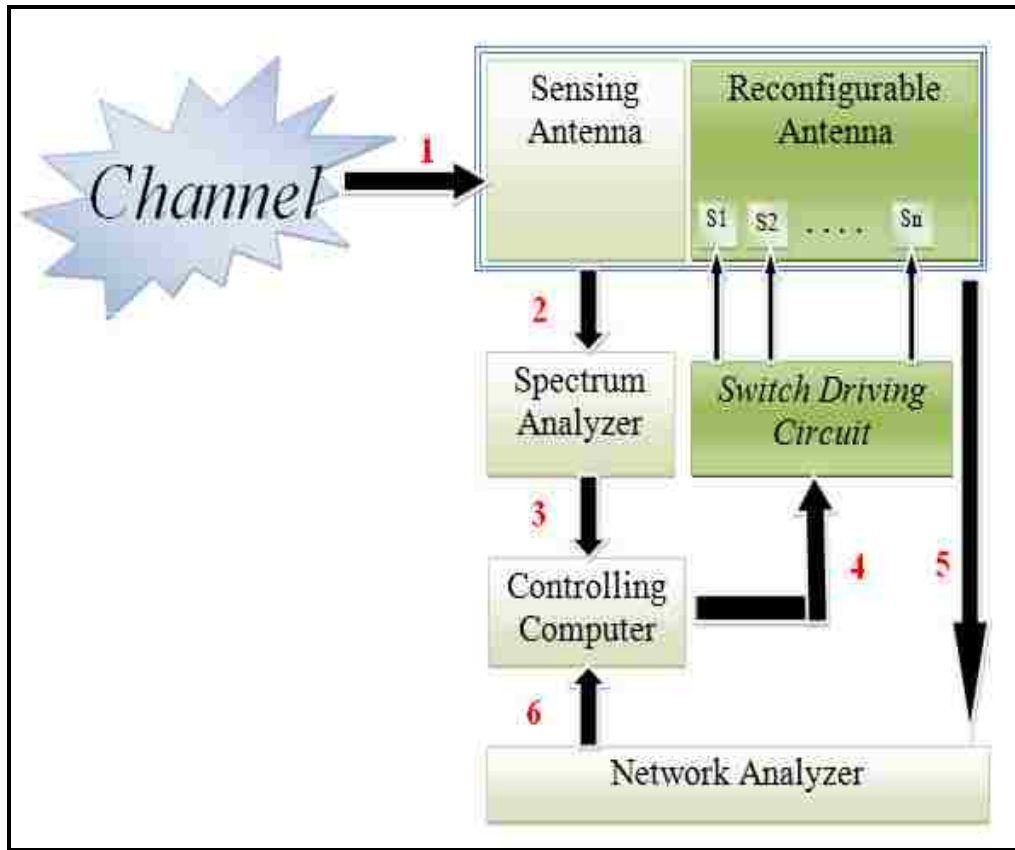


Figure 6.2 The cognitive radio receive channel experiment work-flow

The experiment work-flow consists of the following steps:

Step 1: Controlling the frequency sweeper via LABVIEW:

A frequency sweeper is used as a model of the wireless channel in a cognitive radio environment. It is programmed to generate a Continuous Wave (CW) every 3 seconds at a

randomly chosen carrier frequency between 3 GHz and 6 GHz. The RF output of the frequency sweeper is connected to the broadband TX horn Antenna. We consider the transmitted randomly chosen carrier frequency by the horn antenna as the “unused” frequency channel in the cognitive radio environment, to which the reconfigurable receive antenna should tune its operating frequency.

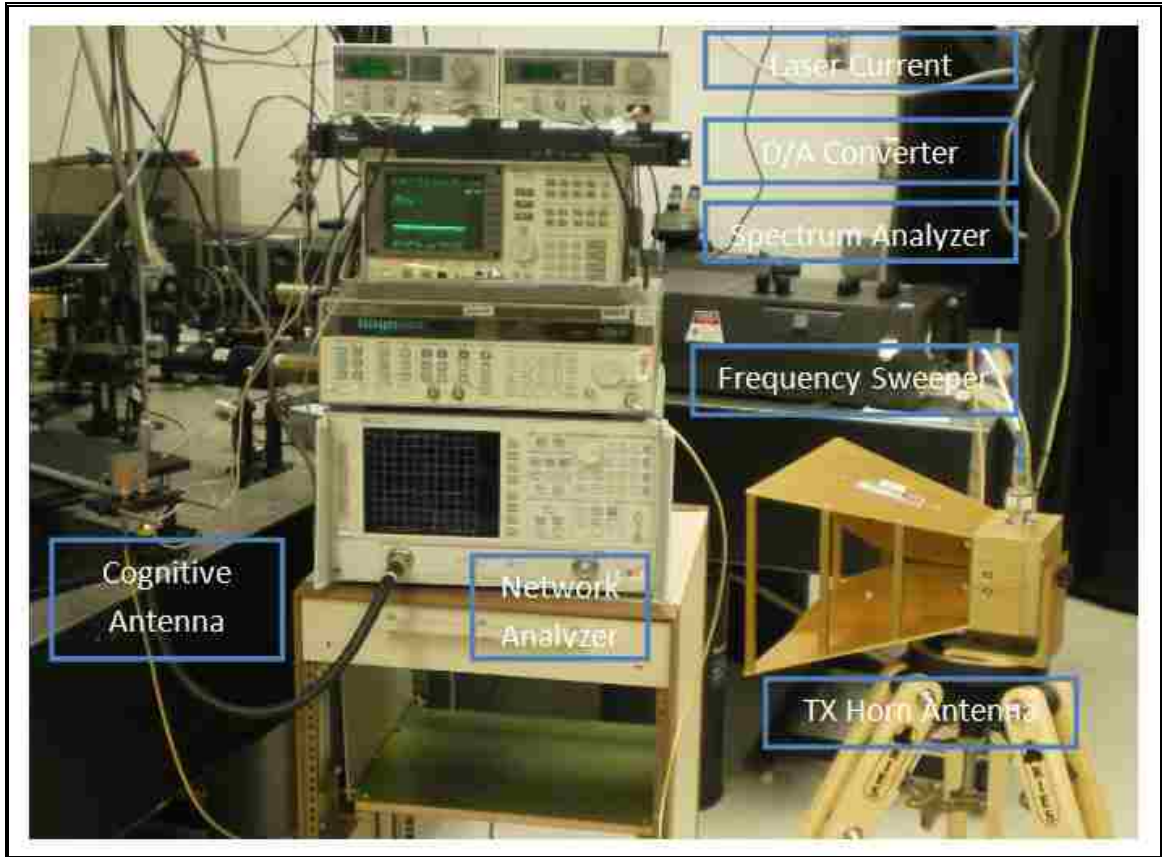


Figure 6.3 The experiment setup

Step 2: Sensing the channel:

The UWB sensing antenna of the cognitive antenna structure discussed in Chapter 5, Section 5.5 is connected to the spectrum analyzer. The spectrum analyzer continuously measures the power-spectral density of the received signal from the UWB sensing antenna.

Step 3: Spectrum Decision:

The signal acquired by the spectrum analyzer is analyzed by a controlling computer, which then determines the dominant frequency component within the signal. Fig. 6.4 shows an example of the power spectral density of the received signal from the UWB antenna, in the case when the TX horn was transmitting at $f=4.238$ GHz. The LABVIEW code used to perform the first three steps is shown in Fig. 6.5

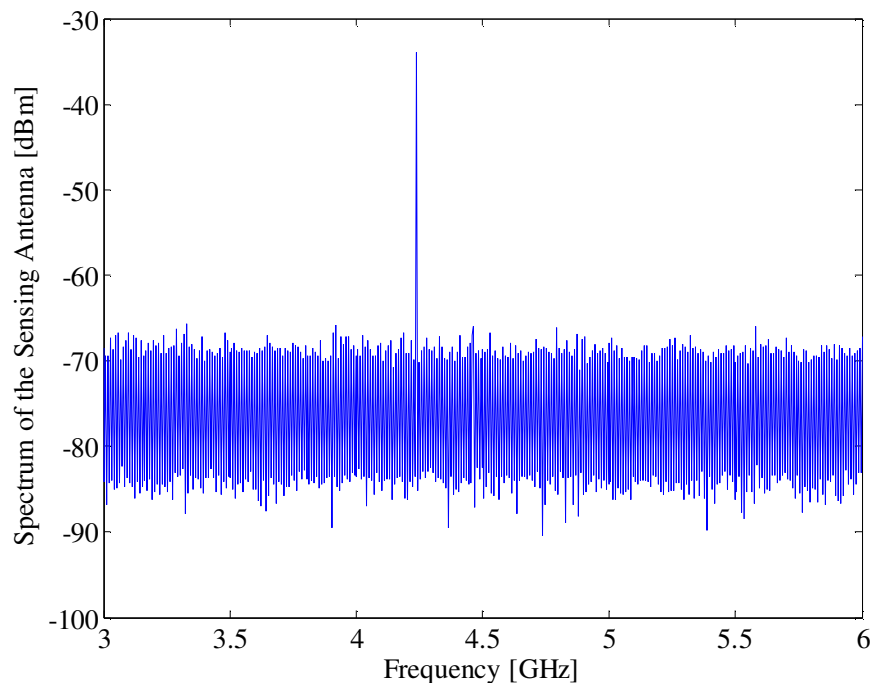


Figure 6.4 The sensing antenna spectrum

Step 4: Switch Controller:

Once the dominant frequency component in the received signal is determined, the controlling computer then activates the appropriate laser-current driver. This is done by providing the appropriate inputs to the laser-current driver through a digital-to-analog converter. The switching decision tree is shown in Fig. 6.6.

Step 5: Reconfigurable Antenna Status:

Based on the defined combination of the activated switches (S1 OFF; S2 ON / S1 OFF; S2 OFF / S1 ON; S2 OFF), the narrow-band reconfigurable antenna then tunes its operating frequency to the appropriate frequency band to receive the incoming signal. A diagnostic algorithm is also introduced within our work-flow controller code (written in LABVIEW) to ensure that the reconfigurable antenna switches are appropriately commanded by the laser drivers. The reconfigurable antenna is connected to a network analyzer (N.A.). The signal acquired by the N.A. is analyzed by the controlling computer to determine the operating frequency band of the reconfigurable antenna. The LABVIEW code to perform Step 5 and Step 6 is not shown here since it is very complicated.

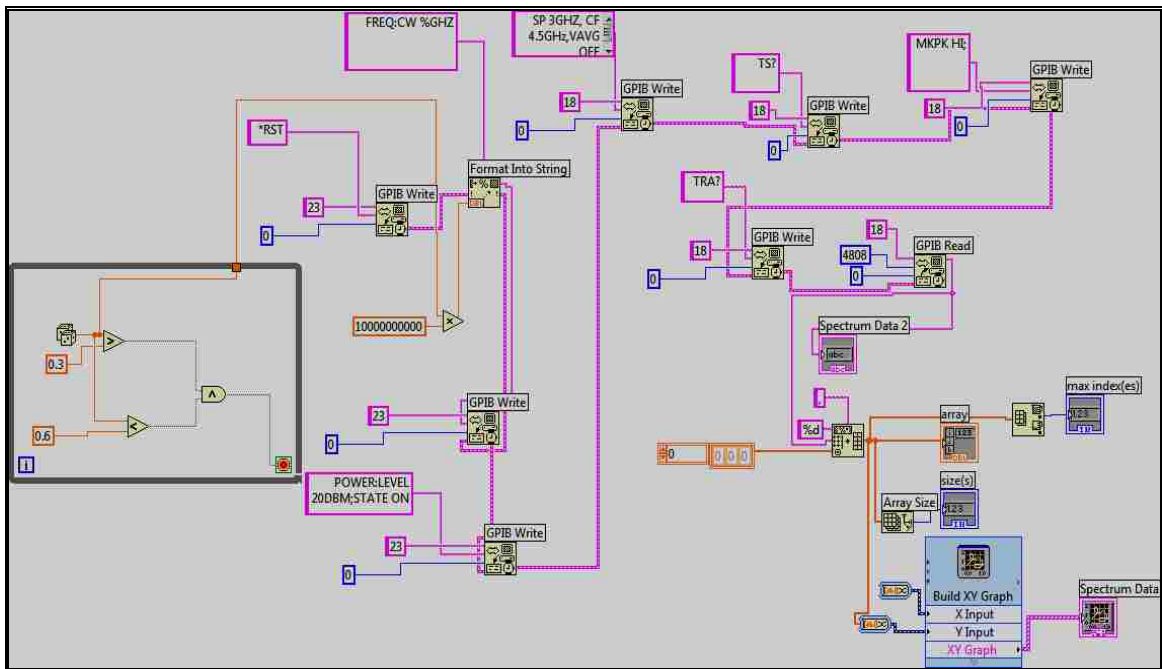


Figure 6.5 Controlling the frequency sweeper and the spectrum analyzer

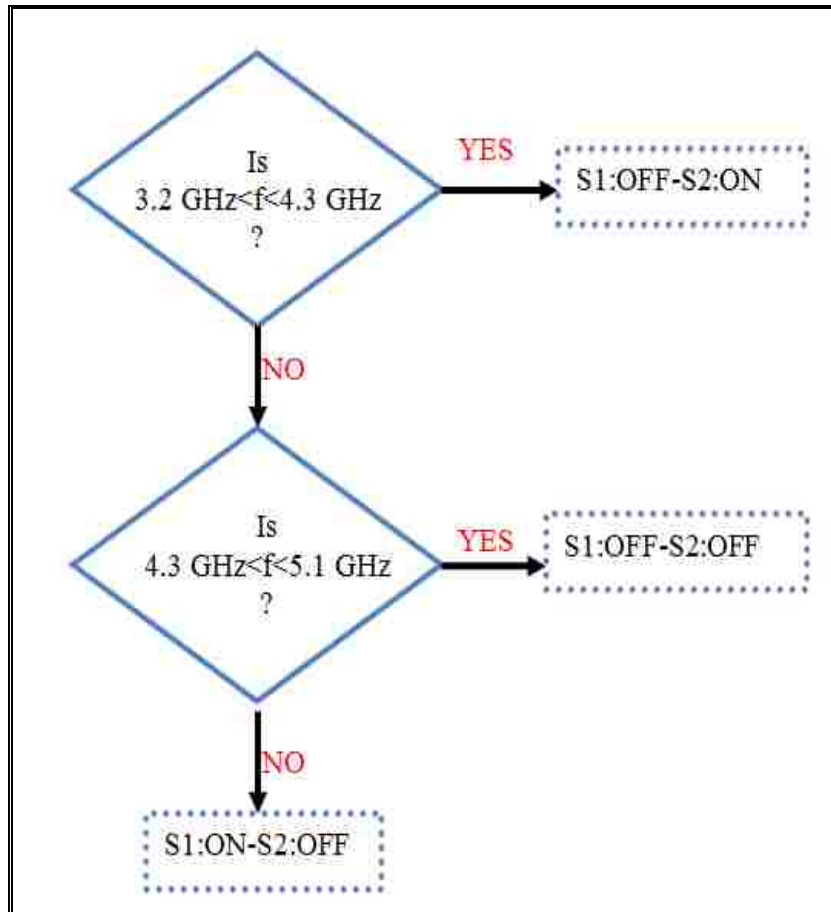


Figure 6.6 The switching decision tree which determines which switch to be activated

Step 6: Resume:

The whole process (Step 1 to Step 5) is repeated every 3 sec. The tuning of the reconfigurable antenna is in the micro-second range. The whole analysis is done instantaneously. The reconfigurable antenna immediately changes its operating frequency once the unused frequency band is determined.

6.3 Conclusion

A cognitive radio receive channel experiment is conducted to demonstrate the applicability of the proposed antenna scheme discussed in Chapter 5. LABVIEW is used to provide the chronological order between all the different steps of the experiment. In the

next chapter, a detailed discussion about the switching speed of the optically reconfigurable antenna structure is presented. The carrier lifetime of the silicon switch and the turning ON/OFF of an optically pumped reconfigurable antenna system (OPRAS) are experimentally computed.

Chapter 7

Measuring the Switching Speed of an Optically Reconfigurable Antenna System

7.1 Introduction

This chapter presents a new technique for measuring the switching speed of an optically pumped reconfigurable antenna system (OPRAS) driven by semiconductor-based photoconductive switches. The experimental setup and measurement technique for estimating the ON \leftrightarrow OFF transition speed of the photoconductive switches activated by a laser diode source on an antenna platform are presented.

In the first section, a discussion about the carrier lifetime in a semiconductor material is presented. The commonly used technique to measure the carrier lifetime, called microwave photoconductive decay μ -PCD, is detailed in the following section. The switching time of the optically driven transmission line presented in Chapter 4 is then discussed. Finally, the switching experiment is performed on an optically reconfigurable antenna structure in order to quantify its turning ON and OFF (t_{on} and t_{off}) speed. This time (t_{on} and t_{off}) is important especially if the OPRAS is going to operate in a dynamic environment such as the cognitive radio environment.

7.2 Carrier Lifetime

Carrier lifetimes fall into two primary categories: *recombination lifetimes*; and *generation lifetimes*. The concept of recombination lifetime τ_r holds when excess carriers decay as a result of recombination. Generation lifetime τ_g applies when there is a scarcity

of carriers, as in the space-charge region (scr) of a reverse biased diode or MOS device and the device tries to attain equilibrium. During recombination an electron-hole pair ceases to exist on average after a time τ_r . The generation lifetime, by analogy, is the time that it takes on average to generate an electron-hole pair [114].

The difficulty in defining a lifetime is that we are describing a property of a carrier within the semiconductor material rather than the property of the semiconductor itself. Although we usually quote a single numerical value, we are measuring some weighted average of the behavior of the carriers influenced by surfaces, interfaces, doping barriers, the density of carriers besides the properties of the semiconductor material and its temperature. Since devices consist of bulk regions and surfaces, both bulk and surface recombination or generation occur simultaneously and their separation is sometimes quite difficult. The measured lifetimes are always effective lifetimes consisting of bulk and surface components [115].

7.2.1 Recombination Lifetime:

The recombination rate depends nonlinearly on the departure of the carrier densities from their equilibrium values. Three main recombination mechanisms determine the recombination lifetime [116-118]:

- 1) Shockley-Read-Hall or multiphonon recombination characterized by the lifetime τ_{SRH}
- 2) Radiative recombination characterized by τ_{rad}
- 3) Auger recombination characterized by τ_{Auger}

These three recombination mechanisms are illustrated in Fig. 7.1.

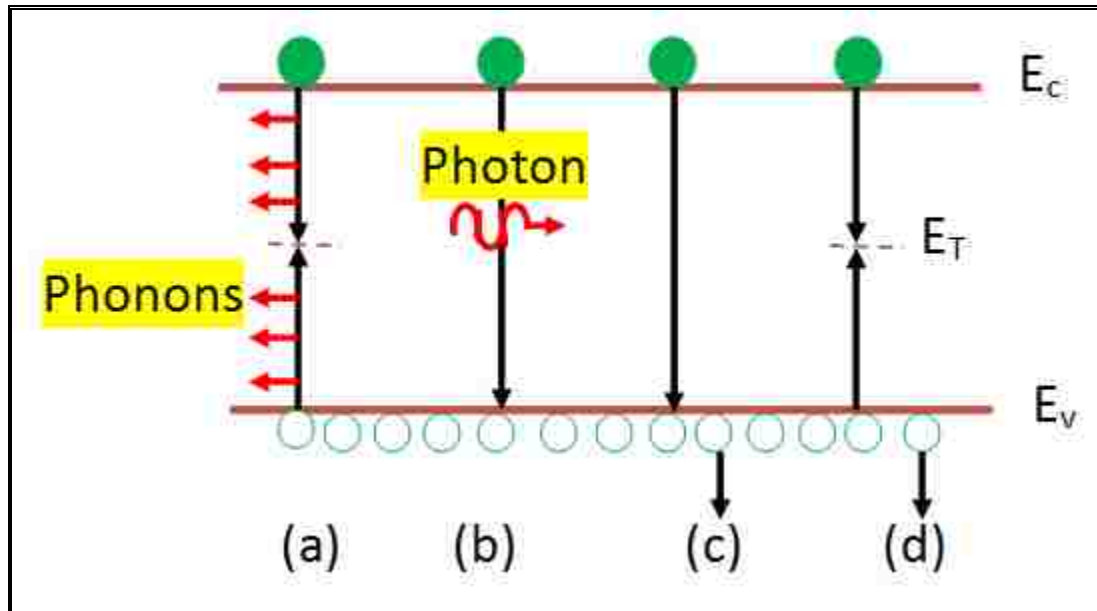


Figure 7.1 Recombination mechanisms: (a) SRH, (b) radiative, (c) direct Auger, and (d) trap assisted
 auger

The recombination lifetime τ_r is determined by the three mechanisms according to the relationship [119]:

$$\tau_r = \frac{1}{\tau_{SRH}^{-1} + \tau_{rad}^{-1} + \tau_{Auger}^{-1}} \quad \text{Eq. 7.1}$$

During SRH recombination, electron-hole pairs recombine through deep level impurities, characterized by the impurity density N_T , energy level E_T in the bandgap, and capture cross section σ_n and σ_p for electrons and holes, respectively. The energy liberated during the recombination event is dissipated by lattice vibrations or phonons, illustrated in Fig. 7.1(a). The SRH lifetime is given by [118]:

$$\tau_{SRH} = \frac{\tau_p (n_0 + n_1 + \Delta n) + \tau_n (p_0 + p_1 + \Delta p)}{p_0 + n_0 + \Delta n} \quad \text{Eq. 7.2}$$

Where p_0 and n_0 are the equilibrium hole and electron densities, Δn and Δp are the excess carrier densities taken to be equal in the absence of trapping.

More details for n_1 , p_1 , τ_n , and τ_p can be found in [117].

During the radiative recombination process, electron-hole pairs recombine directly from band to band with the energy carried away by photons as shown in Fig. 7.1(b). The radiative lifetime is [119].

$$\tau_{rad} = \frac{1}{B(p_0 + n_0 + \Delta n)} \quad \text{Eq. 7.3}$$

B is usually termed the radiative recombination coefficient.

The radiative lifetime is inversely proportional to the carrier density because in band-to-band processes both electrons and holes must be present simultaneously for a recombination event to take place [120].

During Auger recombination, shown in Fig. 7.1(c), the recombination energy is absorbed by a third carrier. Because three carriers are involved in the recombination event, the Auger lifetime is inversely proportional to the carrier density squared. For a p-type semiconductor, the Auger lifetime is given by [119]:

$$\tau_{Auger} = \frac{1}{C_p(p_0^2 + 2p_0\Delta n + \Delta n^2)} \quad \text{Eq. 7.4}$$

Where C_p is the Auger recombination coefficient

It is essential to note that the SRH recombination takes place whenever there are impurities or defects in the semiconductor. Since semiconductors always contain some impurities, this mechanism is always active. It is particularly important for indirect

bandgap semiconductors. Radiative recombination is important in direct bandgap materials like GaAs and InP, where the conduction band minimum lies at the same crystal momentum value as the valence band maximum. During the recombination event, phonons are not required, since the energy is dissipated by photons. Radiative recombination is relatively unimportant in silicon because its radiative lifetime is extremely high. Auger recombination is typically observed in both direct and indirect bandgap semiconductors. Similar to the radiative lifetime, the Auger lifetime is independent of any impurity density. It is the dominant recombination mechanism for narrow bandgap semiconductors [115].

Besides SRH bulk recombination there is also SRH surface recombination at bar surfaces or interface recombination at insulator/semiconductor interface. The SRH surface recombination velocity s_r can be found in [119].

The bulk recombination lifetime itself is independent of surface recombination. However, the measured recombination lifetime, frequently referred to as the effective recombination lifetime $\tau_{r,eff}$, is dependent on the surface recombination as carriers recombine both in the bulk as well as at the surface. $\tau_{r,eff}$ can be expressed as [119]:

$$\tau_{r,eff} = \left(\frac{1}{\tau_r} + \frac{1}{\tau_s} \right)^{-1} = \frac{\tau_r}{1 + \frac{\tau_r}{\tau_s}} \quad \text{Eq. 7.5}$$

τ_s is the surface lifetime and it is related to the surface recombination velocity s_r [119].

7.2.2 Generation Lifetime:

Each of the recombination processes of Fig. 7.1 has a generation counterpart [115]. Optical electron-hole pair generation is the counterpart of radiative recombination

and impact ionization is that of Auger recombination. The inverse of multiphonon recombination is thermal electron-hole pair generation characterized by the generation lifetime [114]:

$$\tau_g = \tau_p e^{(E_T - E_i)/KT} + \tau_n e^{-(E_T - E_i)/KT} \quad \text{Eq. 7.6}$$

τ_g is due to SRH generation and is the only generation lifetime usually considered. It is the time to generate one electron-hole pair thermally, and depends inversely on the impurity density and the capture cross section for electrons and holes.

The surface generation velocity s_g can be found in [119]. It can be thought of as that velocity with which carrier, generated at the surface or interface, leave the surface. It is proportional to the surface or interface state density.

The effective generation lifetime $\tau_{g,eff}$ given by [121]:

$$\tau_{g,eff} = \frac{\tau_g}{1 + \frac{\tau_g}{\tau_s}} \quad \text{Eq. 7.7}$$

is a combination of space-charge region bulk and surface generation. τ_s is the surface generation lifetime and it is related to the surface generation velocity s_g [115].

7.3 Microwave Photoconductive Decay (μ -PCD)

Photoconductive decay is a family of related lifetime measurement techniques that utilizes a transient decay of an excess of carriers generated by light in order to produce an associated detection response from which the desired recombination parameters can be extracted. Since photoconductivity in a semiconductor is a property dependent upon

mobile free carriers, the time-dependence of the photoconductivity is directly related to the recombination rates of the carriers [122-123].

The microwave photoconductive decay (μ -PCD) takes place as follows. When the conductivity of the measurement sample is temporarily increased, its microwave absorbing and reflecting properties change accordingly. In other words, when the sample is in equilibrium it will reflect a constant percentage of the impinging microwave energy, but when the sample contains an excess of decaying carriers, the reflected microwaves will vary with a time-dependence that is related to the excess conductivity present. Since carrier decay in the sample is determined by the recombination and transport parameters of the sample, the microwave reflectance decay data contains this decay information. Therefore, by continuously directing microwaves towards a post-excited sample and recording the time dependence of the reflected microwave energy, a time decay curve is obtained that allows the measurement of the recombination lifetime of the sample [122]. The basic idea of the microwave photoconductive decay is summarized in Fig. 7.2

Fig. 7.3 shows the diagram of the typical μ -PCD apparatus [124]. The physical configuration places a sample over the opening of a vertically oriented rectangular TE_{10} mode waveguide. The measurement sample is kept within a light-insulated enclosure. Single mode microwaves are continuously guided toward the sample.

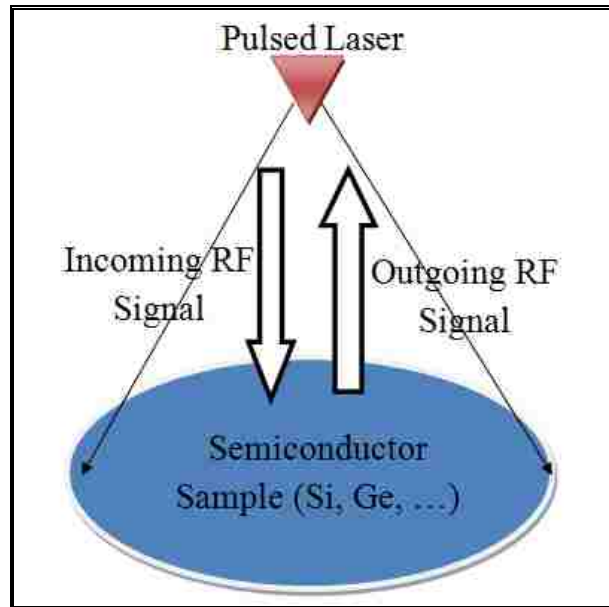


Figure 7.2 The change in the reflected power due to the change in the sample conductivity

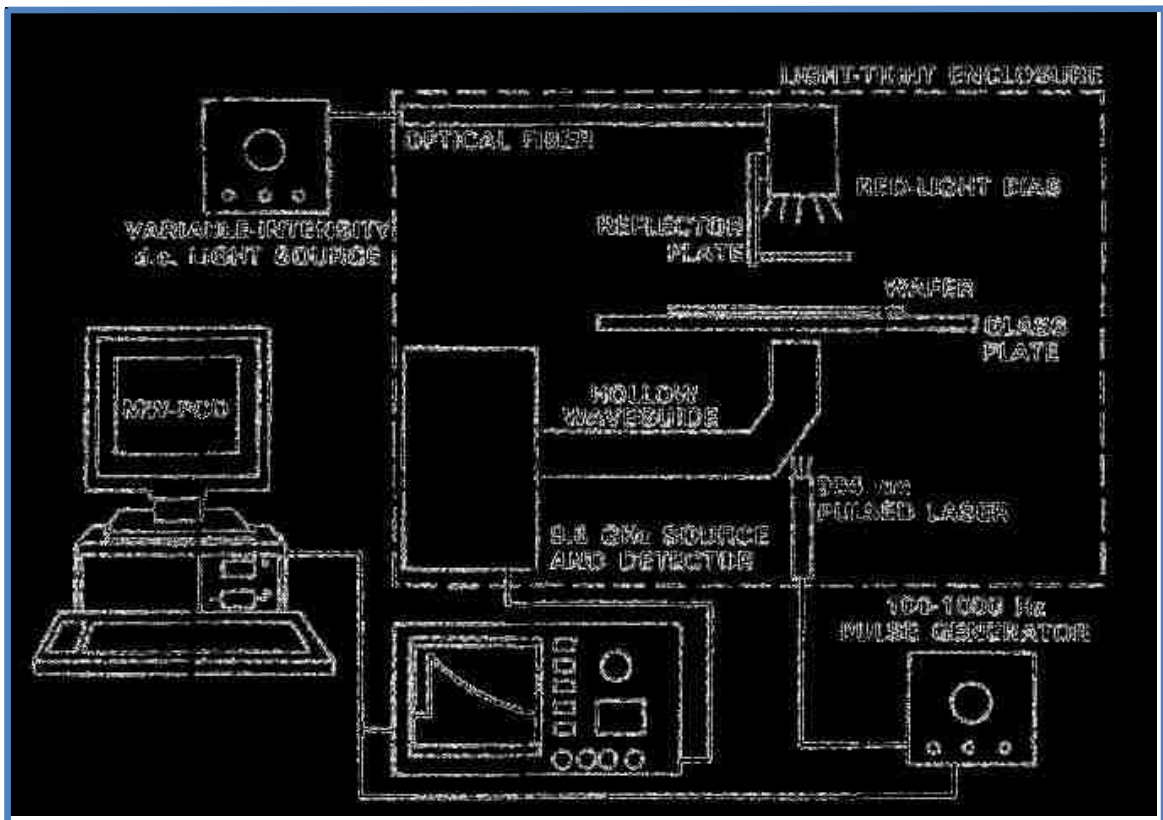


Figure 7.3 The μ -PCD system used at Sandia National Laboratory

The pulsed laser generates electron-hole pairs in a spot on the sample at the center of the waveguide opening. The excess carriers stimulate a transient microwave reflectance. A square-law detector within the waveguide senses this microwave transient. The decaying output voltage from the detector is sampled and stored in a digital oscilloscope. The carrier lifetime can be computed from the reflectance curve [122].

To understand the theory of μ -PCD, one can use the wave-impedance theory to determine the microwave reflected power R from the sample as illustrated in Fig. 7.4 [125-126].

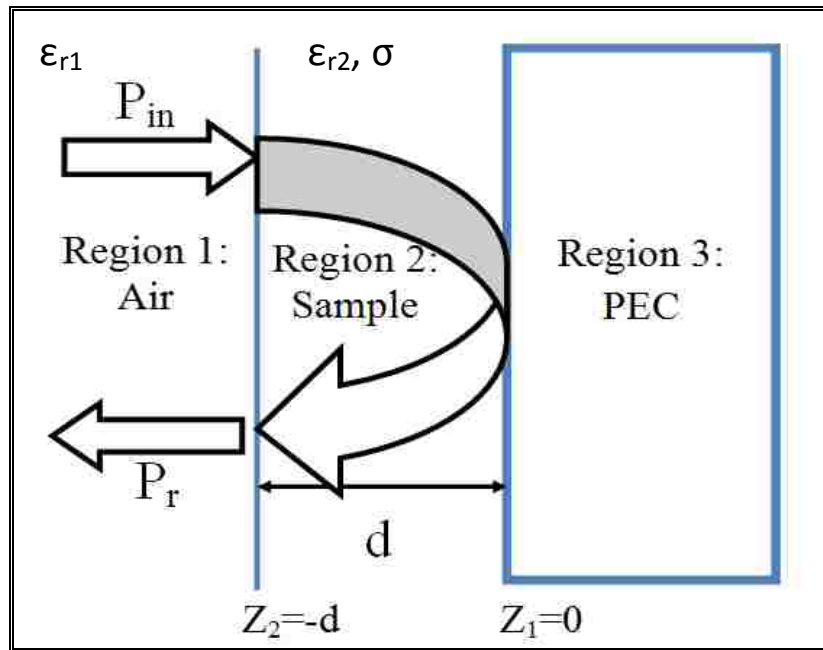


Figure 7.4 The three different regions of the μ -PCD technique

The power reflection coefficient R is calculated from the voltage reflection coefficient:

$$\Gamma = \frac{V_r}{V_{in}} \quad \text{Eq. 7.8}$$

$$R = \frac{P_r}{P_{in}} = \left(\frac{V_r}{V_{in}} \right) \left(\frac{V_r}{V_{in}} \right)^* = \Gamma \Gamma^* \quad \text{Eq. 7.9}$$

$$\Gamma = \frac{\Gamma_{12} - e^{-2\gamma_2 d}}{1 - \Gamma_{12} e^{-2\gamma_2 d}} \quad \text{Eq. 7.10}$$

Where

d is the sample thickness

and

$$\Gamma_{12} = \frac{\gamma_1 - \gamma_2}{\gamma_1 + \gamma_2} = a + jb$$

$$\gamma_{1,2} = \sqrt{\left(\frac{\Pi}{w} \right)^2 - \omega^2 \mu_0 \epsilon_0 \epsilon_{r1,2} + j\omega \mu_0 \sigma} = \alpha_{1,2} + j\beta_{1,2} \quad \text{Eq. 7.11}$$

After doing the corresponding calculation:

$$R = \frac{R_{12} + e^{-4\alpha_2 d} - 2e^{-2\alpha_2 d} [a \cos(2\beta_2 d) - b \sin(2\beta_2 d)]}{1 + R_{12} e^{-4\alpha_2 d} - 2e^{-2\alpha_2 d} [a \cos(2\beta_2 d) - b \sin(2\beta_2 d)]} \quad \text{Eq. 7.12}$$

Where

$$R_{12} = \Gamma_{12} \Gamma_{12}^* \quad \text{Eq. 7.13}$$

The change of the dielectric constant of the sample is modeled as:

$$\epsilon_{r2} = \epsilon_{r2}^{initial} - \sum_{i=e,h} \frac{Nq^2}{\epsilon_0 m_i [(2\pi f)^2 + \nu_i^2]} \left(1 + j \frac{\nu_i}{2\pi f} \right) \quad \text{Eq. 7.14}$$

7.4 Switching Speed Experiment for an Optically Driven Transmission Line

In this section, the setup for measuring the switching speed of the integrated photoconductive switch on the transmission line discussed in Chapter 4 (Section 4.2) is shown. The turning ON/OFF of the switch corresponds to the carrier generation/recombination lifetime in the silicon switch. The fabricated structure, its activation mechanism and its return loss are shown in Fig. 7.5. The side view of the integrated switch and the corresponding current flow are also shown in Fig. 7.5.

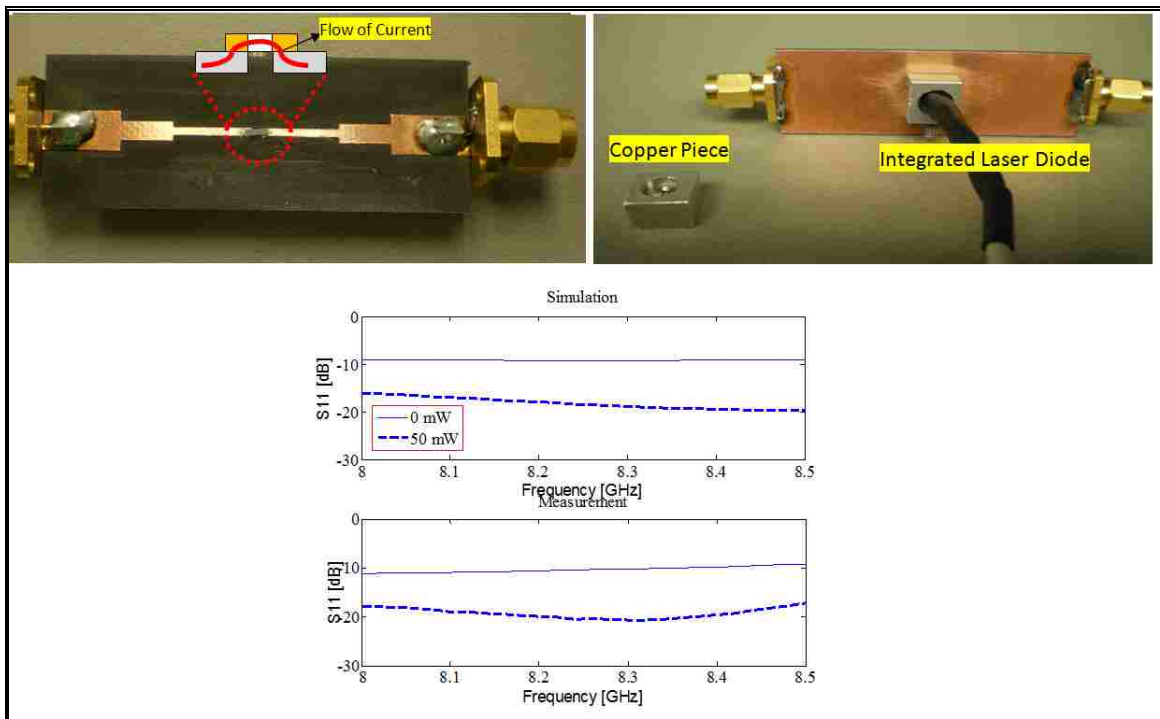


Figure 7.5 The optically switched transmission line and its return loss for 0 mW and 50 mW

In this experiment setup, two different cases are considered. The first case is to continuously drive the laser diode via a current source (CW case). For this case, the laser diode is either continuously turned ON or OFF. The second case is to drive the laser diode via a pulsed current source of a given duration (Pulsed case). From this case, the switching

time can be estimated. The experiment flowchart for both cases is shown in Fig. 7.6 [127-128].

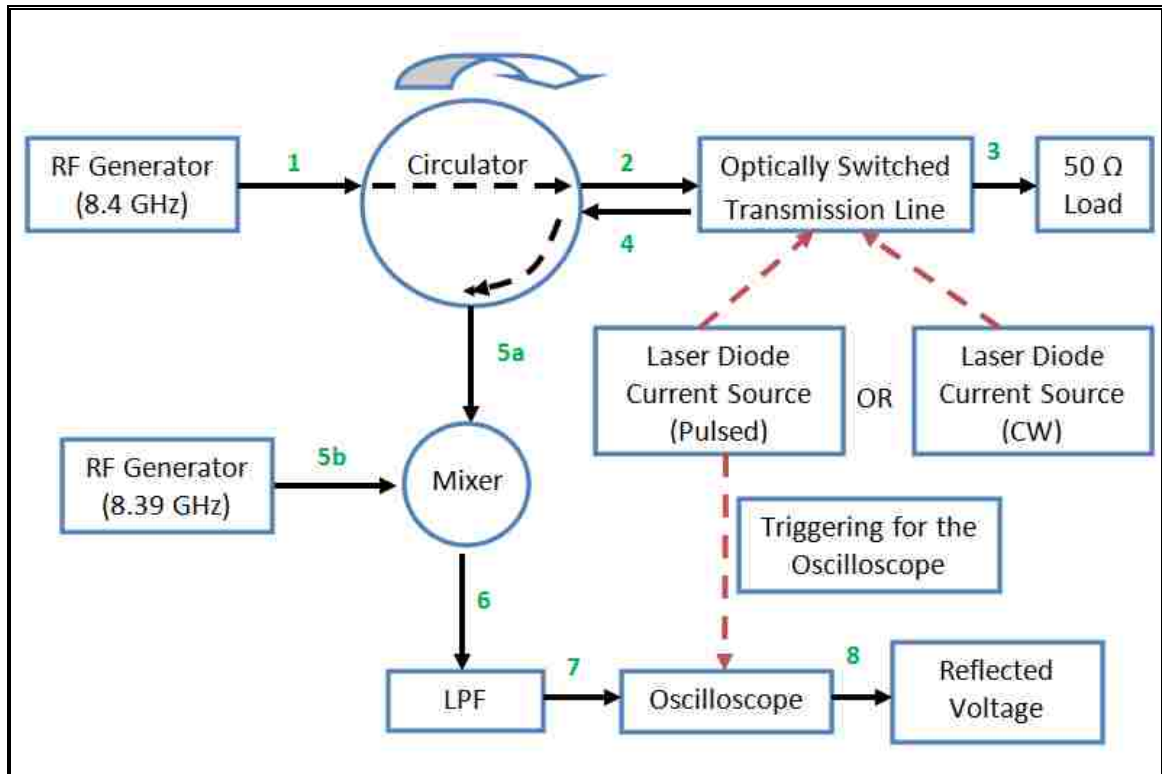


Figure 7.6 The flowchart for the experiment setup using the optically switched transmission line

The experiment setup can be divided into the following steps:

Step 1:

A frequency sweeper is used to generate a CW signal at the same design frequency of the transmission line discussed in Chapter 4, i.e. $f_c=8.4$ GHz.

Step 2:

The RF output of the frequency sweeper is connected to port 1 (P1) of the circulator.

Step 3:

The power entering P1 is transmitted to the next port (P2) of the circulator that is connected to one of the inputs of the optically switched transmission line. The second

input of the TL is terminated by a matched 50Ω load. Based on the status of the photoconductive switch, the amount of power that is reflected at P2 will vary. When the switch is OFF (laser diode is OFF), a maximum amount of reflected power is obtained. By driving the laser diode via a current source (CW or Pulsed), the amount of reflected power is going to decrease and most of the power is absorbed by the terminated load. The change of the reflected voltage at the input port of the TL is going to give the time needed to turn OFF/ON the switch.

Step 4:

The reflected voltage at P2 is transmitted to port 3 (P3) of the circulator. An oscilloscope is used to capture the change in the reflected voltage. In order to satisfy the Nyquist rate for sampling $\{f_s \geq 2*f_c; f_s: \text{ sampling frequency}\}$ and to increase the time window of the captured signal by the oscilloscope $\{t_{\text{window}}= 30000(\text{samples})/f_s\}$, the frequency component of the signal at P3 should be lowered so that the sampling frequency is decreased.

Step 5:

The output signal at P3 is fed to the first port P'1 of the mixer.

Step 6:

An RF signal at $f_{LO}=8.39$ GHz is connected to the second port P'2 of the mixer. The output of the mixer consists of f_c , f_{LO} , $f_c-f_{LO}=10$ MHz, and other intermodulation products.

Step 7:

A 400 MHz low pass filter (LPF) is used to retain only the 10 MHz signal. The output of the LPF is connected to the oscilloscope that samples at $f_s=250$ Msamples/sec which corresponds to a time window of $t_{\text{window}}=120$ μsec .

Step 8:

For CW case, no triggering is needed for the oscilloscope since the laser diode is either always ON or OFF. However for the pulsed laser, the oscilloscope is triggered by an external output signal from the pulse generator that is used to drive the laser diode. The data captured by the oscilloscope is sent to a controlling computer using LABVIEW. The experiment setup is shown in Fig. 7.7. A zoomed view for the experiment is shown in Fig. 7.8.

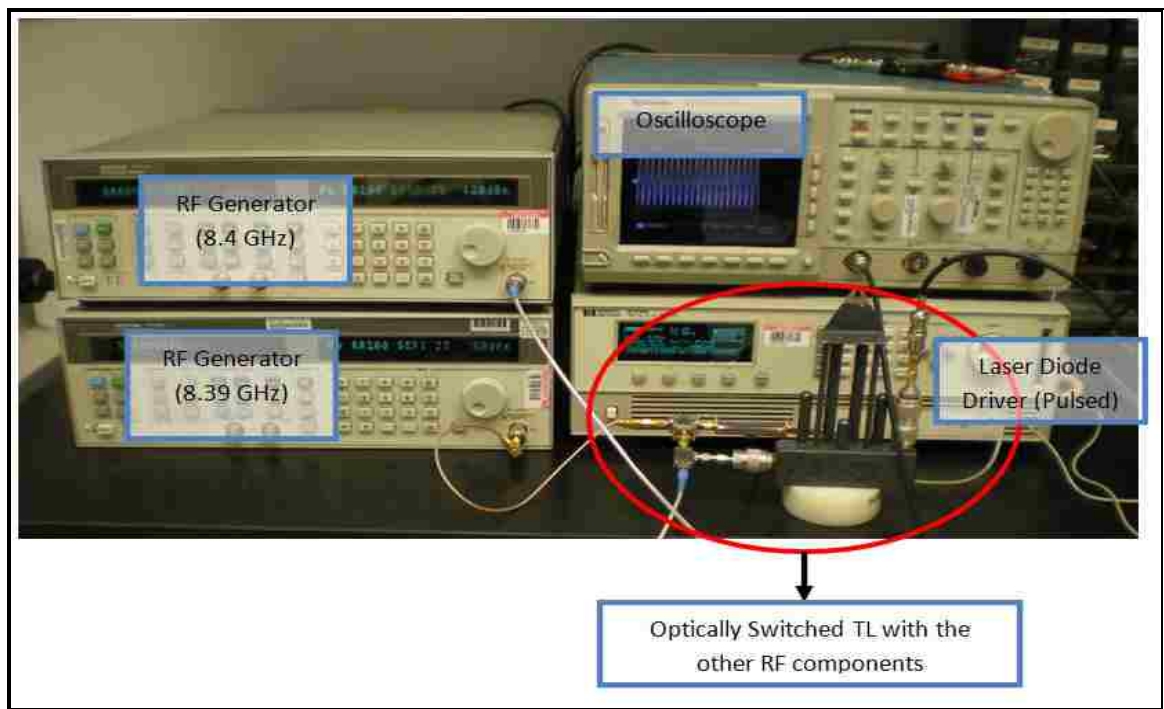


Figure 7.7 The experiment setup for measuring the switching time for the optically reconfigurable transmission line

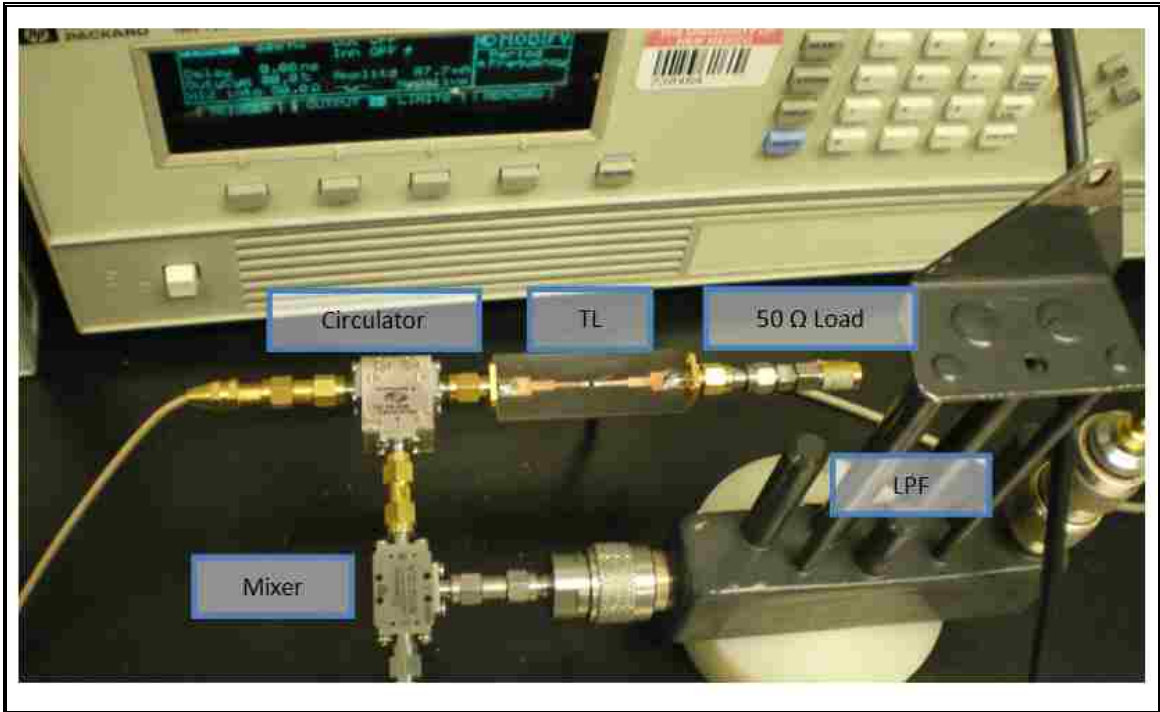


Figure 7.8 A zoomed view for the experiment setup

The measurement analysis is divided into two different cases:

Case 1: CW Driven Laser Diode:

In this case, the change in the reflected voltage is investigated using the optically switched transmission line. The switching time can't be quantified since the laser diode is either continuously OFF or ON. Two different measurements are taken:

Measurement 1: The reflected voltage by the transmission line when the switch is OFF.

Measurement 2: The reflected voltage by the transmission line when the switch in ON.

When the switch is OFF, most of the power that is fed to the transmission line is going to get reflected. When continuously driving the laser diode via an 87.7 mA current source the switch changes its physical properties and the current begins to flow. The voltage fed to

the transmission line is absorbed by the load. A drop in the reflected voltage is noticed. A comparison between both measurements is shown in Fig. 7.9.

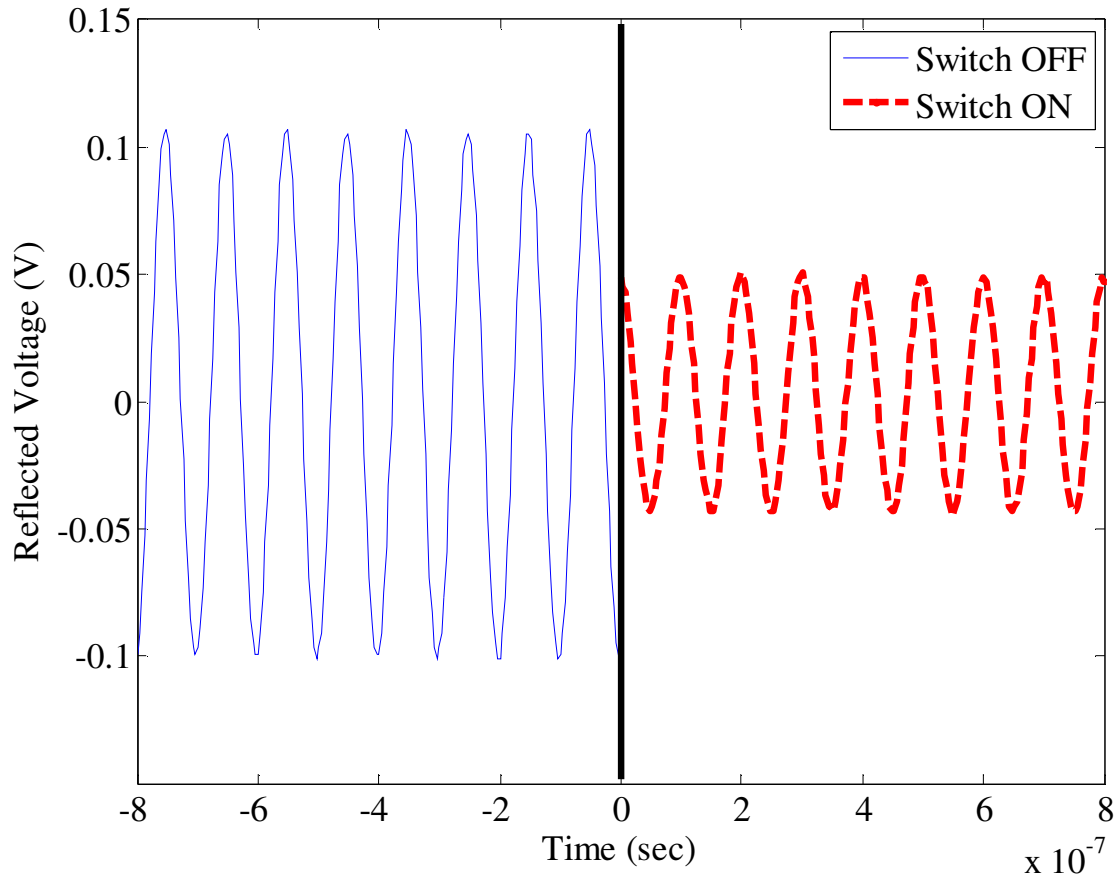


Figure 7.9 The reflected voltage for the CW driven laser diode

Case 2: Pulsed Driven Laser Diode:

In this case, the laser diode that is connected to a pulse generator is driven by a pulse that has an ON duration of 40 μsec . Therefore the laser diode is going to be ON for the duration of $t_{\text{pulse}}=40 \mu\text{sec}$ and OFF for the duration of $t_{\text{window}}-t_{\text{pulse}}=80 \mu\text{sec}$ in the measured data. The triggering of the oscilloscope is set to begin capturing data 30 μsec before the laser diode turns ON. Fig. 7.10 shows the driving signal for the laser diode and

the triggering signal for the oscilloscope. The change in the reflected voltage at port 1 of the switched transmission line is shown in Fig. 7.11. This plot is divided into three time windows (30 μsec , 40 μsec , 50 μsec). From this plot, one can compute the turning ON and OFF of the switch.

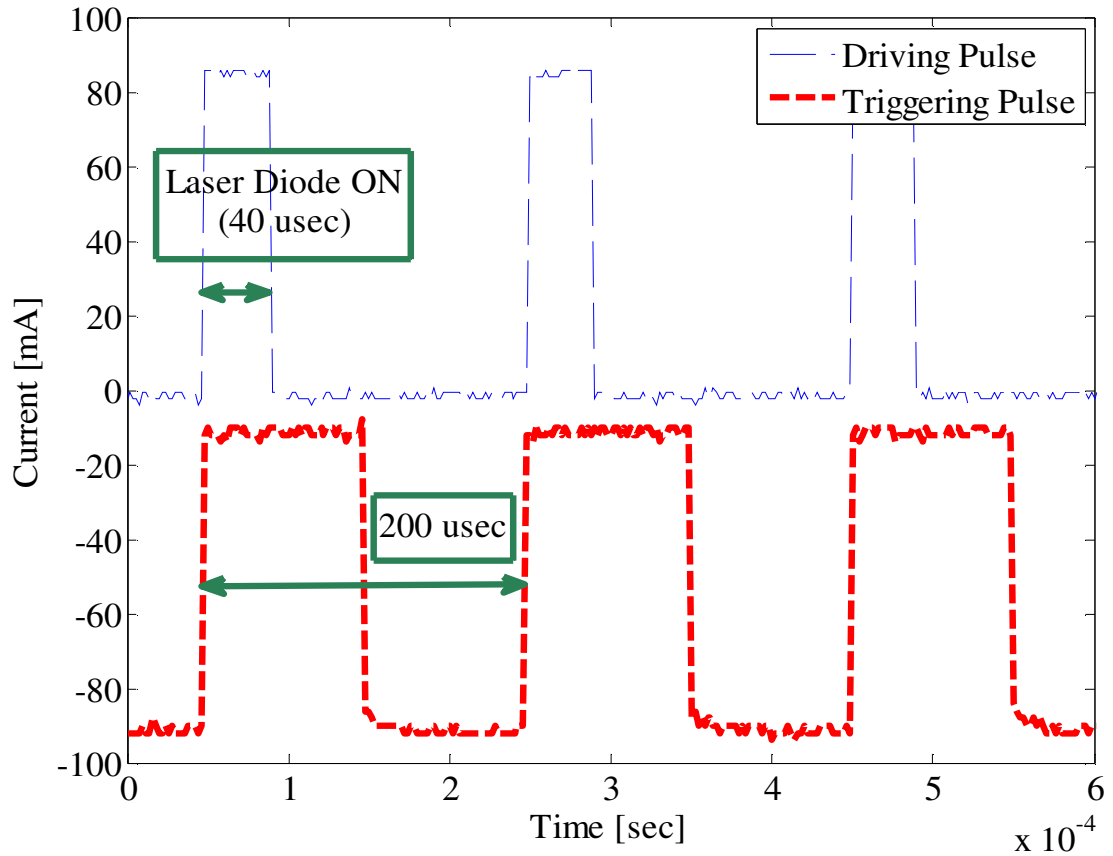


Figure 7.10 The driving and the triggering pulse for the experiment setup

The change in the reflected voltage at the input port of the optically switched transmission line is shown in Fig. 7.12 where the oscilloscope is set to capture data for a duration of 80 μsec after the trigger. This duration corresponds to the time where the laser diode is either ON or OFF.

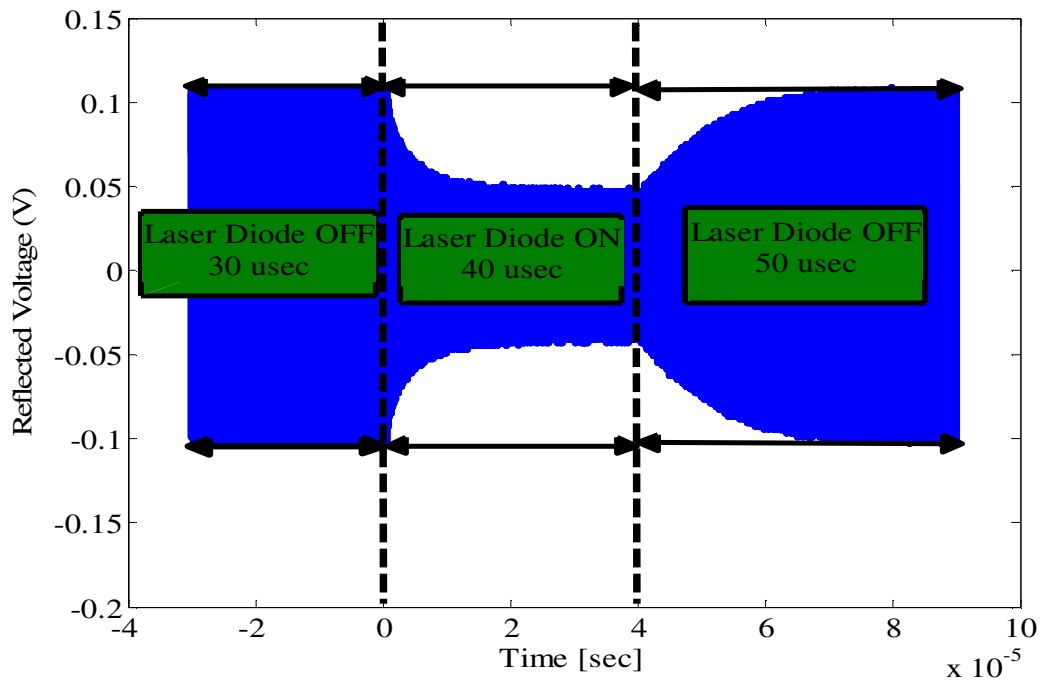


Figure 7.11 The change in the reflected voltage for the pulsed driven laser diode

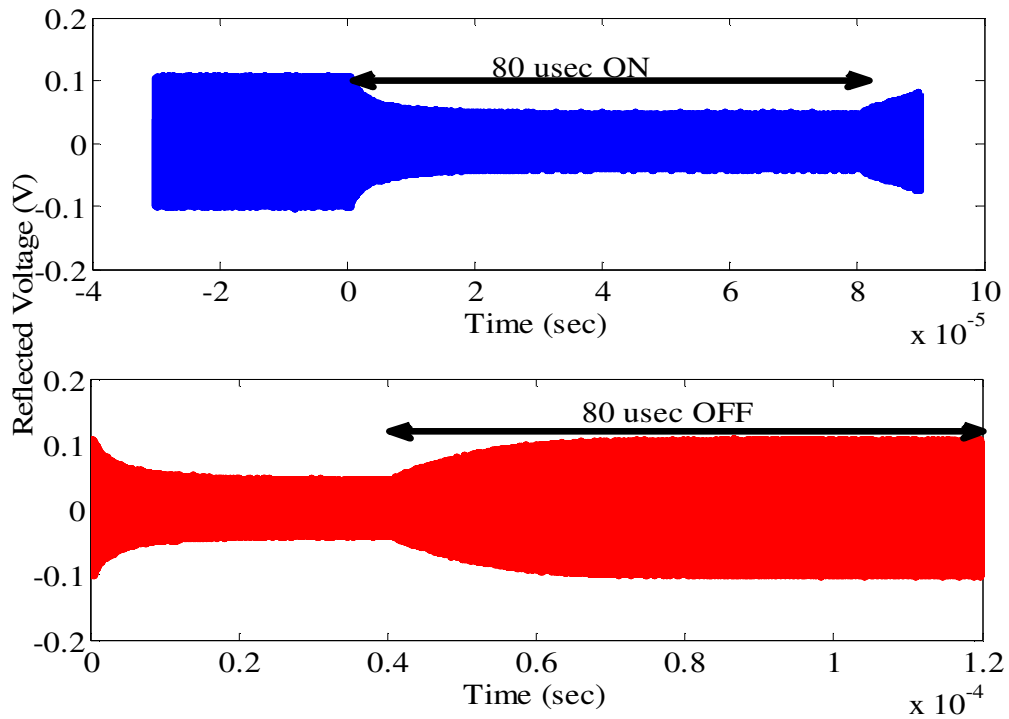


Figure 7.12 The change in the reflected voltage when the laser diode in ON/OFF for a duration of 80 μ sec

Fig. 7.13 shows the measured values and the fitted data for the reflected voltage envelope from 0 μsec to 40 μsec . The required time needed for the switch to go from OFF state to ON state is: $t_{\text{OFF} \rightarrow \text{ON}} = 3.935 \mu\text{sec} \pm 0.7 \mu\text{sec}$. This time corresponds to the effective carrier generation lifetime discussed in the previous section. The R^2 for the fitted data is 0.9926, where R^2 is a measure of how well future outcomes are likely to be predicted by the fit (correlation coefficient).

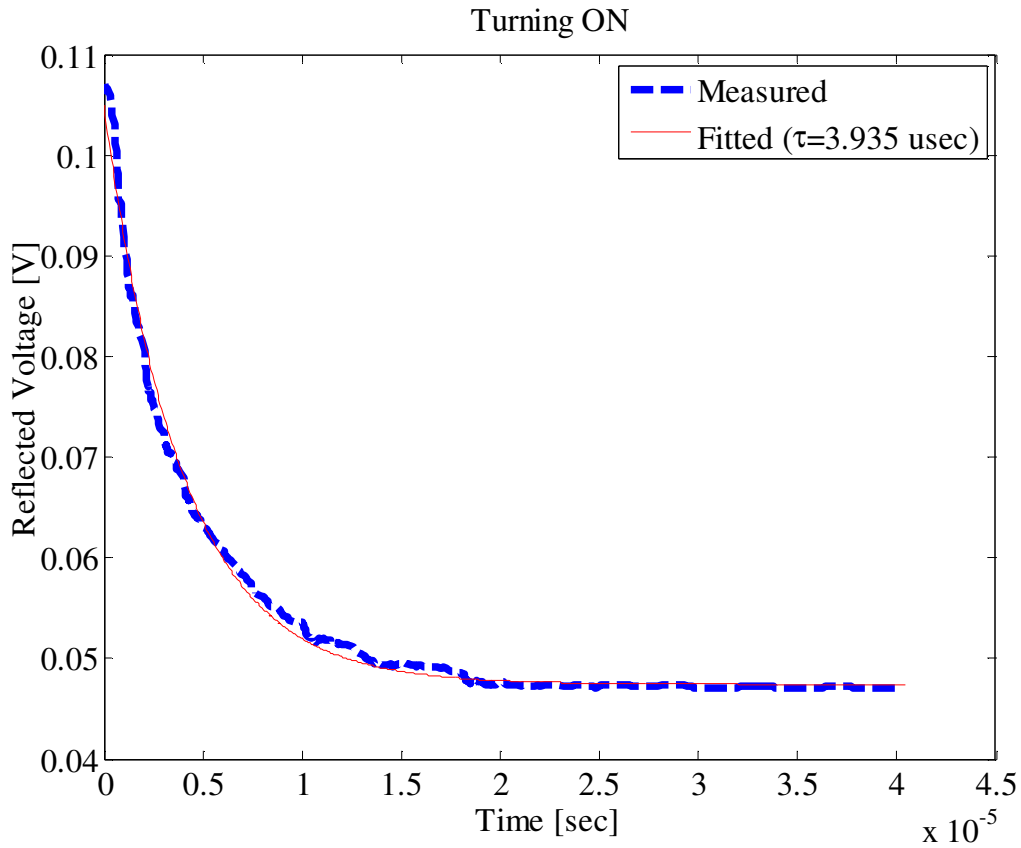


Figure 7.13 The turning ON of the switch integrated with the optically switched transmission line

Fig. 7.14 shows the measured values and the fitted data for the reflected voltage envelope from 40 μsec to 90 μsec . The required time needed for the switch to go from ON state to OFF state is: $t_{\text{ON} \rightarrow \text{OFF}} = 9.8 \mu\text{sec} \pm 1.2 \mu\text{sec}$. This time corresponds to the

effective carrier recombination lifetime in the silicon switch. It is essential to note that $t_{\text{OFF} \rightarrow \text{ON}}$ and $t_{\text{ON} \rightarrow \text{OFF}}$ are computed from the time constant of the fitted data.

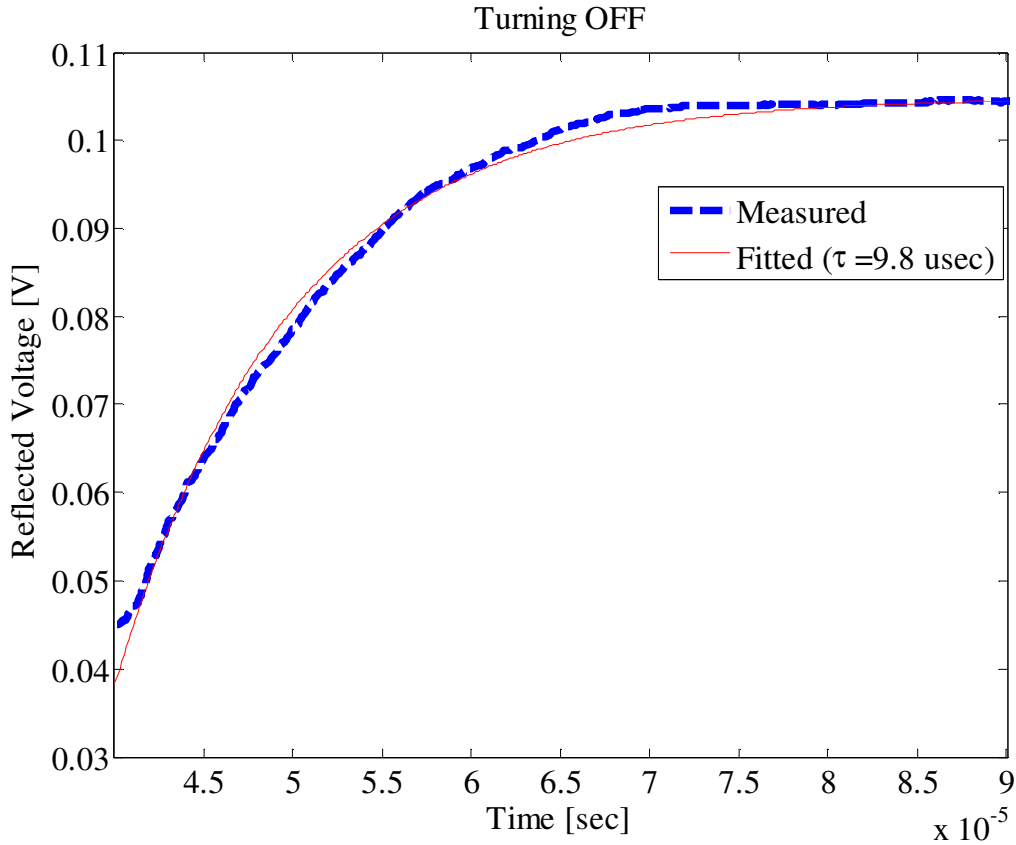


Figure 7.14 The turning OFF of the switch integrated with the optically switched transmission line

7.5 The turning ON and OFF for an Optically Pumped Reconfigurable Antenna System (OPRAS)

In this section the turning ON and OFF of the OPRAS is studied. The experiment is performed on a frequency reconfigurable antenna structure. The computation of this time is important especially if the OPRAS is going to be integrated in a very dynamic environment where fast antenna reconfiguration is required. The antenna structure is

detailed first then the experiment setup is discussed. Analysis of the measurement data is presented as well.

7.5.1 Antenna Structure:

The proposed antenna structure consists of a full ground probe fed patch. The patch is composed of two sections. The outer section has a rectangular shape with dimensions of 4 cm x 3cm. A rectangular slot of dimensions 2.8 cm x 0.8 cm separates the outer section from an inner E-shaped section as shown in Fig. 7.15. The antenna patch and the E-shaped patch are connected via a silicon switch.

The antenna structure is printed on Rogers Duroid 5880 substrate, with a dielectric constant of 2.2 and a height of 1.6 mm. The dimension of the substrate is 5 cm x 4.5 cm. On the back of the antenna, a metal piece is mounted to the antenna ground for fixing the laser diode and providing the necessary thermal radiation sink as a safety measure. The light from the laser diode is coupled to the switch via a 1mm hole drilled through the antenna substrate. The photoconductive switch used in this work is n-type silicon (Si) with an initial carrier concentration of 10^{15} cm^{-3} . It is 1mm x 1mm in area.

The antenna structure and its corresponding dimensions are shown in Fig. 7.15. The fabricated prototype is shown in Fig. 7.16. A voltage of 1.9 V and a current of 87 mA are sufficient to drive the laser diode to produce an output laser power of 50mW. This power level is sufficient to make the silicon switch transition from the OFF state to the ON state and this transition is manifested by the increase in the silicon total conductivity (DC+RF) [129].

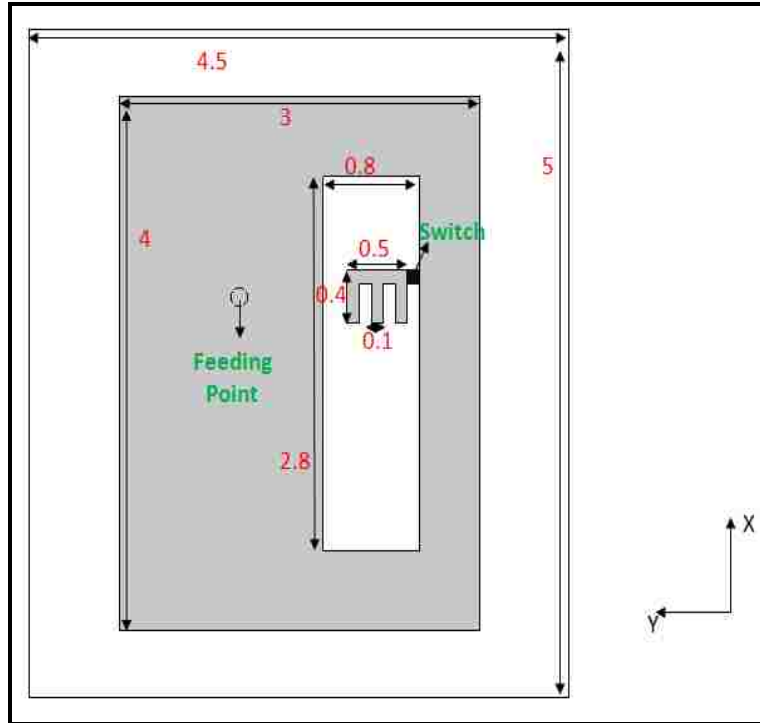
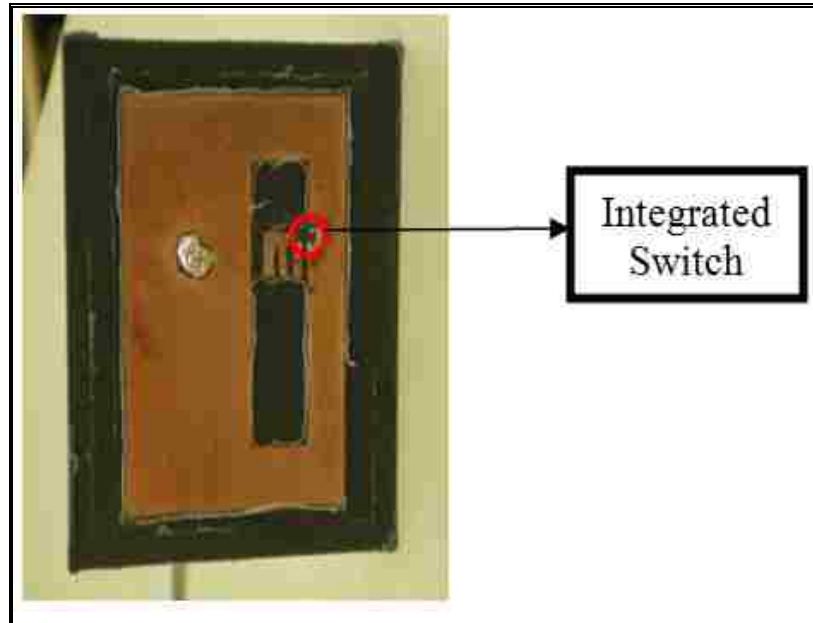
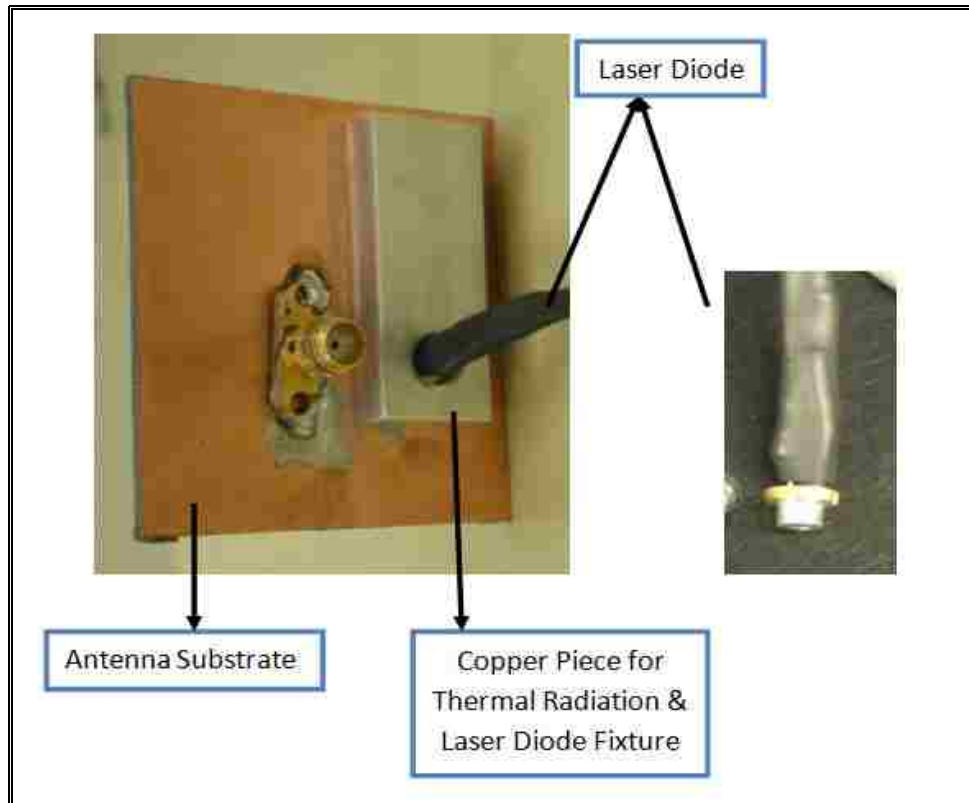


Figure 7.15 The antenna structure for the switching speed experiment



(a)



(b)

Figure 7.16 The fabricated antenna structure (a) top layer (b) bottom layer

When the laser diode is OFF, only the slotted rectangular patch section is fed; this produces a resonance at 2.21 GHz. By driving the laser diode with a current of 87 mA, an optical power of 50 mW is generated. This optical power has the effect of changing the physical parameters of the silicon switch. This enables the surface currents to pass into the E-shaped patch section. The antenna structure now resonates at 2.17 GHz. The measured return loss for the two switch configurations is shown in Fig. 7.17. A comparison between the simulated and the measured antenna return loss for the case when the switch is OFF and ON is shown in Fig. 7.18(a) and Fig. 7.18(b).

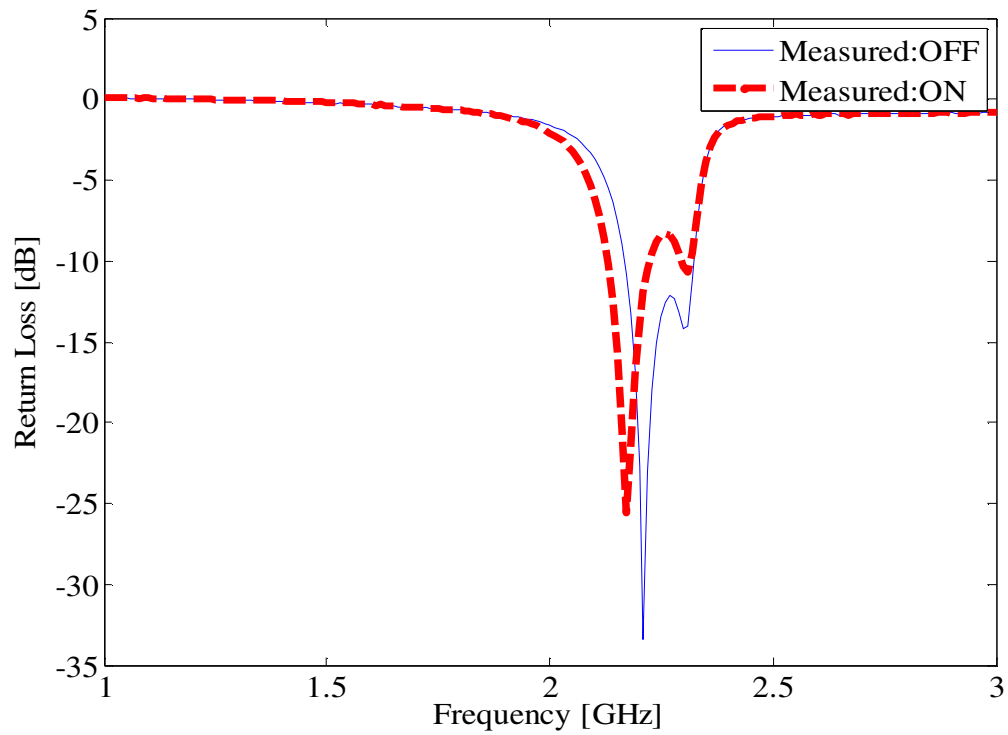
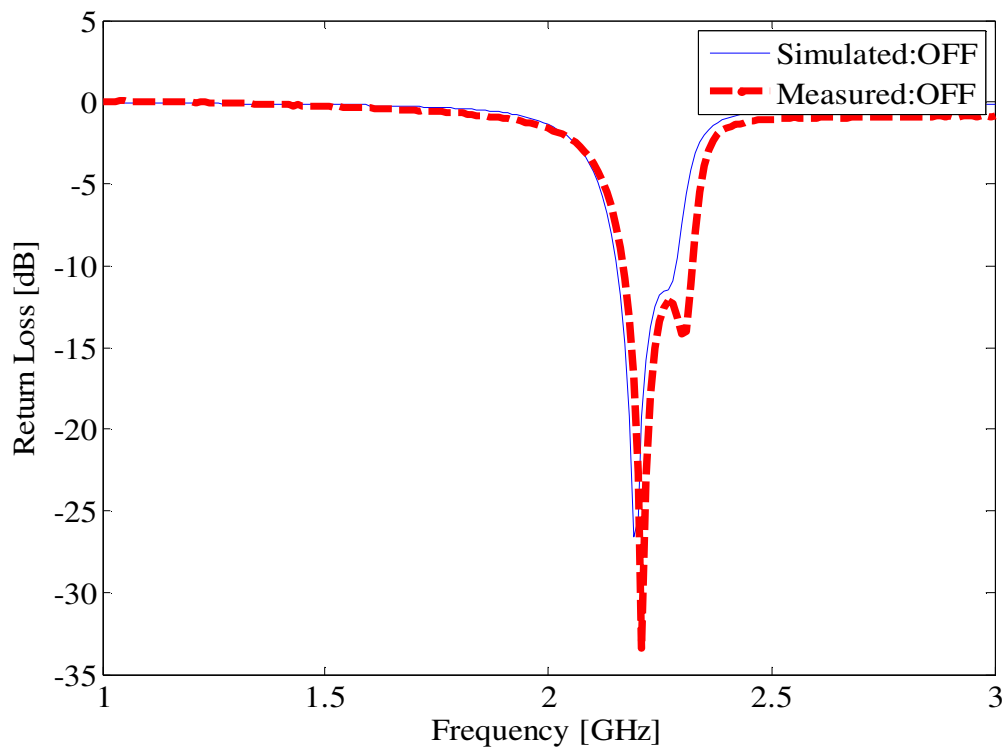


Figure 7.17 The measured tuning in the antenna return loss



(a)

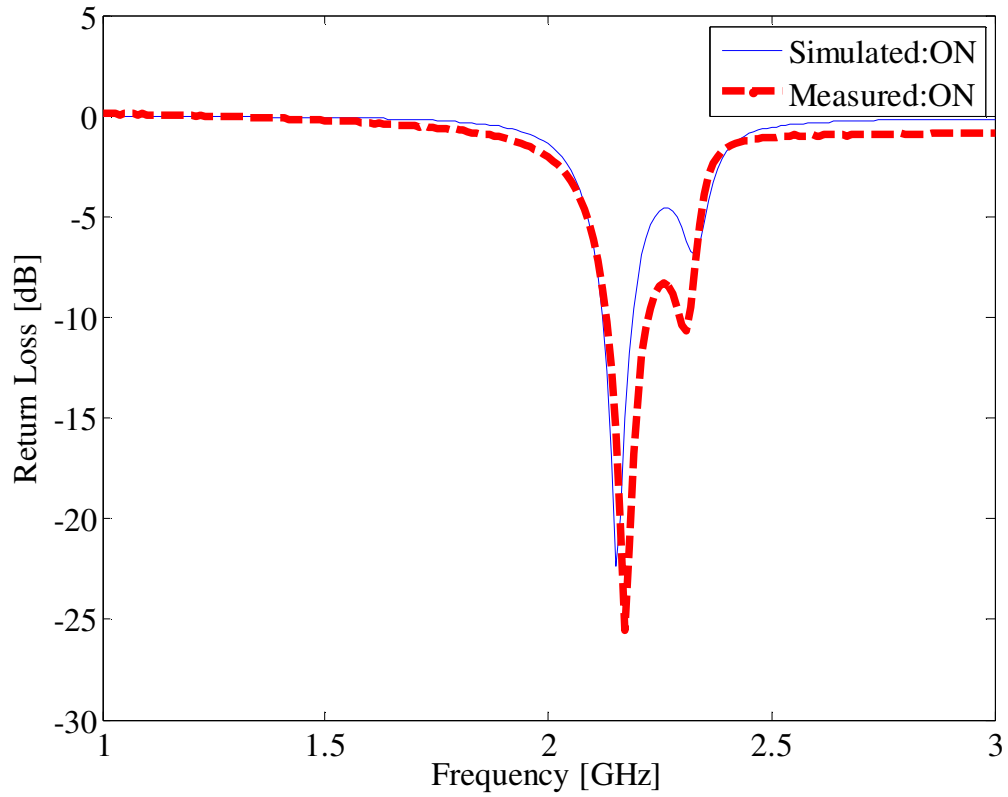


Figure 7.18 The comparison between the simulated and the measured antenna return loss (a) switch OFF
(b) switch ON

The normalized antenna radiation pattern when the switch is OFF at $f=2.21$ GHz (solid line) and when the switch is ON at $f=2.17$ GHz is shown in Fig. 7.19 for the XZ plane. It is observed that the antenna preserves its omnidirectional radiation property.

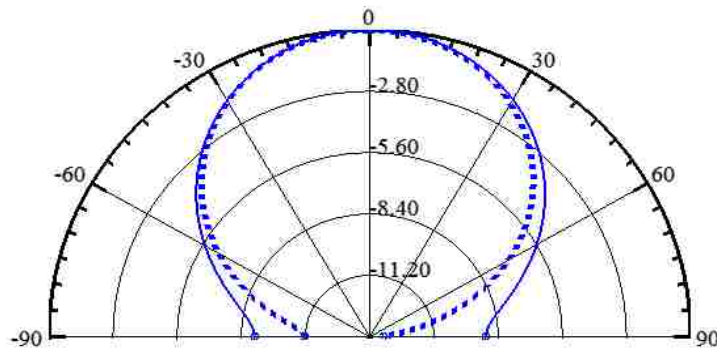


Figure 7.19 The normalized antenna radiation pattern in the XZ plane when the switch is OFF (solid line, $f=2.21$ GHz) and ON (dotted line, $f=2.17$ GHz).

7.5.2 Experimental Setup:

The first step in the experiment is to drive continuously the laser diode via a current driver. A frequency generator is used to generate a CW signal at 2.21 GHz. The RF output of the frequency sweeper is connected to a horn antenna that is placed in the far field region of the reconfigurable antenna structure shown in the previous subsection. Two different measurements are taken:

Measurement 1: The received voltage by the reconfigurable antenna when the switch is OFF.

Measurement 2: The received voltage by the reconfigurable antenna when the switch is ON.

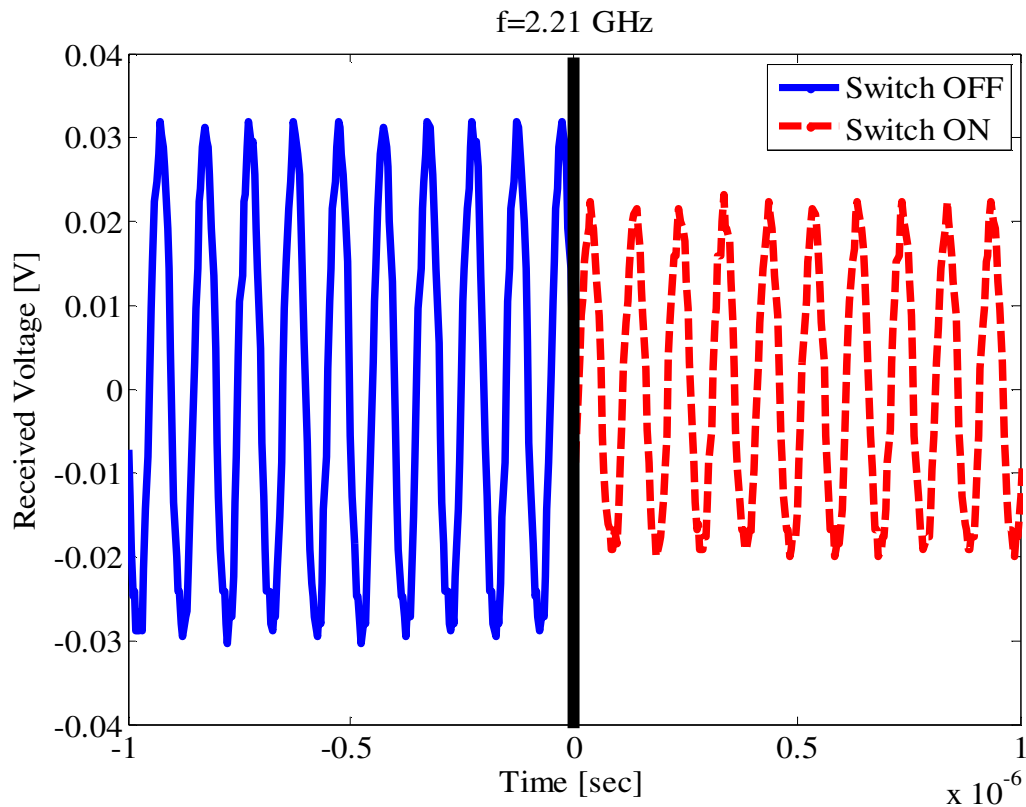


Figure 7.20 The change in the received voltage by the reconfigurable antenna at $f=2.21$ GHz

When the switch is OFF, the antenna resonates at 2.21 GHz. Therefore; when turning ON the laser diode by driving it continuously via 87 mA, the antenna no longer resonates at 2.21 GHz and the received voltage by the antenna should drop. The change in the antenna received voltage at $f=2.21$ GHz is shown in Fig. 7.20. A drop in the received voltage is obtained by turning the switch from OFF to ON state. Fig. 7.21 shows also the change in the received voltage when the horn antenna is tuned to operate at $f=2.17$ GHz. In this case, an increase in the received voltage is obtained by turning the silicon switch from OFF to ON state. It is essential to note that in these plots we are just looking for the change in the received voltage by the reconfigurable antenna. The switching time can't be quantified since the laser diode is either continuously OFF or ON.

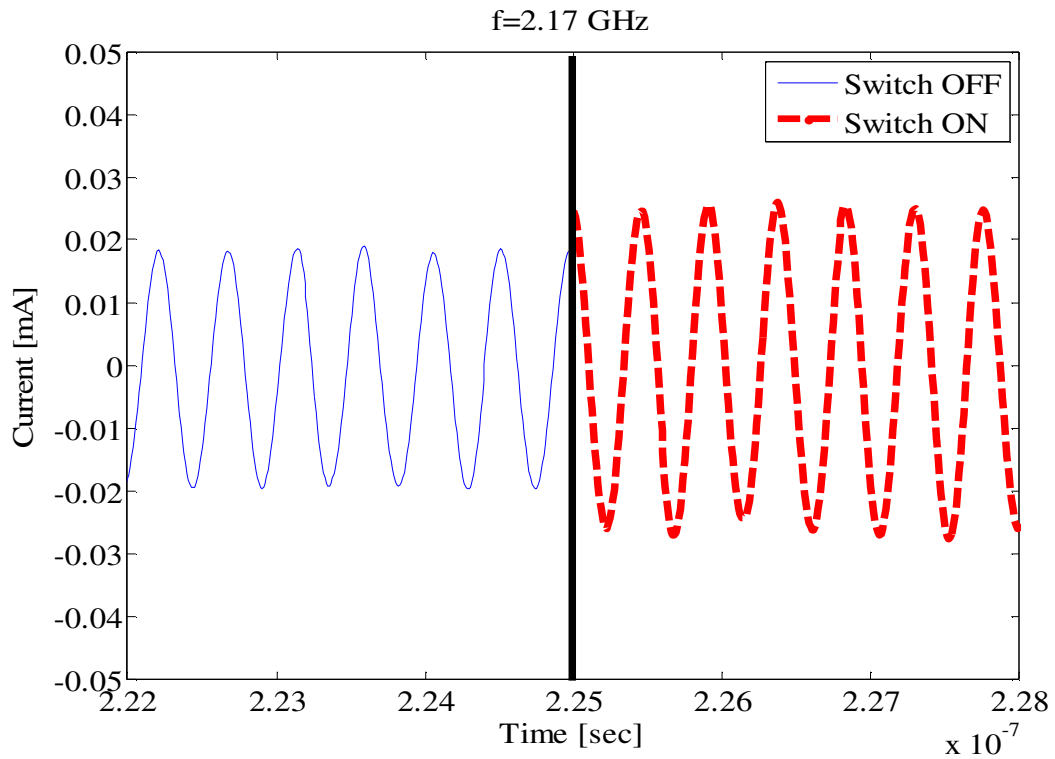


Figure 7.21 The change in the antenna received voltage when the horn antenna is transmitting at $f=2.17$

GHz

The next step is to drive the laser diode by a pulse with a given duration. A horn antenna is placed in the far field region of the reconfigurable antenna and is connected to a frequency sweeper that generates a continuous wave (CW) signal at 2.21 GHz which corresponds to the operating frequency of the reconfigurable antenna when the switch is OFF. Similar to the optically switched transmission line experiment shown in the previous section, an oscilloscope is used to capture the change in the received voltage by the reconfigurable antenna. In order to increase the time window t_{window} of the oscilloscope, the frequency component of the received voltage by the reconfigurable antenna should be lowered so that sampling can be performed at a lowest frequency. The received voltage signal which has a frequency component $f_c = 2.21GHz$ is mixed with another RF signal that has a frequency component $f_{LO} = 2.2GHz$. The output of the mixer consists of the following frequency components: $f_c, f_{LO}, f_c - f_{LO} = 10MHz, f_c + f_{LO} = 4.41GHz$, and many more products due to the nonlinear behavior of the mixer [130]. The output of the mixer is connected to a 400MHz low pass filter (LPF) to filter all the high frequency components. The output of the LPF consists only of: $f_c - f_{LO} = 10MHz$. Now, this output is fed to the oscilloscope that is connected to a computer via a GPIB cable. The sampling rate of the oscilloscope is chosen to be 250 Msamples/sec which provides a time window $t_{window} = 120\mu sec$. The data captured by the oscilloscope is sent to the computer by using LABVIEW. In order to exactly capture the OFF-ON and the ON-OFF transitions of the reconfigurable antenna, the oscilloscope is triggered from the pulse generator by an external output signal that is synchronized with the pulse generated to drive the laser

diode. The flowchart of the whole experiment process is summarized in Fig. 7.22. The experiment setup is shown in Fig. 7.23.

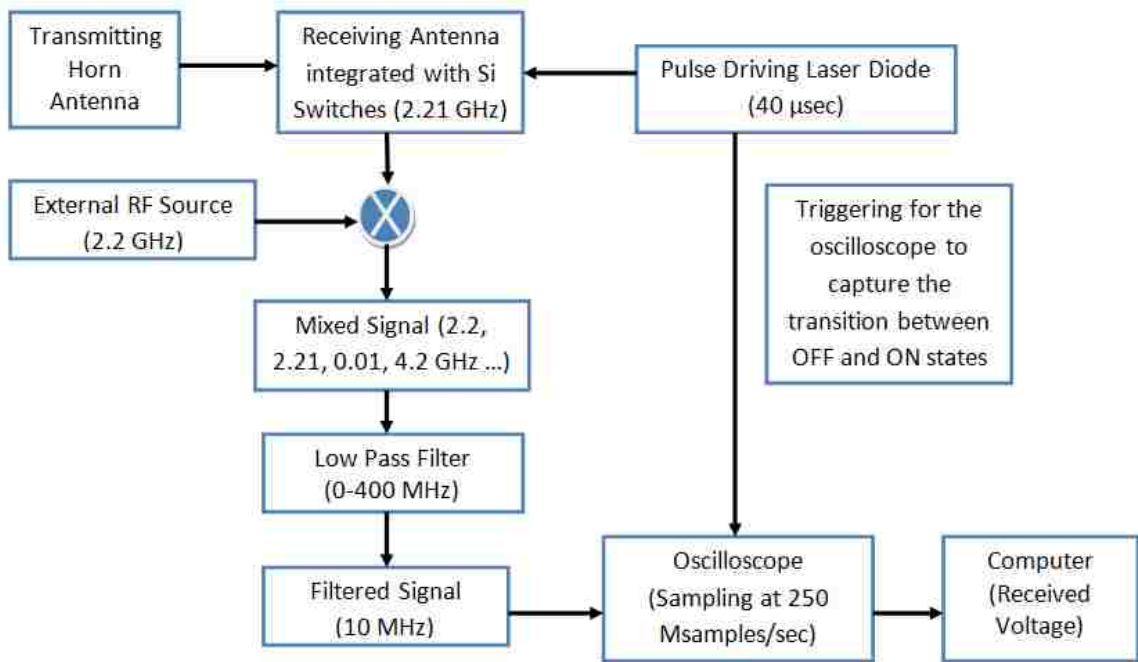


Figure 7.22 The flowchart to compute the turning ON and OFF of the OPRAS

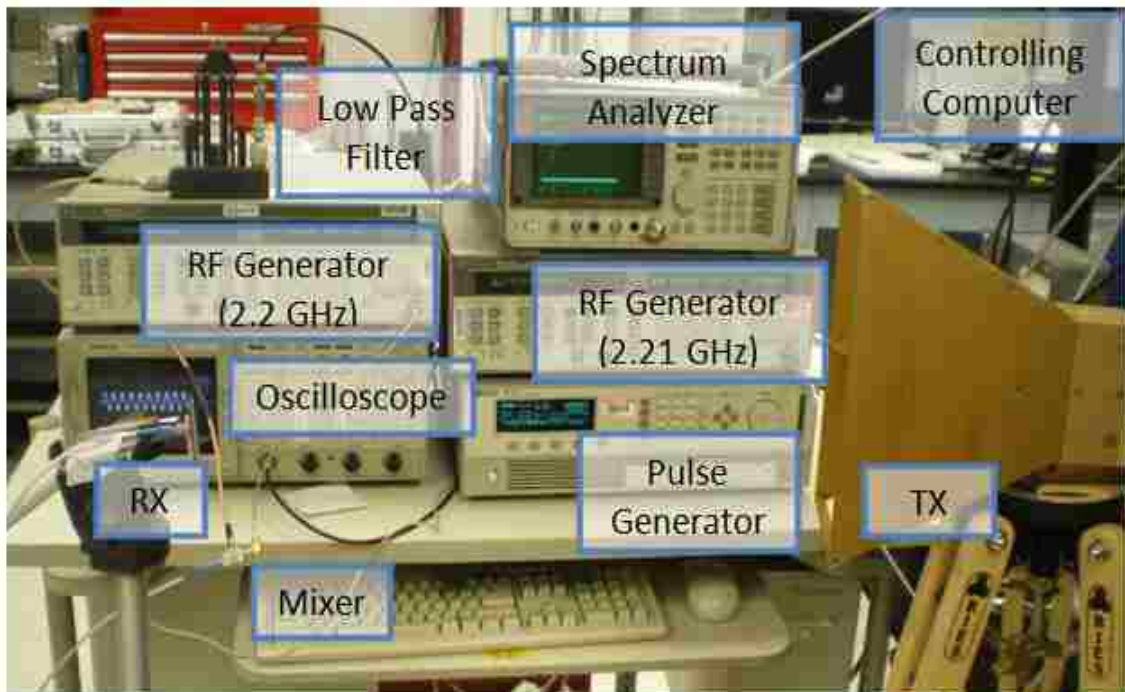


Figure 7.23 The experiment setup for the switching speed of the OPRAS

The spectrum of the output of the mixer is shown in Fig. 7.24; as expected it contains the fundamentals and the 10 MHz frequency components. The spectrum of the filtered signal is plotted in Fig. 7.25 where only the 10 MHz frequency component remains.

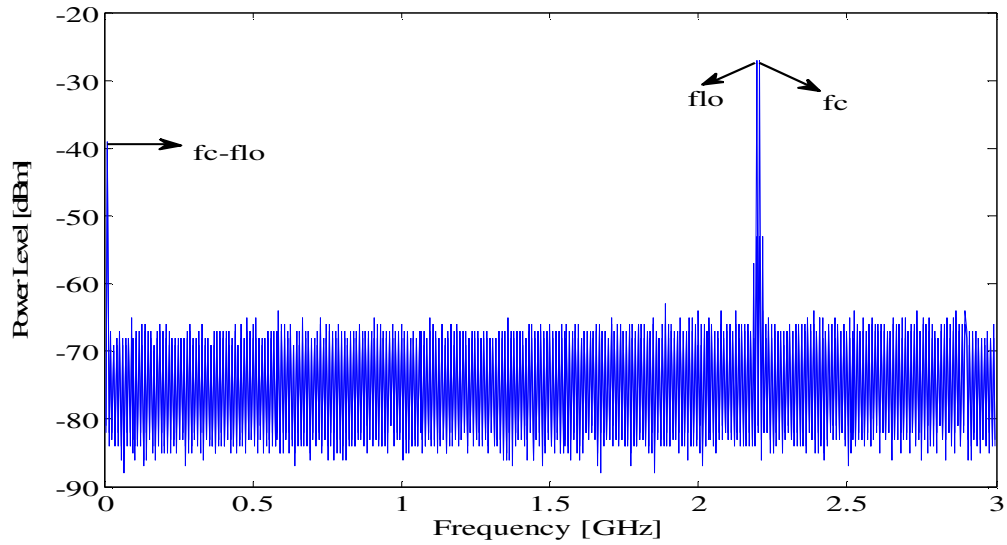


Figure 7.24 The spectrum of the output of the mixer

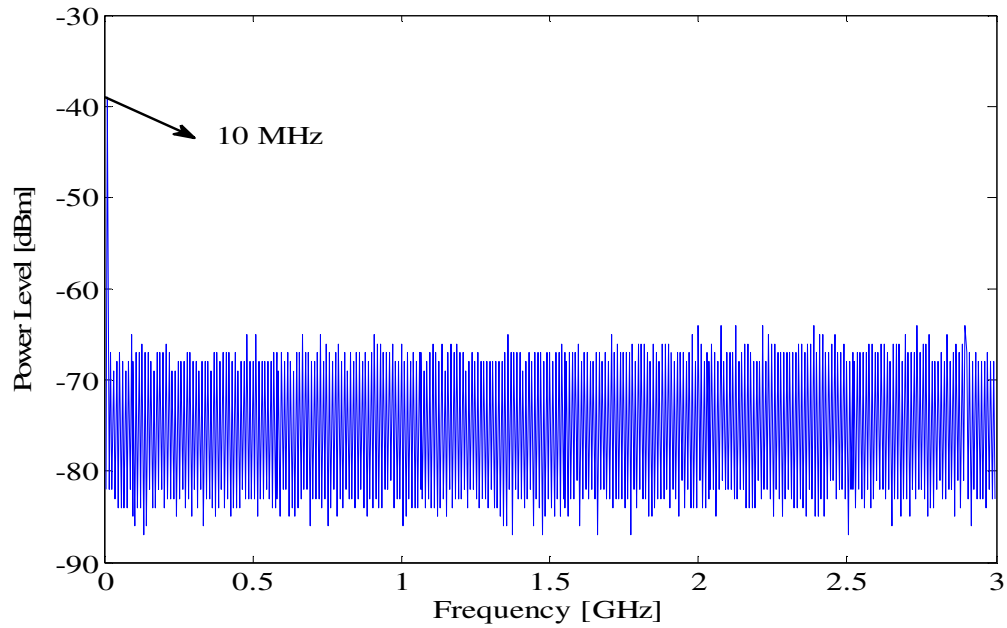


Figure 7.25 The spectrum of the output of the low pass filter

The change in the received voltage is shown in Fig. 7.26. From this plot, one can compute the required time needed for the reconfigurable antenna to switch between the two frequencies. The time window for the data acquired by the oscilloscope is 120 μsec , and the oscilloscope is set to acquire data for the duration of 30 μsec before the triggering (laser diode turns ON) happens.

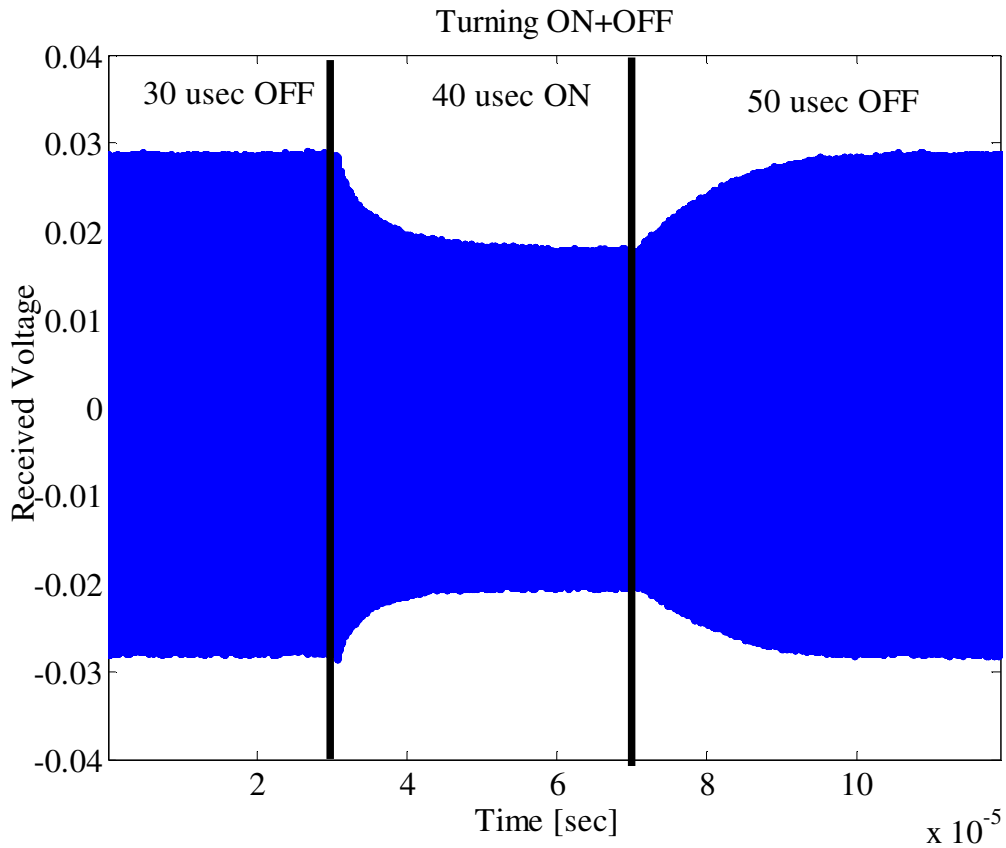


Figure 7.26 The change in the antenna received voltage at $f=2.21$ GHz

To determine the time needed for the reconfigurable antenna to tune from $f=2.21$ GHz to $f=2.17$ GHz ($t_{\text{OFF} \rightarrow \text{ON}}$), a curve fitting is done on the envelope of the received voltage for the duration of 40 μsec . From the plot shown in Fig. 7.27 one can compute

that the time needed for the reconfigurable antenna to tune its operating frequency is: $t_{\text{OFF} \rightarrow \text{ON}} = 4.07 \mu\text{sec} \pm 0.9 \mu\text{sec}$. The R^2 for the fitted data is 0.9905.

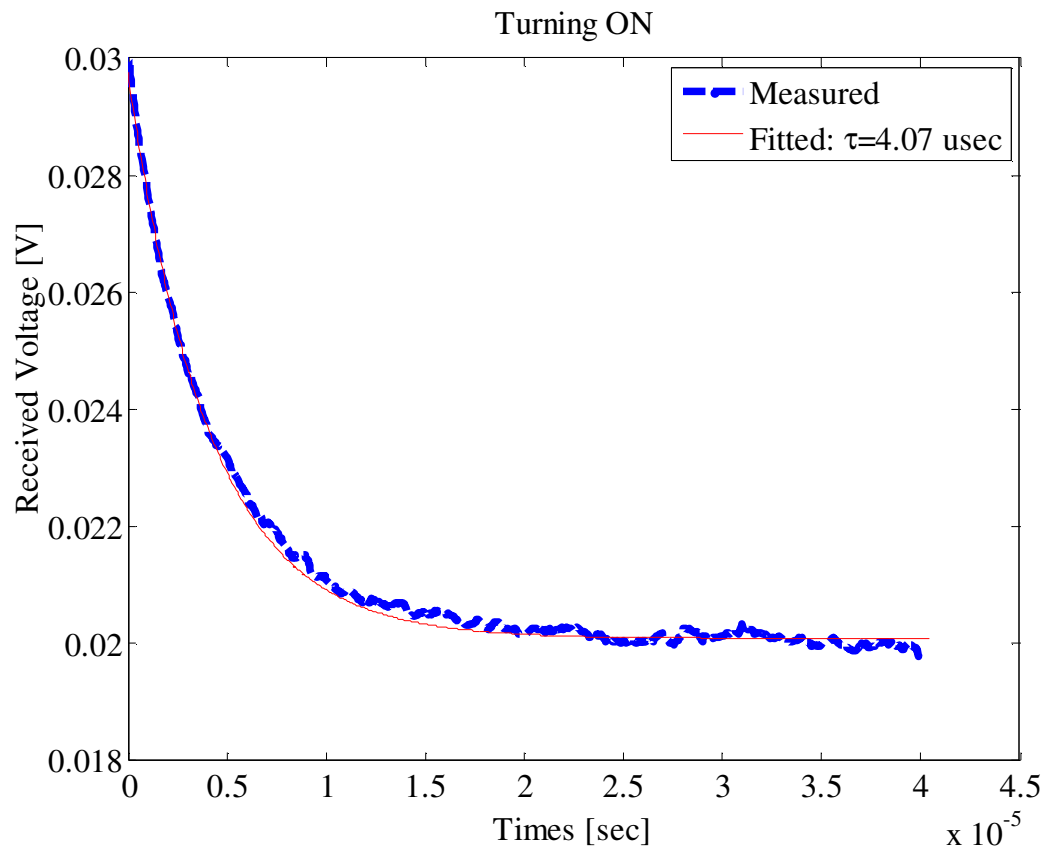


Figure 7.27 The change in the received voltage by the reconfigurable antenna when tuning from 2.21 GHz to 2.17 GHz

The same procedure is repeated to determine the time needed for the reconfigurable antenna to tune from $f=2.17$ GHz (Switch ON) to $f=2.21$ GHz (Switch OFF). The change in the envelope of the received voltage by the reconfigurable antenna and the corresponding fitted curve are shown in Fig. 7.28. From the fitted data, one can compute that $t_{\text{ON} \rightarrow \text{OFF}}$ is $8.4 \mu\text{sec} \pm 1.1 \mu\text{sec}$. The R^2 for the fitted data is 0.9934.

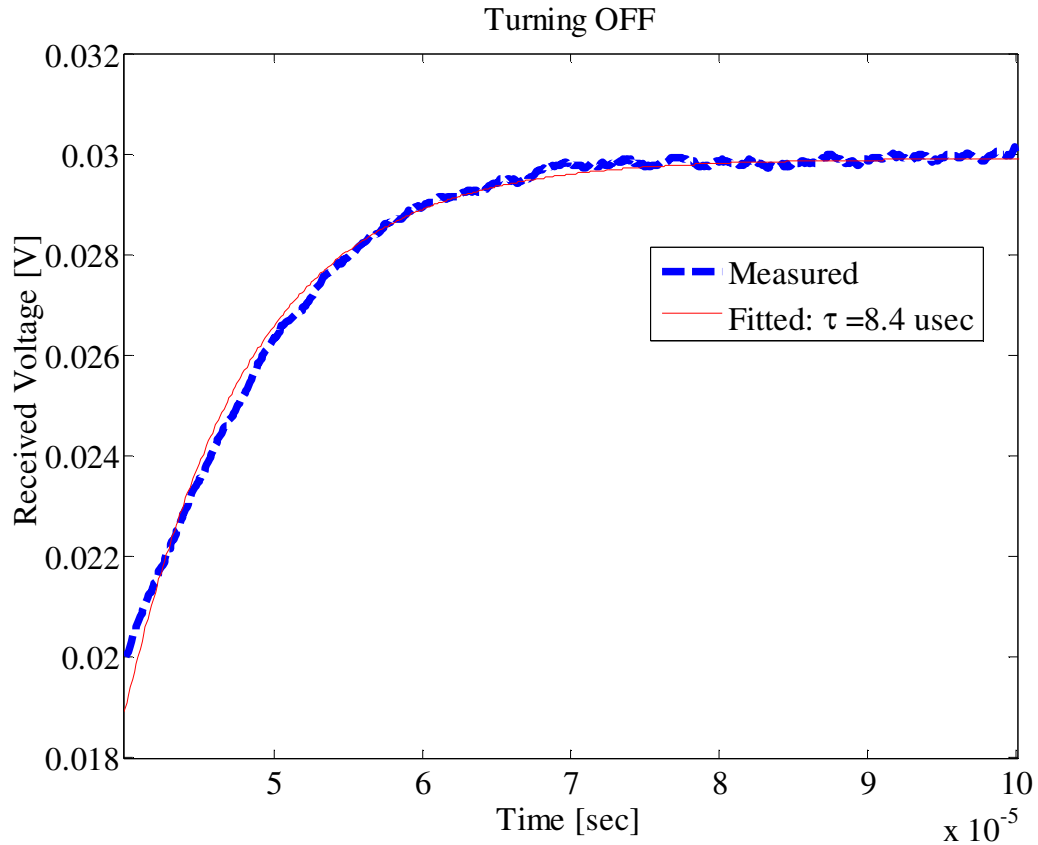


Figure 7.28 The change in the received voltage by the reconfigurable antenna when tuning from 2.17 GHz to 2.21 GHz

The comparison between the time needed for the reconfigurable antenna and the optically switched transmission line to turn ON/OFF is summarized in Table 7.1. It is noticed that the time required for the reconfigurable antenna to tune its frequency (2.21 GHz → 2.17 GHz) when turning the switch ON is almost equal to the time needed for the electrons to go from the valence band to the conduction band ($t_{OFF \rightarrow ON}$ of the transmission line). This time is called the effective carrier generation lifetime in the photoconductive switch.

As for the turning OFF ($t_{ON \rightarrow OFF}$) of the OPRAS, it is found that a shorter time is needed as compared to the transmission line. This is due to the fact that the antenna tunes

its operating frequency from 2.17 GHz (switch ON) to 2.21 GHz (switch OFF) before the switch completely turns OFF. In OPRAS, $t_{ON \rightarrow OFF}$ should be equal or less than the effective carrier recombination lifetime of the switch.

An antenna needs full switch connection before it changes its function which explains that the time to switch ON the optically reconfigurable antenna structure is the same as the transmission line. However, as soon as the switch starts changing its property to non-conductive the antenna tunes its frequency back to its original state. The antenna doesn't need the disconnection to be complete to tune the frequency. This is due to the capacitive effect and the capacitance existing between the two terminals of the antenna being reconfigured. This capacitive effect highly influences the antenna return loss.

Table 7.1 The switching time for the optically driven transmission line and the OPRAS

	<i>Transmission Line</i>	<i>OPRAS</i>
OFF → ON (μsec)	3.935	4.07
ON → OFF (μsec)	9.8	8.4

Also from both experiments (transmission line/reconfigurable antenna), one can notice that deactivating the switch (turn OFF) takes longer than turning it ON. When the electrons are excited from the valence to the conduction band (turning ON), the transition time depends upon the activation energy of the incoming photons. This should be higher than the bandgap of the silicon switch. For ON → OFF transition, the electrons have to stay in the conduction band until they expand their energy and decay back to the valence. In materials such as silicon, which have indirect band-gaps, the minima of the conduction

band and the maxima of the valence band are not aligned in k-space. The conduction band minimum energy and the valence band maximum energy doesn't correspond to the same value of the wavenumber k. Conduction electrons thus have to lose energy and momentum through multiple phonon interactions, which is a longer process.

7.6 Delay Measurement

In this section, the delays induced by the cables and the equipments are computed. For both experiments (transmission line/reconfigurable antenna), the same length of cables is used to connect the different components of the experiment. Fig. 7.29 shows the flowchart of the setup used to compute the delay in the cables. A 10 MHz signal is modulated via a 1 KHz square pulse then fed to the cables. The output from the cable is connected to an oscilloscope. It is found that the delay is ≈ 19.9 nsec.

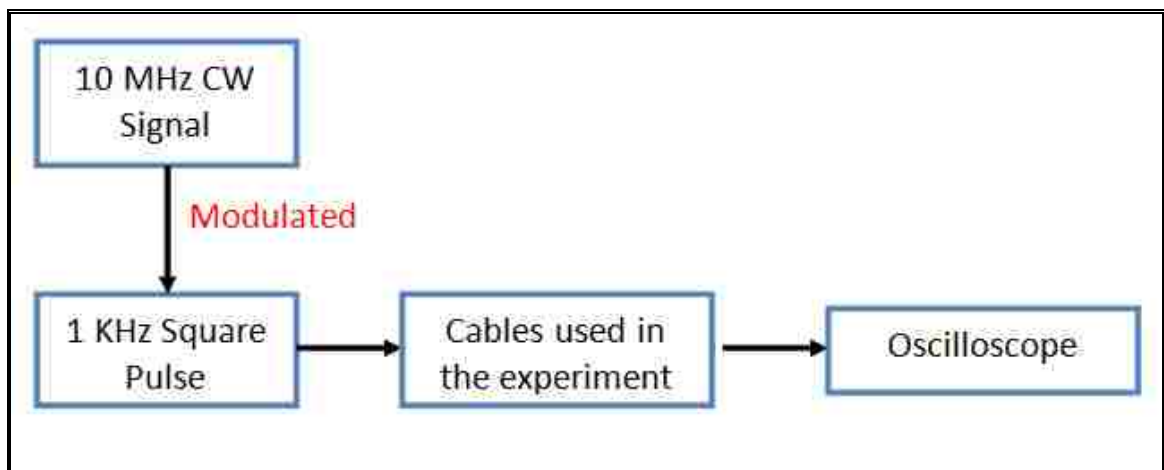


Figure 7.29 The flowchart to compute the delay in the cables used in the experiment

Fig. 7.30 shows the flowchart of the experiment used to measure the delay in the cables and the equipments used in both experiments. It is found that the same delay is

produced (≈ 19.9 nsec). This delay is negligible compared to the computed switching speed which is in the μ sec range.

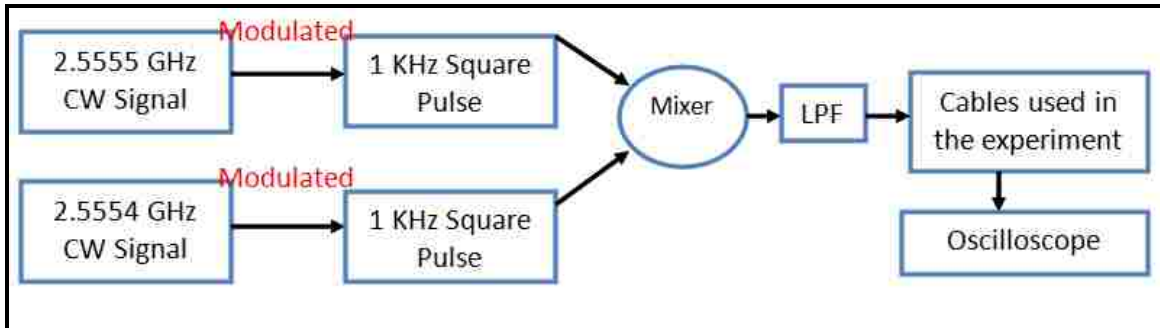


Figure 7.30 The flowchart to compute the delay in the cables and the equipments used in the experiment

7.7 Conclusion

In this chapter, a discussion about the carrier lifetime in semiconductor materials is presented. A new RF technique to measure this lifetime is proposed using an optically switched transmission line. The importance of this technique is that it can be extended to measure the carrier lifetime for various types of semiconductor materials. The switching speed of an optically pumped reconfigurable antenna system is demonstrated and the results are analyzed.

In the next chapter, a rotatable reconfigurable antenna designs are discussed. Designs for cognitive radio communication are demonstrated. Similar to the photoconductive switches, reconfigurable antennas based on the rotation of the radiating structure does not require the use of bias lines.

Chapter 8

Software Controlled Rotatable Reconfigurable Antenna System

8.1 Introduction

In this chapter, a new technique is proposed to produce a frequency reconfigurable antenna design without the use of switches. The frequency tuning is achieved via a rotational motion of an antenna part. The importance of this technique lies in the fact that it does not require biasing networks or laser diode as with the designs discussed previously. However, a stepper motor is required to perform the desired rotation. Frequency reconfigurable antenna designs based on this new technique are presented for cognitive radio applications. The use of cellular automata and neural network are also detailed.

8.2 Frequency Reconfigurable Rotatable Microstrip Antenna Design

In this section, a new reconfigurable antenna design is investigated. The antenna patch has a circular form that rotates to feed different shapes. Frequency reconfigurability is achieved while maintaining the same omni-directional radiation pattern in both the E and H-planes. Four different rotations can be done making the antenna cover five different bands (from 2 GHz up to 7 GHz) correspondingly.

The concept of the antenna structure is shown in Fig. 8.1. It consists of two layers. The bottom layer is a partial ground to allow radiation above and below the substrate. The top layer is a rotating circular section composed of four different patches. The chosen

substrate is Taconic TLY with a dielectric constant of 2.2 and a thickness of 1.6 mm [131]. The different dimensions for the four RF shapes that constitute the antenna radiating elements are shown in Fig. 8.2.

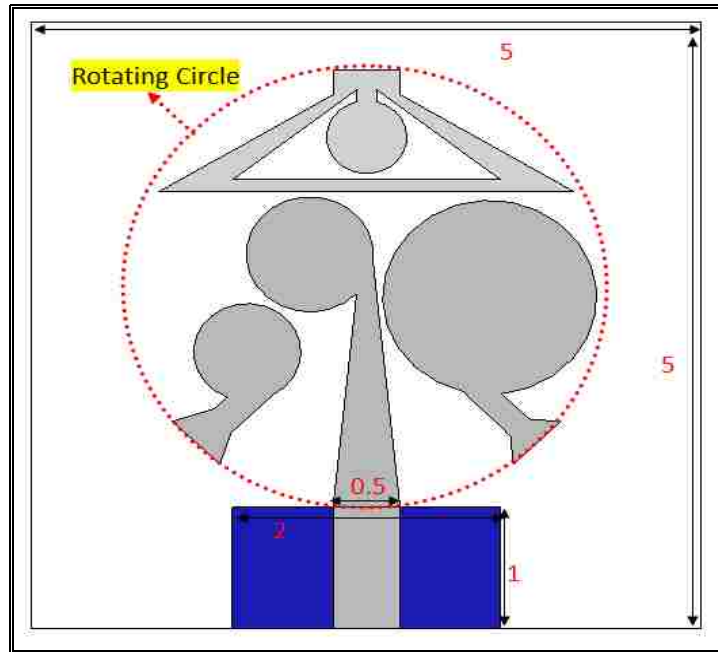


Figure 8.1 Rotatable Reconfigurable Antenna Structure

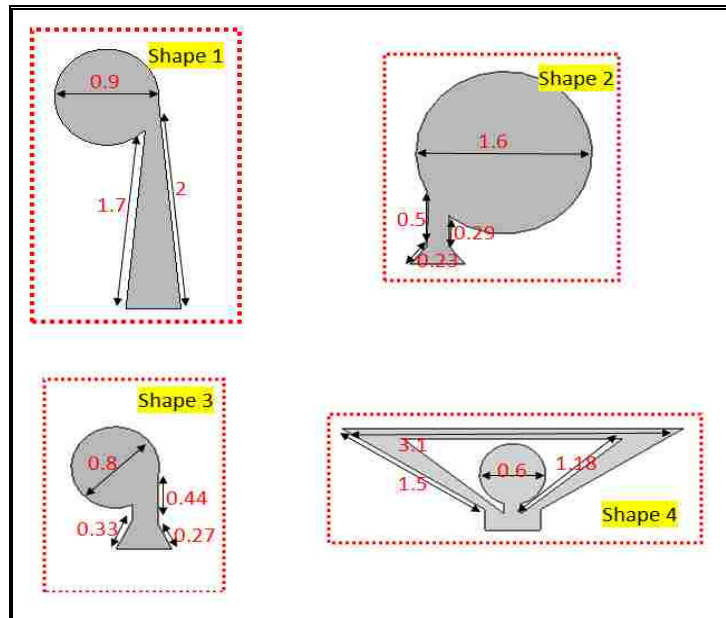


Figure 8.2 The dimensions for the different shapes of the reconfigurable antenna structure

The rotating circular part includes four different patches as shown in Fig. 8.2. It has a radius of 1.8 cm. It consists of three circular patches and one slotted triangle. With every rotation, a different antenna shape is fed. If the antenna position shown in Fig. 8.1 is taken as a reference, then we can rotate either clockwise or counterclockwise by 45° to feed one of the two remaining circles. A rotation of 180° is needed to feed the slotted triangle. The process of rotation and the fabricated antenna prototype is summarized in Fig. 8.3. The dimensions for the different parts are optimized using HFSS v11 to operate at the corresponding resonant frequency.

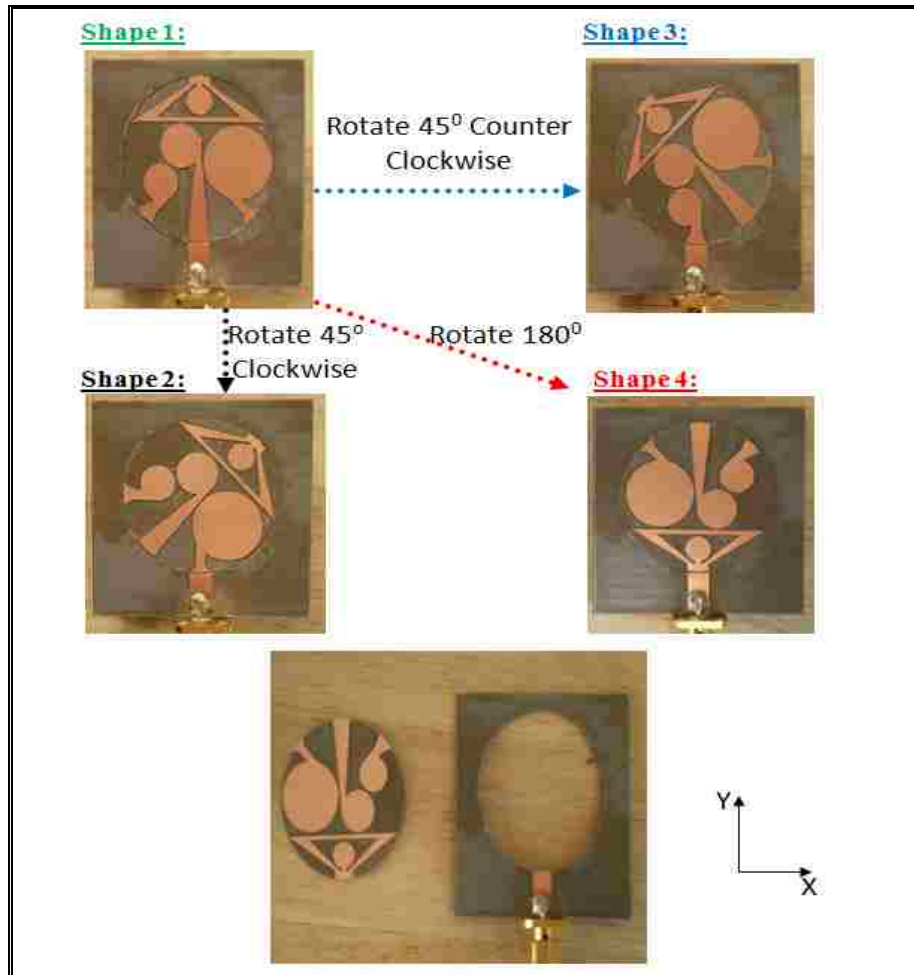


Figure 8.3 The fabricated antenna prototype

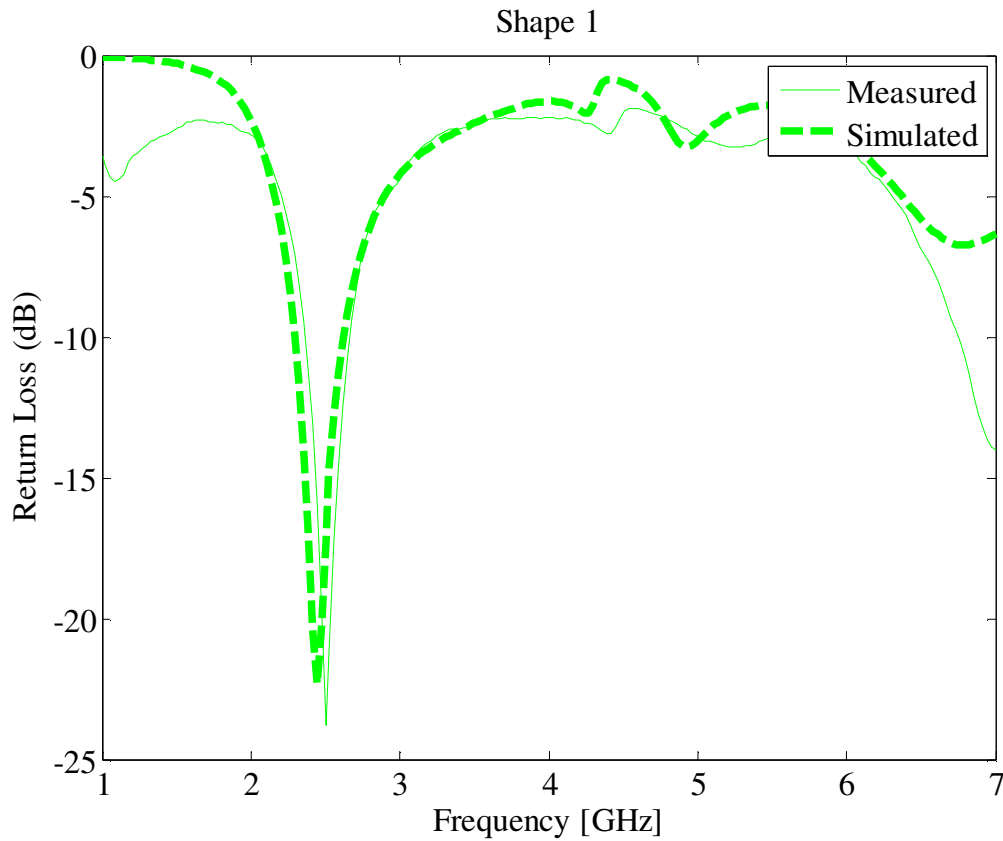
The comparison between the simulated and the measured return loss for each rotation are shown in Fig. 8.4. By comparing the different plots, one can easily notice the frequency tuning:

For shape 1: the band 2.3 GHz-2.6 GHz is covered. (Fig. 8.4(a))

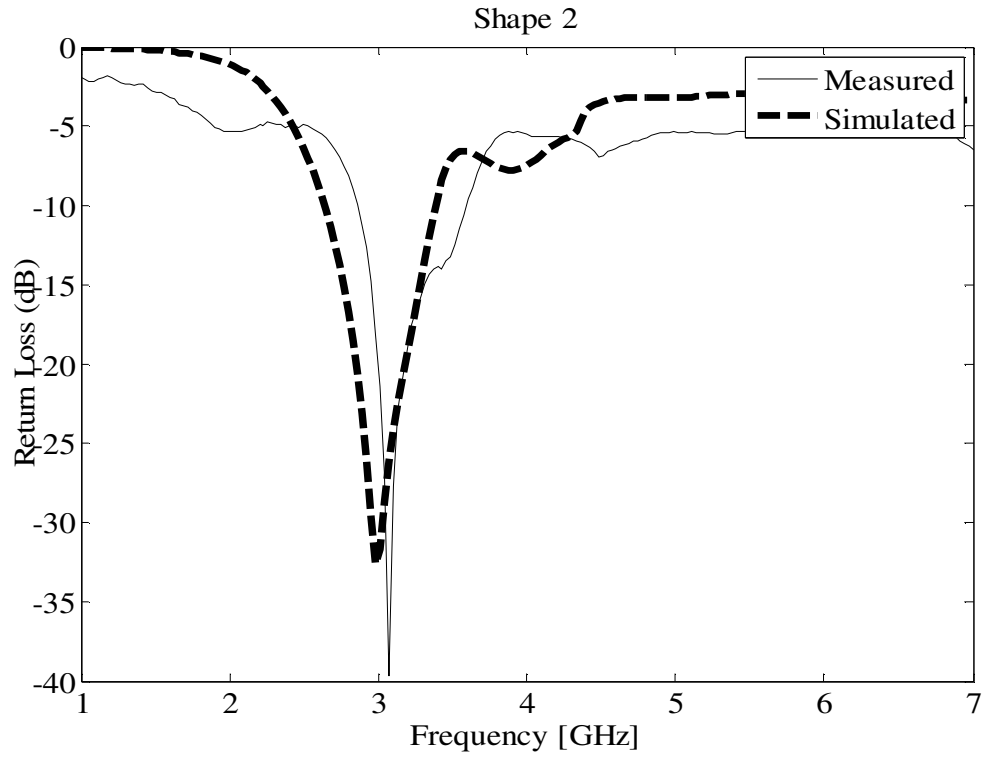
For shape 2: the band 2.6 GHz-3.4 GHz is covered. (Fig. 8.4(b))

For shape 3: the band 4 GHz-5 GHz is covered. (Fig. 8.4(c))

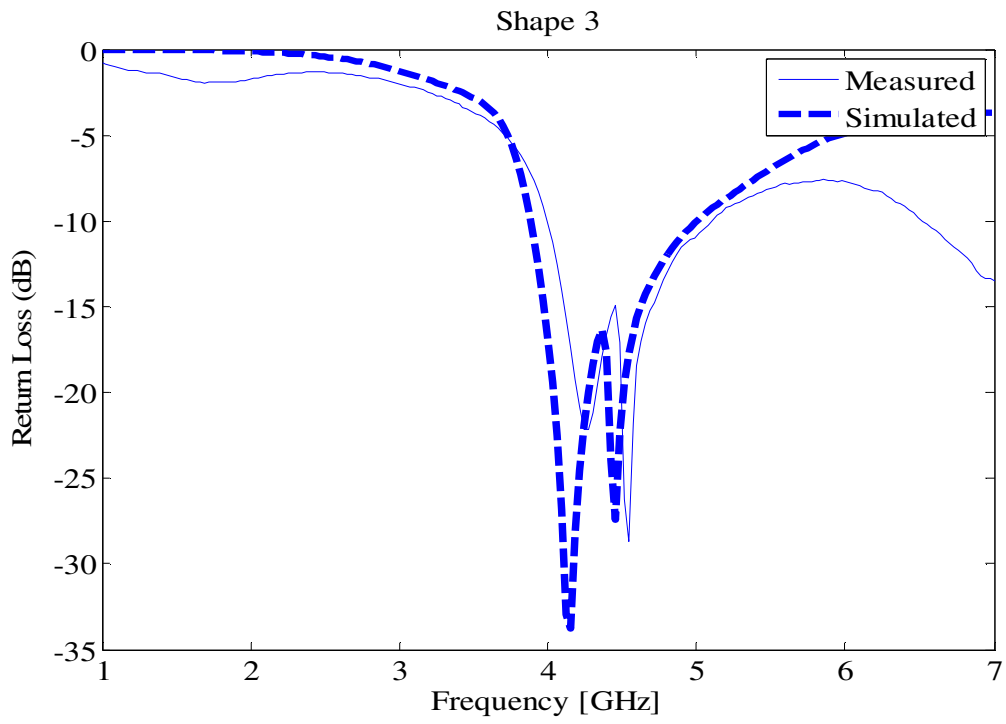
For shape 4: the bands 3 GHz-4 GHz / 5.26 GHz- 7 GHz are covered. (Fig. 8.4(d))



(a)



(b)



(c)

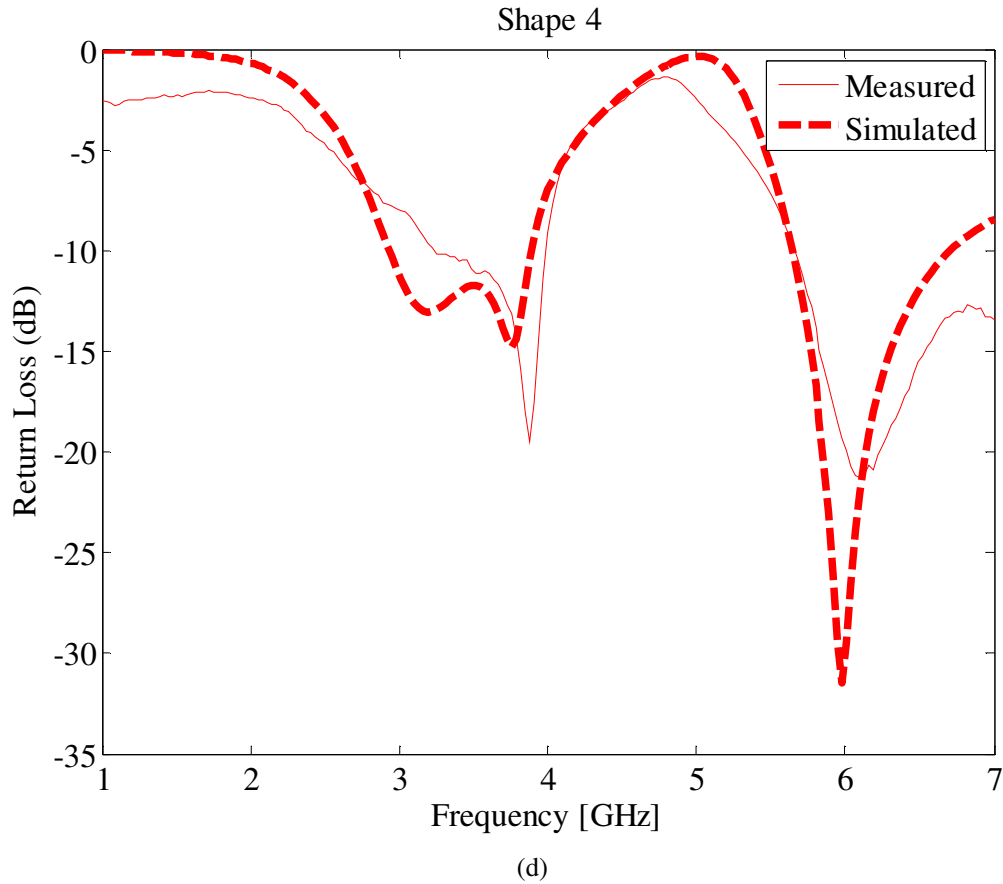


Figure 8.4 The comparison between the simulated and the measured return loss for the reconfigurable antenna structure

The antenna radiation pattern at $\phi=0^\circ$ (xz plane) for the different configurations is shown in Fig. 8.5. The antenna preserves its omnidirectional pattern while changing its resonant frequency; a property that is essential for current wireless applications especially for cognitive radio systems. The antenna gain at $\phi=0^\circ$ and for $0^\circ \leq \theta \leq 360^\circ$ is summarized in Fig. 8.6 for $f = \{2.44 \text{ GHz (shape 1), 3 GHz (shape 2), 4 GHz (shape 3), 6 GHz (shape 4)}\}$. The antenna peak gain values are summarized in Table 8.1 for the different configurations at the same resonant frequencies of Fig. 8.6.

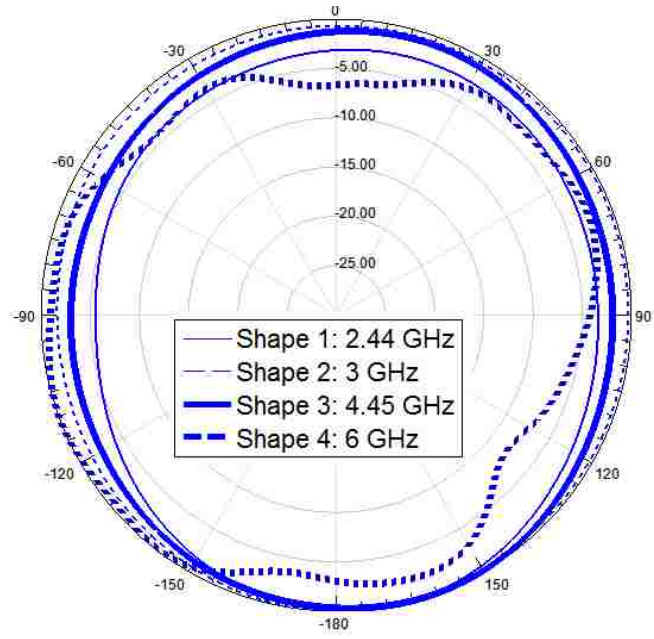


Figure 8.5 The antenna radiation pattern in the xz plane

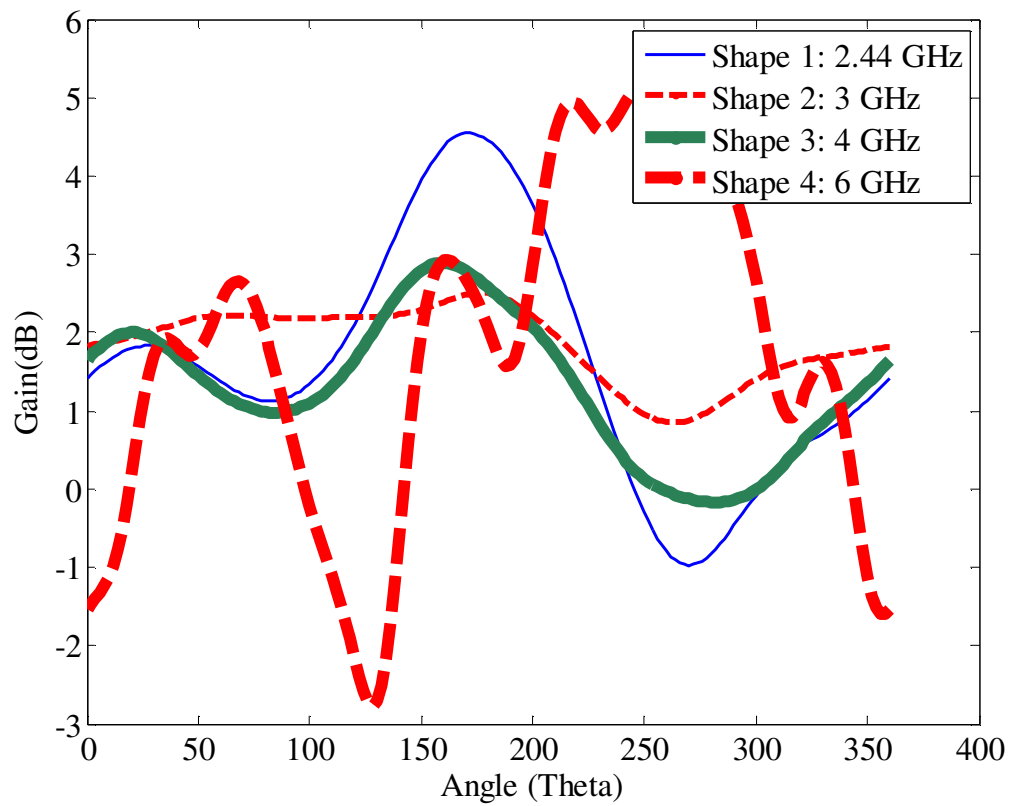


Figure 8.6 The antenna gain for the rotatable reconfigurable antenna design

Table 8.1 The antenna peak gain values

	<i>Shape 1</i>	<i>Shape 2</i>	<i>Shape 3</i>	<i>Shape 4</i>
Frequency [GHz]	2.44	3	4	6
Gain [dB]	4.57	3.12	2.72	5.9

8.3 A Cellular Automata Reconfigurable Microstrip Antenna Design

In this section, a reconfigurable patch antenna is designed by using cellular automata theory and a slot rotation of certain parts of a microstrip antenna. Different slot configurations are applied and hence different resonant frequencies are obtained. The transition between stages is done via a rotation leading to the replacement of the typical way of implementing reconfigurable antennas by using PIN diodes, transistors or RF-MEMs switches [132-133].

Cellular automata can be defined as a mathematical finite state machine that changes the state of its cells step by step. The automaton can be one-dimensional where the cells are lined up like a chain or two-dimensional where cells are arranged in an array. Two entities of information are needed to run cellular automata: an initial state of the cells and a set of rules or laws. The rules determine the state of a cell in a new stage from the state of a group of cells in the preceding stage [134-137].

In a cellular automata model, time is discrete, and space is divided into an N-dimensional lattice of cells. Each cell represents a finite state machine or automaton. All cells change state simultaneously using the same function δ or rule table. The next state is a function of the current state and the state of the neighboring cells. The set of adjacent

cells is called a neighborhood. Its size, n , is commonly five or nine cells in 2-D models. Also, each cell can be in one of k possible states, one of which is designated the quiescent or inactive state. When a quiescent cell has an entirely quiescent neighborhood, a widely accepted convention is that it will remain quiescent at the next time step. Fig. 8.7 shows the common neighborhood template in 2-D cellular automata [11].

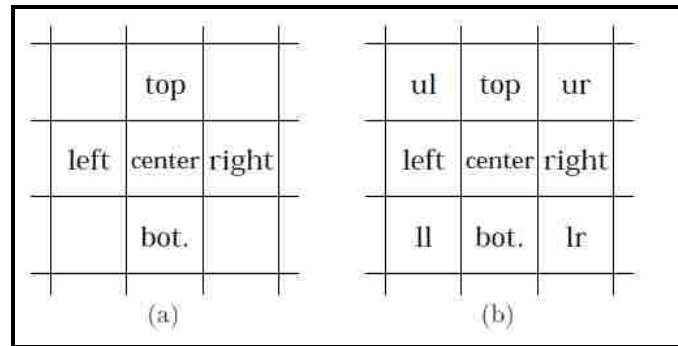


Figure 8.7 Common neighborhood in 2-D cellular automata (a) 5-cell von Neuman neighborhood (b) 9-cell Moore neighborhood.

The cellular automata rule table is defined as a list of transition rules that specify the next state for every possible neighborhood combination. The underlying space of cellular automata models is typically defined as being isotropic, meaning that the absolute directions of north, south, east and west are indistinguishable. However, the rotational symmetry of cell states is frequently varied. We can distinguish 2 types:

- 1- Strong rotational symmetry implies that all cells states are unoriented, meaning that each neighbor to a cell has no distinguishable position.
- 2- Weak rotational symmetry implies that at least one cell state is directionally oriented, meaning that the cell designates specific neighbors as being its top, right, bottom, and left neighbors.

In cellular automata models with weak rotational symmetry, an automaton is sensitive to the orientation of states of its neighboring cells and uses this input to make a state transition. We call this method of cell input *orientation sensitive input (osi)*. An alternative method in which an automaton receives only information about its neighboring cell's state type, and not the component's orientation was also introduced. Such automaton is called *orientation insensitive input (oii)*.

The rule table is significantly reduced in size by decreasing the amount of input information each automaton receives using orientation insensitivity. The advantages of using smaller rule tables are:

- 1- Decreased computational load
- 2- Decreased search space size.

The amount of rule table reduction under orientation insensitive input can be calculated by comparing the expressions for rule table sizes under both methods of input.

Letting $|\delta|$ represent rule table size, the ratio for the rule table sizes is

$$\frac{|\delta|_{osi}}{|\delta|_{oii}} \quad \text{Eq. 8.1}$$

Where

$|\delta|_{osi}$ denotes the rule table size under orientation sensitive input

$|\delta|_{oii}$ denotes the rule table size under orientation insensitive input.

This ratio is derived in [135] and can be expressed as

$$\frac{|\delta|_{osi}}{|\delta|_{oii}} = \frac{(\beta c + 1)^{CP_{n-1} + c(\beta c + 1)^{n-1}}}{(c + 1)^{CP_{n-1} + c(c + 1)^{n-1}}} \quad \text{Eq. 8.2}$$

Where β denotes the number of coordinate systems rotations permitted, c is the number of component (state) types, and $K^{CP_{n-1}}$ denotes the circular permutation function used to count distinct neighborhood patterns [136]. This ratio converges to a constant as the number of components c is increased:

$$\lim_{c \rightarrow \infty} \frac{(\beta c + 1)^{CP_{n-1} + c(\beta c + 1)^{n-1}}}{(c + 1)^{CP_{n-1} + c(c + 1)^{n-1}}} = \beta^{n-1} \quad \text{Eq. 8.3}$$

Thus as we increase the number of components, models using orientation insensitive input have rule tables that are approximately β^{n-1} smaller than models using orientation sensitive input. For a typical coordinate system with $\beta=4$, and using the von Neumann and Moore neighborhoods shown in Fig. 8.7, it is seen that the $|\delta|$ ratios are 256 and 65536 respectively. This multiplicative increase translates into orders of magnitude increases in search space sizes:

$$|D_n^K|_{osi} = K^{(|\delta|_{osi})} \cong K^{\beta^{n-1}(|\delta|_{oii})} \cong (|D_n^k|_{oii})\beta^{n-1} \quad \text{Eq. 8.4}$$

Where $|D_n^K|$ denotes the size of the set of all possible rule tables for a cellular automata with k states and n neighbors. From the last equation, it is seen that by using orientation insensitive input, the search space is decreased by approximately β^{n-1} orders of magnitude.

In this work, the ‘‘Game of Life’’ two dimensional cellular automata rule is applied to a microstrip antenna. This rule is played on a grid of square cells where each cell can be

alive or dead and changes in its state occur according to the state of its neighbor. The “Game of Life” cellular automata can be categorized as orientation insensitive cell input.

The rule of the game can be summarized as follows [134]:

1 – A cell that is alive remains alive in the next step when two or three cells among its eight neighbours are alive.

2 – If more than three neighbours are alive, the cell will die from over crowdedness.

3 – If fewer than two neighbours are alive, the cell will die from loneliness.

4 – A dead cell will come to life when surrounded by exactly three live neighbours.

An example of the “Game of Life” cellular automata rule is shown in Fig. 8.8. It is essential to note that after stage 4, the automaton will resume to stage 1. One can notice that by going from stage 1 to stage 3 a rotation of 180 degree is needed; also by going from stage 2 to stage 4 the same rotation is needed.

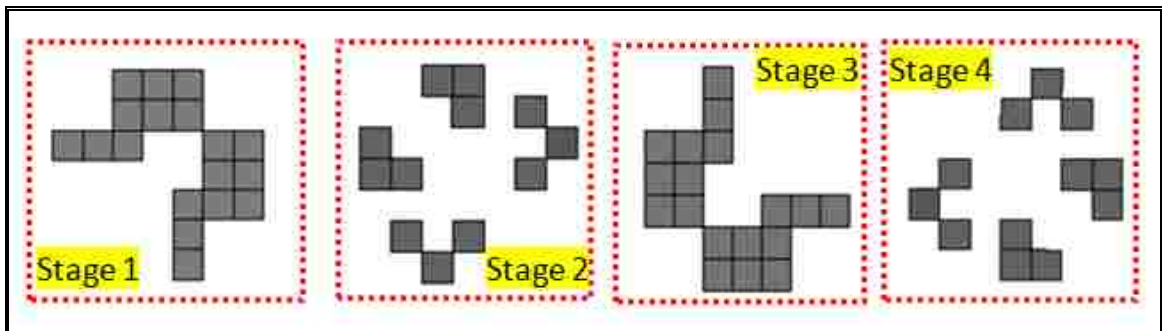


Figure 8.8 A cellular automata “Game of Life” example

The structure of the antenna that is studied in this work is based on the cellular automata stages that are shown in Fig. 8.7. The chosen substrate is Rogers Duroid 5880 with a dielectric constant of 2.2 and a thickness of 0.32 cm. The corresponding antenna structures are shown in Fig. 8.9. The cellular automata area that constitutes a part of the

antenna patch is divided into 8x8 squares. Each square has a side of 2 mm for stages 1 and 3 and a side of 2.4 mm for stages 2 and 4. The substrate size is 5 cm x 4.5 cm and the patch size is 4 cm x 3cm. Different feed position is used for each antenna set.

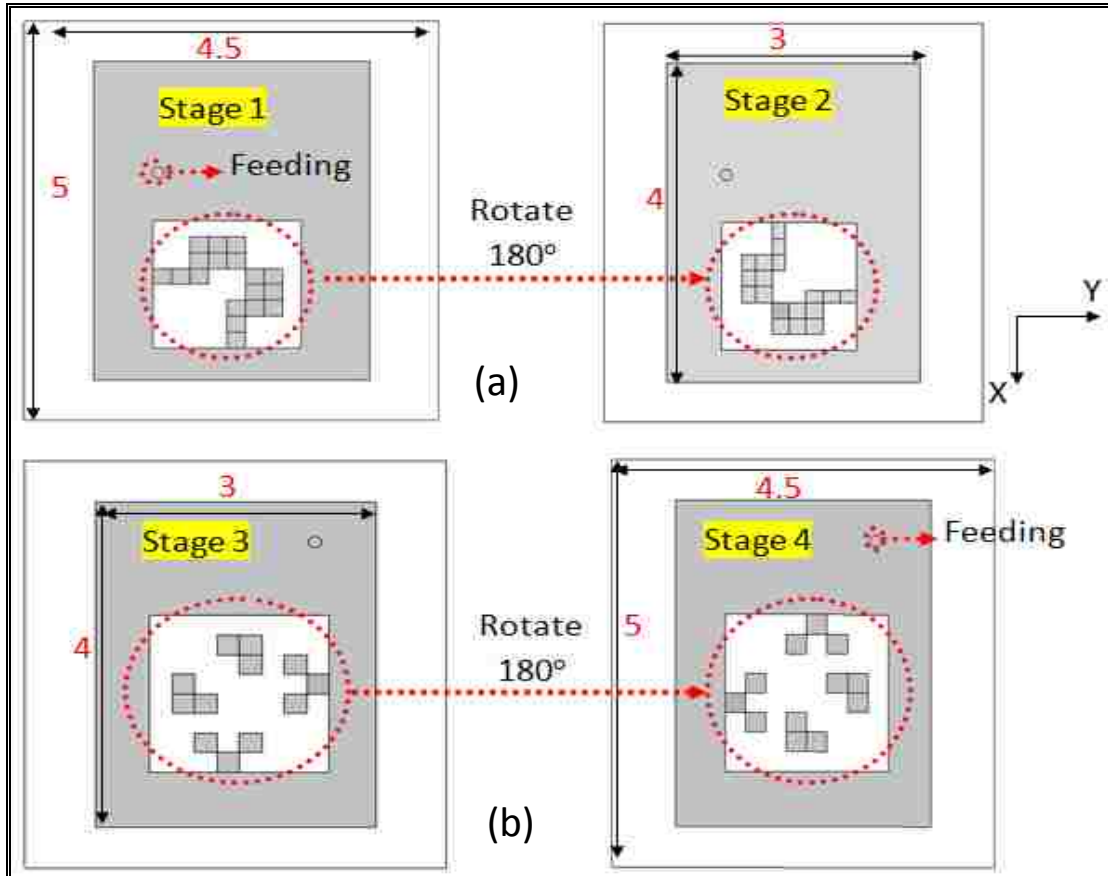


Figure 8.9 The two antennas set (a) For stages 1 and 3 (b) For stages 2 and 4

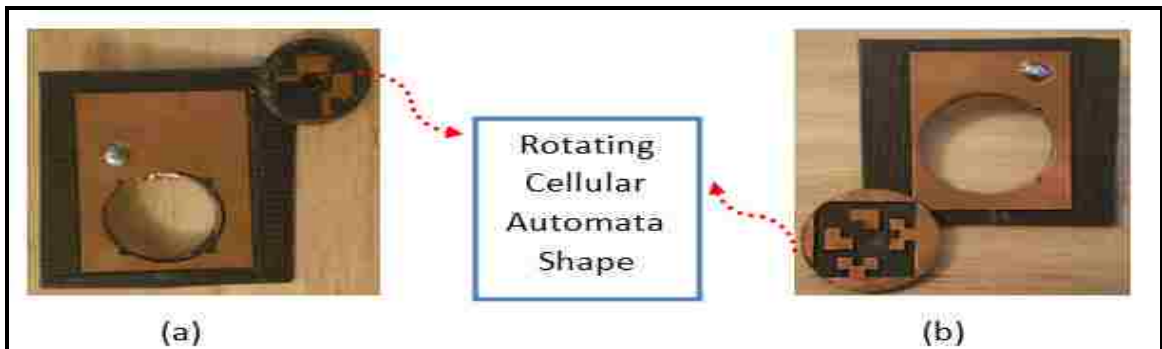
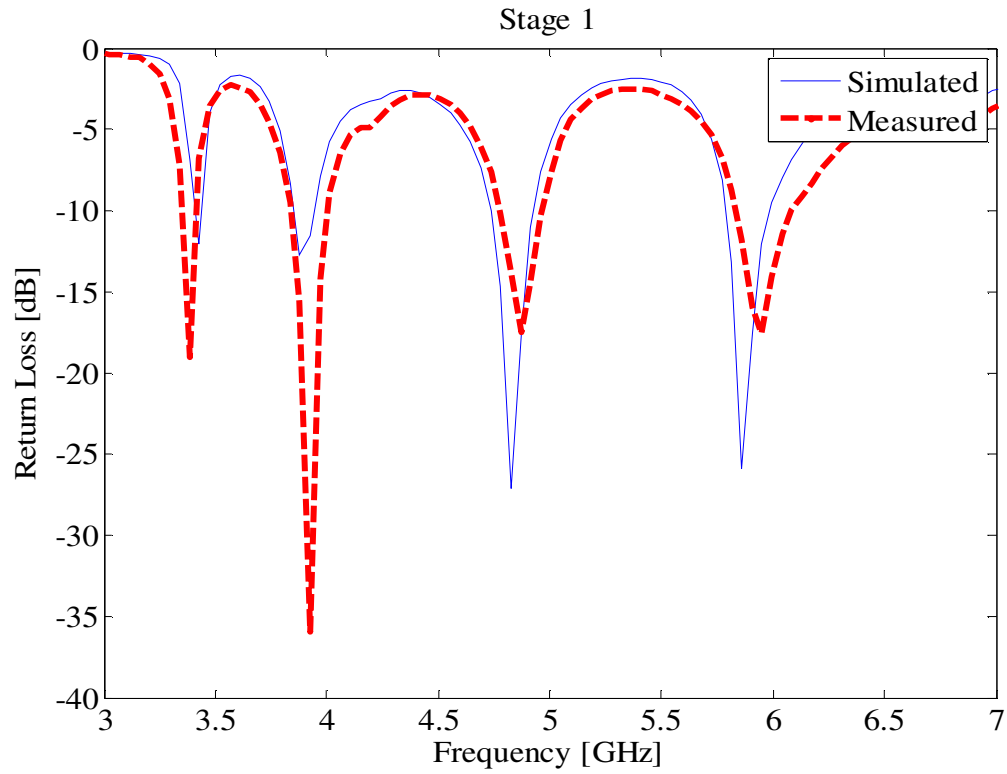


Figure 8.10 Fabricated Antenna Structure for Stages: (a) 1 and 3 (b) 2 and 4

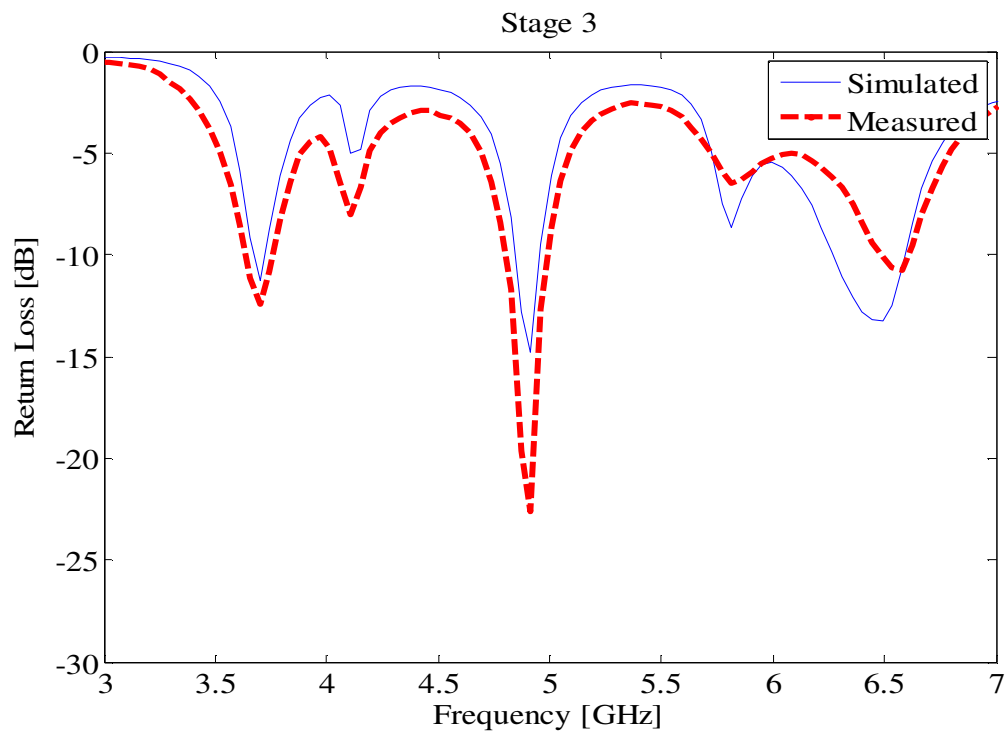
The fabricated antenna structures for the two cases are shown in Fig. 8.10. The comparison between the simulated and the measured antenna return loss are shown in Fig. 8.11 and Fig. 8.12. The tuning of the resonant frequencies between stages 1 or 2 and 3 or 4 can be shown by comparing the two plots in Fig. 8.11 or Fig. 8.12.

All the stages of the “Game of Life” cellular automata can also be used to train an ARTMAP neural network so that the slot positions and the corresponding antenna return loss are linked. Different configurations for the game of life cellular automata rule are applied to a patch antenna. The chosen substrate is Rogers Duroid 5880 with a dielectric constant of 2.2 and a thickness of 0.32 cm. In order to apply cellular automata to a microstrip antenna, the patch is divided into 10 x 13 squares. Each square has a side of 3 mm. The substrate size is 5 cm x 4.5 cm. The different slot configurations for each stage for one possible implementation of the “Game of Life” cellular automata rules are shown in Fig. 8.13. After stage 5, the same pattern is repeated. By going from one stage to another the antenna produces different resonant frequencies while maintaining the same omni-directional radiation pattern. The antenna is simulated for the same feed position for all the different cases [138].

To determine which aperture distribution to use for a given set of frequencies, a neural network is used. Different cases using cellular automata rules are used to train an ARTMAP neural network.

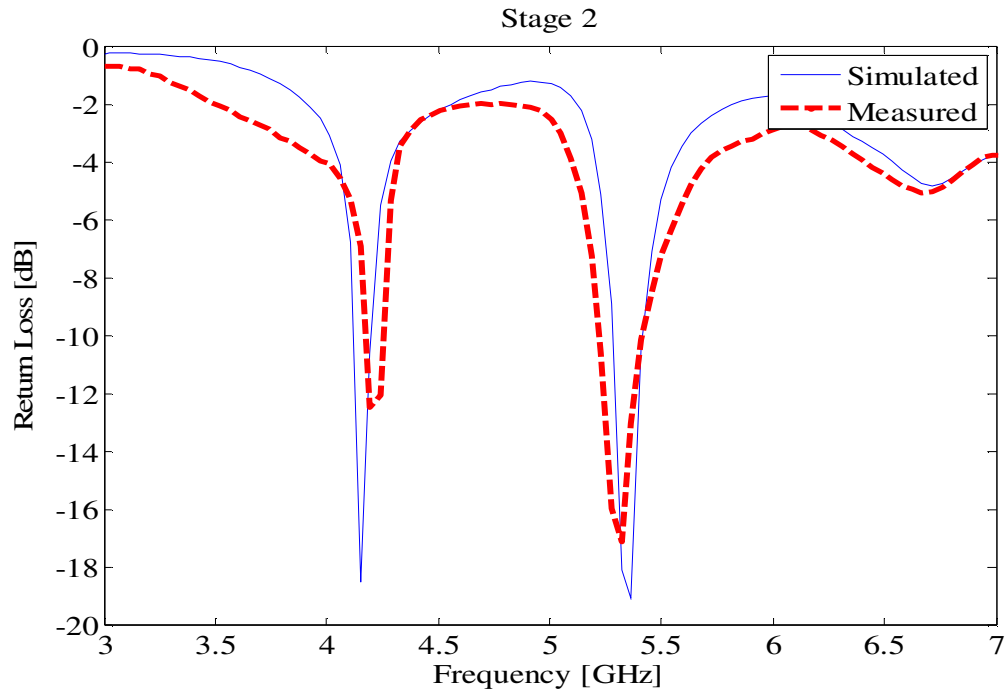


(a)

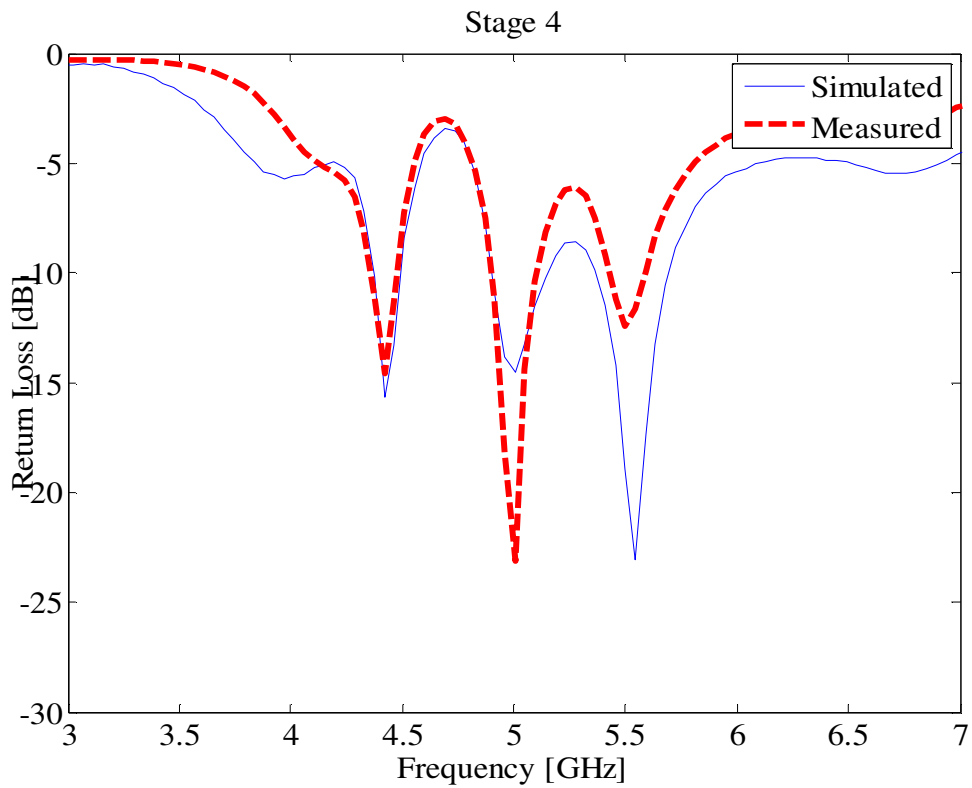


(b)

Figure 8.11 The simulated and the measured antenna return loss for (a) stage 1 (b) stage 3



(a)



(b)

Figure 8.12 The simulated and the measured antenna return loss for (a) stage 2 (b) stage 4

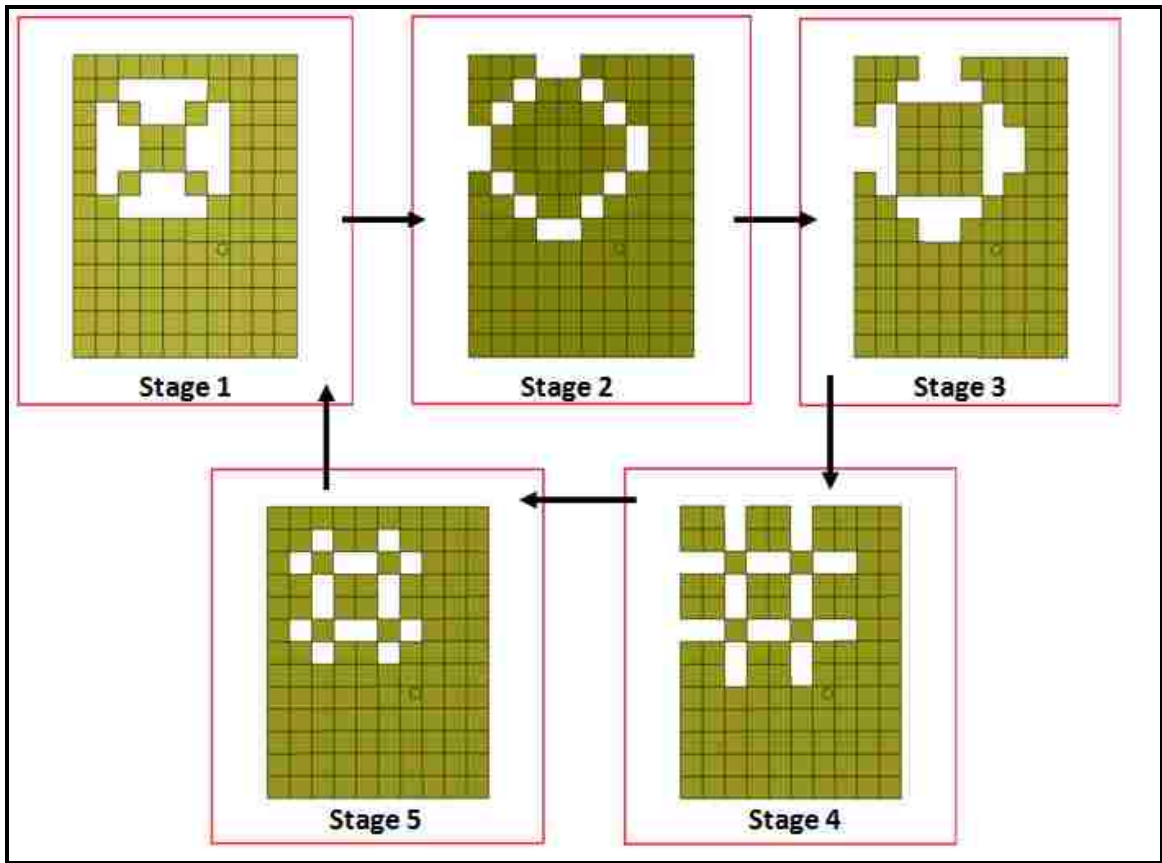


Figure 8.13 An example of “Game of Life” cellular automata applied to a microstrip antenna

Neural networks are used whenever closed form solutions do not exist and trial and error methods are the main approach to tackle a problem at hand. It is essential to note that the fuzzy ARTMAP architecture is chosen in this work because it has several advantages compared to other neural networks. First, the fuzzy ARTMAP neural network is faster to train. Second, once it is trained with a list of training data, it does not require extensive retraining with the old data when new training data are added to the training list. Moreover it is guaranteed to converge to a solution for any collection of training data provided to the network [139].

Fuzzy ARTMAP consists of three modules: ARTa, ARTb and an inter-ART module. The ARTa and ARTb both have architecture of fuzzy ART so that they can accept analog patterns as their inputs. Each of ARTa and ARTb classifies its input into an appropriate category by some similarity rule. The function of inter-ART module is to learn the mapping between the pattern pair fed to ARTa and ARTb [139].

The structures of cellular automata presented above are used to train the fuzzy ARTMAP neural network. Basically, the input to the network is the different configurations of the patch antenna. The small square metallic parts are represented by 1 while the square areas without metal are encoded as 0. The size of the input stream is 130 which correspond to the 130 squares that constitute the patch of the antenna.

For each antenna structure, a different return loss is obtained and fed to the output of the ARTMAP neural network. The size of the output is 201 which is the same number of points taken between 1 GHz and 10 GHz.

After completing the required neural network training, a return loss (S11) profile is presented to the neural network and the corresponding aperture distribution that yields this specific S11 profile is derived. Fig. 8.14 shows the fabricated antenna structure based on the neural network approach. The comparison between the simulated, the measured data and the obtained data using ARTMAP neural network is shown in Fig. 8.15. This antenna is able to cover the range of frequency from 5.8 GHz till 8.6 GHz, in addition to three other resonances at 2.6 GHz, 3.4 GHz and 5.2 GHz. A good agreement is obtained between the three data sets. A neural network can be used to link the structure of the antenna that is based on cellular automata to the corresponding return loss.



Figure 8.14 The fabricated antenna structure for the fuzzy ARTMAP neural network testing

8.4 A New Reconfigurable Antenna for Cognitive Radio

This section presents a new antenna design suitable for cognitive radio communication. Similar to the designs presented in the previous chapters, the antenna consists of two structures incorporated together into the same substrate. The first structure is an ultra wideband antenna covering the spectrum from 3.1 GHz to 11 GHz for channel sensing. The second structure is a frequency reconfigurable triangular shaped patch for establishing communication with another RF device. The antenna reconfigurability is achieved via a rotational motion. A prototype antenna is fabricated and tested in order to validate the suggested method.

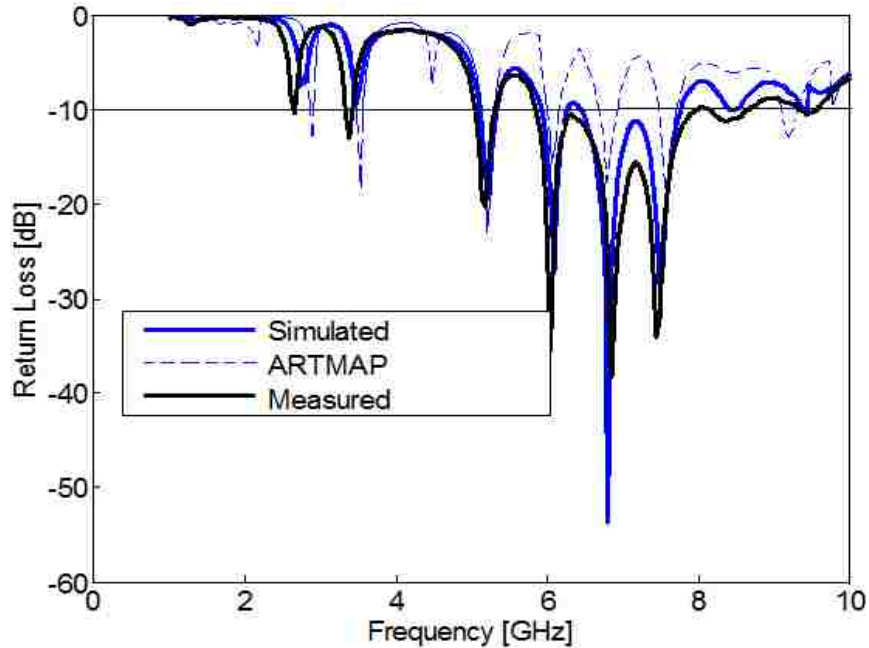


Figure 8.15 The simulated, measured and ARTMAP tested return loss

8.4.1 Sensing Antenna Design:

As discussed in the previous chapters, in cognitive radio system one needs the capability to:

- 1- Sense the spectrum (“sensing” antenna)
- 2- Communicate (“reconfigurable communicating” antenna)
- 3- Re-sense the spectrum (“sensing” antenna)

A wideband antenna is necessary in order to be able to achieve the channel sensing. This section details the “sensing” wideband antenna structure. The antenna topology is based on the antenna design shown in Fig. 8.16. Its corresponding return loss is also included [140].

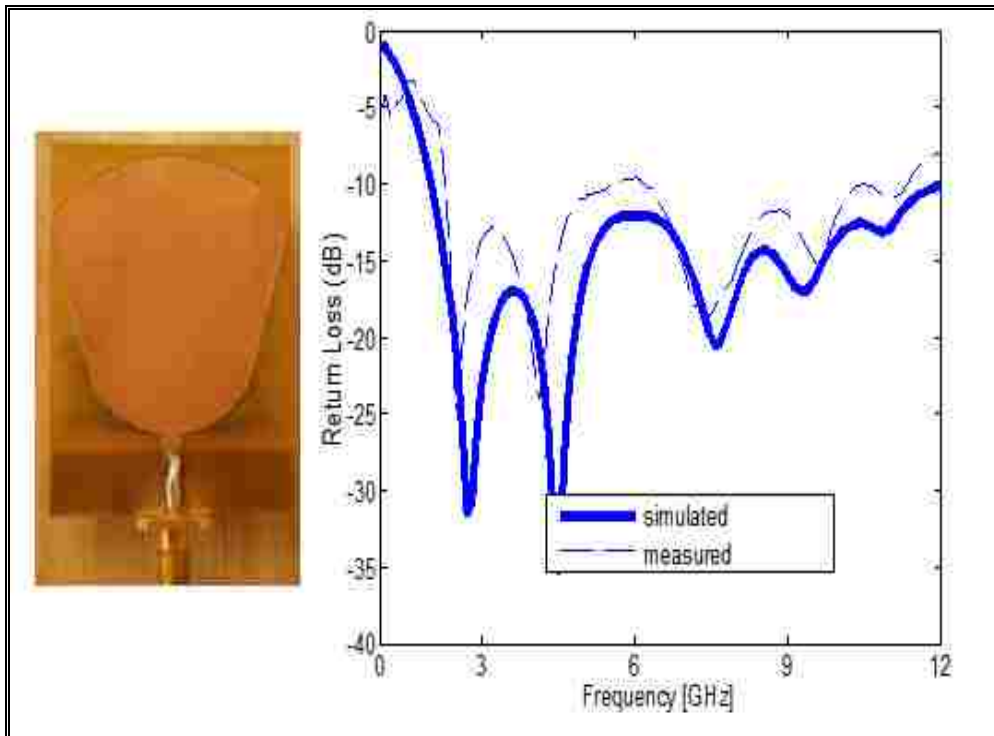


Figure 8.16 The antenna structure and its return loss

Our goal is to achieve a “sensing” antenna and a “reconfigurable communicating” antenna in the same substrate. The idea is to remove a slot from the antenna shown in Fig. 8.16 in order to have space for the “reconfigurable communicating” antenna. The corresponding antenna topology is shown in Fig. 8.17. It consists of 2 layers. The top layer is the slotted polygon shaped patch. The bottom layer is the partial ground. It is fed via a microstrip line to produce radiation above and below the substrate. The chosen substrate is Rogers Duroid 5880 with dielectric constant 2.2 and height 1.6 mm. All simulations are done using HFSS v11. The corresponding antenna return loss is shown in Fig. 8.18. It exhibits coverage from 3.3 GHz till 11 GHz making it suitable for channel sensing in cognitive radio systems.

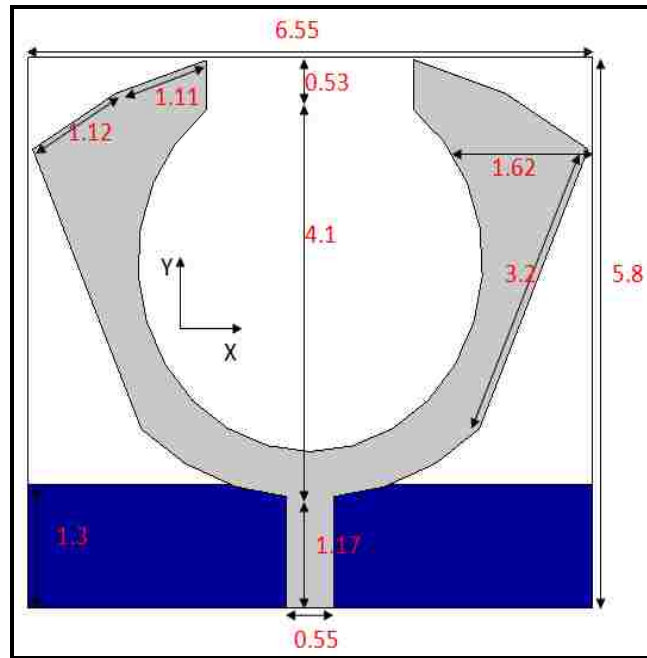


Figure 8.17 The sensing antenna structure

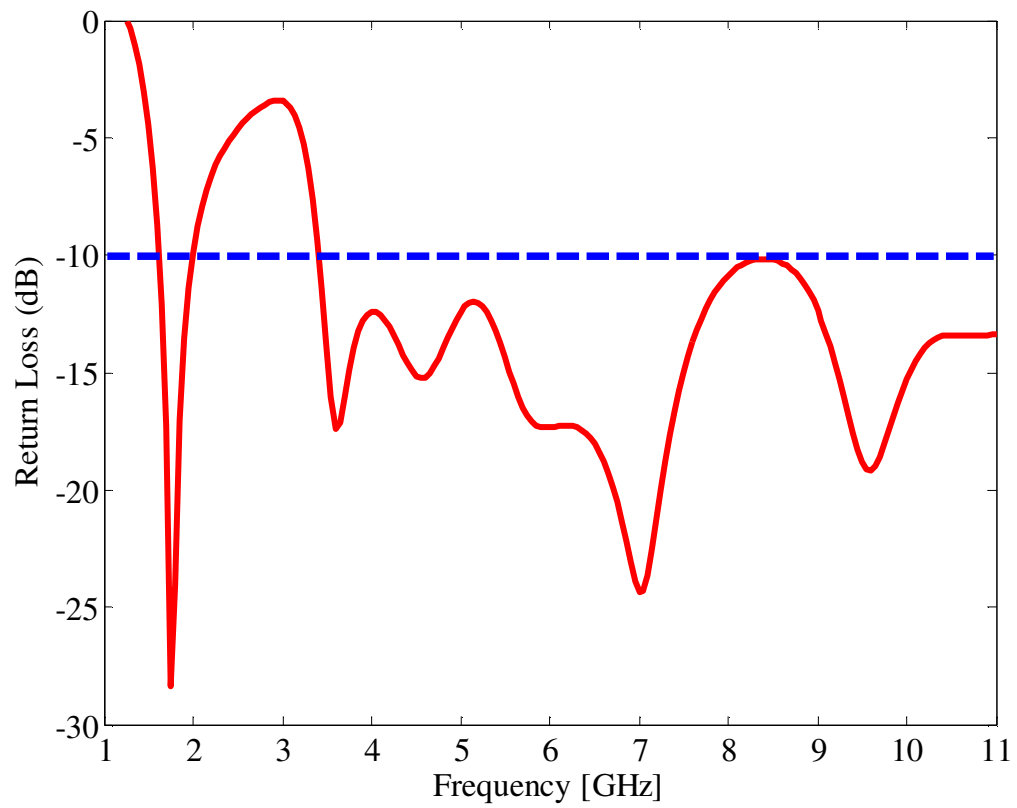


Figure 8.18 The return loss for the sensing antenna

For an antenna to be suitable for channel sensing it should possess an omnidirectional radiation pattern. The antenna structure investigated in this section satisfies this requirement. The computed radiation pattern in the X-Z plane at 4.5 GHz (thin line), 7.5 GHz (thick line), and 10.5 GHz (dotted line) is shown in Fig. 8.19.

It is essential to note that the incorporation of the rounded shape just after the stripline feed line is responsible for producing the required ultra wide bandwidth for the antenna. This rounded shape has the effect of making the antenna input impedance close to 50Ω for the band from 3.3 GHz till 11 GHz. This antenna structure also shows a resonance at 1.9 GHz.

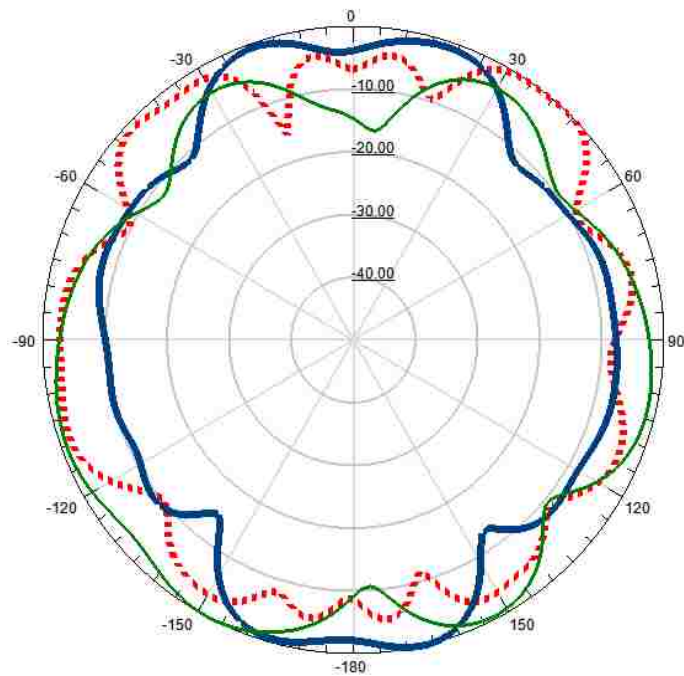


Figure 8.19 The normalized antenna radiation pattern for $f=4.5$ GHz (thin line), $f=7.5$ GHz (thick line) and $f=10.5$ GHz (dotted line) in the XZ plane

8.4.2 Reconfigurable Communicating Antenna Design:

The structure for the “reconfigurable communicating” antenna is detailed herein. The “reconfigurable communicating” antenna structure is summarized in Fig. 8.20. By rotating the antenna patch by 180°, a different structure is being fed by the microstrip line. This rotation produces different resonances making the antenna suitable to communicate at the frequency specified by the “sensing” antenna. The antenna top layer consists of two triangular shaped patches that are separated by a given distance. Similar to the “sensing” antenna, this structure is fed via a microstrip line and has a partial ground. Since this antenna is going to be incorporated with the “sensing” antenna, its substrate size is taken the same as the “sensing” antenna. Its ground dimension is 18 mm x 9 mm so that it will not affect the radiation from the patch of the “sensing” antenna. The process of rotation is shown in Fig. 8.21; the structure shown in the left corresponds to position 1 and the structure shown in the right corresponds to position 2.

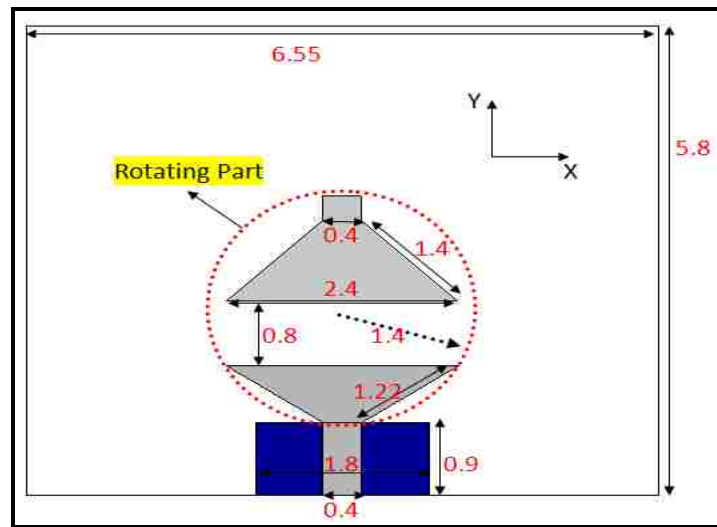


Figure 8.20 The “reconfigurable communicating” antenna structure

The frequency reconfigurability of this antenna can be noticed by comparing the return loss plot presented in Fig. 8.22. This antenna has the property to tune from 5.3

GHz-9.15 GHz (position 1) to 3.4 GHz-4.85 GHz (position 2).

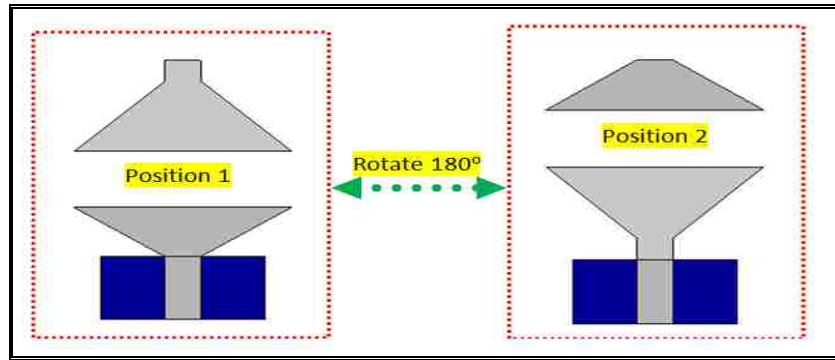


Figure 8.21 The process of rotation

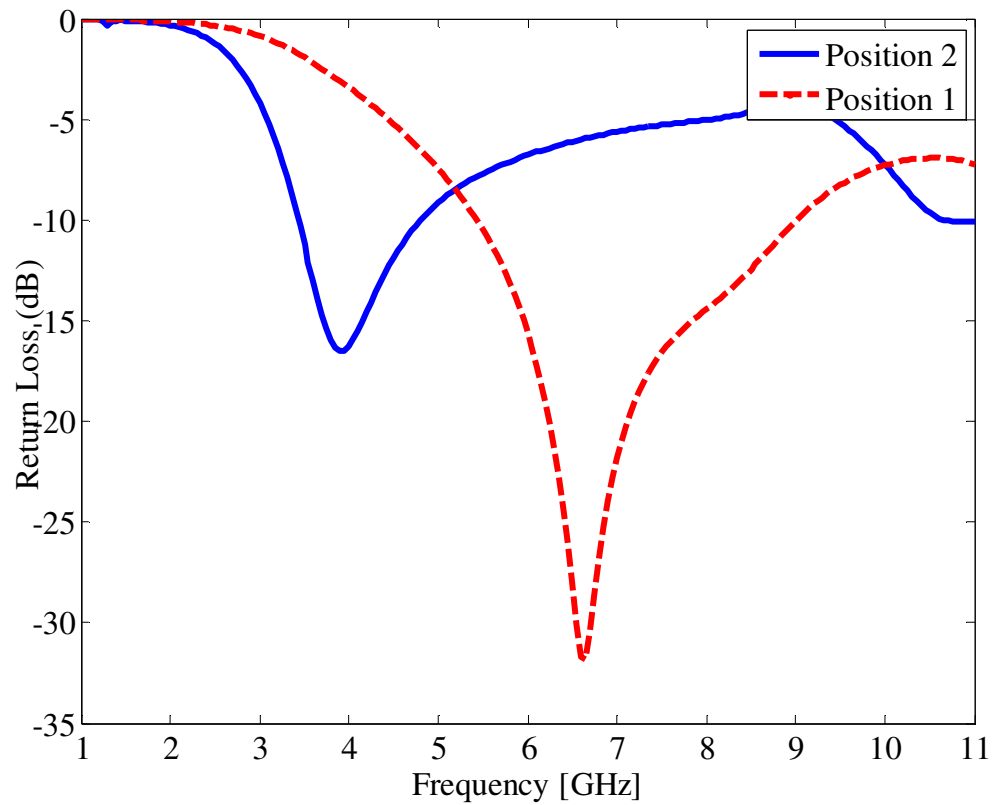


Figure 8.22 Frequency tuning for the “reconfigurable communicating” antenna

The computed radiation pattern in the XZ plane at 6.65 GHz for position 1 (thick line) and at 4 GHz for position 2 (thin line) are shown in Fig. 8.23. It is proven that the antenna satisfies the omnidirectional property for both positions.

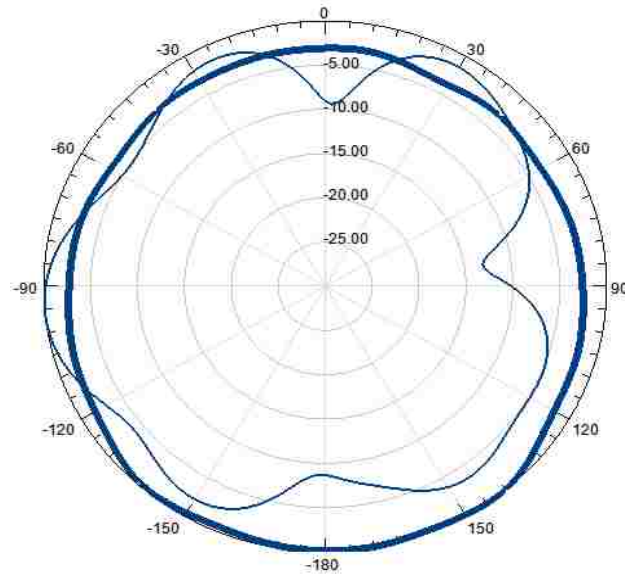


Figure 8.23 The normalized reconfigurable antenna radiation pattern at $f=6.65$ GHz (thick line) and $f=4$ GHz (thin line)

8.4.3 Cognitive Radio Antenna Design:

In the previous two sections, we have separately discussed the design of the “sensing” and the “reconfigurable communicating” antenna. In this section, we incorporate both designs into the same antenna substrate. This has the advantage of reducing space requirements and making the two antennas required for cognitive radio communication lie in the same plane. The suggested antenna structure is provided in Fig. 8.24. The dimensions of the different parts of the antenna are the same as those mentioned in the previous two sections. The fabricated prototype is shown in Fig. 8.25.

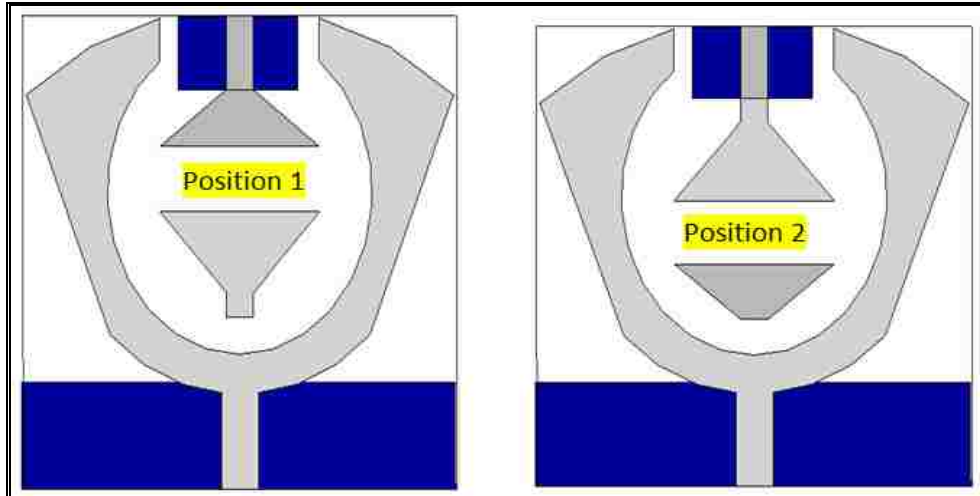


Figure 8.24 The cognitive antenna structure

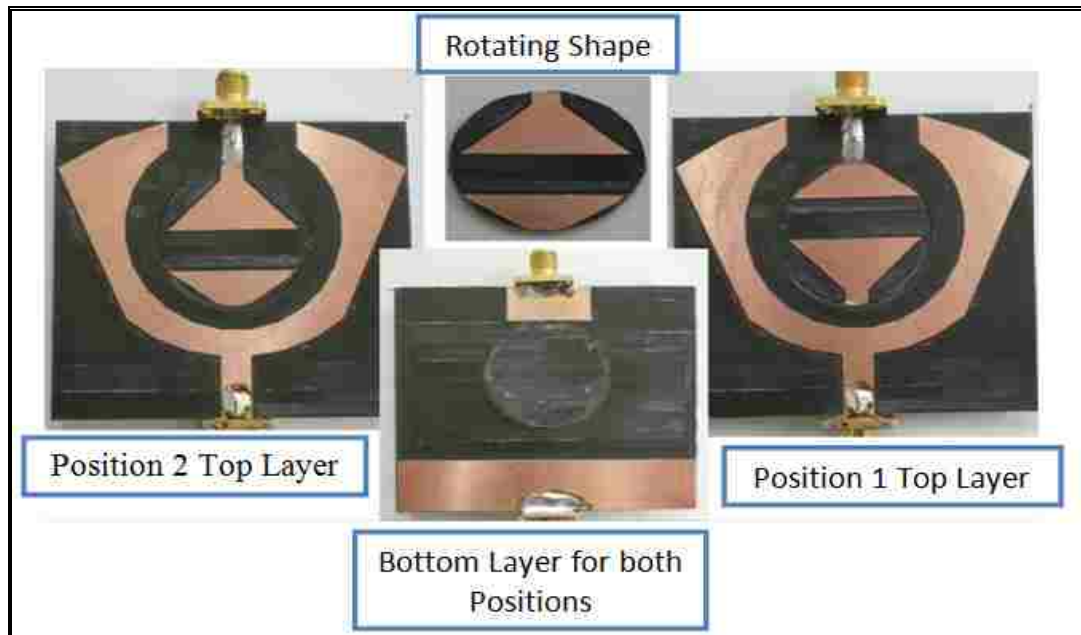


Figure 8.25 The fabricated antenna prototype

The comparison between the simulated and the measured return loss for the “sensing” antenna is shown in Fig. 8.26. This data is for the antenna taken when it is at position 1. The same return loss is produced for the “sensing” antenna if the entire antenna structure is at position 2.

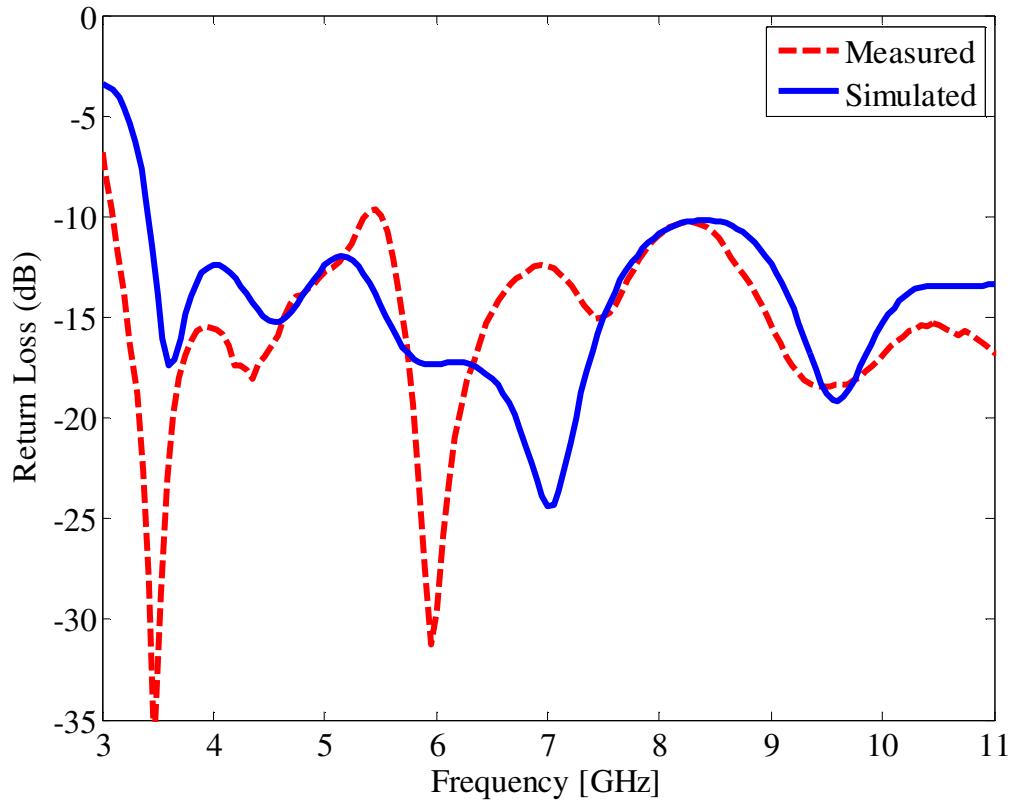
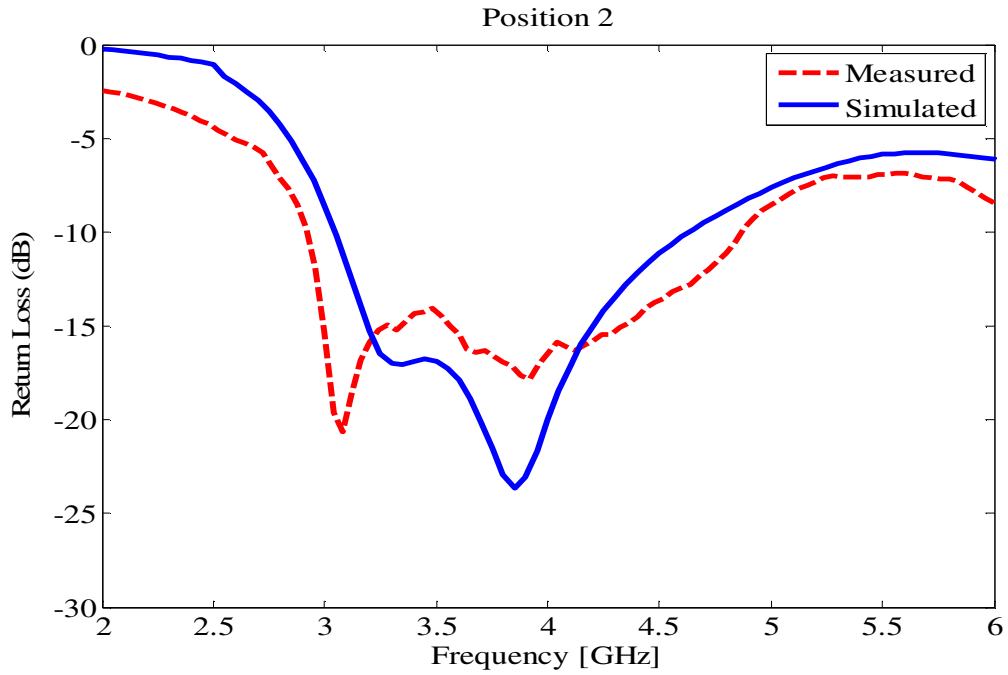


Figure 8.26 The sensing antenna return loss for position 1

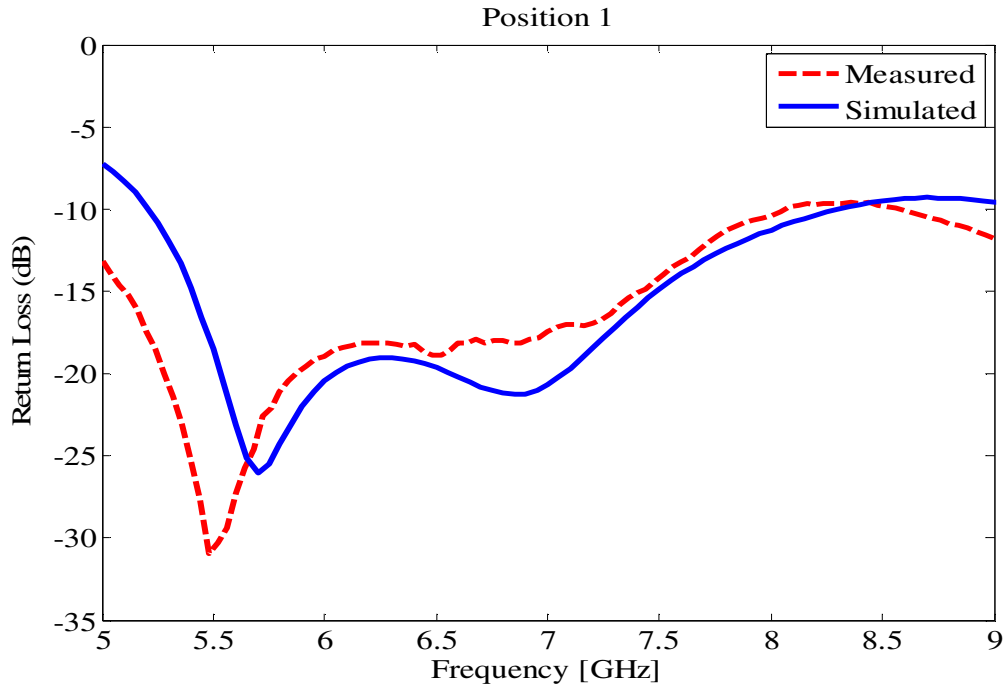
Fig. 8.27(a) and Fig. 8.27(b) show the measured and the simulated return loss of the “reconfigurable communicating” antenna for both positions. The required frequency reconfigurability is achieved. The first plot corresponds to position 2 and covers the band from 3 GHz to 5 GHz. The second plot corresponds to position 1 and covers the band from 5 GHz to 9 GHz.

Since the “sensing” and the “reconfigurable communicating” antennas are both incorporated into the same substrate, it is crucial to look at the coupling between them. For both positions, the transmission between the two antennas is below -10 dB for the

whole band of interest. Fig. 8.28 shows the simulated and the measured coupling for position 1 in the first plot and for position 2 in the second plot.



(a)



(b)

Figure 8.27 The “reconfigurable communicating” return loss for (a) position 2 (b) position 1

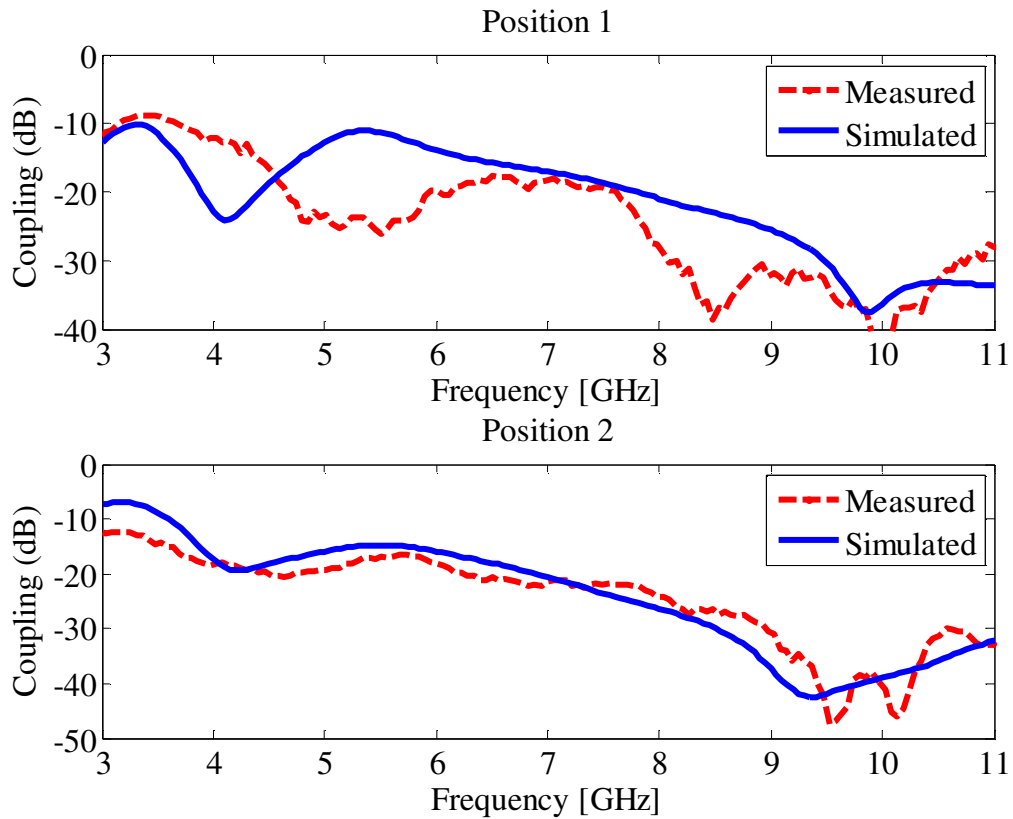


Figure 8.28 The antenna coupling for both positions

8.5 Cognitive Radio Front-End Using Rotatable Controlled Reconfigurable Antennas

In this section, another cognitive radio antenna is presented. The difference between the design shown in this section and the previously discussed design is that wider frequency range is covered with better coupling. The antenna also relies on the rotation of the antenna patch to achieve reconfiguration, however in this section the whole system is software controlled. The rotation is achieved by a stepper motor mounted on the back of the antenna structure. The motor's rotation motion is controlled by LABVIEW on a computer connected to the motor through its parallel port. The computer's parallel port is

connected to a NPN Darlington array that is used to drive the stepper motor. The antenna is simulated with the driving motor being taken into consideration. A good agreement is found between the simulated and the measured antenna radiation properties [141-142].

8.5.1 Antenna Structure:

The antenna is printed on a 70mm x 50mm Rogers Duroid 5880 substrate with a dielectric constant of 2.2 and a height of 1.6 mm. The corresponding antenna structure is shown in Fig. 8.29. The left module is the sensing antenna while the right part is the reconfigurable section. The sensing antenna is a modified egg-shaped printed monopole antenna. It has a partial ground plane of dimensions 32mm x 7mm. A tapered stripline is feeding the antenna for better impedance match over the entire bandwidth of interest. This antenna is able to scan the spectrum from 2 to 10 GHz. The computed antenna radiation patterns at $f=3$ GHz, 6 GHz and 9 GHz in the X-Z plane are shown in Fig. 8.30. The antenna possesses an omni-directional radiation pattern and is able to radiate above and below the substrate due to the fact that it has a partial ground.

The frequency tuning is achieved by physically altering the patch shape. A circular substrate section holding five different antenna patches is rotated via a stepper motor. A 50Ω stripline extends beyond the rotating section in order to guarantee contact between the rotating circular patch and the feeding line. At each rotation stage, the stripline excites a different patch and a different frequency is achieved. The rotation mechanism is described briefly in Fig.8.31. The stepper motor is modeled in HFSS with the antenna structure to account for its effect. The stepper motor's characteristics are extracted from [143].

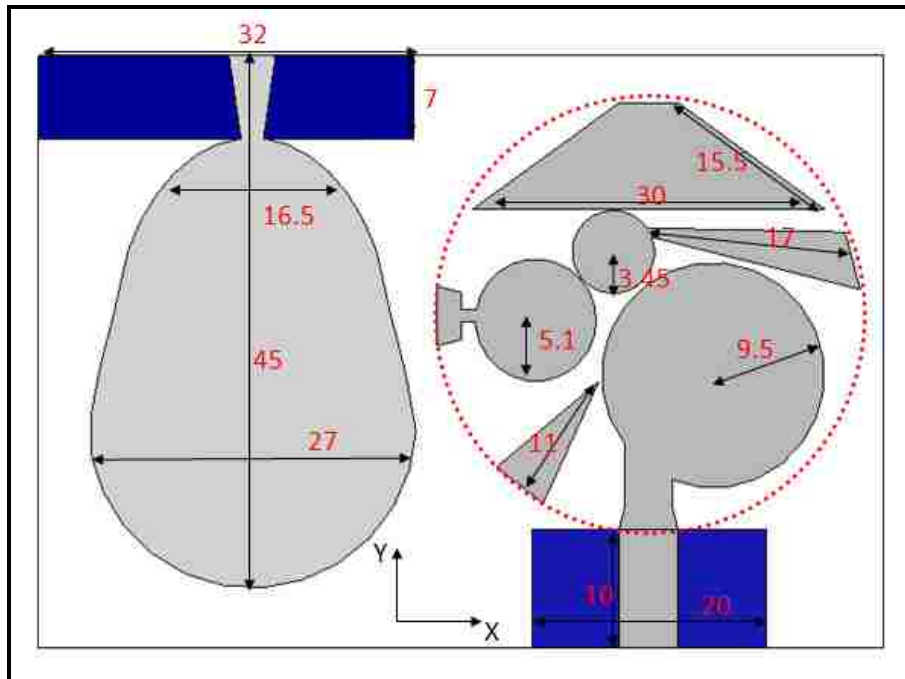


Figure 8.29 The antenna structure (dimensions in mm)

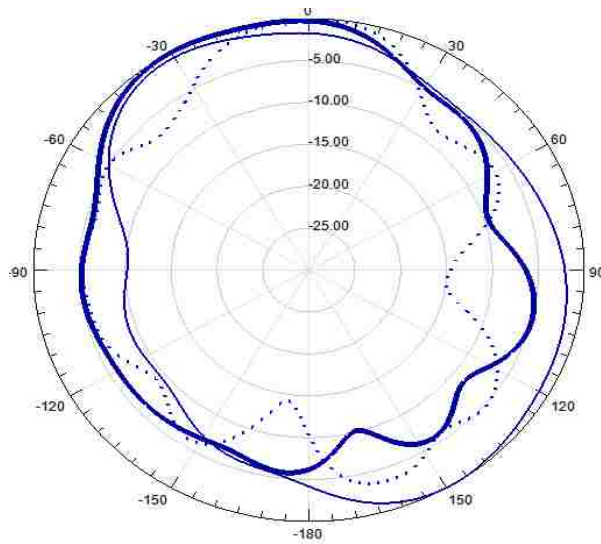


Figure 8.30 UWB Antenna Radiation Pattern at $f=3$ GHz (thin line), 6 GHz (thick line), and 9 GHz (dotted line)

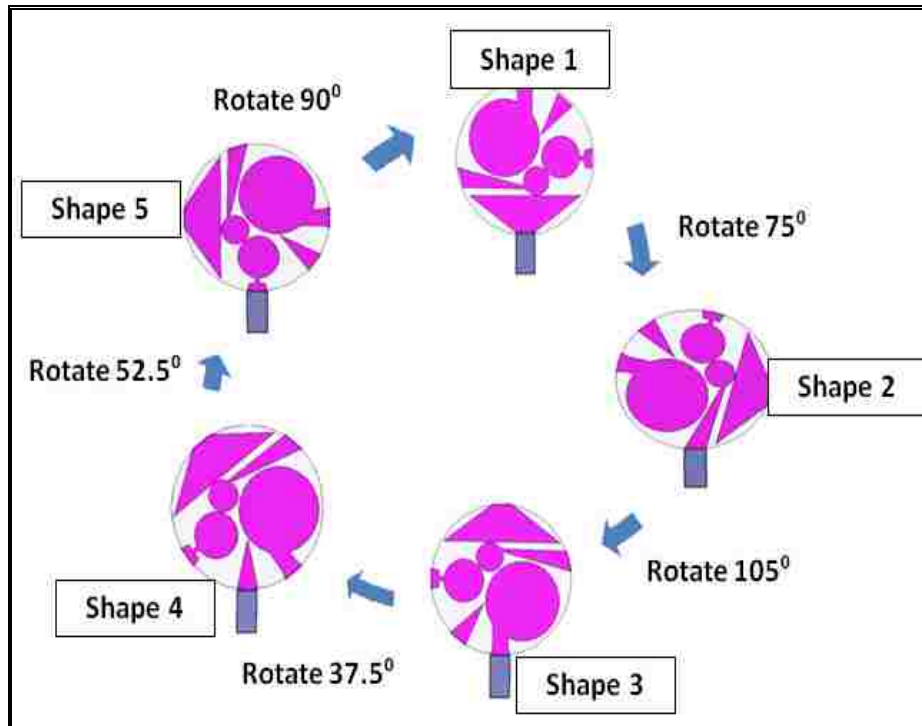


Figure 8.31 Antenna reconfigurability process

8.5.2 Stepper Motor Controller:

The stepper motor used in this work rotates in 7.5 degree steps, and for each step 2 coils should be activated simultaneously [143]. The sequences of coil activation are summarized in Table 8.2, where “1/0” denotes whether the corresponding coil is “activated / deactivated”. The amount of steps needed to go from one shape to another is summarized in Fig. 8.32. The stepper motor is attached to the back of the rotatable circular patch. Two plastic screws are used to hold the stepper motor to the antenna substrate as shown in Fig. 8.33. The motor rotating part consists of a metallic cylinder of length 1 cm and diameter 1 cm. This part is soldered to the back of the rotating circular patch in order to achieve the required rotation.

The stepper motor is connected to a computer via a parallel port and the control of

the motor is achieved by using LABVIEW. A LABVIEW code is implemented to send to the pins of the parallel port (pin 2 till 5) one of the four sequences shown in Table 8.2. Each of the four outputs from the parallel port (0V/5V TTL signal) is connected to a high voltage, high current Darlington array. The Darlington array, considered as the driver of the stepper motor, consists of two pairs of transistors for higher gain. Each output from the Darlington array is connected to one of the four coils of the stepper motor. In this work, the ULN2003 seven open collector Darlington pairs is used [144]. A 12 V power supply is needed for the stepper motor and the ULN2003. The whole process is shown in Fig. 8.34. A flowchart of the LABVIEW code is shown in Fig. 8.35.

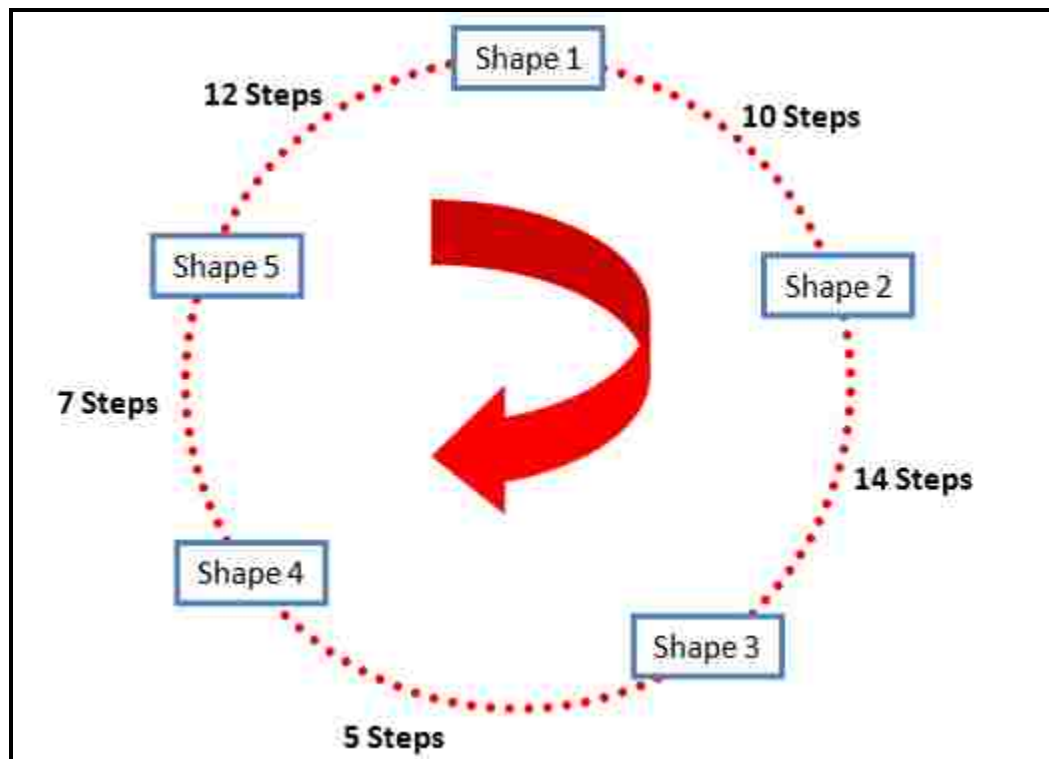


Figure 8.32 The number of steps needed for each rotation

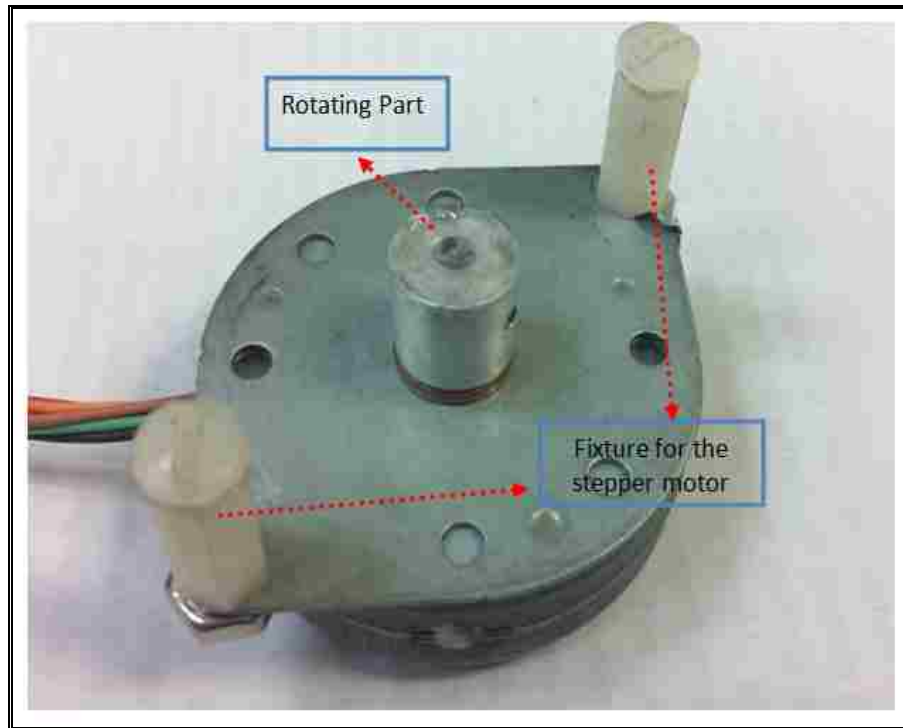


Figure 8.33 The stepper motor used in this work

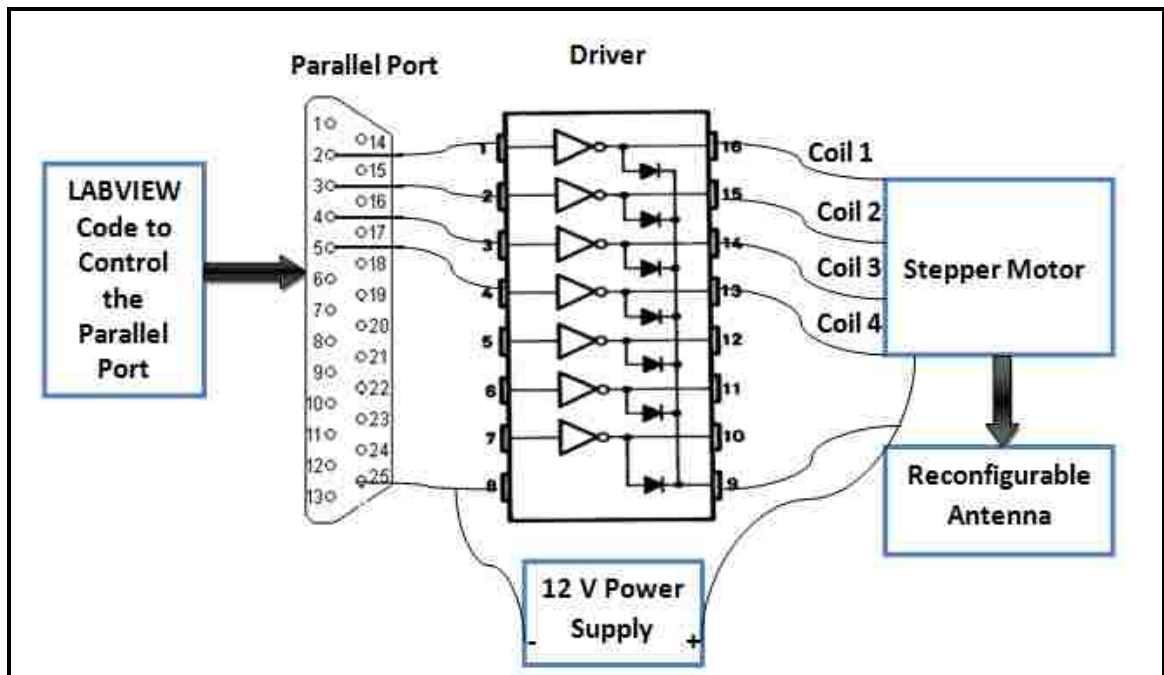


Figure 8.34 The experiment setup

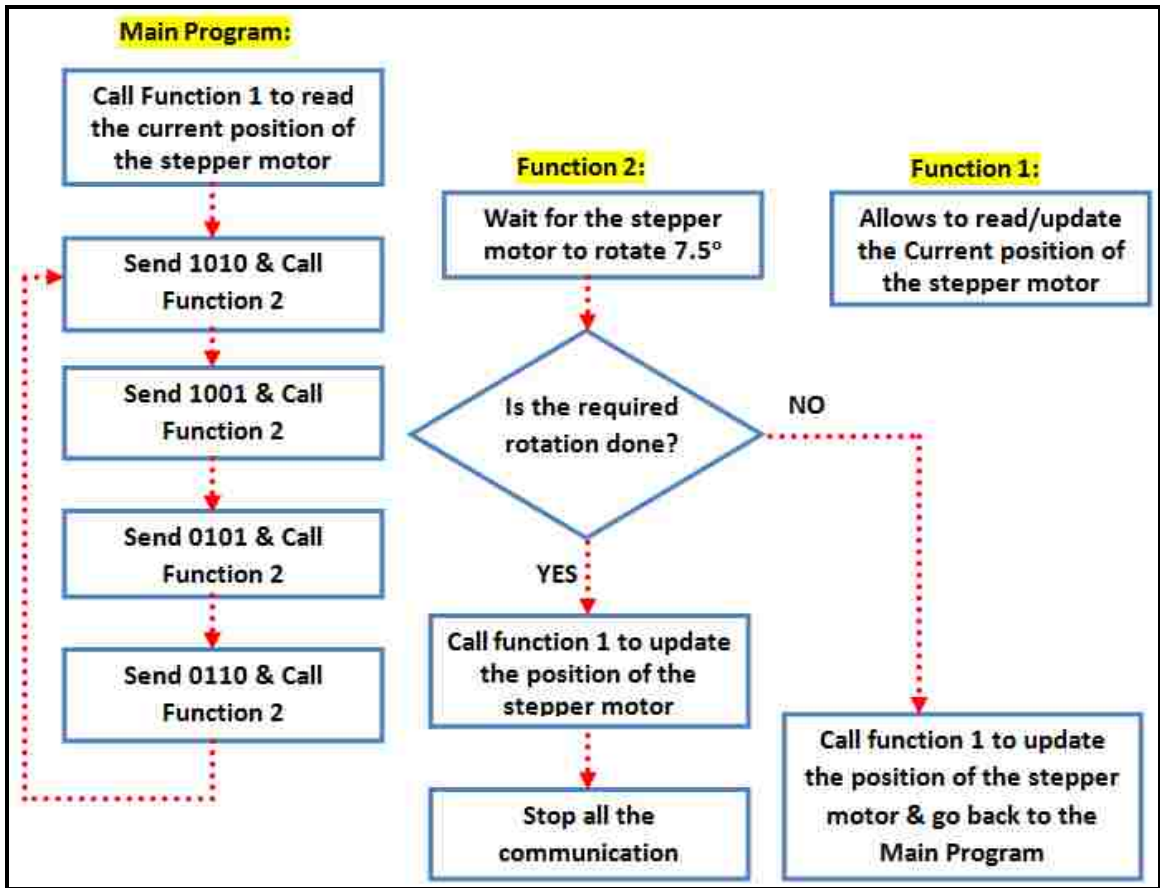


Figure 8.35 The flowchart of the LABVIEW algorithm

Table 8.2 Coil activation sequence

	<i>Coil 1</i>	<i>Coil 2</i>	<i>Coil 3</i>	<i>Coil 4</i>
Sequence 1	1	0	1	0
Sequence 2	1	0	0	1
Sequence 3	0	1	0	1
Sequence 4	0	1	1	0

8.5.3 Fabrication and Results:

A prototype antenna is fabricated and tested. The stepper motor incorporated in the back of the reconfigurable rotating antenna section is connected to the controlling circuit as discussed in the previous section. The fabricated antenna is shown in Fig. 8.36.

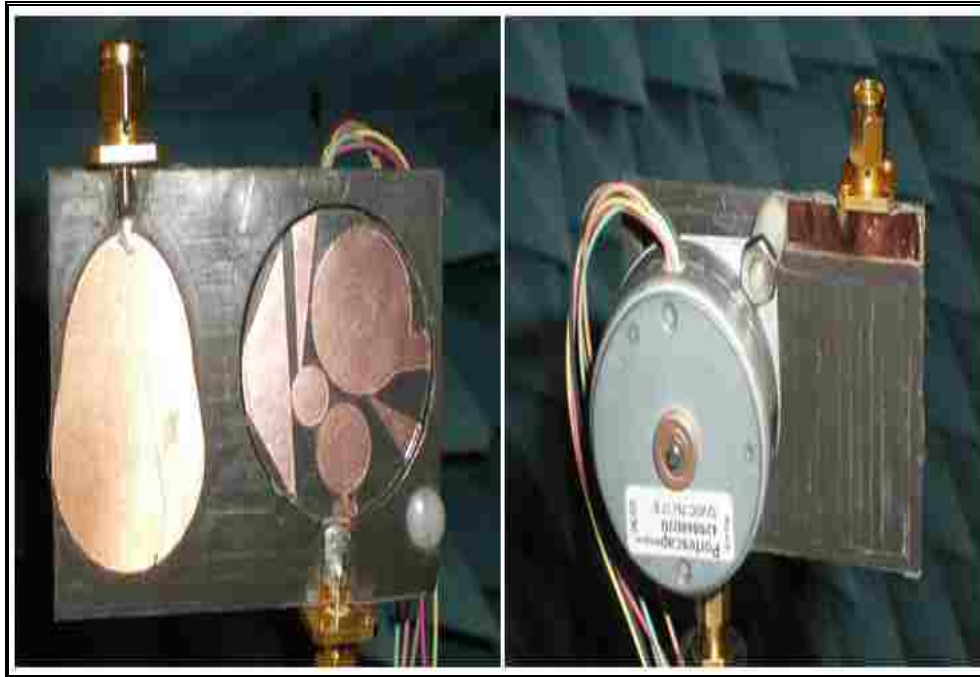


Figure 8.36 The fabricated antenna prototype

a- Sensing Antenna Results:

As shown in Fig. 8.29, the sensing antenna has a total length of $38\text{mm} \approx 0.25 \times \lambda$ (where λ corresponds to the lowest frequency at '2 GHz'). The comparison between the simulated and the measured return loss for the sensing antenna is shown in Fig. 8.37. This comparison corresponds to the case when the reconfigurable section is at the initial position shown in Fig. 8.36. It is noted that the UWB performance of the antenna remains constant for all the reconfigurable section positions.

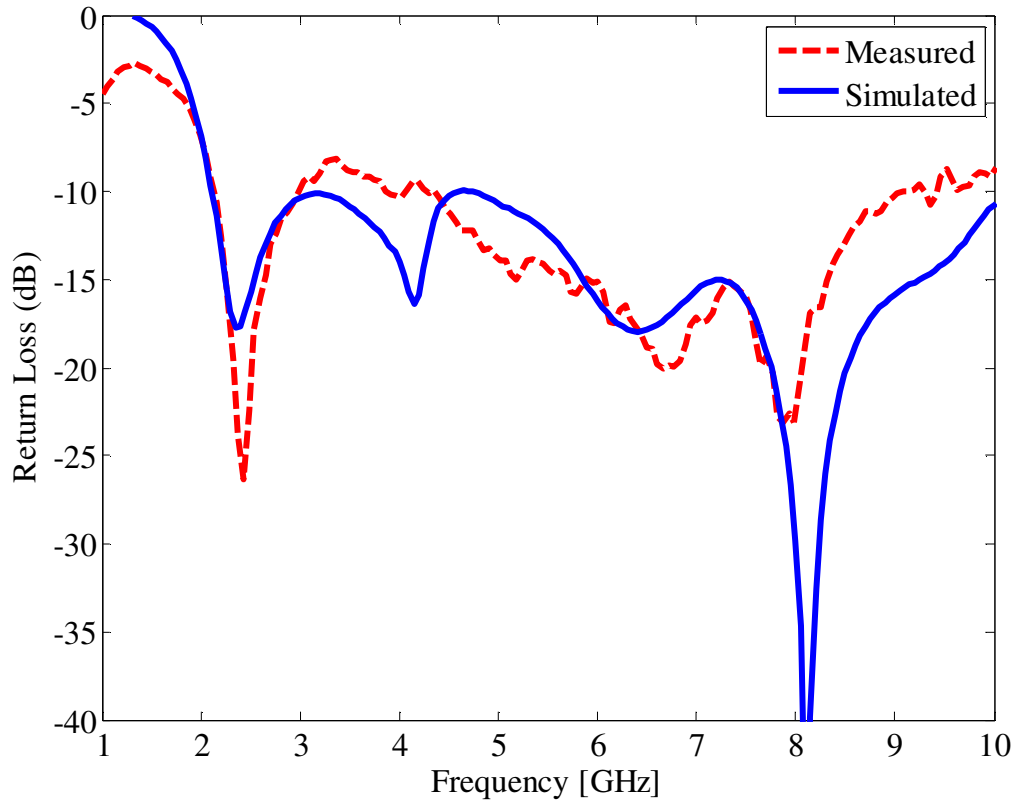


Figure 8.37 The sensing antenna return loss

b- Reconfigurable Section Results

The reconfigurable section consists of a rotating 18 mm radius circular substrate section that carries five different patches. Each patch on the rotating section resonates at a different band from 2GHz up to 10 GHz. The five different patches cover collectively the whole band (2- 10 GHz). The dimensions and the position of the different shapes are optimized using HFSS. All the shapes are fed via a 10mm × 5mm feeding line and they share a 20 mm × 10mm partial ground. The covered band for each shape is summarized in Table 8.3.

Table 8.3 Frequency reconfigurability

	<i>Covered Band [GHz]</i>
Shape 1	3.4-5.56
Shape 2	6.3-10
Shape 3	2.1-3
Shape 4	5.4-6.2

To ensure a good connection between the rotating circular patch and the feed line, a 50 Ω stripline overflows the rotating circular section. It is soldered to the feed line; a zoomed view of the connection between the feed line and the rotating circular part is shown in Fig. 8.38.

The comparison between the simulated and the measured return loss for the rotating section is shown in Fig. 8.39. Each band is labeled by the corresponding antenna shape number. An agreement is noticed between both data.

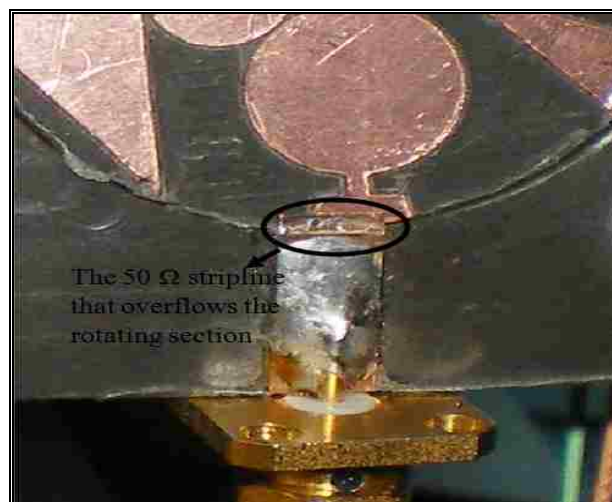


Figure 8.38 A zoomed view of the connection between the feed line and the rotating part

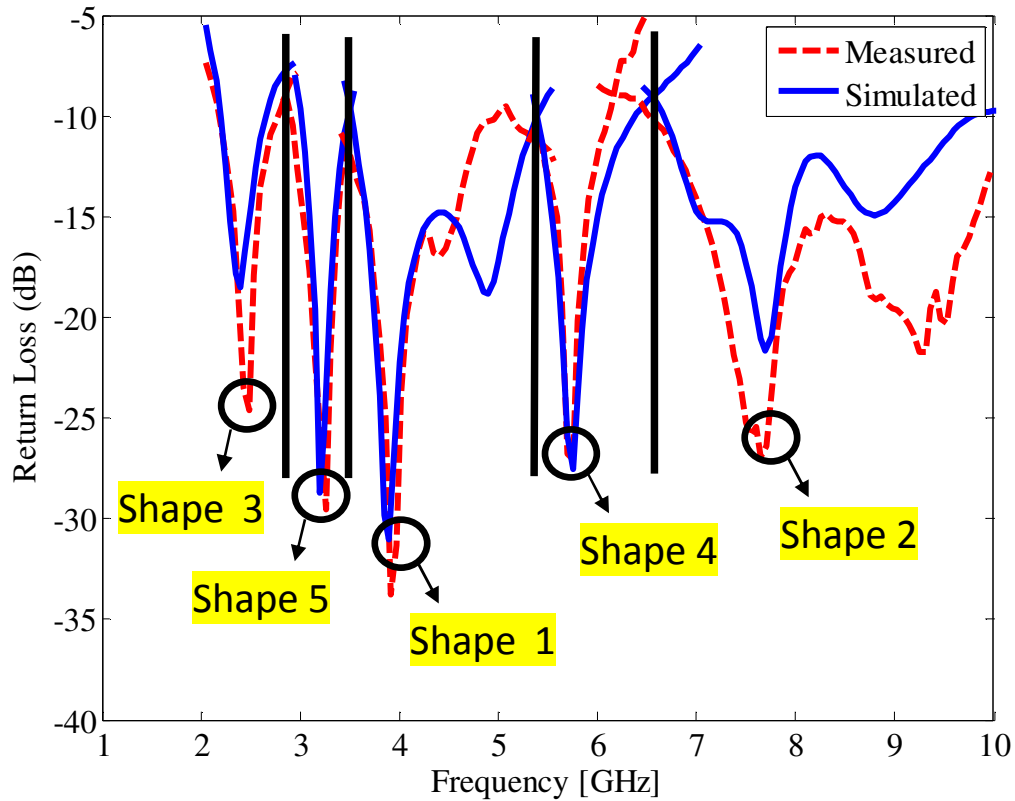


Figure 8.39 A comparison between the measured and simulated return loss for the reconfigurable antenna section

c- Coupling between the two antenna sections:

For any cognitive radio application the sensing and the reconfigurable antennas must be isolated. In order to quantify the amount of mutual-coupling induced between the two antenna sections, we should look at the isolation between the two antenna ports. The comparison between the simulated and the measured coupling ($|S_{21}|^2$) is shown in Fig. 8.40. This plot corresponds to the case when the reconfigurable antenna is at the position shown in Fig. 8.36.

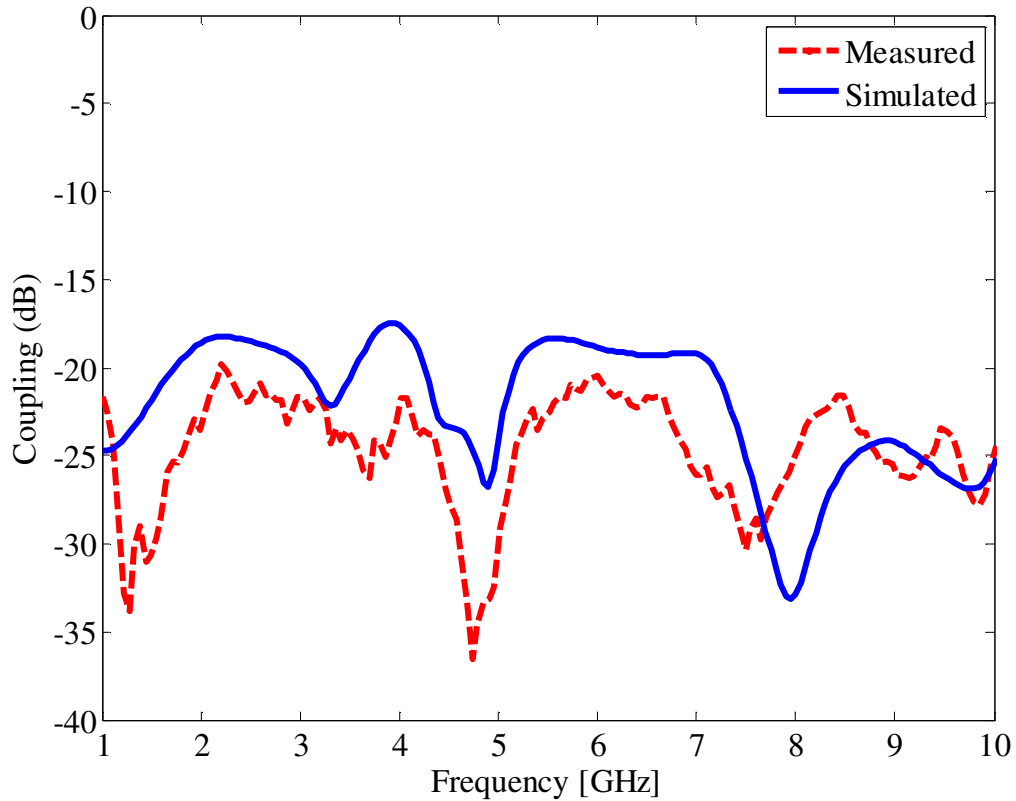


Figure 8.40 The coupling between the two sections

A coupling of less than -20 dB is obtained due to the fact that the two antenna structures are fed from the opposite edges of the substrate. The min/max values of the measured coupling for the other positions of the reconfigurable antenna are summarized in Table 8.4. These values correspond to the frequency band where each shape of the reconfigurable antenna operates as summarized in Table 8.3.

Table 8.4 The measured coupling

	<i>Min/Max [dB]</i>
Shape 1	-45/-25
Shape 2	-32/-23

Shape 3	-30/-20
Shape 4	-28/-25

d- Radiation Pattern of the Reconfigurable Antenna:

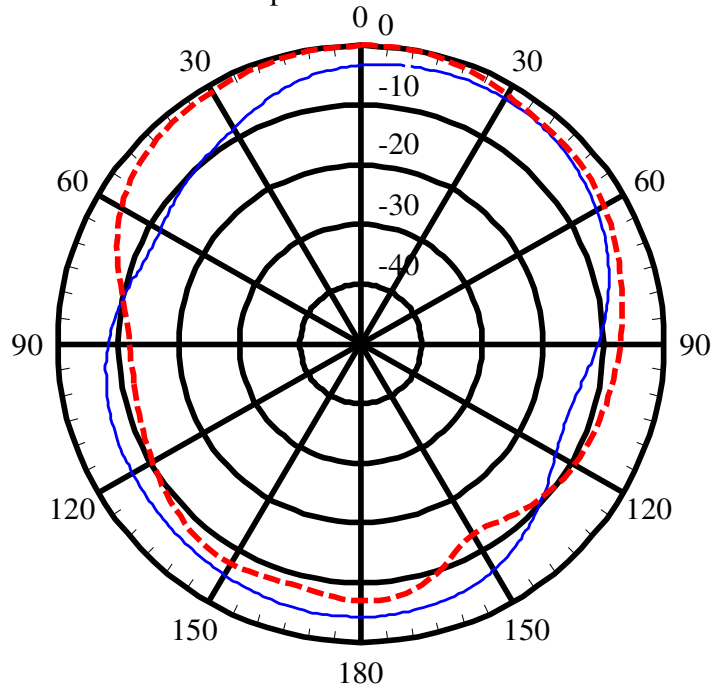
The comparison between the simulated (thick line) and the measured (thin line) radiation pattern for the reconfigurable antenna section in the X-Z plane is shown in Fig. 8.41 for different frequencies. A good agreement is noticed and the antenna preserves its omni-directional radiation pattern for all the different stages of the rotating section making it very convenient for cognitive radio applications. It is noticed that the stepper motor adds constructively to the antenna radiation pattern.

The peak antenna gain values for the 5 different patches of the rotating section, at the same frequencies used in the radiation pattern measurement shown in Fig. 8.41, are summarized in Table 8.5.

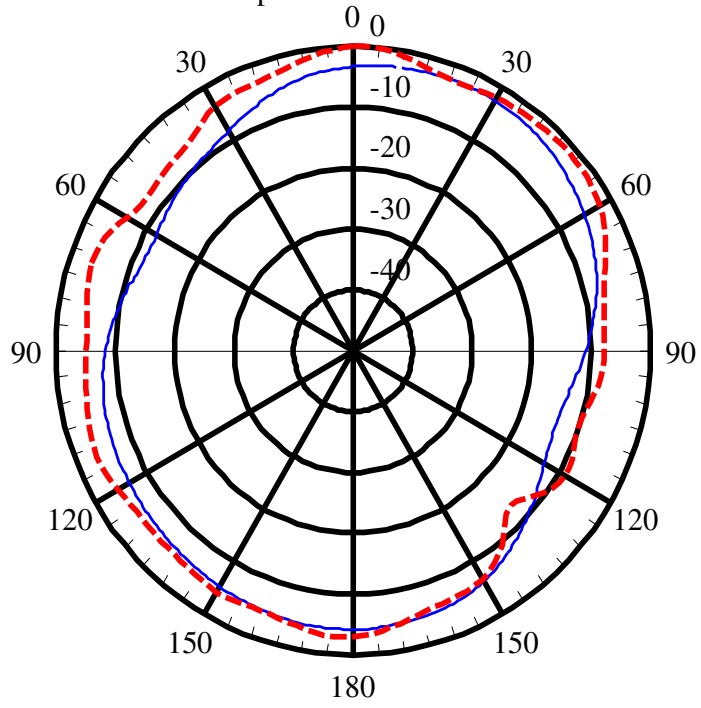
Table 8.5 The antenna peak gain

	<i>Gain [dB]</i>
Shape 1	6.62
Shape 2	8.45
Shape 3	7.77
Shape 4	6.67

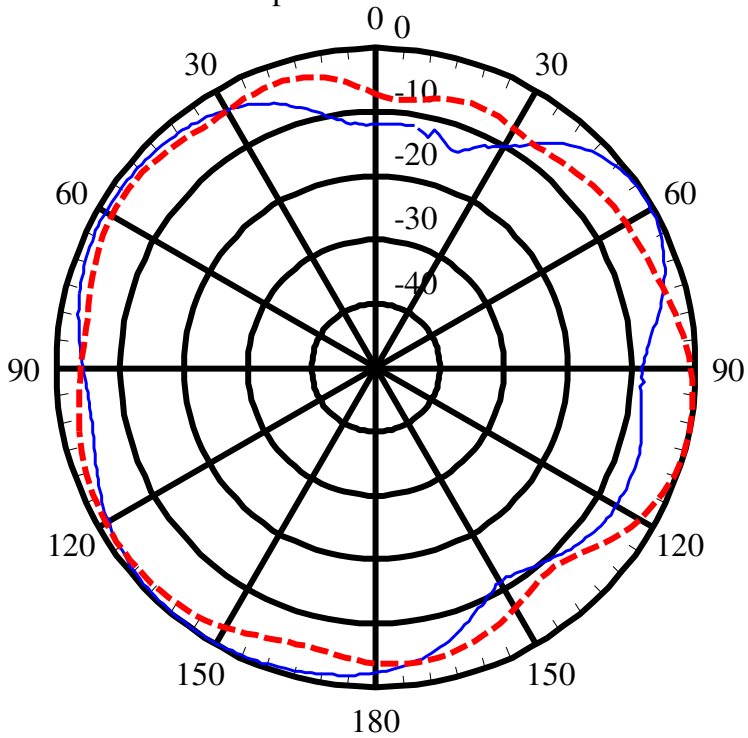
Shape 1 at $f=3.9$ GHz



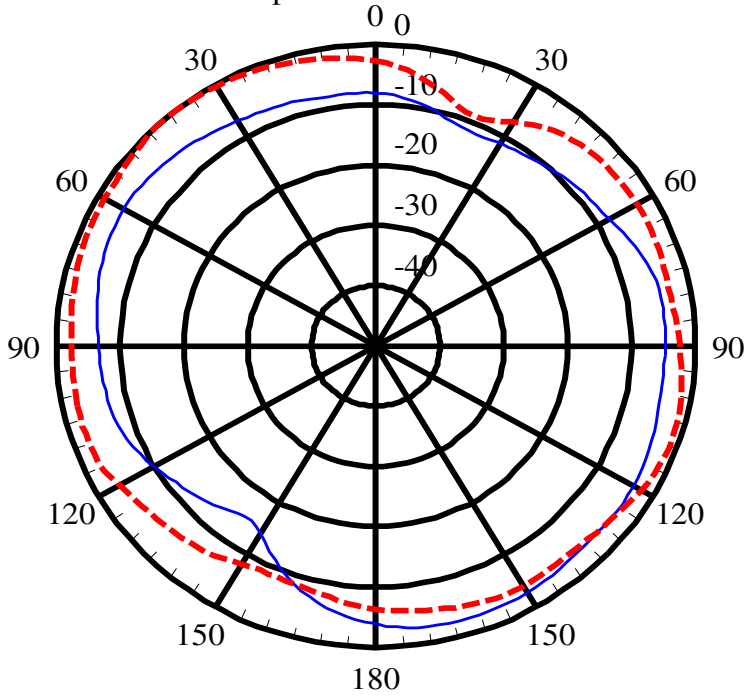
Shape 2 at $f=7.35$ GHz



Shape 3 at f=2.45 GHz



Shape 4 at f=6.05 GHz



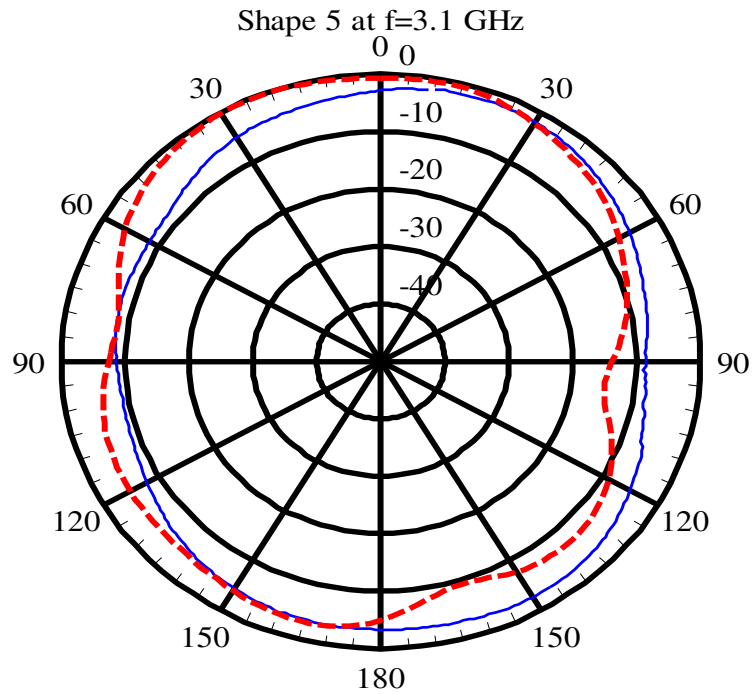


Figure 8.41 The simulated (solid line) and the measured (dotted line) radiation pattern for the reconfigurable antenna

8.6 Conclusion

In this chapter, a new technique to achieve reconfigurable antenna structure is discussed. The idea is based on rotating parts of the antenna patch. This new technique is implemented on reconfigurable antenna for cognitive radio applications. The use of cellular automata, neural network, and rotatable reconfigurable antennas are discussed and elaborated. The importance of this technique is that no switch activation is required.

Concluding remarks about the work that is presented in all the chapters of this dissertation and future work are discussed in the next chapter.

Chapter 9

Conclusions and Future Work

In this dissertation the design, analysis, and implementation of new front-end reconfigurable antenna systems (FERAS) are discussed. Two different configuration techniques are presented. The first one is based on the design of optically reconfigurable antenna systems (OPRAS) where a new light delivery procedure is adopted to activate the switches. The second configuration relies on the implementation of rotatable reconfigurable antenna structures.

The advantage of using these two techniques lies in the fact that they negate the use of bias lines as opposite to RF-MEMS, PIN diodes, lumped elements and varactors. This has the effect of minimizing perturbations affecting the radiation properties of the antenna structure.

Front-End optically and rotatable reconfigurable antenna structures are implemented for cognitive radio environment. This new scenario of wireless communications is gaining lot of attention since it aims to improve the spectrum utilization and minimize the interference between the different types of cognitive radio users.

Characterizing the carrier lifetime of a photoconductive switch using the OPRAS methodology is discussed. This new RF technique is based on capturing the reflected voltage from one of the ports of an optically switched transmission line. The switch is driven by a laser diode via a pulsed current source. The experimental setup is then modified to characterize the turning ON and OFF of an optically reconfigurable antenna system.

Additional steps can be added by extending the work presented in this dissertation.

Such steps are summarized below:

- Controlling the photoconductive switch status via a switching circuit that is integrated within or underneath the antenna substrate and controlled via a microcontroller or a Field Programmable Gate Array (FPGA)
- Extending the light delivery to the photoconductive switches by guiding the laser light through waveguides with the laser flip-chip bonded to the antenna substrate
- Investigating other photoconductive switches by studying the electrical and optical properties of the corresponding materials. The study should be based on the semiconductor band gap energy, the density of states and other physical properties
- Implementing optically reconfigurable antennas/metamaterials using results from the above three steps
- Extending the carrier lifetime measurement technique to include other photoconductive elements
- Improving the performance of the rotatable reconfigurable antenna by incorporating smaller and faster stepper motor

References

- [1] D. Schaubert, "Frequency-agile polarization diversity microstrip antennas and frequency scanned arrays," *US Patent # 4,367,474*, Jan. 1983.
- [2] J. K. Smith, "Reconfigurable aperture antenna (RECAP)," *DARPA*, 1999.
- [3] S. Yang, C. Zhang, H. K. Pan, A. E. Fathy, and V. K. Nair, "Frequency reconfigurable antennas for multiradio wireless platforms," *IEEE Microwave Magazine*, pp. 66- 83, Feb. 2009.
- [4] C. A. Balanis , *Modern Antenna Handbook*, John Wiley and Sons, 2008
- [5] J. T. Bernhard, *Reconfigurable antennas*, Morgan and Claypool Publishers, 2007.
- [6] J. Costantine, "Design, optimization and analysis of reconfigurable antennas," *Ph.D Dissertation*, Dec. 2009.
- [7] A. Patnaik, D. E. Anagnostou, C. G. Christodoulou, and J. C. Lyke, " A frequency reconfigurable antenna design using neural networks," *IEEE Antennas and Propagation Society International Symposium*, pp. 409-412, Jul. 2005.
- [8] G. M. Rebeiz and J. B. Muldavin "RF-MEMS switches and switch circuits," *IEEE Microwave Magazine*, vol. 2, pp. 59-71, 2001.
- [9] www.microsemi.com : Application Notes For PIN Diode
- [10] <http://www.designers-guide.org/Modeling/varactors.pdf>
- [11] P. A. Howson, R. Miller, D. M. Ryder " Photoconductive switch design and applications," *IEEE International Symposium on Electrical Insulation* , pp. 461-464, 1990
- [12] B. A. Cetiner, H. Jafarkhani, J. Qian, H. J. Yoo, A. Grau, and F. De Flaviis, "Multifunctional reconfigurable MEMS integrated antennas for adaptive MIMO systems," *IEEE Communications Magazine*, pp.62-70, Dec. 2004.
- [13] C. W. Jung and F. De Flaviis, "RF-MEMS capacitive series switches of CPW & MSL configurations for reconfigurable antenna application," *IEEE International Symposium on Antennas and Propagation*, pp. 425-428, Jul. 2005.

- [14] E. Erdil, K. Topalli, O. A. Civi, T. Akin, "Reconfigurable CPW-fed dual-frequency rectangular slot antenna using RF MEMS technology," *IEEE International Symposium on Antennas and Propagation*, pp. 392-395, Jul. 2005.
- [15] C. W. Jung, M. Lee, G. P. Li, and F. De Flaviis, "Reconfigurable scan-beam single-arm spiral antenna integrated with RF-MEMS switches," *IEEE Transactions on Antennas and Propagation*, vol. 54, no. 2, pp. 455-463, Feb. 2006.
- [16] D. E. Anagnostou, G. Zheng, M. T. Chryssomallis, J. C. Lyke, G. E. Ponchak, J. Papapolymerou, and C. G. Christodoulou, "Design, fabrication, and measurements of an RF-MEMS based self-similar reconfigurable antenna," *IEEE Transactions on Antennas and Propagation*, vol. 54, no. 2, pp. 422-432, Feb. 2006.
- [17] G. H. Huff and J. T. Bernhard, "Integration of packaged RF MEMS switches with radiation pattern reconfigurable spiral microstrip antennas," *IEEE Transactions on Antennas and Propagation*, vol. 54, no. 2, pp. 464-469, Feb. 2006.
- [18] S. Yang, H. K. Pan, A. E. Fathy, S. El-Ghazaly, and V. N. Nair, "A novel reconfigurable mini-maze antenna for multi-service wireless universal receiver using RF MEMS," *IEEE International Microwave Symposium*, pp. 182-185, Jun. 2006.
- [19] E. Erdil, K. Topalli, M. Unlu, O. A. Civi, and T. Akin, "Frequency tunable patch antenna using RF MEMS technology," *IEEE Transactions on Antennas and Propagation*, vol. 55, no. 4, pp. 1193-1196, Apr. 2007.
- [20] K. Topalli, O. A. Civi, A. Civi, S. Demir, S. Koc, and T. Akin, "Dual-frequency reconfigurable slot dipole array with a CPW based feed network using RF MEMS technology for X- and Ka- band applications," *IEEE International Symposium on Antennas and Propagation*, pp. 825-828, Jul. 2007.
- [21] C. W. Jung, M. -J. Lee, and F. De Flaviis, "Reconfigurable dual-band antenna with high frequency ratio (1.6:1) using MEMS switches," *IEEE Electronics Letters*, vol. 44, no. 2, pp. 76-77, Jan. 2008.
- [22] N. Gokalp and O. A. Civi, "Millimeter-wave frequency reconfigurable slot dipole array with packaged RF-MEMS switches," *3rd European Conference on Antennas and Propagation*, pp. 1334-1336, Mar. 2009.

- [23] S. Nikolaou, N. D. Kingsley, G. E. Ponchak, J. Papapolymerou, and M. M. Tentzeris, "UWB elliptical monopoles with a reconfigurable band notch using MEMS switches actuated without bias lines," *IEEE Transactions on Antennas and Propagation*, vol. 57, no. 8, pp. 2242-2251, Aug. 2009.
- [24] A. Grau, J. Romeu, M. Lee, S. Blanch, L. Jofre, and F. De Flaviis, "A dual linearly polarized MEMS-reconfigurable antenna for narrowband MIMO communication systems," *IEEE Transactions on Antennas and Propagation*, vol. 58, no. 1, pp. 4-16, Jan. 2010.
- [25] B. A. Cetiner, G. R. Crusats, L. Jofre, and N. Biyikli, "RF MEMS integrated frequency reconfigurable annular slot antenna," *IEEE Transactions on Antennas and Propagation*, vol. 58, no. 3, pp. 626-632, Mar. 2010.
- [26] A. Vasychenko, X. Rottenberg, B. X. Broze, M. Nuytemans, W. De Raedt, and G. A. E. Vandenbosch, "A frequency switchable antenna based on MEMS technology," *4th European Conference on Antennas and Propagation*, pp. 1-3, Apr. 2010.
- [27] I. Kim and Y. Rahmat-Samii, "Integrated DC bias line RF MEMS switch for reconfiguring the patch-slot antenna: simulations and measurements," *IEEE International Symposium on Antennas and Propagation*, pp. 1-4, Jul. 2010.
- [28] N. Sepulveda, D. E. Anagnostou, M. T. Chryssomallis, and J. L. Ebel, "Integration of RF-MEMS switches with a band-reject reconfigurable ultra-wideband antenna on SiO₂ substrate," *IEEE International Symposium on Antennas and Propagation*, pp. 1-4, Jul. 2010.
- [29] M. K. Fries, M. Grani, and R. Vahkdieck, "A reconfigurable slot antenna with switchable polarization," *IEEE Microwave and Wireless Components Letters*, vol. 13, no. 11, pp. 490-492, Nov. 2003.
- [30] S. Nikalaou, R. Bairavasubramanian, C. Lugo, I. Carrasquillo, D. C. Thompson, G. E. Ponchak, J. Papapolymerou, and M. M. Tentzeris, "Pattern and frequency reconfigurable annular slot using PIN diodes," *IEEE Transactions on Antennas And Propagation*, vol. 54, no. 2, pp. 439-447, Feb. 2006.

- [31] N. Jin, F. Yang, and Y. Rahmat-Samii, "A novel patch antenna with switchable slot (PASS): dual-frequency operation with reversed circular polarizations," *IEEE Transactions on Antennas and Propagation*, vol. 54, no. 4, pp.1031-1043, Mar. 2006.
- [32] S.-H. Chen, J.-S. Row, and K.-L Wong, "Reconfigurable square-ring patch antenna with pattern diversity," *IEEE Transactions on Antennas and Propagation*, vol. 55, no. 2, pp. 472-475, Feb. 2007.
- [33] M. Donelli, R. Azaro, L. Fimognari, and A. Massa, "A planar electronically reconfigurable Wi-Fi band antenna based on a parasitic microstrip structure," *IEEE Antennas and Wireless Propagation Letters*, vol. 6, pp. 623-626, 2007.
- [34] B. Poussot, J.-M Laheurte, L. Cirio, O. Picon, D. Delcroix, and L. Dussopt, "Diversity measurements of a reconfigurable antenna with switched polarizations and patterns," *IEEE Transactions on Antennas and Propagation*, vol. 56, no. 1, Jan. 2008.
- [35] W. S. Kang, J. A. Park, and Y. J. Yoon, "Simple reconfigurable antenna with radiation pattern," *IEEE Electronics Letters*, vol. 44, no. 3, pp. 182-183, Jan. 2008.
- [36] S.-J. Wu and T.-G. Ma, "A wideband slotted bow-tie antenna with reconfigurable CPW-to slotline transition for pattern diversity," *IEEE Transactions on Antennas and Propagation*, vol. 56, no. 2, Feb. 2008.
- [37] B. Kim, B. Pan, S. Nikolaou, Y.-S Kim, J. Papapolymerou, M. M. Tentzeris, "A novel single-feed circular microstrip antenna with reconfigurable polarization capability," *IEEE Transactions on Antennas and Propagation*, vol. 56, no. 3, pp. 630-638, Mar. 2008.
- [38] R.-H Chen and J.-S Row, "Sing-fed microstrip patch antenna with switchable polarization," *IEEE Transactions on Antennas and Propagation*, vol. 56, no. 4, pp. 922-926, Apr. 2008.
- [39] Y. J. Sung, "Reconfigurable patch antenna for polarization diversity," *IEEE Transactions on Antennas and Propagation*, vol. 56, no. 9, pp. 3053-3054, Sep. 2008.
- [40] J. Sarrazin, Y. Mahe, S. Avrillon, and S. Toutain, "Pattern reconfigurable cubic antenna," *IEEE Transactions on Antennas and Propagation*, vol. 57, no. 2, pp. 310-317, Feb. 2009.

- [41] M.-I. Lai, T.-Y. Wu, J.-C Hsieh, C.-H Wang, and S.-K Jeng, "Design of reconfigurable antennas based on an L-shaped slot and PIN diodes for compact wireless devices," *IET Microwave and Antennas Propagation*, vol. 3, no. 1, pp. 47-54, 2009.
- [42] S. W. Yoon; L. H. Truong; H. S. Lee, E. J. Park, H. M. Park, J. K. Rhee, H. C. Park, "UWB antenna with frequency diversity characteristics using PIN-diode switches," *International Conference on Advanced Communication Technology*, vol. 1, pp. 344-346, Feb. 2009.
- [43] W. -C. Wu, J.-S. Row, T.-Y. Han, and C.-Y.-D. Sim, "An aperture-coupled microstrip antenna with frequency agility and polarization diversity," *Asia Pacific Microwave Conference*, pp. 763-765, Dec. 2009.
- [44] K.-H. Chen, S.-J. Wu, C.-H. Kang, C.-K. Chan and J.-H. Tarng, "A frequency reconfigurable slot antenna using PIN diodes," *Asia Pacific Microwave Symposium*, pp. 1930-1933, Dec. 2009.
- [45] T. -Y. Han and C. -T. Huang, "Reconfigurable monopolar patch antenna," *IEEE Electronics Letters*, vol. 46, no. 3, pp. 199- 200, Feb. 2010.
- [46] M. R. Hamid, P. S. Hall, P. Gardner, and F. Ghanem, "Frequency reconfigurable Vivaldi antenna," *4th European Conference on Antennas and Propagation*, pp. 1-4, April 2010.
- [47] P. Y. Qin, A. R. Weily, Y. J. Guo, C. H. Liang, Y. Cai, "A pattern reconfigurable U-slot patch antenna," *IEEE International Symposium on Antennas and Propagation*, pp. 1-4, Jul. 2010.
- [48] J. Perruisseau-Carrier, P. Pardo-Carrera, and P. Miskovsky, "Modeling, design and characterization of a very wideband slot antenna with reconfigurable band rejection," *IEEE Transactions on Antennas and Propagation*, vol. 58, no. 7, pp. 2218-2226, Jul. 2010.
- [49] P.-Y. Qin, A. R. Weily, Y. J. Guo, T. S. Bird, and C.-H. Liang, "Frequency reconfigurable quasi-yagi folded dipole antenna," *IEEE Transactions on Antennas and Propagation*, vol. 58, no. 8, pp. 2742-2747, Aug. 2010.

- [50] I. Tekin and M. Knox, "Reconfigurable dual band microstrip patch antenna for software defined radio applications," *IEEE International Conference on Wireless Information Technology*, pp. 1-4, Aug. 2010.
- [51] N. Behdad and K. Sarabandi, "A varactor-tuned dual-band slot antenna," *IEEE Transactions on Antennas and Propagation*, vol. 54, no. 2, pp. 401-408, Feb. 2006.
- [52] E. A.-Daviu, M. C.-Fabres, M. F.-Bataller, and A. V.-Jimenez, "Active UWB antenna with tunable band-notched behavior," *IEEE Electronics Letters*, vol. 43, no. 18, pp.959-960, Aug. 2007.
- [53] W.-S. Jeong, S.-Y. Lee, W.-G. Lim, H. Lim, J.-W. Yu, "Tunable band-notched ultra wideband (UWB) planar monopole antennas using varactor," 38th European Microwave Conference, pp. 266-268, Oct. 2008.
- [54] C. R. White and G. M. Rbeiz, "Single and dual-polarized tunable slot-ring antennas," *IEEE Transactions on Antennas and Propagation*, vol. 57, no. 1, pp. 19-26, Jan. 2009.
- [55] H. Jiang, M. Patterson, C. Zhang, and G. Subramanyan, "Frequency tunable microstrip patch antenna using ferroelectric thin film varactor," *IEEE National Aerospace & Electronics Conference*, pp. 248-250, Jul. 2009.
- [56] S.-S. Oh, Y.-B. Jung, Y. -R. Ju, and H.-D. Park, "Frequency-tunable open ring microstrip antenna using varactor," *International Conference on Electromagnetics in Advanced Applications*, pp. 624-626, Sept. 2010.
- [57] A. S. Daryoush, K. Bontzos, and P. R. Herczfeld, "Optically tuned patch antenna for phased array applications," *IEEE International Symposium on Antennas and Propagation*, pp. 361-364, Jun. 1986.
- [58] P. A. Howson, R. Miller, D. M. Ryder, "Photoconductive Switch Design and Applications," *IEEE International Symposium on Electrical Insulation*, pp. 461-464, 1990.
- [59] D. Liu, D. Charette, M. Bergeron, H. Karwacki, S. Adams, B. Lanning, and F. kustas, "Structurally embedded photoconductive silicon bowtie antenna", *IEEE Photonics Technology Letters*, vol. 10, no. 5, May 1998.

- [60] M. L. VanBlaricum, "Photonic antenna reconfiguration: a status survey," *Proceedings of the SPIE, Photonics and Radio frequency*, pp. 180-189, Jul. 1998.
- [61] C. J. Panagamuwa and J. C. Vardaxoglou, "Optically reconfigurable balanced dipole antenna," *International Conference on Antennas and Propagation*, pp. 237-240, Apr. 2003.
- [62] L. N. Pringle, P. H. Harms, S. P. Blalock, G. N. Kiesel, E. J. Kuster, P. G. Friederich, R. J. Prado, J. M. Morris, and G. S. Smith, "A reconfigurable aperture antenna based on switched links between electrically small metallic patches," *IEEE Transactions on Antennas and Propagation*, vol. 52, no. 6, pp. 1434-1445, Jun. 2004.
- [63] C. J. Panagamuwa, A. Chauraya, and J. C. Vardaxoglou, "Frequency and beam reconfigurable antenna using photoconductive switches," *IEEE Transactions on Antennas and Propagation*, vol. 54, no. 2, Feb. 2006.
- [64] R. P. Tuffin, I. C. Sage, B. J. Hughes, and G. J. Ball, "Electronically controlled metamorphic antenna," *4th EMRS DTC Technical Conference*, pp. A9, 2007.
- [65] Y. Yashchyshyn and J. Modelski, "Reconfigurable semiconductor antenna," *International Conference on CAD Systems in Microelectronics*, pp. 146-150, Feb. 2007.
- [66] P.-J. Liu, D.-S. Zhao, and B.-Z. Wang, "Design of optically controlled microwave switch for reconfigurable antenna systems," *International Conference on Microwave and Millimeter Wave Technology*, pp. 1-4, Apr. 2007.
- [67] R. L. Haupt and J. R. Flemish, "Reconfigurable and adaptive antennas using materials with variable conductivity," *Second NASA/ESA Conference on Adaptive Hardware and Systems*, pp. 20-23, Aug. 2007.
- [68] B. J. Hughes, I. C. Sage, and G. J. Ball, "Optically controlled metamorphic antenna," *5th EMRS DTC Technical Conference*, pp. B24, 2008.
- [69] R. N. Lavalley and B. A. Lail, "Optically-controlled reconfigurable microstrip patch antenna," *IEEE International Symposium on Antennas and Propagation*, pp. 1-4, Jun. 2008.

- [70] A. Karabegovic, R. M. O'Connell, and W. C. Nunnally, "Photoconductive switch design for microwave applications," *IEEE Transactions on Dielectrics and Electrical Insulation*, vol. 16, no. 4, pp. 1011-1019, Aug. 2009.
- [71] J. R. Reid, J. S. Derov, and P. H. Carr, "Spatially light modulated reconfigurable photoconductive antenna," *US Patent 6,177,909 B1*, Jan. 2001.
- [72] M. J. Morant, "Introduction to semiconductor devices," *Addison Wesley Publishing Company*, 1964.
- [73] R. F. Pierret, *Semiconductor Fundamentals*, *Addison Wesley Publishing Company*, 1989.
- [74] B. E. A. Saleh and M. C. Teich, *Fundamentals of photonics*, *John Wiley & Sons*, Second Edition, 2007.
- [75] S. M. Sze, *Physics of semiconductor devices*, *John Wiley & Sons*, 1981.
- [76] C. Kittel, "Introduction to solid state physics," *John Wiley & Sons*, Seventh Edition 1996.
- [77] C. A. Balanis, "Advanced engineering electromagnetic", *John Wiley & Sons*, 1989.
- [78] R. S. Muller, T. I. Kamins, and M. Chan, "Device electronics for integrated circuits", *John Wiley & Sons*, Third Edition, Oct. 2003.
- [79] Y. Tawk, A. R. Albrecht, S. Hemmady, G. Balakrishnan, and C. G. Christodoulou, "Optically pumped frequency reconfigurable antenna design," *IEEE Antennas and Wireless Propagation Letters*, Vol. 9, pp. 280-283, Mar. 2010.
- [80] Y. Tawk, A. R. Albrecht, S. Hemmady, G. Balakrishnan, and C. G. Christodoulou, "Optically pumped reconfigurable antenna systems (OPRAS)," *IEEE International Symposium on Antennas and Propagation*, pp. 1-4, Jul. 2010.
- [81] C. H. Lee, P. S. Mak, and A. P. DeFonzo, "Optical control of millimeter-wave propagation in dielectric waveguides," *IEEE Journal of Quantum Electronics*, vol. QE-16, no. 3, Mar. 1980.
- [82] Y. Tawk, M. El-Husseini, A. R. Albrecht, S. Hemmady, G. Balakrishnan, and C. G. Christodoulou, "Implementation of a cognitive radio front-end using optically

- reconfigurable antennas,” *International Conference on Electromagnetics in Advanced Applications (ICEAA)*, pp. 294-297, Sep. 2010.
- [83] Y. Tawk, J. Costantine, S. E. Barbin, and C. G. Christodoulou, “Front-End optically reconfigurable antenna system,” *5th European Conference on Antennas and Propagation*, Apr. 2011.
- [84] C. Balanis, *Antenna theory and design*, John Wiley & Sons, Third Edition 2005.
- [85] J. A. Stratton, *Electromagnetic theory*, John Wiley & Sons, 2007.
- [86] S. Silver, *Microwave antenna theory and design*, IEE *Electromagnetic Waves Series*, 1997.
- [87] Q. Zhao and B. M. Sadler, “A survey of dynamic spectrum access,” *IEEE Signal Processing Magazine*, vol. 24, no. 3, pp. 79–89, May 2007.
- [88] FCC, “Report of the spectrum efficiency working group,” FCC spectrum policy task force, Tech. Rep., Nov. 2002.
- [89] ———, “ET docket no 03-322 notice of proposed rulemaking and order,” Tech. Rep., Dec. 2003.
- [90] K.-L. Yau, P. Komisarczuk, and P. Teal, “A context-aware and intelligent dynamic channel selection scheme for cognitive radio networks,” *4th International Conference on Cognitive Radio Oriented Wireless Networks and Communications*, pp. 1–6, June 2009.
- [91] J. Mitola, “Cognitive radio: An integrated agent architecture for software defined radio,” Ph.D. dissertation, Royal Institute of Technology (KTH), Stockholm, Sweden, 2000.
- [92] S. Haykin, “Cognitive radio: Brain-empowered wireless communications,” *IEEE Journal on Selected Areas in Communications*, vol. 23, no. 2, pp. 201–220, Feb. 2005.
- [93] S. Jayaweera and C. Mosquera, “A dynamic spectrum leasing (DSL) framework for spectrum sharing in cognitive radio networks,” *Conference Record of the Forty-Third Asilomar Conference on Signals, Systems and Computers*, pp. 1819–1823, Nov. 2009.

- [94] A. Molisch, L. Greenstein, and M. Shafi, "Propagation issues for cognitive radio," *Proceedings of the IEEE*, vol. 97, no. 5, pp. 787–804, May 2009.
- [95] W. Lehr and J. Crowcroft, "Managing shared access to a spectrum commons," *First IEEE International Symposium on New Frontiers in Dynamic Spectrum Access Networks*, pp. 420-444, Nov. 2005.
- [96] R. Etkin, A. Parekh, and D. Tse, "Spectrum sharing for unlicensed bands," *IEEE Journal on Selected Areas in Communications*, vol. 25, no. 3, pp. 517–528, Apr. 2007.
- [97] A. Goldsmith, S. Jafar, I. Maric, and S. Srinivasa, "Breaking spectrum gridlock with cognitive radios: An information theoretic perspective," *Proceedings of the IEEE*, vol. 97, no. 5, pp. 894–914, May 2009.
- [98] S. K. Jayaweera, G. Vazquez-Vilar, and C. Mosquera, "Dynamic spectrum leasing: A new paradigm for spectrum sharing in cognitive radio networks," *IEEE Transactions on Vehicular Technology*, vol. 59, no. 5, pp. 2328–2339, June 2010.
- [99] Y.-E. Lin, K.-H. Liu, and H.-Y. Hsieh, "Design of power control protocols for spectrum sharing in cognitive radio networks: A game-theoretic perspective," *IEEE International Conference on Communications (ICC'10)*, pp. 1–6, May 2010.
- [100] "The Next Generation Program," <http://www.darpa.mil/sto/smallunitops/xg.html>.
- [101] Q. Xiao, Q. Gao, L. Xiao, S. Zhou, and J. Wang, "An Optimal Opportunistic Spectrum Access Approach," *IEEE International Conference on Communications Workshops*, pp. 1–5, 2009.
- [102] A. T. Hoang, Y.-C. Liang, D. Wong, Y. Zeng, and R. Zhang, "Opportunistic spectrum access for energy-constrained cognitive radios," *IEEE Transactions on Wireless Communications*, vol. 8, no. 3, pp. 1206–1211, Mar. 2009.
- [103] L. Pillutla and V. Krishnamurthy, "Game theoretic rate adaptation for spectrum-overlay cognitive radio networks," in *IEEE Global Telecommunications Conference (GLOBECOM'08)*, pp. 1-5, Nov. 2008.
- [104] C. G. Christodoulou, "Cognitive Radio: The New Frontier for Antenna Design," *IEEE Antennas and Propagation Society Feature Article*, www.ieeeaps.org, 2009.

- [105] Y. Tawk, S. Hemmady, G. Balakrishnan, and C. G. Christodoulou, "Demonstration of a cognitive radio front-end using optically pumped reconfigurable antenna systems (OPRAS)," *submitted to the IEEE Transaction on Antennas and Propagation*.
- [106] Y. Tawk, and C. G. Christodoulou, "A new reconfigurable antenna design for cognitive radio applications," *IEEE Antennas and Wireless Propagation Letters*, vol. 8, pp. 1378-1381, Dec. 2009.
- [107] Y. Tawk, M. Bkassiny, G. El-Howayek, S. K. Jayaweera, and C. G. Christodoulou, "Reconfigurable antenna for cognitive radio application," *Accepted for publication in the IEE Proceedings IET Microwaves, Antennas and Propagation*, Nov. 2010.
- [108] Y. Tawk, S. Hemmady, G. Balakrishnan, and C. G. Christodoulou, "A cognitive Radio antenna design based on optically pumped reconfigurable antenna system (OPRAS)," *submitted to the IEEE International Symposium on Antennas and Propagation*, Jul. 2011.
- [109] A. Carton, C. G. Christodoulou, C. Dyck and C. Nordquist "Investigating the impact of Carbon Contamination on RF MEMS Reliability," *IEEE Antennas and Propagation International Symposium*, pp.193-196, Jul. 2006.
- [110] R. H. Caverly and G. Hiller, "Distortion properties of MESFET and PIN diode microwave switches," *IEEE MTT-S International Microwave Symposium*, pp. 533-536, vol. 2, Jun. 1992.
- [111] Y. Yashchyshyn, "Reconfigurable antennas by RF switches technology," *5th International Conference on Perspective Technologies and Methods in MEMS design*, pp. 155-157, Apr. 2009.
- [112] G. M. Rebeiz, RF MEMS Theory, Design, and Technology, *John Wiley and Sons*, 2003.
- [113] Y. Tawk, S. Hemmady, C. G. Christodoulou, J. Costantine, and G. Balakrishnan, "A cognitive radio antenna design based on optically pumped reconfigurable antenna system (OPRAS)," *submitted to IEEE International Symposium on Antennas and Propagation*, Jul. 2011.

- [114] D. K. Schroder, "The concept of generation and recombination lifetimes in semiconductors," *IEEE Transaction on Electron Devices*, vol. ED-29, pp. 1336-1338, Aug. 1982.
- [115] D. K. Schroder, "Carrier lifetime in silicon," *IEEE Transaction on Electron Devices*, vol. 44, no. 1, pp. 160-170, Jan. 1997.
- [116] R. N. Hall, "Electron-hole recombination in germanium," *Physical Review*, vol. 87, pp. 387, Jul. 1952.
- [117] W. Shockley and W. T. Read, "Statistics of the recombination of holes and electrons," *Physical Review*, vol. 87, pp. 835-842, Sep. 1952.
- [118] R. N. Hall, "Recombination processes in semiconductors," *IEE Proceedings*, vol. 106B, pp. 923-931, Mar. 1960.
- [119] D. K. Schroder, *Semiconductor material and device characterization*, New York: Wiley, 1990.
- [120] S. K. Pang and A. Rohatgi, "Record high recombination lifetime in oxidized magnetic Czochralski silicon," *Applied Physics Letters*, vol. 59, pp. 195-197, Jul. 1991.
- [121] D. K. Schroder, J. D. Whitfield, and C. J. Varker, "Recombination lifetime using the pulsed MOS capacitor," *IEEE Transaction Electron Devices*, vol. ED-31, pp. 463-467, Apr. 1984.
- [122] F. P. Giles and R. J. Schwartz, "Computational separation of bulk and surface recombination using contactless photoconductive decay," *ECE Technical Report*, Purdue University, 1996.
- [123] M. C. Chen, "Photoconductivity lifetime measurements on HgCdTe using a contactless microwave technique," *Journal of Applied Physics*, vol. 64, pp. 945-947, Jul. 1988.
- [124] P. A. Basore and B. R. Hansen, "Microwave-detected photoconductance decay," *IEEE Photovoltaic Conference*, pp. 374-379, May 1990.
- [125] M. Kunst and G. Beck, "The study of charge carrier kinetics in semiconductors by microwave conductivity measurements," *Journal of Applied Physics*, vol. 60, pp. 3558-3566, Nov. 1986.

- [126] D. C. Gupta, F. R. Bacher, and W. M. Hughes, Recombination lifetime measurements in silicon, *American Society for Testing and Materials*, Jul. 1998.
- [127] Y. Tawk, S. Hemmady, G. Balakrishnan, and C. G. Christodoulou, "Measuring the transition switching speed of a semiconductor-based photoconductive switch using RF techniques," *IEEE International Symposium on Antennas and Propagation*, Jul. 2011.
- [128] Y. Tawk, J. Costantine, S. Hemmady, G. Balakrishnan, and C. G. Christodoulou, "An RF technique for measuring the switching time of a silicon based photoconductive switch," *submitted to the IEEE Microwave and Wireless Components Letters*.
- [129] Y. Tawk, J. Costantine, S. E. Barbin, and C. G. Christodoulou, "Front end optically reconfigurable antenna system," *5th European Conference on Antennas and Propagation*, Apr. 2011.
- [130] D. M. Pozar, Microwave Engineering, *John Wiley & Sons*, 3rd edition, 2008.
- [131] Y. Tawk, J. Costantine, and C. G. Christodoulou, "A frequency reconfigurable rotatable microstrip antenna design," *IEEE International Symposium on Antennas and Propagation*, pp. 1-4, Jul. 2010.
- [132] Y. Tawk, and C. G. Christodoulou "A cellular automata reconfigurable microstrip antenna design," *IEEE International Symposium on Antennas and Propagation*, pp. 1-4, Jun. 2009.
- [133] H.-O. Peitgen, H. Jurgens and D. Saupe, Chaos and Fractals New Frontiers of Science, *Springer*, 2004.
- [134] J. D. Lohn and J. A. Reggia, "Automatic discovery of self-replicating structures in cellular automata," *IEEE transactions on Evolutionary Computation*, vol. 1, pp 165-178, 1997.
- [135] J. D. Lohn, "Automated discovery of self-replicating structures in cellular space automata models", *Dept. of Computer Science Tech. Report CS-TR-3677*, Univ. of Maryland at College Park, 1996.
- [136] M. Hall, Combinatorial Theory, *Waltham, MA: Blaisdell Publishing*, 1967.

- [137] J. D. Lohn, H-H Chou, and J. A. Reggia, "Cellular automata models of self-replicating systems", in *Advances in Computers*, Academic Press, New York, vol. 47, pp. 141-183, 1998.
- [138] Y. Tawk, J. Costantine, S. E. Barbin, and C. G. Christodoulou, "A multi-band microstrip antenna design using cellular automata and Fuzzy ARTMAP Neural Network," *3rd European Conference on Antennas and Propagation*, pp.23-27, Mar. 2009.
- [139] C. G. Christodoulou, M. Georgiopoulos, *Applications of Neural Networks in Electromagnetics*, Artech House, 2001.
- [140] Y. Tawk and C. G. Christodoulou, "A new reconfigurable antenna design for cognitive radio applications," *IEEE Antennas and Wireless Propagation Letters*, Vol. 8, pp. 1378-1381, Dec. 2009.
- [141] Y. Tawk, J. Costantine, and C. G. Christodoulou, "A Rotatable reconfigurable antenna for cognitive radio applications," *IEEE Radio and Wireless Symposium*, Jan. 2011.
- [142] Y. Tawk, J. Costantine, K. Avery, and C. G. Christodoulou, "Implementation of a cognitive radio front-end using rotatable controlled reconfigurable antenna," *To Appear in the IEEE Transaction on Antennas and Propagation*, 2011.
- [143] <http://www.digikey.com>
- [144] http://www.datasheetcatalog.com/datasheets_pdf/U/L/N/2/ULN2003A.shtml